Defense Nuclear Agency
Alexandria, VA 22310-3398

DNA-TR-95-59-V1

Advanced Simulator Power Flow Technology/Advanced Radiation Simulation
Volume 1—POS and Power Flow Modeling and Experiments

Don Parks, et al.
Maxwell Laboratories Inc
S-Cubed Division
P.O. Box 1620
La Jolla, CA 92038-1620

March 1996

Technical Report

CONTRACT No. DNA 001-93-C-0229

Approved for public release;
distribution is unlimited.

19960319034

DESTRUCTION NOTICE:

Destroy this report when it is no longer needed.
Do not return to sender.

PLEASE NOTIFY THE DEFENSE SPECIAL WEAPONS
AGENCY, ATTN: CSTI, 6801TELEGRAPH ROAD,
ALEXANDRIA, VA 22310-3398, IF YOUR ADDRESS IS
INCORRECT, IF YOU WISH IT DELETED FROM THE
DISTRIBUTION LIST, OR IF THE ADDRESSEE IS NO
LONGER EMPLOYED BY YOUR ORGANIZATION.

DSWA

DISTRIBUTION LIST UPDATE

This mailer is provided to enable DNA to maintain current distribution lists for reports. (We would appreciate your providing the requested information.)

☐ Add the individual listed to your distribution list.

☐ Delete the cited organization/individual.

☐ Change of address.

NOTE:
Please return the mailing label from the document so that any additions, changes, corrections or deletions can be made easily. For distribution cancellation or more information call DNA/IMAS (703) 325-1036.

NAME: _____

ORGANIZATION: _____

OLD ADDRESS	**CURRENT ADDRESS**
_____	_____
_____	_____
_____	_____

TELEPHONE NUMBER: ( ) _____

DNA PUBLICATION NUMBER/TITLE	**CHANGES/DELETIONS/ADDITIONS, etc.)** *(Attach Sheet if more Space is Required)*
_____	_____
_____	_____
_____	_____

DNA OR OTHER GOVERNMENT CONTRACT NUMBER: _____

CERTIFICATION OF NEED-TO-KNOW BY GOVERNMENT SPONSOR (if other than DNA):

SPONSORING ORGANIZATION: _____

CONTRACTING OFFICER OR REPRESENTATIVE: _____

SIGNATURE: _____

CUT HERE AND RETURN

DEFENSE NUCLEAR AGENCY
ATTN: TITL
6801 TELEGRAPH ROAD
ALEXANDRIA, VA 22310-3398

ERRATA

for

DNA-TR-95-59

UNCLASSIFIED

Advance Simulator Power Flow Technology/Advance Radiation Simulation

Since this report was published additional information has been added on the front cover and the SF 298.
The title should have the following subtitle: Volume 1—POS and Power Flow Modeling and Experiments.
The TR number should read: DNA-TR-95-59-V1.

Please insert the corrected cover and SF 298 provided.

19960319034

REPORT DOCUMENTATION PAGE

1. AGENCY USE ONLY (Leave blank)	2. REPORT DATE 960301	3. REPORT TYPE AND DATES COVERED Technical 931001 – 940930

4. TITLE AND SUBTITLE
Advanced Simulator Power Flow Technology/Advanced Radiation Simulation Volume 1—POS and Power Flow Modeling and Experiments

6. AUTHOR(S)
Don Parks, Randall Ingermanson, Eric Salberta, Paul Steen and Jack Thompson

5. FUNDING NUMBERS
C - DNA 001-93-C-0229
PE - 4662
PR - AB
TA - AJ
WU - DH341660

7. PERFORMING ORGANIZATION NAME(S) AND ADDRESS(ES)
Maxwell Laboratories Inc
S-Cubed Division
P.O. Box 1620
La Jolla, CA 92038-1620

8. PERFORMING ORGANIZATION REPORT NUMBER
SSS-DTRI-94-14855

9. SPONSORING/MONITORING AGENCY NAME(S) AND ADDRESS(ES)
Defense Nuclear Agency
6801 Telegraph Road
Alexandria, VA 22310-3398
RAST\Filios

10. SPONSORING/MONITORING AGENCY REPORT NUMBER
DNA-TR-95-59-V1

11. SUPPLEMENTARY NOTES
This work was sponsored by the Defense Nuclear Agency under RDT&E RMC Code B4662D GE 00011 3200A AB 25904D.

12a. DISTRIBUTION/AVAILABILITY STATEMENT

Approved for public release; distribution is unlimited.

12b. DISTRIBUTION CODE

13. ABSTRACT (Maximum 200 words)
This report describes work conducted in FY 94 for the Advanced Simulator Power Flow Technology/Advanced Radiation Simulation Program. The report deals with analytical, computational and experimental studies of power flow in vacuum feed and switch regions of power, inductive energy store systems. The first section describes a method for the calculation of magnetic fields and inductances in 3-D convolute geometry, and results for convolute vacuum fields in ACE-4 and in SATURN. Section 2 describes hydrodynamic calculations of the evolution of the switch plasma without pulsed power and compares the computed and measured densities. Section 3 concerns the effect of insulated electron flow on gag formation in a switch, and the ultimate fate of the launched electrons as they drift from the switch into the vacuum feed. Section 4 summarizes improvements in our snowplow, circuit analysis and mesh generation codes. In Section 5, power flow experiments, techniques used to measure electron density and other plasma characteristics are described. The characteristics of the ACE-4 radial and coaxial plasma opening switches are measured, and the results compared with analogous results obtained from the HAWK generator at the Naval Research Laboratory, and with results calculated by means of the snowplow code.

14. SUBJECT TERMS
Pulsed Power
Above Ground Simulation
Plasma Open Switch
Inductive Energy Store

15. NUMBER OF PAGES 174

16. PRICE CODE

17. SECURITY CLASSIFICATION OF REPORT UNCLASSIFIED	18. SECURITY CLASSIFICATION OF THIS PAGE UNCLASSIFIED	19. SECURITY CLASSIFICATION OF ABSTRACT UNCLASSIFIED	20. LIMITATION OF ABSTRACT SAR

i

CLASSIFIED BY:

N/A since Unclassified.

DECLASSIFY ON:

N/A since Unclassified.

DISCLAIMER NOTICE

UNCLASSIFIED

Technical Report
distributed by

DEFENSE
TECHNICAL
INFORMATION
CENTER

DTIC Acquiring Information
Preparing Knowledge

Alexandria, Virginia 22304-6145

UNCLASSIFIED

THIS DOCUMENT IS BEST QUALITY AVAILABLE. THE COPY FURNISHED TO DTIC CONTAINED A SIGNIFICANT NUMBER OF PAGES WHICH DO NOT REPRODUCE LEGIBLY.

SUMMARY

This report describes work carried out in Fiscal Year 1994 (FY'94) under contract DNA001-93-C-0229, the first year of a three-year program titled *Advanced Simulator Power Flow Technology for Advanced Radiation Simulation.*

The objective of the program is to model, design and validate means for achieving more efficient power transfer form the capacitor prime energy storage systems up to and including the dynamic radiation source of the simulator. This report deals primarily with analytical, computational and experimental studies related to this objective, focusing primarily on power flow in the plasma opening switch and in the vacuum feed region separating switch and load regions in pulsed power, inductive energy store systems.

In generators such as ACE-4 (Section 5.1.1) and SATURN, the power flow in multiple transmission lines join through a convolute before coupling into a plasma radiating source (PRS). Potentially significant loss of power through leakage current can result from loss of magnetic insulation in the neighborhood of magnetic nulls, and generally, in regions of weak magnetic field. Section 1 describes a computer code, based on boundary element methods for the calculation of magnetic (and electric) fields in complex three-dimensional convolute structures. It has been applied to the calculation of fields and inductances of existing ACE-4 and SATURN convolutes, and will, in the future be used for the design of improved convolutes for ACE-4.

During FY'94, substantial effort was committed to computational analysis of the dynamics of the POS plasma prior to the application of pulsed power. Knowledge of the plasma state, in particular, the density profile from cathode to anode, is important, as explained in Section 5, for designing switches which can both conduct for one microsecond or longer and then open rapidly to a high impedance. While high density favors a long conduction time, a low one favors rapid opening. The transition from the high density initial condition to the low density final state can be influenced by the initial distribution of plasma mass in the A-K gap, as well as by geometrical and other design factors.

Techniques of laser interferometry applied to the measurement of the plasma produced by the ACE-4 flashboards gave direct results for line integrated electron densities in the anode-cathode gap, a well as outside the gap in the region extending from the anode to the flash-boards. Measured line integrated density in the A-K gap as a function of distance from the cathode was used to validate, at least partially, our ability to calculate redistribution of plasma mass between the instants of injection and the application of pulsed power. Density data measured at the probe nearest the anode (the anode probe) provide a time-dependent boundary condition for a hydro-dynamic calculation of the fluid properties in the gap. The velocity and temperature of the assumed ideal gas at the anode probe can be chosen to give good agreement between most features of the time-dependent line integral density measured at other probes. At each location, the calculations agree with the measured results up to the time that the measurements indicate that reflection from the cathode causes a disturbance at this location. The reflected signal arrives at a given probe location in a time that can be reconciled with

the calculated time only if the plasma is assumed to cool, on contact with the cathode, to a temperature substantially less than that of the incident plasma. From the late arrival time one infers as well that the plasma, having contacted the surface, rebounds with a speed low compared to that of the incident plasma, and a density within a few millimeters of the cathode that is several times higher than that elsewhere in the plasma. If not recognized, phase shifts produced in the laser light by the ions and neutrals in this dense plasma can lead to substantial underestimates of electron density by techniques of single-color interferometry, and render difficult the determinations of densities of heavy particles. This latter difficulty, in turn, contributes a large uncertainty in the distribution of plasma mass in the switch throughout the conduction phase and at the onset of the opening phase. The spectroscopic methods discussed later can help to reduce, if not completely remove this uncertainty.

The opening model, considered in Section 3, is based on the concept of gap formation by erosion of the switch plasma in the state that exists at the end of the conduction phase. The gap formation rate depends on plasma parameters such as ion density and ion thermal speed at the time opening begins. None of these parameters are easy to measure. For this reason alone opening models are much more difficult than conduction models to validate completely by means of experiments, although predicted scaling of switch limited voltage with cathode radius, for example, can be examined experimentally.

PIC calculations are invoked in Section 3 to examine the accuracy of the model used to predict gap voltage for a given gap size and generator current. The model gives a self-consistent relation between voltage, current and gap size for the case of energy conserving, Brillouin drift of electrons in a sheath adjacent to and parallel with the cathode surface. Within this context, the model compares favorably with PIC calculations. The theory is extended to take account of space charge limited ion flow across the gap.

Although the theory does not consider the ultimate fate of electrons drifting in the gap, the PIC calculations do. For switch limited operation, that is for a high impedance load, most of the drifting electrons strike the anode in the vacuum feed downstream of the switch (Figure 3.8). This could lead to the production of an anode plasma, and the injection of ions into the vacuum feed. This would be a source of plasma in the feed that is additional to the switch plasma. When the load impedance is reduced to match the switch impedance, the drifting electrons form a diamagnetic current loop in the vacuum feed downstream of the switch, but electrons still strike the anode. About one-half of the generator current is lost, the other half goes into the load. It is important to understand and quantify these effects in order to optimize current transfer into a load.

Section 5 describes power flow experiments conducted during FY'94. Interferometry was performed with pulsed power for the first time on the ACE-4 with a radial POS. Characterization of the time evolution of the measured integrated electron line densities was made both with and without pulsed power. The measurements were made using a fast plasma flashboard source in the radial POS geometry. Interferometric measurements were made in the radial line of sight, along the direction of power flow. A comparison with predicted snowplow model time evolution of $\int n_e dl$ showed significant disagreement, even considering the magnitude of

iv

uncertainty of the measurement near the time of switch opening. This is not understood at this time but may be related to temporal or spatial dependence of the average ionization states used to infer the mass distribution from the measured integrated electron line densities, or to snowplow model boundary conditions. This issue must be clarified before a well-validated model of the conduction phase of the POS is in hand.

Coaxial POS experiments on ACE-4 have been performed which provide new insight into understanding how plasma thinning and downstream geometry may affect long conduction time opening switches. A phenomenological model to explain the observed POS operation with and without a transition region downstream of the POS has been proposed that is consistent with the observed plasma and electrical measurements. The model assumes that current is carried downstream of the POS injection region by the plasma channel, which exists at the end of the snowplow process in the POS injection region. Although some plasma leakage downstream without pulsed power is observed it appears not to dominate the downstream current propagation process. Interferometry suggests that in the case of the standard ACE-4 coaxial POS, thinning near the end of the POS injection region is insufficient to allow opening there. This model does not specifically address the opening process that occurs when the plasma channel finally thins sufficiently for the POS to open. The existing snowplow model underestimates the integrated electron density near the cathode. This may be due to densities near the cathode that are higher than measured because of the buildup of neutrals, or because of a modification to the snowplow front due to mass introduction from the cathode. This mass could be associated with actual cathode material or stagnation of snowplowed POS plasma at the cathode surface. A series of experiments both in the test stand and in ACE-4 are planned to address the measurement and modeling questions raised in this report.

Optical spectroscopy is well-suited for the determination of the state of ionization of the plasma and the electron temperature. In Section 5.7 both time-integrated and time-resolved spectroscopy are applied for this purpose. The survey of spectral lines from time integrated spectroscopy indicates that the flashboard-produced plasma contained singly and doubly ionized carbon and fluorine, and hydrogen. Roughing pump oil is thought to be the main source of hydrogen. The intensity of hydrogen lines varied considerably between the different series of measurements and may be correlated with the quality of vacuum or how recent the vacuum chamber was pumped down after opening. Most measurements were made for the flashboard plasma, but the data obtained for the cable guns indicate that all of the plasmas were of similar composition.

The ionization state or effective charge of the plasma (Z_{avg}) is one of the parameters that may be readily incorporated into the models of the conduction phase. Z_{avg} may be deduced from the time resolved measurement of line intensity ratios. This parameter is required in order to convert interferometrically measured electron line densities to mass densities. This would allow us to better validate models of switch conduction.

An initial estimate of the Z_{avg} of the flashboard plasma from the time integrated measurements of line intensities has been made.

The preliminary time resolved data indicate that the flashboard plasma consists mainly of three and four times ionized species at the beginning of the discharge but changes substan-

tially over one or two microseconds to a plasma consisting of once and twice ionized species. It is not clear at this point how this fact will influence the conclusions based on time integrated measurements.

The application of pulse power considerably alters the radiated spectrum. In the case of the radial POS, we were able to detect an influx of neutral iron, presumably ablated from the electrode surface. For the coaxial POS, the time integrated measurements were often overwhelmed by a high intensity burst of continuum light which, based on our preliminary time-resolved measurements, seems to be associated with the opening process. This is consistent with the observation the coaxial POS configurations tested generally opened to much higher voltages than those observed in the radial POS configuration. As the intensity of this light seems to increase with the voltage developed by the switch, one may speculate that high energy particles produced during the opening ablate the electrode surface material in the form of macro-particles, as no line spectrum is observed that could be attributed to atomic particles. Consistent with poor or no-opening in the radial POS, the continuum light was not observed in this configuration. It is interesting that the high intensity continuum light was also seen with radial observation in the center of the coaxial switch, indicating that it is produced in the whole switch volume and not only in the region where the switch opens.

As the continuum light appears after the switch opening, this phenomenon may not influence the switch performance. On the other hand, the influx of cold particles during the conduction phase, as observed in the radial switch and most probably occurring also in the coaxial switch, may have an effect on the opening process. Both of these phenomena should be further studied and eventually included in the POS modeling.

CONVERSION TABLE

Conversion factors for U.S. Customary to metric (SI) units of measurement

MULTIPLY ————————➤ BY ————————➤ TO GET

TO GET ◀———————— BY ◀———————— DIVIDE

angstrom	$1.000\,000 \times E -10$	meters (m)
atmosphere (normal)	$1.013\,25 \times E +2$	kilo pascal (kPa)
bar	$1.000\,000 \times E +2$	kilo pascal (kPa)
barn	$1.000\,000 \times E -28$	meter^2 (m^2)
British thermal unit (thermochemical)	$1.054\,350 \times E +3$	joule (J)
calorie (thermochemical)	$4.184\,000$	joule (J)
cal (thermochemical)/cm^2	$4.184\,000 \times E -2$	mega joule/m^2 (MJ/m^2)
curie	$3.700\,000 \times E +1$	* giga becquerel (GBq)
degree (angle)	$1.745\,329 \times E -2$	radian (rad)
degree Fahrenheit	$t_K = (t\degree f + 459.67)/1.8$	degree kelvin (K)
electron volt	$1.602\,19 \times E -19$	joule (J)
erg	$1.000\,000 \times E -7$	joule (J)
erg/second	$1.000\,000 \times E -7$	watt (W)
foot	$3.048\,000 \times E -1$	meter (m)
foot-pound-force	$1.355\,818$	joule (J)
gallon (U.S. liquid)	$3.785\,412 \times E -3$	meter^3 (m^3)
inch	$2.540\,000 \times E -2$	meter (m)
jerk	$1.000\,000 \times E +9$	joule (J)
joule/kilogram (J/kg) (radiation dose absorbed)	$1.000\,000$	Gray (Gy)
kilotons	4.183	terajoules
kip (1000 lbf)	$4.448\,222 \times E +3$	newton (N)
kip/inch^2 (ksi)	$6.894\,757 \times E +3$	kilo pascal (kPa)
ktap	$1.000\,000 \times E +2$	newton-second/m^2 (N-s/m^2)
micron	$1.000\,000 \times E -6$	meter (m)
mil	$2.540\,000 \times E -5$	meter (m)
mile (international)	$1.609\,344 \times E +3$	meter (m)
ounce	$2.834\,952 \times E -2$	kilogram (kg)
pound-force (lbs avoirdupois)	$4.448\,222$	newton (N)
pound-force inch	$1.129\,848 \times E -1$	newton-meter (N•m)
pound-force/inch	$1.751\,268 \times E +2$	newton/meter (N/m)
pound-force/foot^2	$4.788\,026 \times E -2$	kilo pascal (kPa)
pound-force/inch^2 (psi)	$6.894\,757$	kilo pascal (kPa)
pound-mass (lbm avoirdupois)	$4.535\,924 \times E -1$	kilogram (kg)
pound-mass-foot^2 (moment of intertia)	$4.214\,011 \times E -2$	kilogram-meter^2 (kg•m^2)
pound-mass/foot^3	$1.601\,846 \times E +1$	kilogram/meter^3 (kg/m^3)
rad (radiation dose absorbed)	$1.000\,000 \times E -2$	** Gray (Gy)
roentgen	$2.579\,760 \times E -4$	coulomb/kilogram (C/kg)
shake	$1.000\,000 \times E -8$	second (s)
slug	$1.459\,390 \times E +1$	kilogram (kg)
torr (mm HG, 0°C)	$1.333\,22 \times E -1$	kilo pascal (kPa)

* The becquerel (Bq) is the SI unit of radioactivity; 1 Bq = 1 event/s.
** The Gray (GY) is the SI unit of absorbed radiation.

A more complete listing of conversions may be found in "Metric Practice Guide E 380-74," American Society for Testing and Materials.

TABLE OF CONTENTS

FIGURES

xv

FIGURES (Continued)

LIST OF TABLES

BOUNDARY ELEMENT CALCULATIONS OF MAGNETIC FIELDS IN CONVOLUTE GEOMETRY

1.1 INTRODUCTION.

Calculation of magnetic fields in complex, three-dimensional (3D) convolute structures is important in order to minimize convolute inductance and to minimize losses due loss of magnetic insulation in regions of weak magnetic field. We have developed a computer code which uses the boundary element method to calculate magnetic (and electric) fields on a finite element model of the convolute's current-carrying surfaces.

The magnetic field calculation code itself is fairly robust and easy to use. We are presently using the Mentat code to generate finite element model input, and homegrown (largely SGI-specific) codes for visualization of results. The code has been tested on simple coaxial geometry, and has been successfully applied to the ACE-4 convolute geometry (12 post-holes) and the proposed Saturn convolute (10 double-post-holes).

1.2 MATHEMATICAL BASIS.

There are many choices of approach for the calculation of magnetic fields. For geometries which are at least topologically simple, scalar potential methods work well. However, to satisfy Ampere's Law these methods require the presence of "cut planes" across which the potential is discontinuous. The cut-plane geometry rapidly becomes nightmarish as the topology becomes more complex. Vector potential methods eliminate the cut-plane problem, but require a larger set of equations with fairly large bandwidth.

We elected to use a "Boundary Element Method" based directly on the magnetic fields themselves. This method has several advantages over either finite-element methods or potential-based methods:

1. Only the boundary surface of the field space need be zoned up; no volume zoning is required.

2. The surface zoning need not be fully "compatible", since the boundary element solution is naturally continuous.

3. No numerical differentiation is required either to specify the boundary conditions or to calculate the fields.

The main disadvantage is that a large, non-sparse, general matrix must be calculated and solved.

To transform the magnetic field problem into a boundary element problem, we decompose the magnetic field into two components:

$$\mathbf{B} = \mathbf{B_W} + \mathbf{B_s} \tag{1.1}$$

$$\nabla \cdot \mathbf{B_w} = \nabla \cdot \mathbf{B_s} = 0$$

The "wire field", $\mathbf{B_w}$, satisfies Ampere's Law,

$$\oint \mathbf{B_w} = \mu_o I \tag{1.2}$$

but not the metal surface boundary conditions. It is calculated as the field of a set of closed wire loops lying outside the computational space (i.e., within the metal members) and representing the logical current flow through the convolute. The "correction field" or "surface field", $\mathbf{B_s}$, is a pure laplace field with vanishing path integrals. Therefore, it can be calculated as the field of a set of "magnetic charge" sheets located behind the current-carrying surface elements:

$$\mathbf{B_s} = \sum_s \sigma_s \int d^2 r_s (\mathbf{r} - \mathbf{r_s}) / |\mathbf{r} - \mathbf{r_s}|^3 \tag{1.3}$$

The magnetic charges, σ_s, are determined by requiring the boundary condition that

$$\mathbf{B} \cdot \mathbf{n} = 0$$

or

$$\mathbf{B_s} \cdot \mathbf{n} = -\mathbf{B_w} \cdot \mathbf{n} \tag{1.4}$$

at the center of each surface element. This leads to a large set of linear equations with a general, non-sparse matrix. We use the LAPACK linear equation solver to obtain the solution for the charges, σ_s.

The inductance is obtained by noting that the magnetic energy of a collection of currents can be written in terms of the vector potential produced by those currents:

$$\tfrac{1}{2} LI^2 = \tfrac{1}{2} \sum_s \int d^2 r_s \mathbf{j} \cdot \mathbf{A} \tag{1.5}$$

However, the currents are the sources for the vector potential:

$$\mathbf{A} = (\mu_0 / 4\pi) \sum_s \int d^2 r_s \mathbf{j} / |\mathbf{r} - \mathbf{r_s}| \tag{1.6}$$

so that the magnetic energy is the sum of pairwise interactions between all the surface element currents:

$$\tfrac{1}{2} LI^2 = (\mu_0 / 8\pi) \sum_s \int d^2 r_s \sum_t \int d^2 r_t \mathbf{j}(\mathbf{r_s}) \cdot \mathbf{j}(\mathbf{r_t}) / |\mathbf{r_t} - \mathbf{r_s}| \tag{1.7}$$

where $\mathbf{j} = \mathbf{n} \times \mathbf{B} / \mu_0$.

The convolute structures are rotationally periodic. In order to keep the model to a tractable size, as well as to allow visualization of the results, it is necessary to use the appropriate symmetry operations (rotations and mirrorings) to obtain the full structure from a minimum primary image. However, the sign of "magnetic charge" may be affected by a mirror operation. If the magnetic field is normal to the mirror plane, the sign of magnetic charge is changed by that mirror operation. If the magnetic field lies in the mirror plane the sign of magnetic charge remains unchanged. Also, the sign of magnetic charge is unchanged under rotation.

In evaluating a convolute design it is also useful to compute the electrostatic surface fields. This can be done using the Boundary Element Method on the same model, requiring potentials of +V/2 on the anode and -V/2 on the cathode. Both the potential and electric field are expressed as surface integrals over electrostatic charge sheets. The signs of electric charges are invariant under mirroring.

1.3   EXAMPLE 1: SIMPLE COAXIAL LINE.

As a simple test, we define a simple coaxial line, shown schematically in Figure 1-1. The primary image is a 60 degree section of a coax line around the Z-axis with inner diameter of 1 meter, outer diameter of 2 meters, and a height of 3 meters. A curved current closure is provided on top. Mirroring about the Y=0 and Z=0 planes provides a 120 degree section of 6 meter long coax with current closures at both ends. A threefold rotation completes the definition of the coax.

The wire loop is defined in the Y=0 plane and goes from (X,Z) = (0.5,0.0) to (0.5,5.0) to (5.0,5.0), to (5.0,0.0). The mirror plane about Z=0 completes the loop. The mirror about Y=0 and threefold rotation makes a total of six loops driving the system.

The model consists of 240 quadrilateral elements and 287 nodes. The magnetic fields (Figure 1–2) at the nodes and at the element centers are all within two percent of the analytic value for a cylinder. The numerically calculated inductance is 935 nH, in excellent agreement with the analytic value of 832 nH for the cylinder plus approximately 105 nH for the end caps.
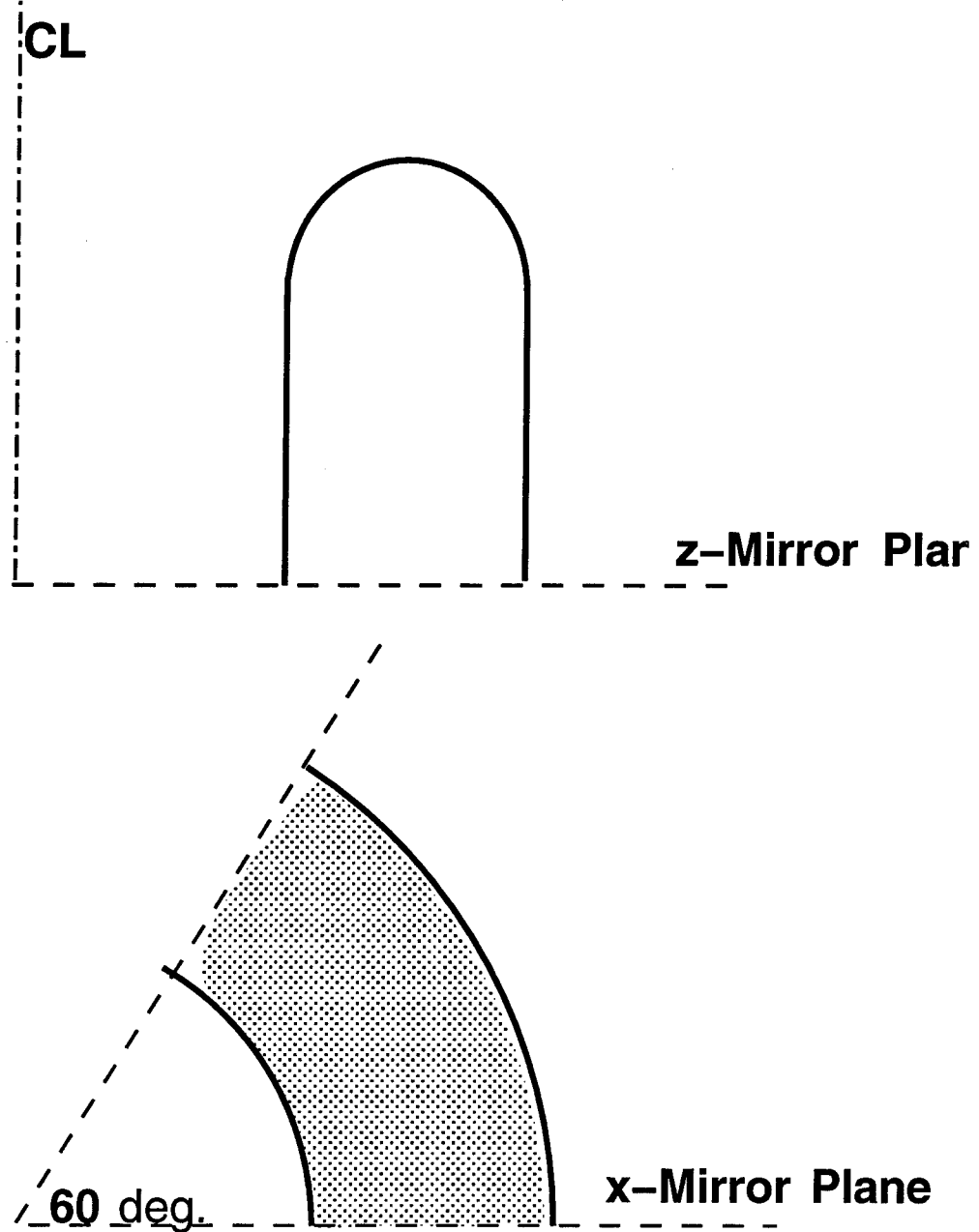
Figure 1-1. Schematic of coax line used as simple test. Two mirror operations plus a three-fold rotation forms a length of coax with rounded end closures.

1-4
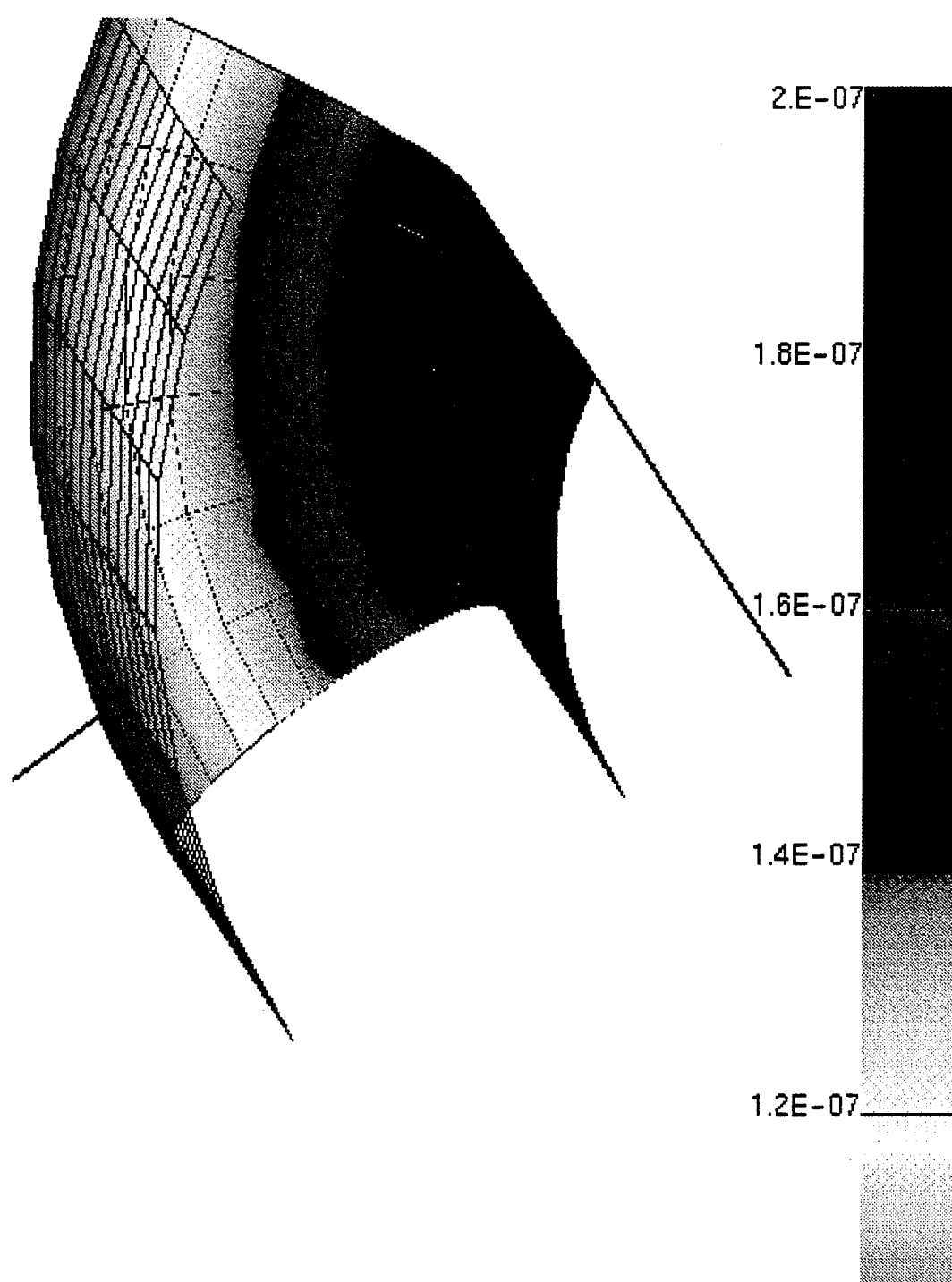
Figure 1-2. Magnetic field [tesla/ampere] for the simple coax. Uniform field of 2×10^{-7} is seen on the inner conductor, varying as r^{-1} on the rounded end closure.

1.4   EXAMPLE 2: ACE-4 POST-HOLE CONVOLUTE.

The ACE-4 Post-Hole convolute (shown schematically in Figure 1-3) consists of twelve radial posts connecting the central cathode of two radial transmission lines to the cathode of a coaxial line, passing through holes in the anode structure. The computational model is a fifteen degree slice of the structure between radial planes at a post center and halfway between two posts. A mirror plane (the plane through the post center) and a twelve-fold rotation complete the model. The primary image consists of 827 quadrilateral elements and 958 nodes. The model is truncated at an outer radius of 14 inches. (Note that current closure paths are provided at the outer radius for each radial transmission line, and at the termination of the coaxial line. These are needed to assure that the inductance is calculated for a well-defined volume.) Two wire loops represent the logical current flow through the radial cathode, post, load, and each radial anode.

Figures 1-4 (a, b) show the results for magnetic field times radius. A null is seen on the cathode ring halfway between the posts, slightly displaced from the cathode midplane. Another problem area is on the coaxial cathode below (i.e., anti-loadward of) the posts, where the magnetic field is very weak. The calculated inductance for this model is 6.10 nH, which compares well with a rough estimate of >5.56 nH based on analytic results for the actual or approximate geometry of the various portions of the model.

We can also calculate the surface electric field using the Boundary Element Method on the same model. Figure 1-5 shows the surface electric fields. Note that the field has a maximum on the coaxial cathode below the point halfway between the posts.

We can analyze these two critical areas more closely using two-dimensional contour plots and ordinary line plots. The magnetic field magnitude, normal electric field, and the dimensionless quantity E/cB are shown for the cathode ring null in Figures 1-6 (a, b, c) and 1-7 (a-f). These results are being used to redesign this portion of the convolute by removing material in the region of largest E/cB.

Similar results for the coaxial cathode problem area are shown in Figures 1-8 (a, b, c) and 1-9 (a, b, c). There is an electric field maximum about one inch below the post centerline halfway between the posts. E/cB is about 1 (for 1 MV and 1 MA) at this point, and continues to increase around the cathode's curved edge. One proposed solution is to elongate and bend the posts so that they attach to the bottom of the coaxial cathode, as shown in Figure 1-10. For this modified geometry the low magnetic field region is limited to the surface within the ring of posts, which also has low electric field due to the presence of the posts. Figure 1-11 (a, b, c) shows the electric and magnetic fields and E/cB for the region where the post attaches to the cathode. As the electric field is reduced to below 2 m^{-1} while the magnetic field remains finite, the values of E/cB are extremely favorable. However, the calculated inductance for this model is significantly increased to 11.9 nH. Other solutions are currently being sought.
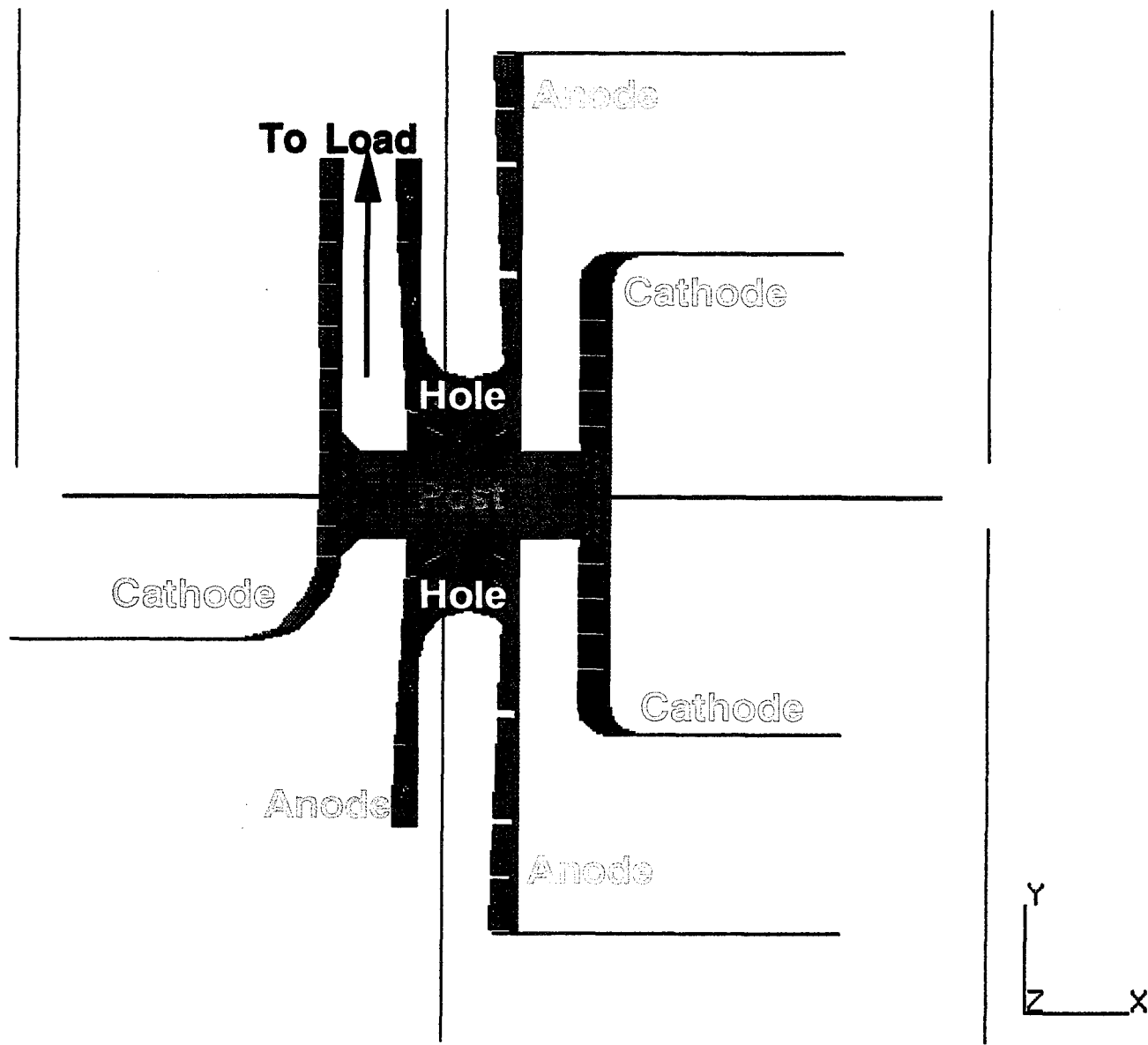
Figure 1-3. Schematic of the ACE-4 Post-Hole Convolute. Twelve post-holes connect the two radial feeds on the right to a coaxial feed on the left. One-twenty-fourth of the convolute lies in the primary image. One mirror operation and a twelve-fold rotation reconstructs the full convolute.
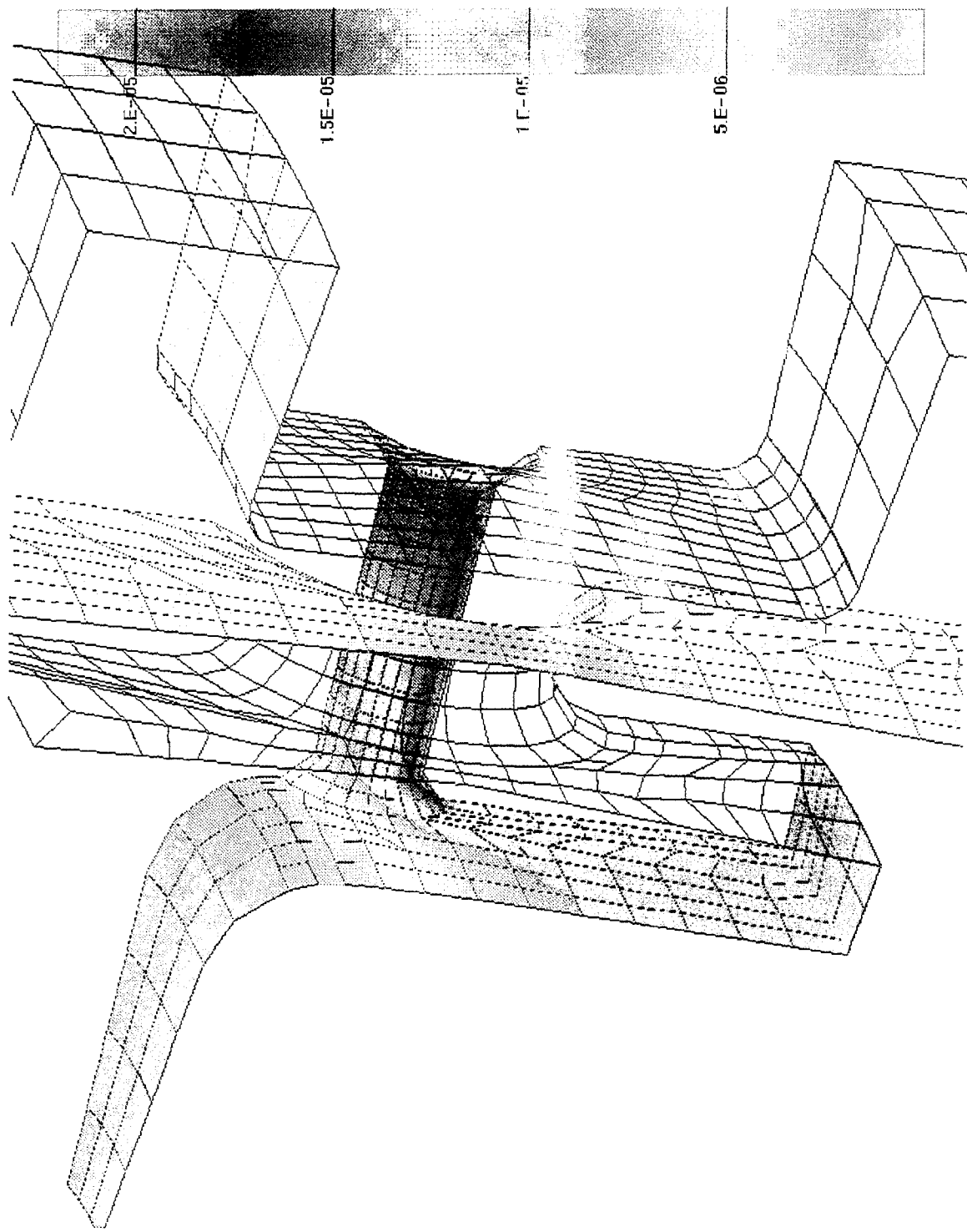
Figure 1-4. Two view of magnetic field times radius for the ACE-4 post-hole convolute. Divide values by 48 to get [tesla-meters/ampere].
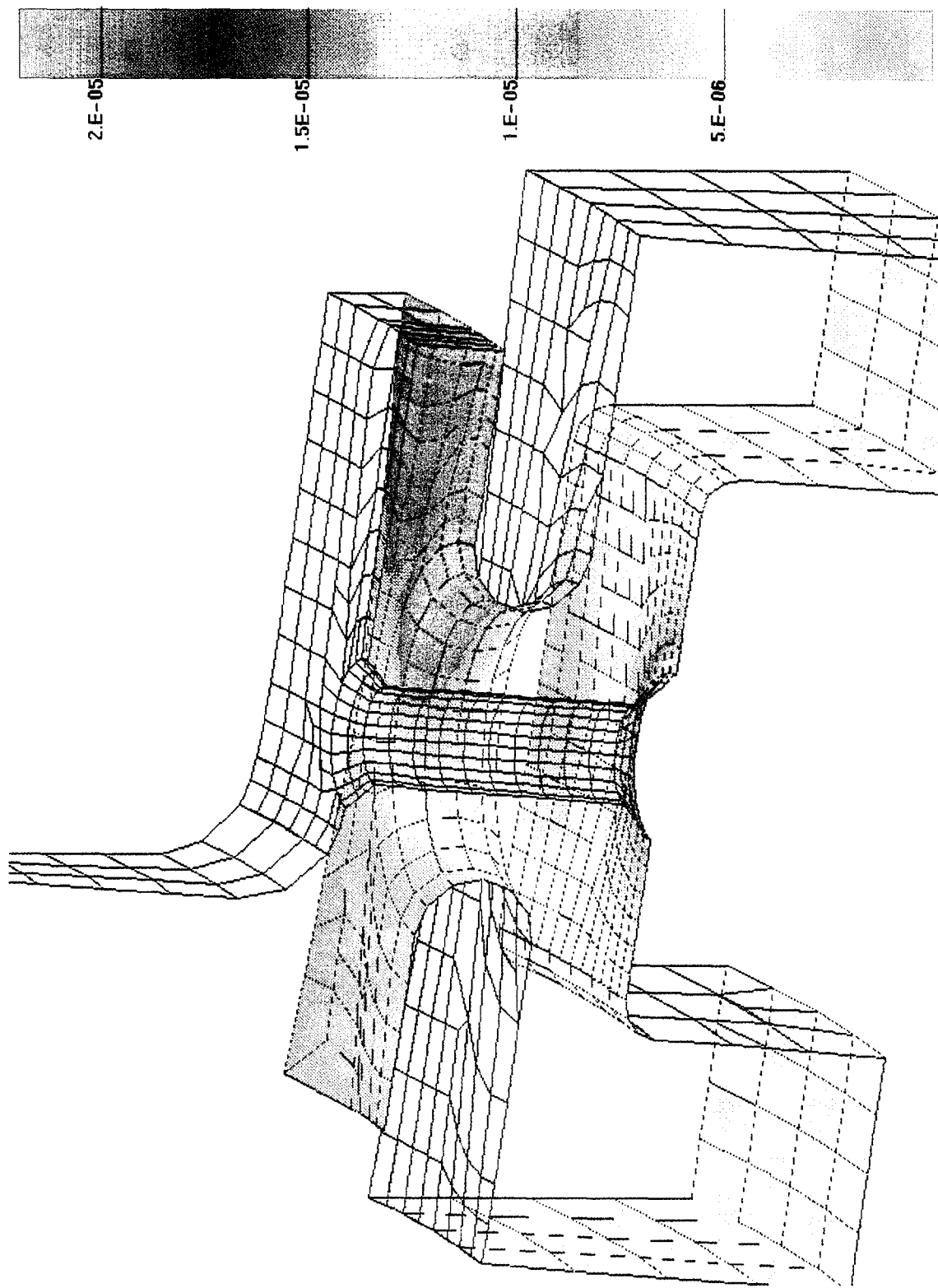
Figure 1-4. Two view of magnetic field times radius for the ACE-4 post-hole convolute. Divide values by 48 to get [tesla-meters/ampere]. (Continued)
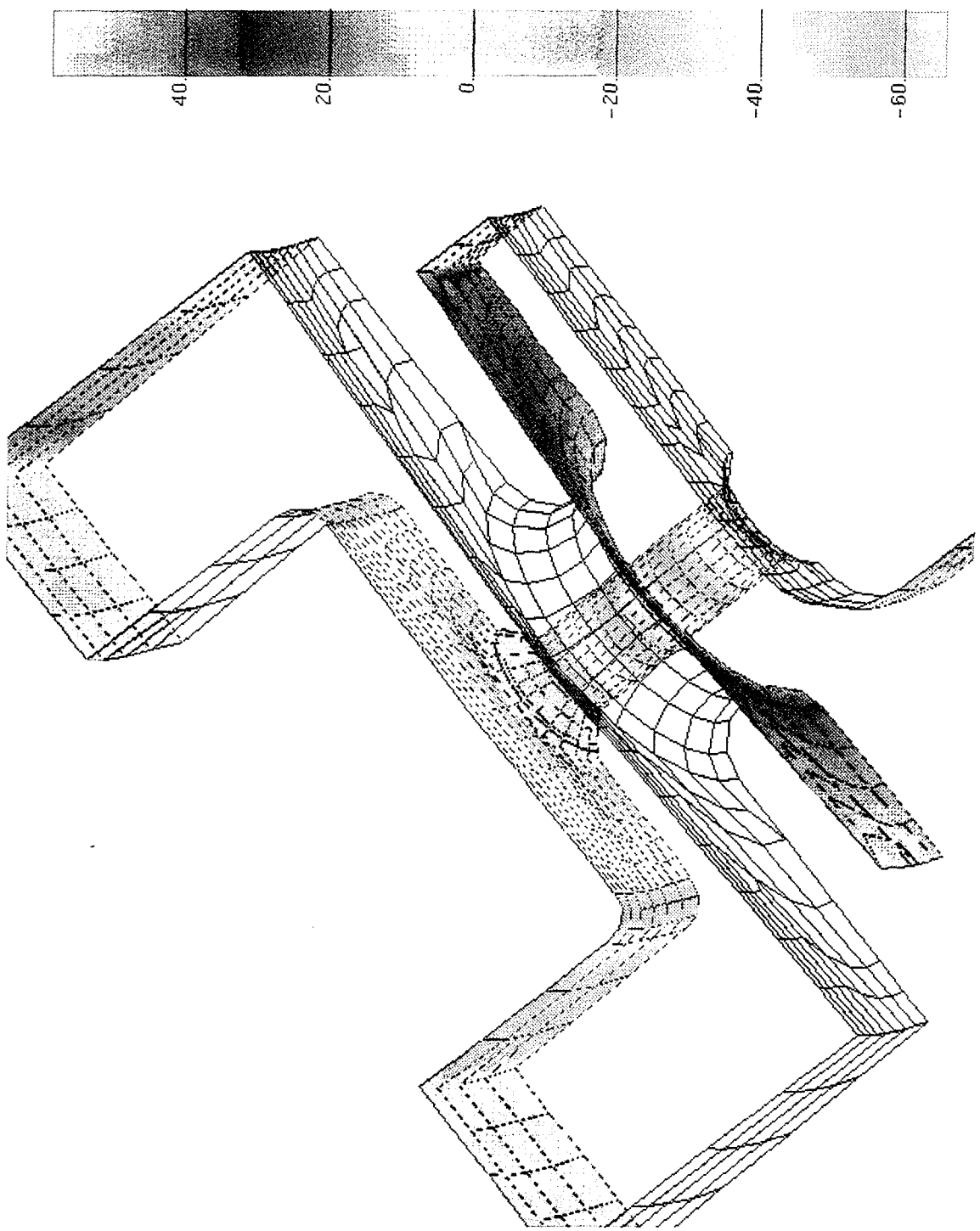
Figure 1-5. Surface electric fields [m⁻¹] for the ACE-4 Post-Hole Convolute, showing the cathode ring and post and the inner surface of anode ring.
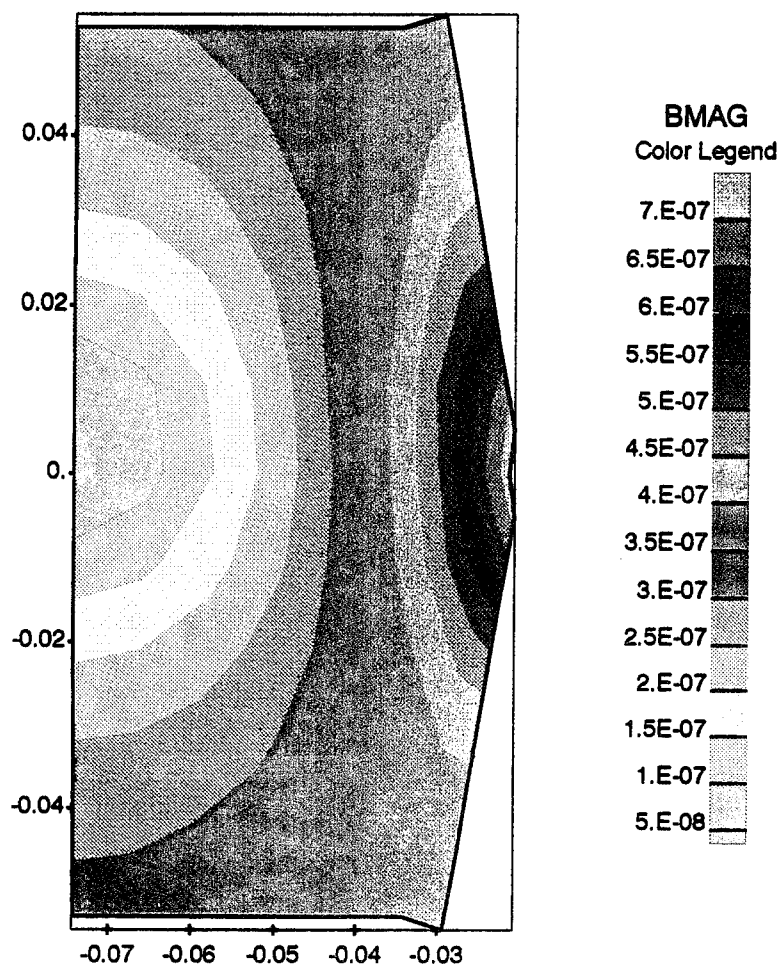
BMAG
Color Legend

7.E-07
6.5E-07
6.E-07
5.5E-07
5.E-07
4.5E-07
4.E-07
3.5E-07
3.E-07
2.5E-07
2.E-07
1.5E-07
1.E-07
5.E-08

(a) Magnetic Field

Figure 1-6.   Two-dimensional contour plots for fields near cathode ring null.

1-11

EMAG
Color Legend

-6.	
-8.	
-10.	
-12.	
-14.	
-16.	
-18.	
-20.	
-22.	
-24.	
-26.	
-28.	
-30.	
-32.	
-34.	
-36.	
-38.	
-40.	

(b) Electric Field

Figure 1-6. Two-dimensional contour plots for fields near cathode ring null. (Continued)

EbyB
Color Legend

0.
-0.2
-0.4
-0.6
-0.8
-1.
-1.2
-1.4
-1.6
-1.8
-2.
-2.2
-2.4
-2.6
-2.8
-3.
-3.2
-3.4
-3.6

(c) E/ cB
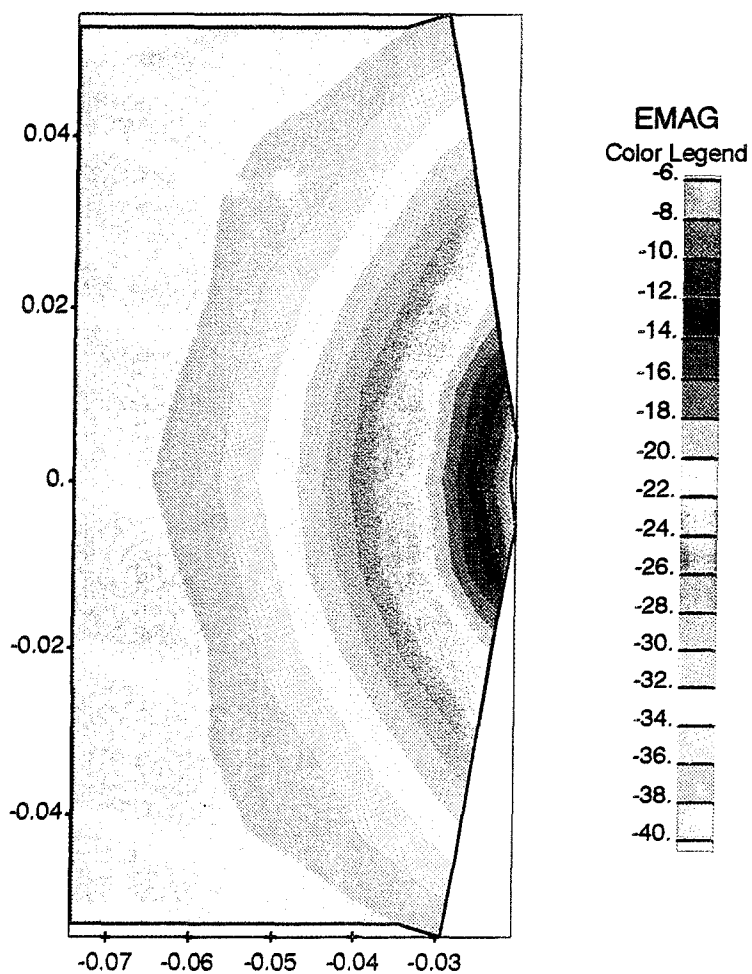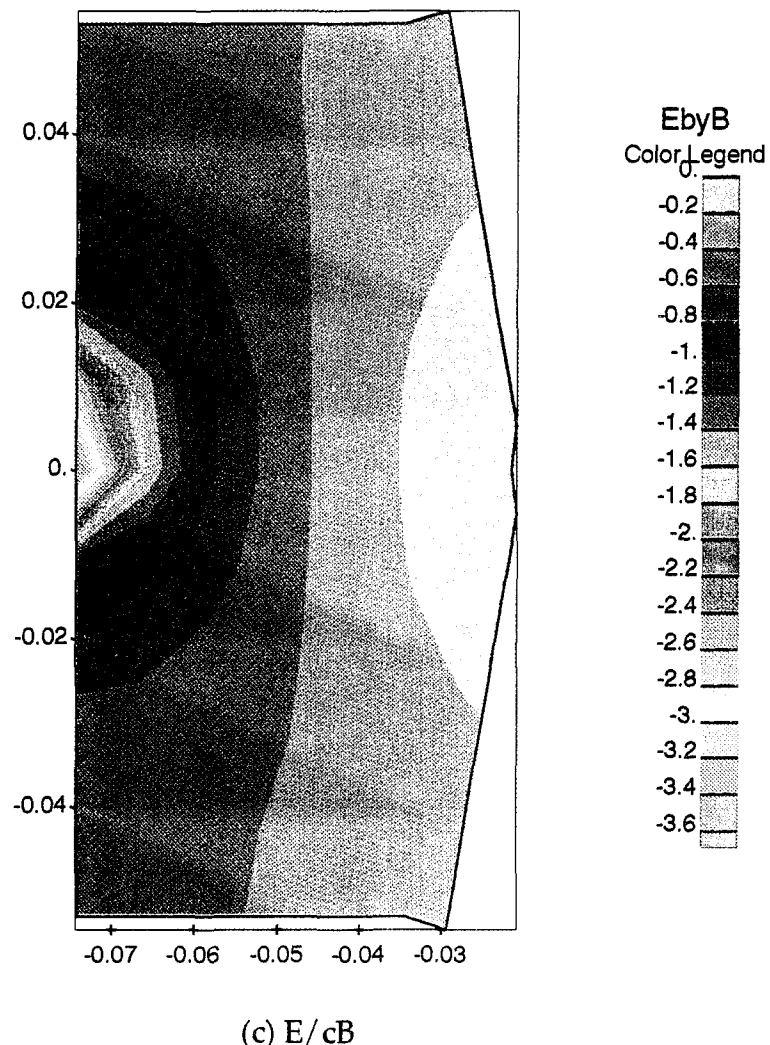
Figure 1-6.   Two-dimensional contour plots for fields near cathode ring null. (Continued)
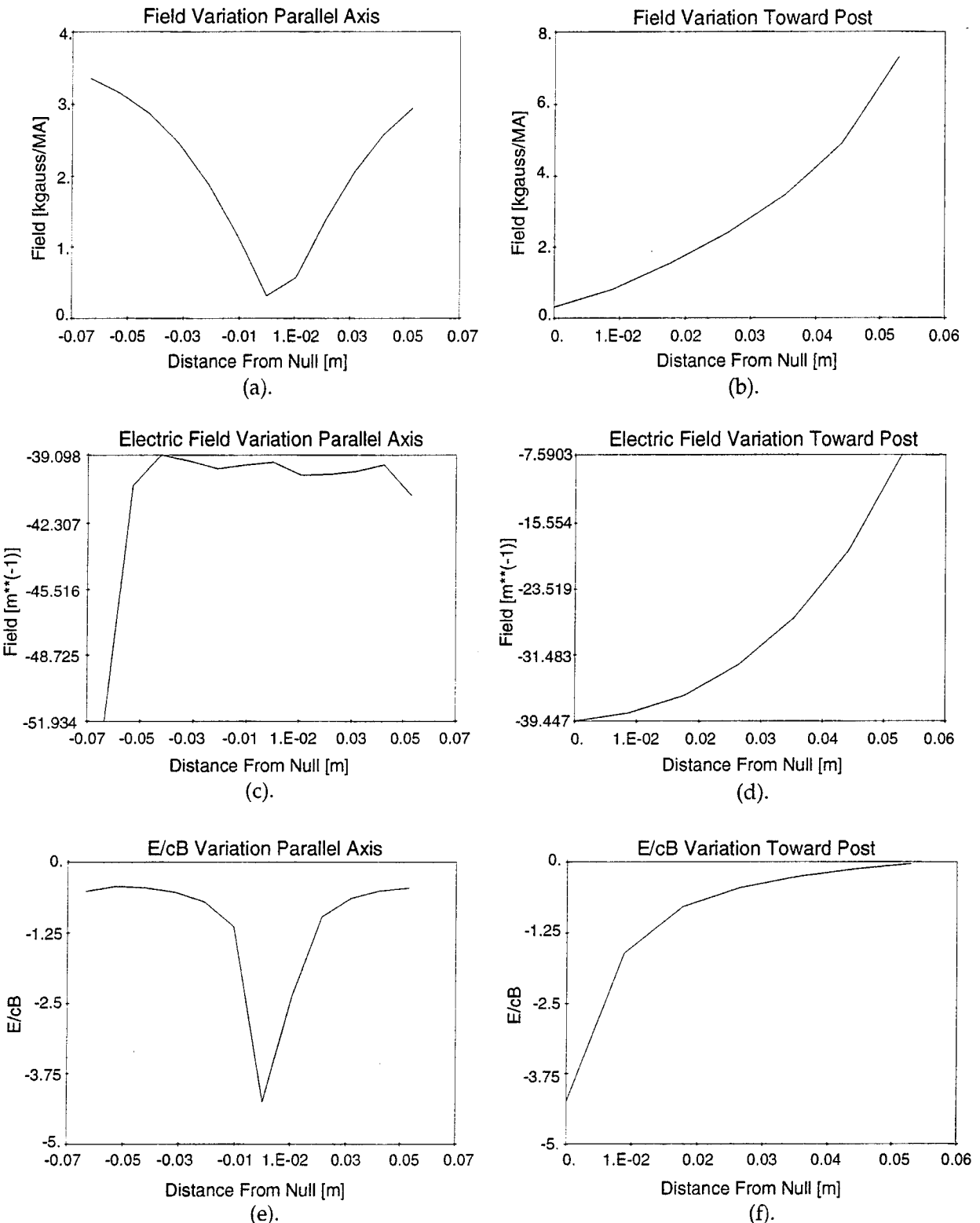
Figure 1-7. Line plots for fields near cathode ring null: (a, c, e) along line parallel to symmetry axis; (b, d, f) along line from null to post; (a, b) magnetic field; (c, d) electric field; (e, f) E/cB.

1-14
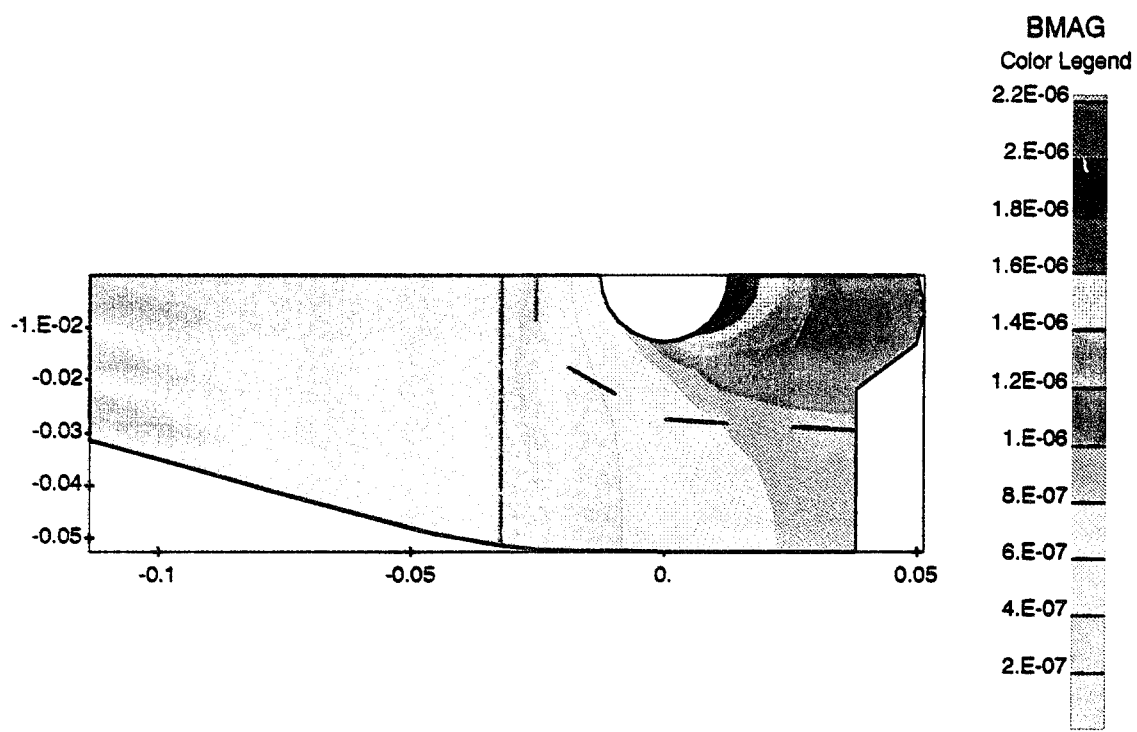
(a) Magnetic Field
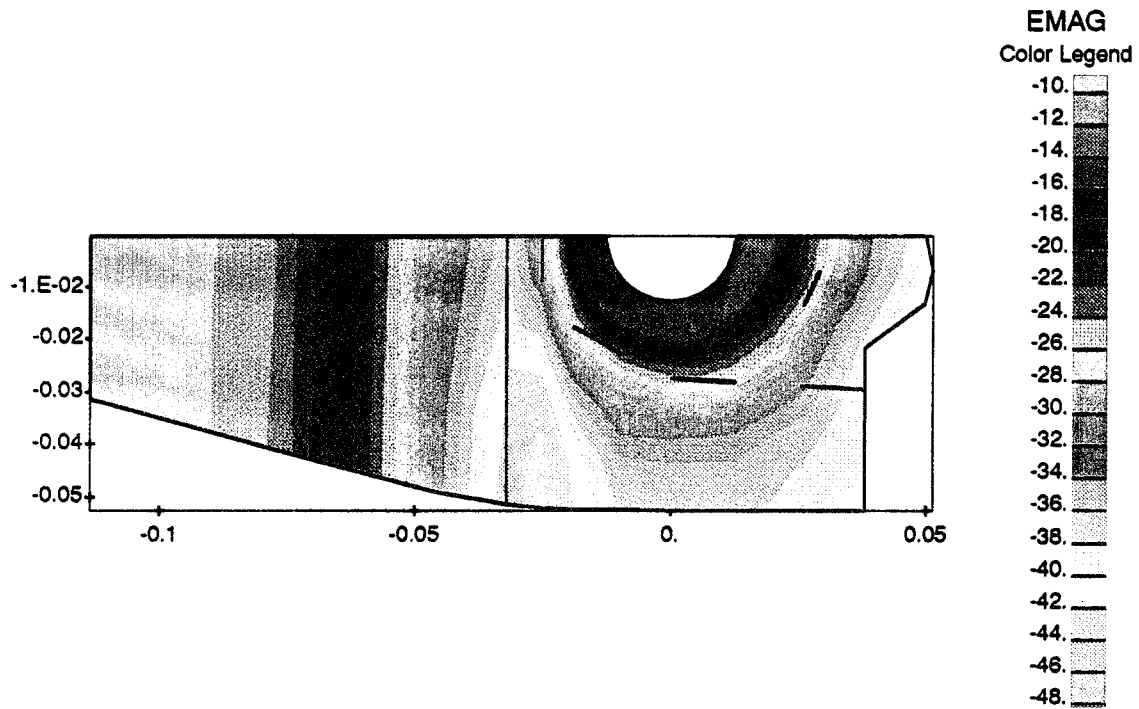
(b) Electric Field

Figure 1-8. Two-dimensional contour plots for the region below where the posts attached to the virtual cathode.
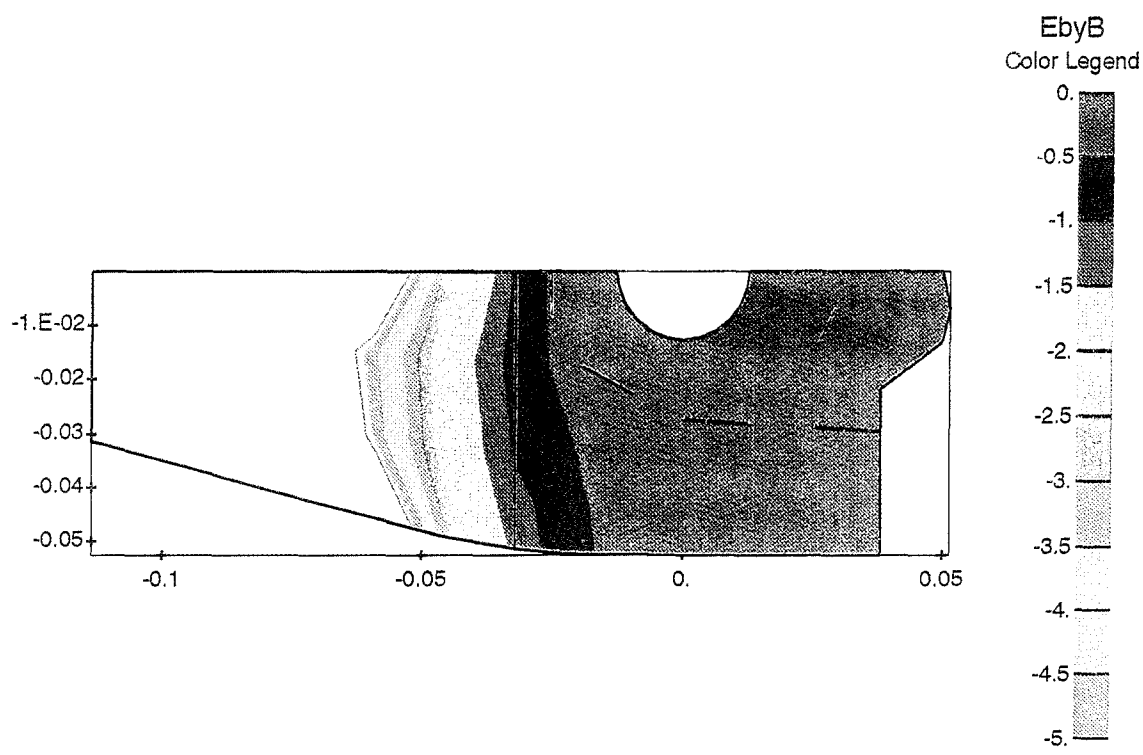
(c) E/cB

Figure 1-8. Two-dimensional contour plots for the region below where the posts attached to the virtual cathode. (Continued)

Field Variation On Coaxial Cathode

(a) Magnetic Field

Electric Field Variation On Coaxial Cathode

(b) Electric Field

E/cB Variation On Coaxial Cathode

(c) E/cB
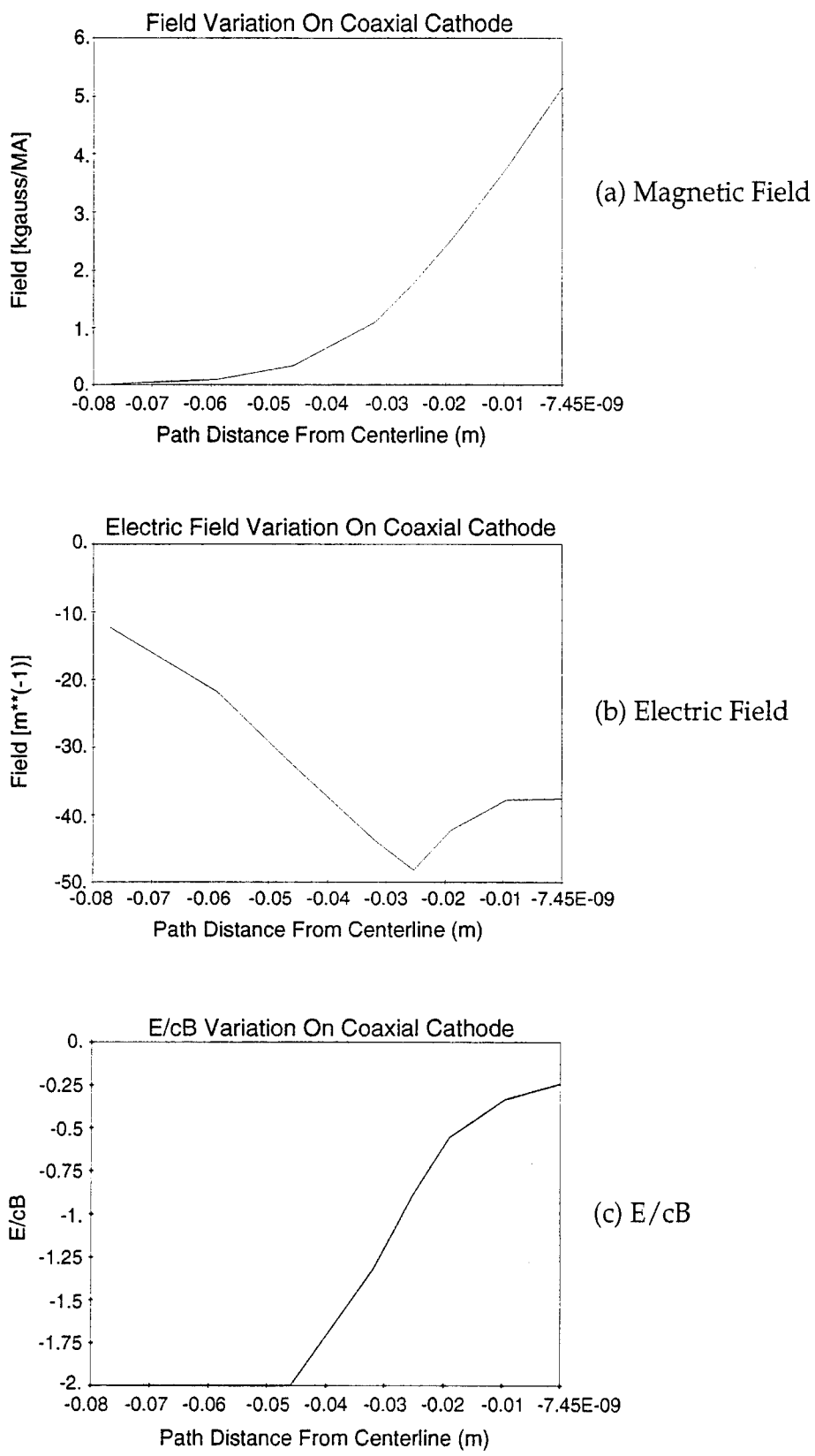
Figure 1-9. Line plots along the coaxial cathode halfway between the posts.

1-17
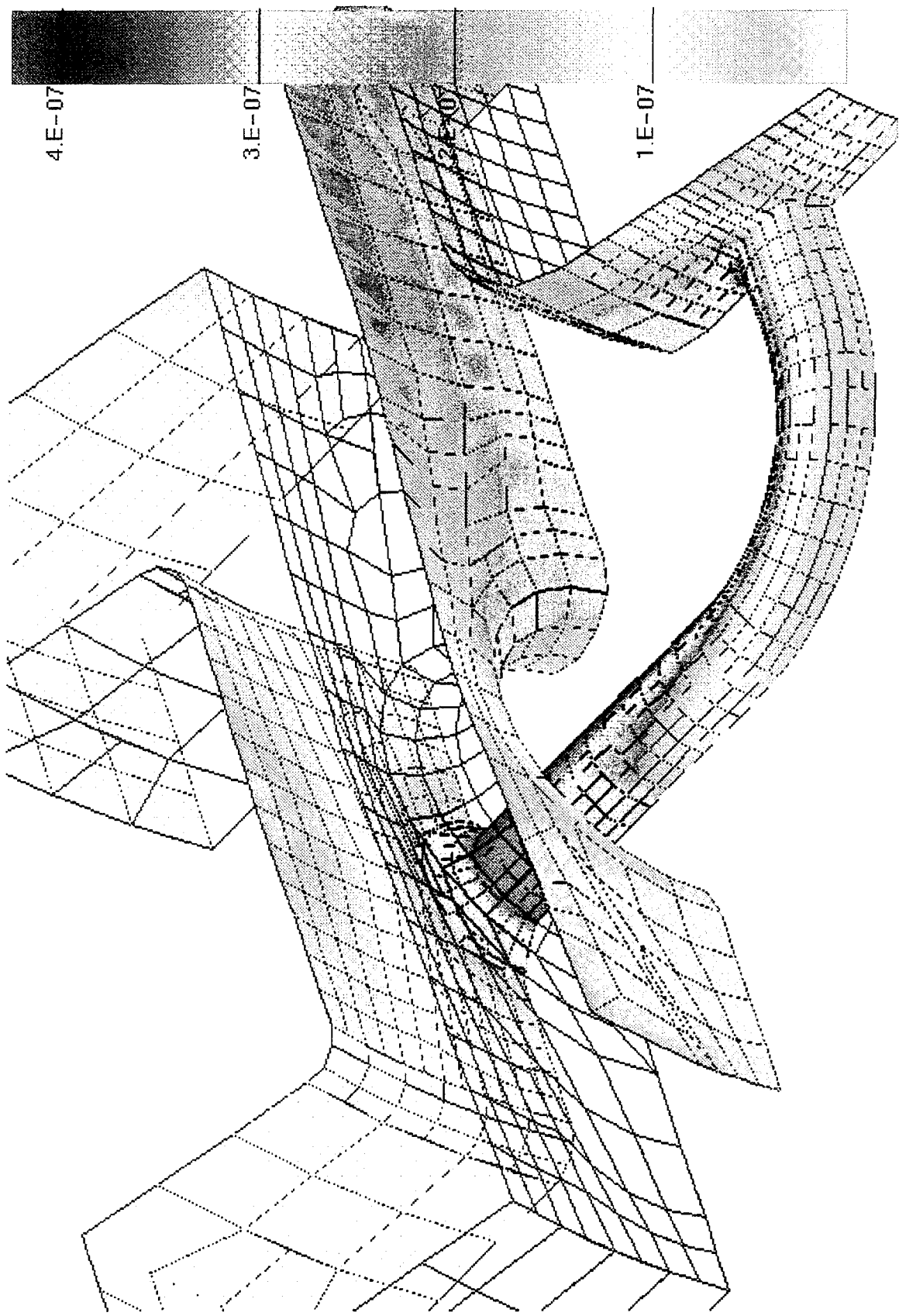
Figure 1-10. Proposed ACE-4 geometry (showing magnetic field times radius [teslam/ampere]) with bent posts to suppress electric field near cathode-post attachment.

4.E-07

3.E-07

1.E-07
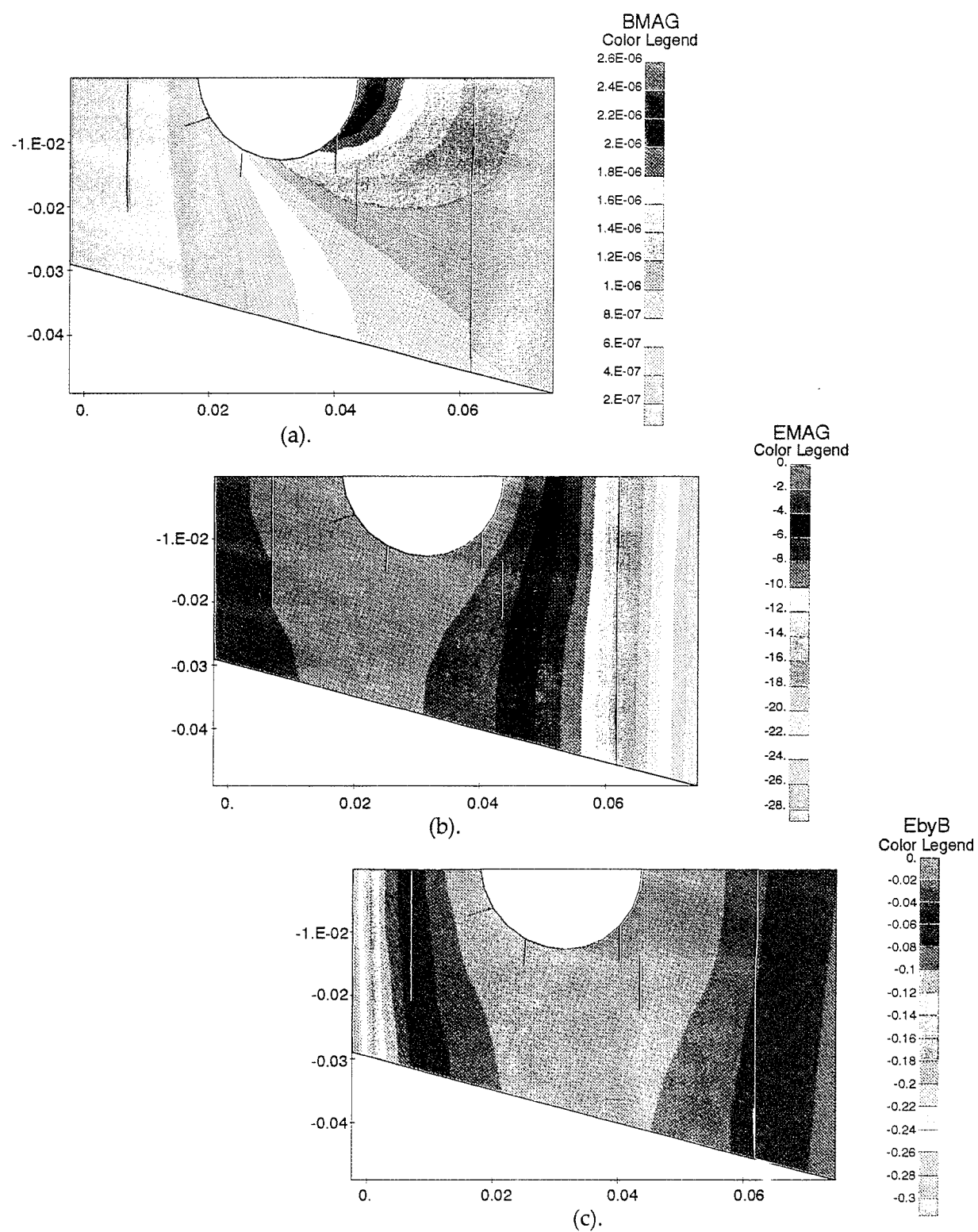
Figure 1-11. Two dimensional plots of the fields on the cathode in the post attachment region for the geometry of Figure 1-10.

1.5   EXAMPLE 3: DOUBLE POST-HOLE CONVOLUTE.

The SATURN Double Post-Hole Convolute (DPHC) [design (Figure 1-12) provided courtesy of Phil Spence of PSI] joins four radial transmission lines to form a single coaxial line. The convolute consists of 10 vertical anode posts, each passing through holes in the two anode plates. Similar to the ACE-4 model, the primary image is an 18 degree slice, with the model filled out by one mirror operation and a ten-fold rotation. The primary image has 667 quadrilateral elements and 799 nodes. Four wire loops represent the logical current flow. Two loops pass through each cathode, with one loop from each cathode through the central anode, and the other through the appropriate outer anode. The outer radius of the model is 12 cm.

Figure 1-13 (a, b) shows the results for magnetic field times radius. There is a large outwardly directed force on the loadward side of the anode post. Magnetic nulls appear on the outward extremities of the two anode holes. Also, a magnetic null appears halfway between the posts on the anti-loadward side of the loadward cathode plate. The most anti-loadward cathode surface also has no magnetic field inside the post-hole structure. The calculated inductance is 4.88 nH, in good agreement with approximate analytic estimates.

Figure 1-14 shows the electric fields on the anti-loadward cathode surfaces. The anode scalloping and the off-center placement of the post in the cathode holes reduces the electric fields in the null regions. Figure 1-15 (a, b, c) shows the field variations along a radial line through the null on the anti-loadward side of the loadward cathode plate. While the anode scalloping reduces the electric field by about a factor of two at the null location, the value of E/cB remains high.
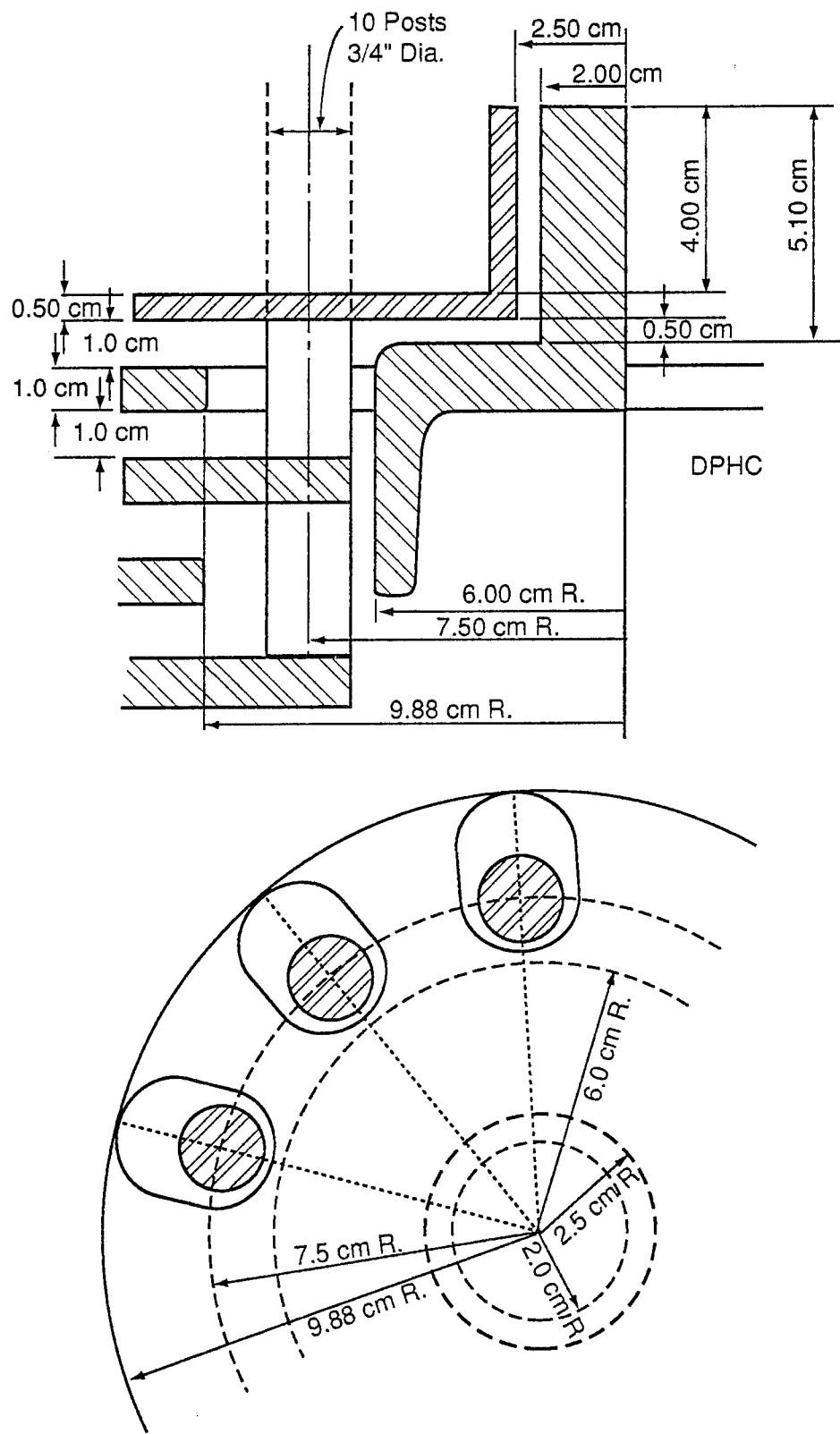
Figure 1-12. SATURN Double Post-Hole Convolute (DPHC) design, as provided by Phil Spence.
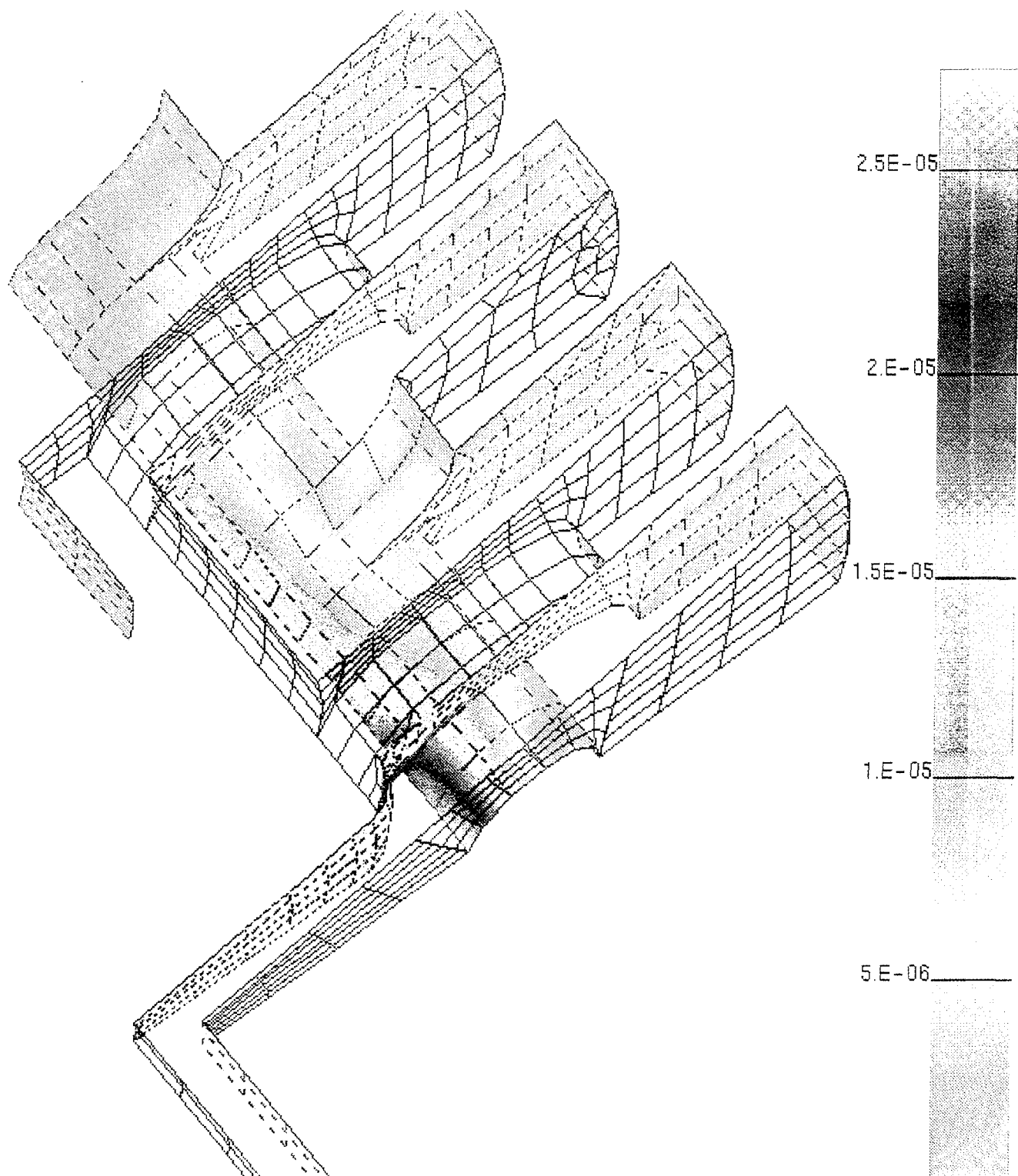
Figure 1-13. Two views of magnetic field times radius for the DPHC. Divide values by 80 to get [tesla-meters/ampere].

2.5E-05

2.E-05

1.5E-05

5.E-06
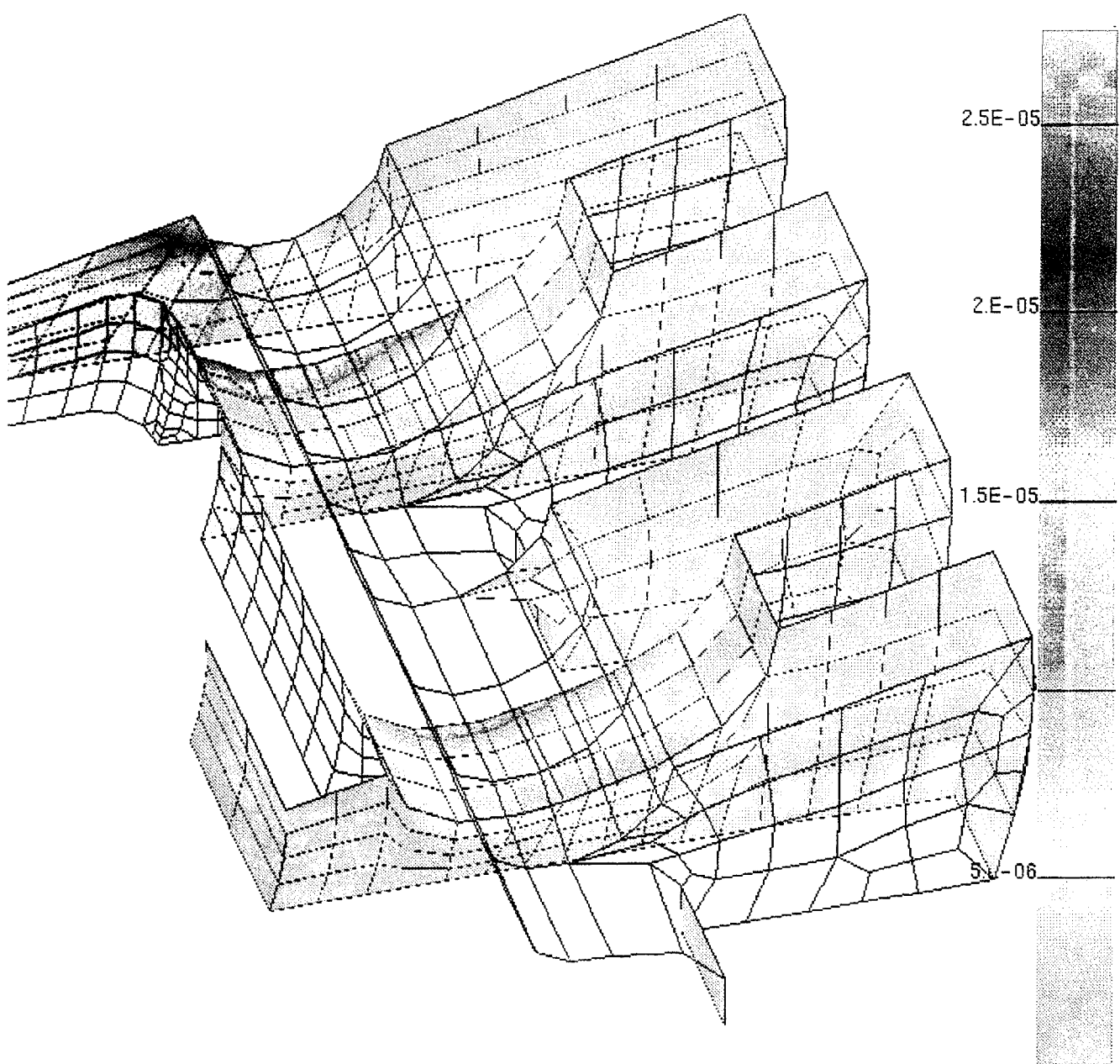
Figure 1-13. Two views of magnetic field times radius for the DPHC. Divide
values by 80 to get [tesla-meters/ampere]. (Continued)
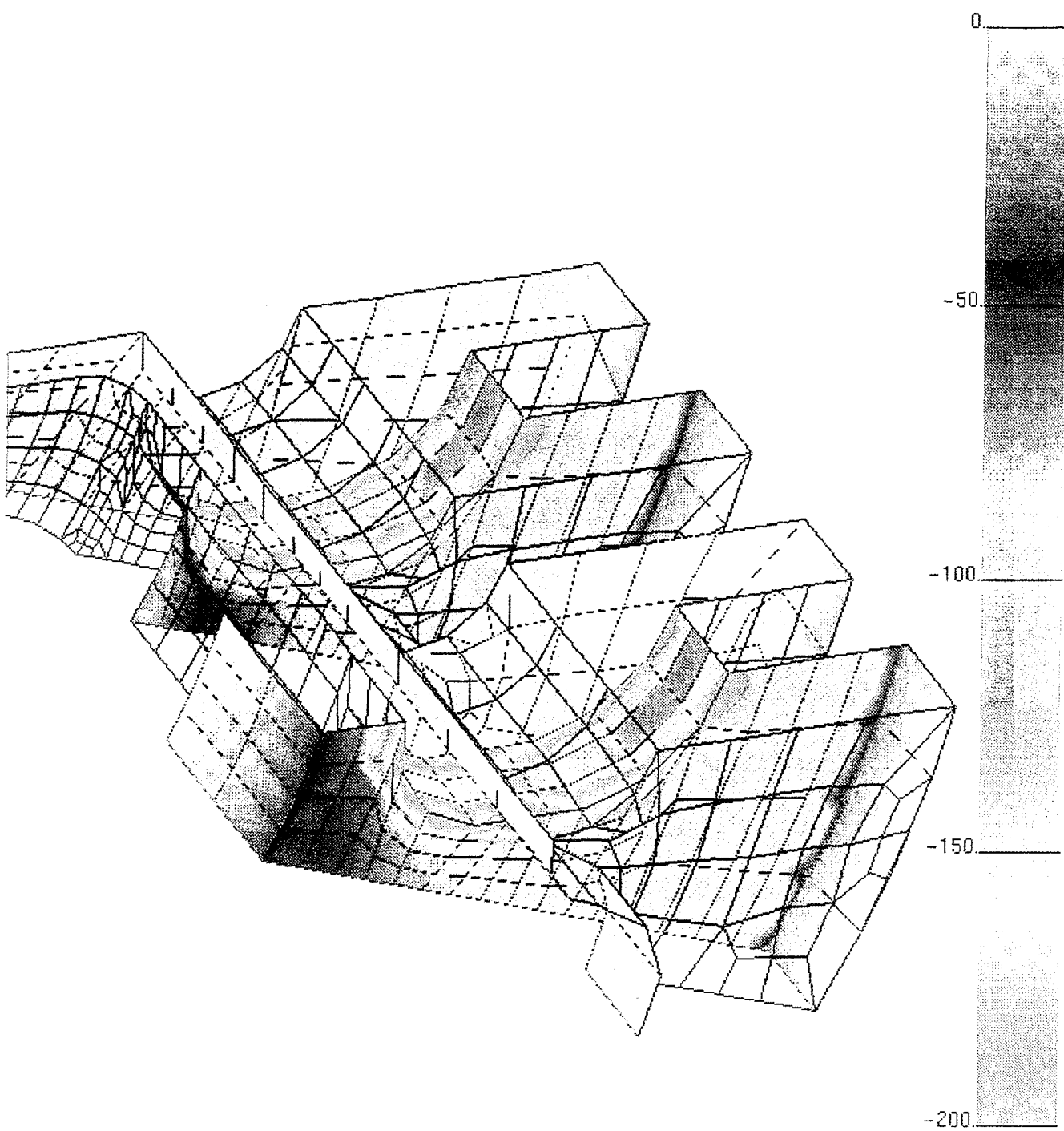
Figure 1-14. Electric fields [m^{-1}] on anti-loadward cathode surfaces for the DPHC.

(a) Magnetic Field

(b) Electric Field

(b) E/cB
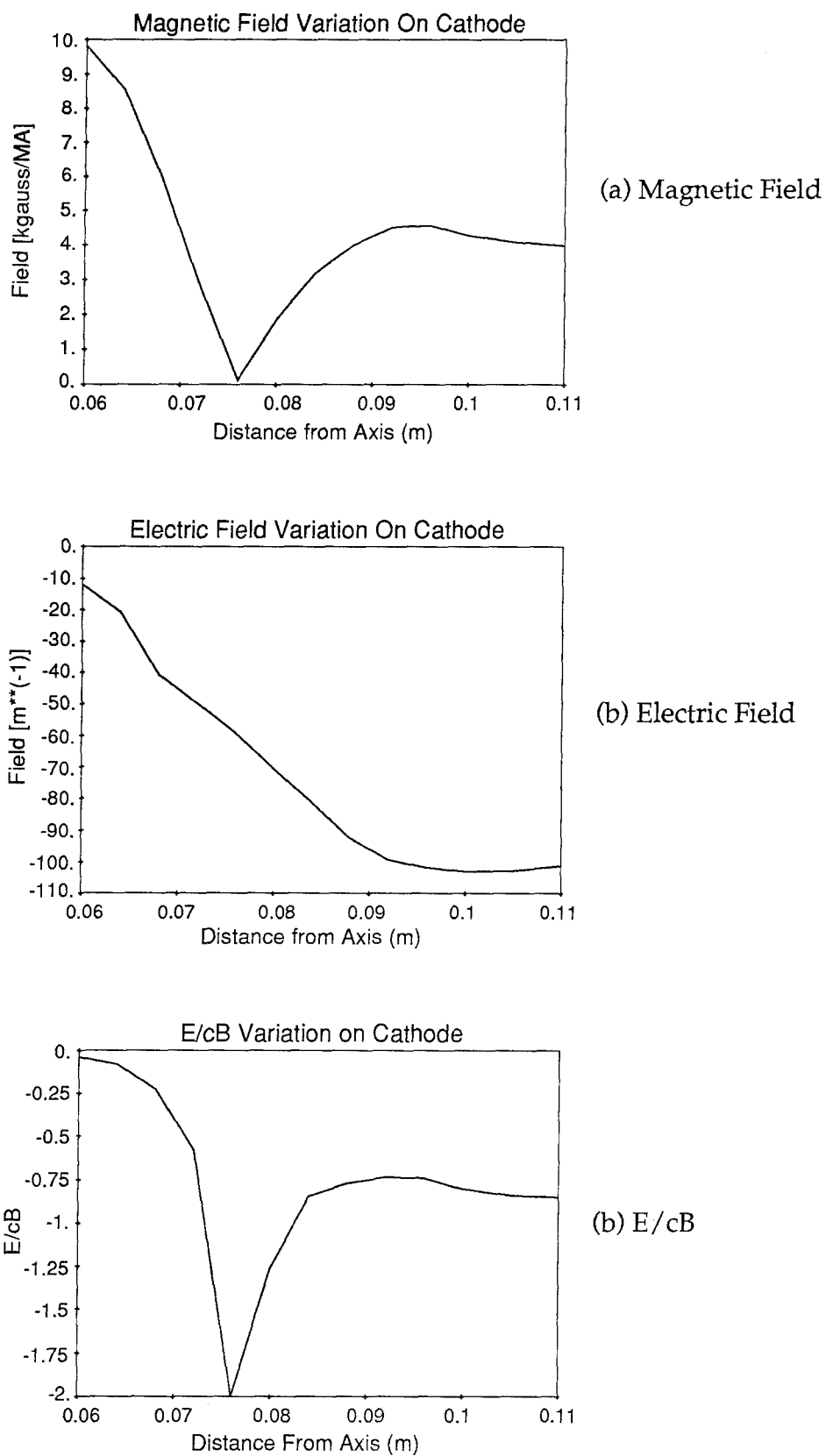
Figure 1-15. Field variations along a radial line through DPHC null.

1.6   CURRENT STATUS.

1.6.1.   Analysis Code.

The analysis code itself is in fairly good shape. Complete surface electric and magnetic field solutions for the problems illustrated are obtained in about two hours of cpu time (on an SGI Indigo/R3000). Most of the time is spent calculating the field of a charge sheet for each quad-quad and node-quad pair. The fields and inductances appear to be sufficiently accurate for the required purposes.

The analysis code was originally written in FORTRAN with C++-like data structures. It has now been converted to C++ for the SGI machines (using the LAPACK++ 1.0β), and to Microsoft Visual C++ (using Microsoft's version of the IMSL mathematics libraries). The C++ versions are about three times slower than the FORTRAN versions.

One of the additional capabilities we would like to have is to segment the model so that the inductance can be apportioned amongst the portions of the structure for better comparison with approximate analytic calculations. We would also like to use this segmentation to allow a portion of the model to be updated without recalculating those matrix elements which remain unchanged.

1.6.2.   Geometry Definition.

The geometry definition is currently a weak point for distributing the code. We have used Mentat, a preprocessor for the MARC analysis code, to generate geometrical input. It is possible to arrange to use PATRAN as a processor, either by converting the PATRAN Neutral File to MARC format or by processing it directly. We have looked at AutoCAD as a geometry generator, and initial impressions are very unfavorable.

Input consists of four files. The file "Node_File" contains the locations (in meters) of the nodes used to define the model. Table 1-1 is a sample node file.

Table 1-1. Sample "Node_File" for a model with 56 nodes.

```
 1 2.0000+00 0.0000+00 0.0000+00
 2 2.0000+00 3.3333-01 0.0000+00
 3 2.0000+00 6.6667-01 0.0000+00
 4 2.0000+00 1.0000+00 0.0000+00
 5 1.9924+00 0.0000+00-1.7420-01
 6 1.9924+00 3.3333-01-1.7420-01
 7 1.9924+00 6.6667-01-1.7420-01
 8 1.9924+00 1.0000+00-1.7420-01
 9 1.9696+00 0.0000+00-3.4741-01
10 1.9696+00 3.3333-01-3.4741-01
11 1.9696+00 6.6667-01-3.4741-01
12 1.9696+00 1.0000+00-3.4741-01
13 1.9319+00 0.0000+00-5.1764-01
14 1.9319+00 3.3333-01-5.1764-01
15 1.9319+00 6.6667-01-5.1764-01
16 1.9319+00 1.0000+00-5.1764-01
17 1.0000+00 1.0000+00 0.0000+00
18 1.0000+00 6.6667-01 0.0000+00
19 1.0000+00 3.3333-01 0.0000+00
20 1.0000+00 1.0000-06 0.0000+00
21 9.9620-01 1.0000+00-8.7100-02
22 9.9620-01 6.6667-01-8.7100-02
23 9.9620-01 3.3333-01-8.7100-02
24 9.9620-01 1.0000-06-8.7100-02
25 9.8480-01 1.0000+00-1.7370-01
26 9.8480-01 6.6667-01-1.7370-01
27 9.8480-01 3.3333-01-1.7370-01
28 9.8480-01 1.0000-06-1.7370-01
29 9.6593-01 1.0000+00-2.5882-01
30 9.6593-01 6.6667-01-2.5882-01
31 9.6593-01 3.3333-01-2.5882-01
32 9.6593-01 1.0000-06-2.5882-01
33 1.9361+00 1.2445+00 0.0000+00
34 1.7445+00 1.4361+00 0.0000+00
35 1.5000+00 1.5000+00 0.0000+00
36 1.2555+00 1.4361+00 0.0000+00
37 1.0639+00 1.2445+00 0.0000+00
38 1.9288+00 1.2445+00-1.6864-01
39 1.7379+00 1.4361+00-1.5195-01
40 1.4943+00 1.5000+00-1.3065-01
41 1.2507+00 1.4361+00-1.0935-01
42 1.0598+00 1.2445+00-9.2664-02
43 1.9067+00 1.2445+00-3.3631-01
44 1.7180+00 1.4361+00-3.0303-01
45 1.4772+00 1.5000+00-2.6055-01
46 1.2364+00 1.4361+00-2.1808-01
47 1.0477+00 1.2445+00-1.8480-01
48 1.8702+00 1.2445+00-5.0111-01
49 1.6851+00 1.4361+00-4.5151-01
50 1.4489+00 1.5000+00-3.8823-01
51 1.2127+00 1.4361+00-3.2494-01
52 1.0276+00 1.2445+00-2.7535-01
53 0.0000+00 0.0000+00 0.0000+00
54 0.0000+00 4.0000+00 0.0000+00
55 3.0000+00 4.0000+00 0.0000+00
56 3.0000+00 4.0000-06 0.0000+00
```

Each line consists of a node number and the (X,Y,Z) coordinates of the node. The format above (I5, 1p3e10.4) is put out by Mentat in the MARC file.

The second file is the "Connectivity_File." It describes how the nodes are connected to make the quad elements and the segments of the wire loops. Table 1-2 is a sample "Connectivity File."

Table 1-2. Sample "Connectivity_File" for a model with 36 quad
elements and 3 wire loop segments.

```
 1 75  1  2  6  5
 2 75  2  3  7  6
 3 75  3  4  8  7
 4 75  5  6 10  9
 5 75  6  7 11 10
 6 75  7  8 12 11
 7 75  9 10 14 13
 8 75 10 11 15 14
 9 75 11 12 16 15
10 75 17 18 22 21
11 75 18 19 23 22
12 75 19 20 24 23
13 75 21 22 26 25
14 75 22 23 27 26
15 75 23 24 28 27
16 75 25 26 30 29
17 75 26 27 31 30
18 75 27 28 32 31
19 75  4 33 38  8
20 75 33 34 39 38
21 75 34 35 40 39
22 75 35 36 41 40
23 75 36 37 42 41
24 75 37 17 21 42
25 75  8 38 43 12
26 75 38 39 44 43
27 75 39 40 45 44
28 75 40 41 46 45
29 75 41 42 47 46
30 75 42 21 25 47
31 75 12 43 48 16
32 75 43 44 49 48
33 75 44 45 50 49
34 75 45 46 51 50
35 75 46 47 52 51
36 75 47 25 29 52
37 52 53 54
38 52 54 55
39 52 55 56
```

The first integer is the element number, and the second is either 75 (indicating a quad element), or 52 (indicating a wire segment). The remaining integers are node numbers, counterclockwise for a quad element, or in the forward direction for a wire segment.

The third file is the "Electrode_File" used to define the anode and cathode elements. (Some quad elements, such as those used for current closure, will belong to neither electrode.) This information is needed to calculate the electric field (and thus E/cB). Table 1-3 shows an example of a simple "Electrode_File."

Table 1-3. Sample "Electrode_File".

```
DEFINE   ELEMENT   SET      Cathode
    10    TO    18
DEFINE   ELEMENT   SET      Anode
     1    TO    9
```

For the sample in Table 1-3 each electrode consists of consecutive elements. For the more common case where such is not true, Mentat uses cards with format (9i8,7x,1hC), where the "C", indicating a continuation, is omitted on the final card of each electrode.

The fourth file is the "Symmetry_Operations" file. It indicates the operations needed to generate the full model from the primary image. Table 1-4 is a sample "Symmetry_Operations" file.

Table 1-4. Sample "Symmetry_Operations" file.

```
Mirror Y Odd
Mirror Z Even
Rotate Y 12
NLoops 1
```

Here the "Mirror" lines indicate a mirror operation about the zero-plane of a specified coordinate. "Odd" indicates the magnetic field lies in the mirror plane, whereas "Even" indicates the magnetic field is normal to the mirror plane. The "Rotate" line specifies n-fold rotation about a specific axis. The NLoops line provides the number of loops in the primary image (and any "Odd" mirror image), needed to normalize the inductance.

1.6.3. Three-Dimensional Visualization.

We have an SGI-specific routine to do three-dimensional visualization of surface electric and magnetic fields. This was used to create the 3D figures in this report. We can also use the AVS visualization program to view the model.

To give an idea of the options available in the 3D visualization program, Table 1-5 presents a sample dialogue setting up a visualization object.

Table 1-5. Sample session with the three-dimensional visualization program Mag3D. (Italics are used for computer output; bold letters are used for user responses).

Mag3D

*Enter 1 for Leo, 2 for Dynapac, 3 for EWB>***4**
Reading Magnetic Field Data

Available Properties:
     6   Magnetic Field Magnitude
     7   Maggnetic Field Magnitude Times Radius
     8   Magnetic Field X-Component
     9   Magnetic Field Y-Component
     10 Magnetic Field Z-Component
     11 Electric Field Normal Component
     12 E-Normal / cB

*Choose One>***12**
*Conversion Factor>***1.0**
   Enter Filename:
Stage2_Fields
   Minimum E/cB   = -1.057E+00
   Maximum E/cB   = 4.107E-01

*Enter New PMin>***-.5**

*Enter New PMax>***0.0**

1.6.4. Lower-Dimensional Visualization.

It is important to provide lower-dimensional visualization (contour plots on flat or flattened surfaces and line plots along specified paths) in order to use the results for design modification. Our method for doing this is less than satisfactory, as it involves operations not readily incorporatable into a simple interface.

(1) From the Mentat display, extract the node numbers (in order; for line plot) or element numbers (need not be in order; for surface plot).

(2) Specify a transformation converting the (X,Y,Z) node coordinates to one dimension (for line plot), or to X-Y (for surface plot).

(3a) For line plot, it is now easy to extract the node coordinates and data from the output, and write a routine calling a plot library to generate the plot.

(3b) For a surface plot, we write the data into a database for the Gilbert code. (Gilbert is a general-purpose 2-D plasma code.) This involves 1) reading the "Coordinate_File" to convert Mentat element numbers to quad numbers; 2) renumbering elements and nodes to be consecutive beginning with 1; 3) reading, transforming, and writing the data. Then, Gilbert software can be used to generate surface contour plots or plots on a path along the surface.

1.7   FURTHER DEVELOPMENT.

Apart from some cleanup, we propose to temporarily stop development of the code at this point. The objectives of developing a friendly user interface seem too ill-defined to pursue at this time. Some limited objectives which might be accomplished (if there is need) include:

(1) Develop an interface to PATRAN.

(2) Develop the ability to calculate fields at an arbitrary point, or on a grid of points.

(3) Develop the ability to partition a model.

(4) Pursue other visualization options.

We would like to further apply the code to real problems in order to develop a feel for how it is applied. We would also like to use it as basis for developing methods of estimating current leakage at weak points in convolutes.

SECTION 2

SWITCH PLASMA CHARACTERIZATION

During this year, we have worked primarily on the problem of explaining the ACE 4 flash-board electron density measurements obtained by Dr. John Thompson. These experiments measure the values of the line integral of the plasma electron density as functions of time at certain specific axial distances from the cathode. Using appropriate normalization, the electron density vs. time can be obtained. Measurements from a typical shot are shown in Figure 2-1. Probe #1 is 2 mm from the cathode. The probes are separated by 2 mm with #9 closest to the anode.

We wished to model the behavior of the injected plasma in hopes of better understanding and controlling it. Our initial approach was to model the injected plasma as a quasi-neutral fluid consisting of singly-ionized carbon ions along with the accompanying electrons. Accordingly, we set up a calculation using a hydrodynamic fluid code on a one-dimensional (1D) mesh extending form the location of the probe nearest to the anode (which is the first position at which we have any data) down to the cathode. At the highest probe position, we injected a plasma of carbon ions with a density value which equaled to that measured by the corresponding probe in the experiment. The injected plasma was assumed to be at a constant temperature (we used 1 eV, but this was not a sensitive parameter) and to be injected with a velocity which was a simple function of time. At the cathode boundary, we assumed a stagnation boundary condition, meaning that the cathode was represented as a solid wall forcing the fluid velocity to zero at that point.

This did not prove to be very successful, as the conversion of kinetic energy to thermal energy at the cathode produced a very hot and rapidly expanding plasma which produced high "reflected" densities much earlier than the experiments actually measured them. This clearly suggested that the plasma was cooled substantially by contact with the cold cathode, and this assumption was then incorporated into the code. With a simple model for cooling, and the further assumption that the plasma is injected into the vacuum with a velocity that decays exponentially with time, our model gives results which are shown in Figure 2-2.
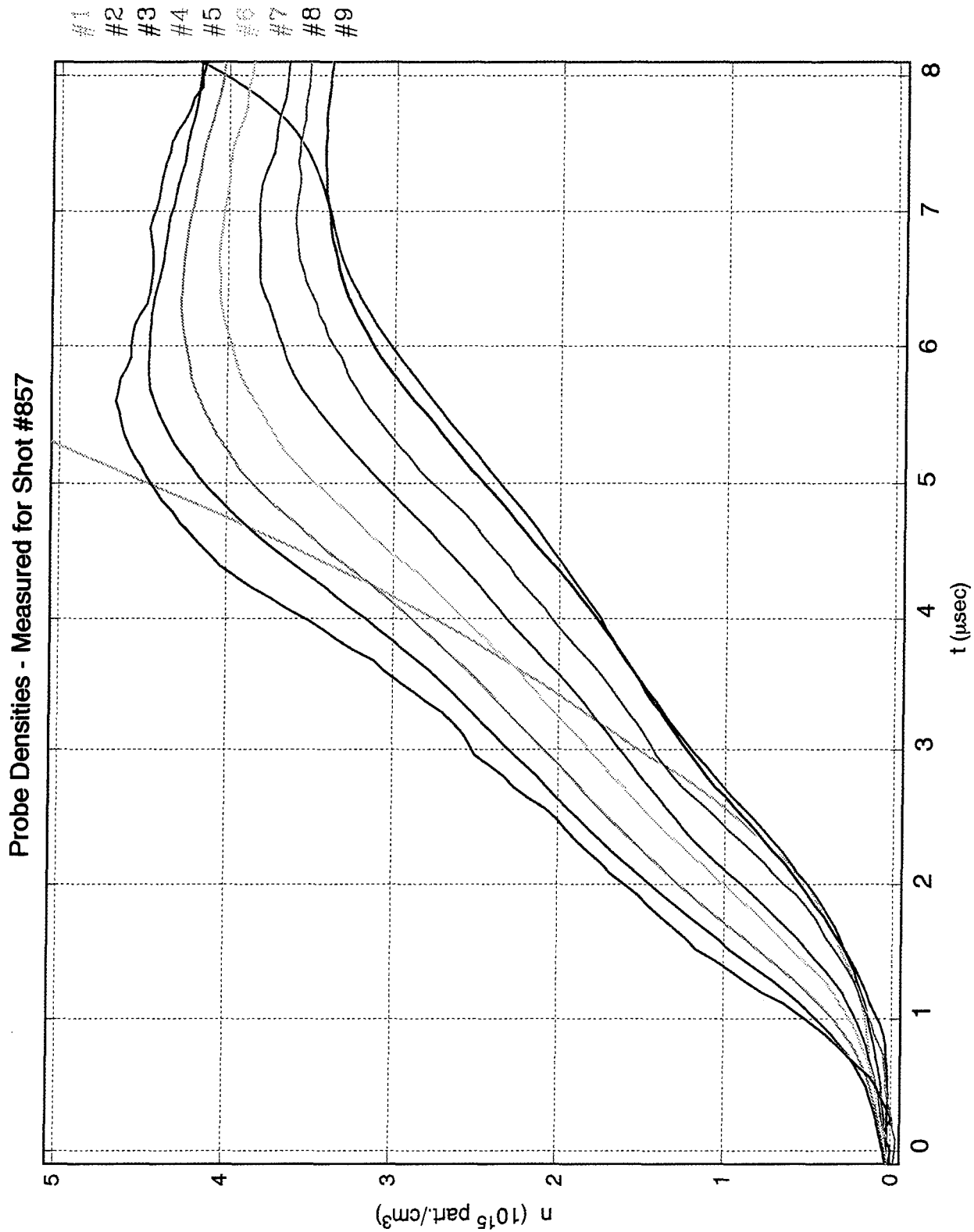
Figure 2-1. Line integrated density - measured.
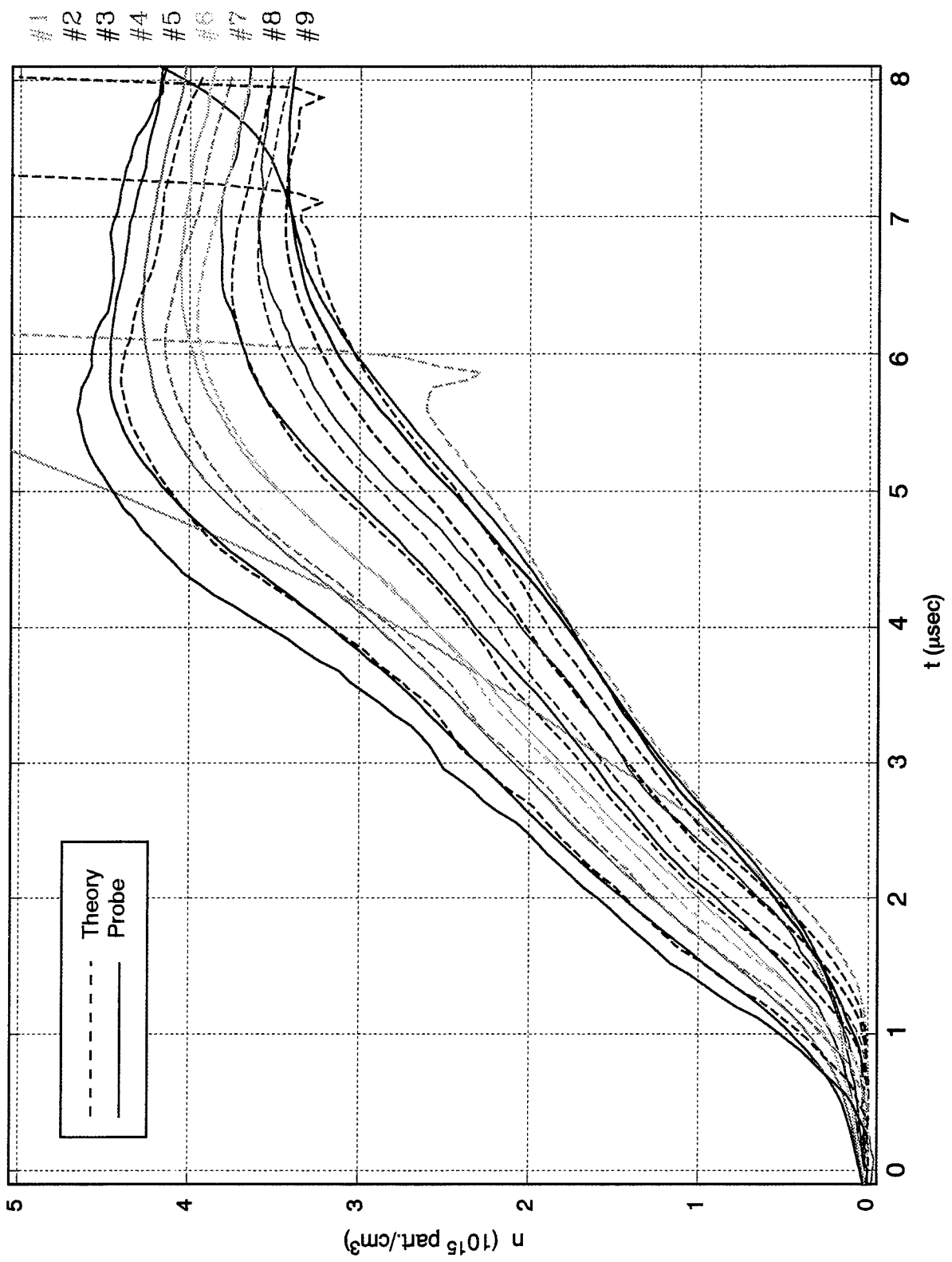
Figure 2-2. Line integrated density - measured *vs.* calculated.

The most significant features of this model are:

1. Given that we inject a density of plasma which exactly equals that at the probe furthest from the cathode (probe #9 in this notation), which therefore must always precisely match the experiment, the calculated densities for the other probes agree very well with the measured values until the time at which the "reflected" cathode plasma becomes significant. Hence, this is not a "first-principles" injection model, meaning that the code does not include a numerical model of the flashboard itself. It should be remarked that this assumed an exponentially decaying injection velocity. The injection temperature does not have a very strong effect upon the results as long as it does not get very high. The velocity profile which we had to use to get agreement was:

$$V(t) = \frac{3 \cdot 10^6 \, cm \, / \, sec}{2^{(t/4 \ microsec)}} \tag{2.1}$$

2. Using this velocity profile, and constant assumptions about cooling rates at the cathode, etc., we were able to fit measurements from a set of three different experiments by changing only one input condition: the injected density at the outermost probe. All other input parameters were kept constant between the shots. This means that, while we don't have a predictive model of flashboard plasma density as a function of pulse voltage, etc., if we are given the measured density at one point, we can reasonably well model the behavior of the plasma as it flows downstream from that point, with one rather large exception.

3. That exception is, of course, the effect of the plasma that "reflects" back from the cathode. While we can adjust the cooling rate to get the "reflected" plasma to reach the first probe (nearest to the cathode) at about the right time, the behavior is very different. In the calculations, the cool, slowly-moving plasma that expands from the cathode encounters a rapidly-moving stream of injected plasma from the flashboards, and produces a shock at this point, which moves slowly out from the cathode. When the position of this shock passes a probe location, the predicted density at that point "jumps" discontinuously upwards. This is in marked contrast to the observed behavior, which is that the probe nearest to the cathode starts to see excess density at a relatively early time, but that this density slowly builds up over a period of several microseconds. Various attempts to reproduce this behavior by refining the cooling model were unsuccessful.

At this point, Dr. Parks made a suggestion that could explain the discrepancy between the predicted and observed cathode plasma behavior. He suggested that as the "leading edge" of the injected plasma reached the cathode, it would also be very likely to neutralize with some accomodation on the surface. The resultant products would then expand slowly from the cathode. He further conjectured that, due to the relatively low collision cross-section between slow particles and fast ions, this gas would not react against the incoming plasma to form a hydrodynamic shock, but would rather inter-penetrate with it. This would lead to reasonable densities of slow particles reaching upstream at relatively early times. Accordingly, we attempted to correct this problem by assuming different physical models for the plasma-cathode interaction. All of these alternate models attempted to replace the shock front with a more gradual

transition region by assuming that the interaction between the incoming and cathode plasmas was weaker than a hydrodynamic collision (*i.e..*, with a lower collision frequency and longer mean-free-path than is implicit in a hydrodynamic model).

The first model that we tried assumed that the plasma, upon interacting with the cathode surface, was not only considerably cooled, but also recombined into a neutral gas. Since the characteristic collision frequency between ions and neutrals is much lower than that between ions and ions, we modeled this neutral gas cloud as moving slowly away from the cathode while freely interpenetrating with the incoming plasma, thus avoiding the shock that we had in the original calculation. However, since Dr. Thompson's measurements only could "see" the plasma electron density, this by itself would be insufficient to reproduce his results. We examined the consequences of several different assumptions about the plasma-neutral interaction, among which were:

1. Assume that the only significant collision mechanism is resonant charge-exchange between carbon ions and carbon neutrals. This results in no immediate change in ion (and thus electron) density, but does result in a frictional "drag" between the two species which both transfers momentum between the two fluids and converts some of the incoming plasma kinetic energy to heat. The slowing of the incident plasma causes the density to increase as the surface is approached.

2. As above, but assuming that ion-neutral collisions, rather than charge-exchange, is the dominant mechanism.

3. Assume no significant ion-neutral collisions, but take the temperature of the incoming electrons to be some fraction of that of the incoming ions, and assume that these hot electrons ionize a fraction of the neutral particles. Here, we assumed that the fraction ionized was given by the Saha equation, assuming quasi-equilibrium.

To summarize the results, all of these models gave more or less equivalent results. When the collision frequency, or incoming electron temperature in the last case, was sufficiently low, there was no significant effect from the cathode plasma on the calculated "measured" densities. When the appropriate parameter was increased, it was indeed possible to produce a slow, gradual increase in "measured" electron density rather than the abrupt "jumps" that had characterized our earlier efforts. However, in all cases, the degree of ion-neutral interaction necessary to match the measured rate of increase of density at each individual probe was also sufficient to destroy the time separation of the different probes. In other words, when the simulation showed Probe #1's density swinging smoothly upward at the right rate to match the measurements, it would also show Probe #2, #3, etc. coming up very closely thereafter (meaning at $< \sim 0.5$ microsecond intervals rather than the measured ~ 1.5-2.0 microsecond intervals). In short, when we gained the ability to reproduce the shapes of the individual probe readings, we lost the ability to reproduce the separation in time of those readings. This was the case with all of the "semi-fluid" models that we tried.

In conclusion, we still do not have a good understanding of the interaction of the incoming plasma with the cathode surface, and our ability to model the surface effects will be limited until we do improve our understanding of this point.

At this point, we began work on a two-dimensional (2D) model of the ACE 4 flashboard and switch regions which could also simulate the effect of the grid which lies between the plasma flashboards and the switch region (this being the region between anode and cathode). Preliminary estimates indicated that this grid would pose a significant impediment to the flow of the plasma from the flashboards to the switch region. We hoped to be able to study this effect, ideally developing an improved, "first-principles" model for the flow rate of plasma into the switch region, and also to check out a conjecture by John Thompson that plasma "leakage" downstream of the POS region might be responsible for poor opening rates by causing "flattening" of the snowplow profile once the snowplow passes the main switch region. Accordingly, we represented the switch region of the POS by the triangular mesh shown in Figure 2-3.
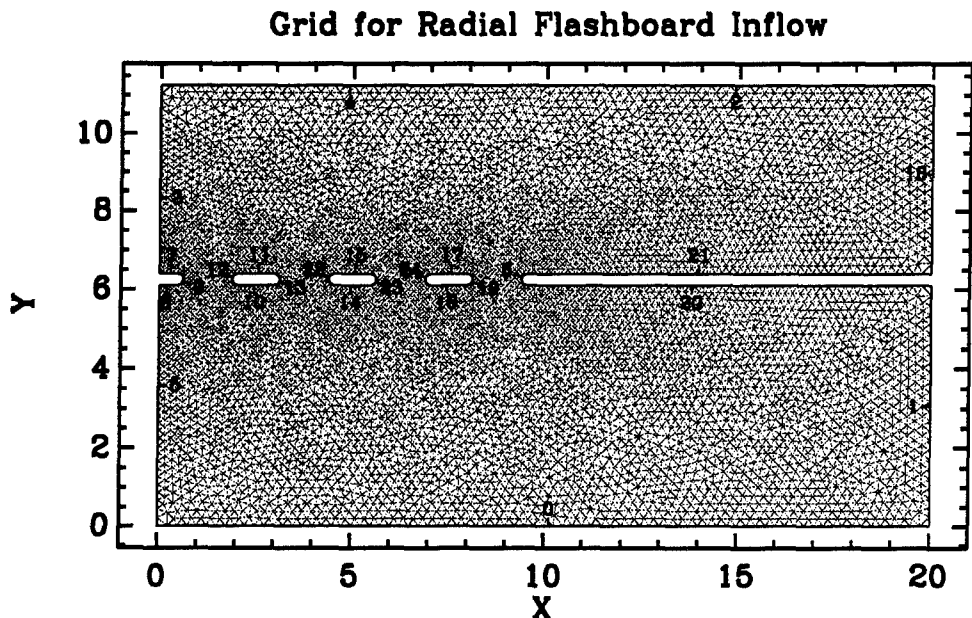
Figure 2-3. Mesh for the ACE 4 Radial POS density simulation.

This mesh models half of the flashboard/anode screen region; the line of reflective symmetry is the left edge of the mesh. Without the application of pulsed power, and ignoring the radial effects as being small out at this radius, the problem is fully symmetric and so we saved computer time by only simulating the downstream half. In the mesh, the flashboard plasma is injected straight down vertically from the dark blue line in the upper left corner; the red lines along the right side are "outflow" boundaries, meaning that plasma can flow freely out through them without obstruction, and all of the green lines are "slip" boundaries, either because of symmetry or because they represent metal surfaces. (No plasma can flow either in or out of a "slip" boundary, but it can flow freely along such a boundary.) Note that the "gaps"

in the mesh near the center represent the metal anode screen. This screen is 50 percent transparent in the POS region (the left half of the mesh) which we represented as a series of metal bars of width equal to half of the center-to center spacing of the real mesh. (The true mesh has a square grid in X and Z directions, with 50 percent transparency, which we could not represent exactly in a 2D code.) In the downstream region, this screen is solid metal, and was so represented here. In accordance with our best current model for plasma-metal interaction, all of the cells adjacent to metal surfaces were limited to a maximum temperature of 0.1 eV. (Recall that this choice of boundary conditions was the one that, in our 1D calculations reported above, had best matched the times of arrival of "reflected" plasma from the cathode at the expense of not being able to correctly match the gradual rate of plasma increase at those probe locations.) Finally, the injection velocity, as a function of time, was taken to be that used in our 1D calculations above, while the injection density was chosen to give good agreement with Dr. Thompson's density measurements.

The most striking difference between this calculation and the 1D calculation was that the injection temperature, which was relatively unimportant in 1D, had a pronounced effect in 2D. Limiting cases are shown in Figures 2-4 and 2-5.
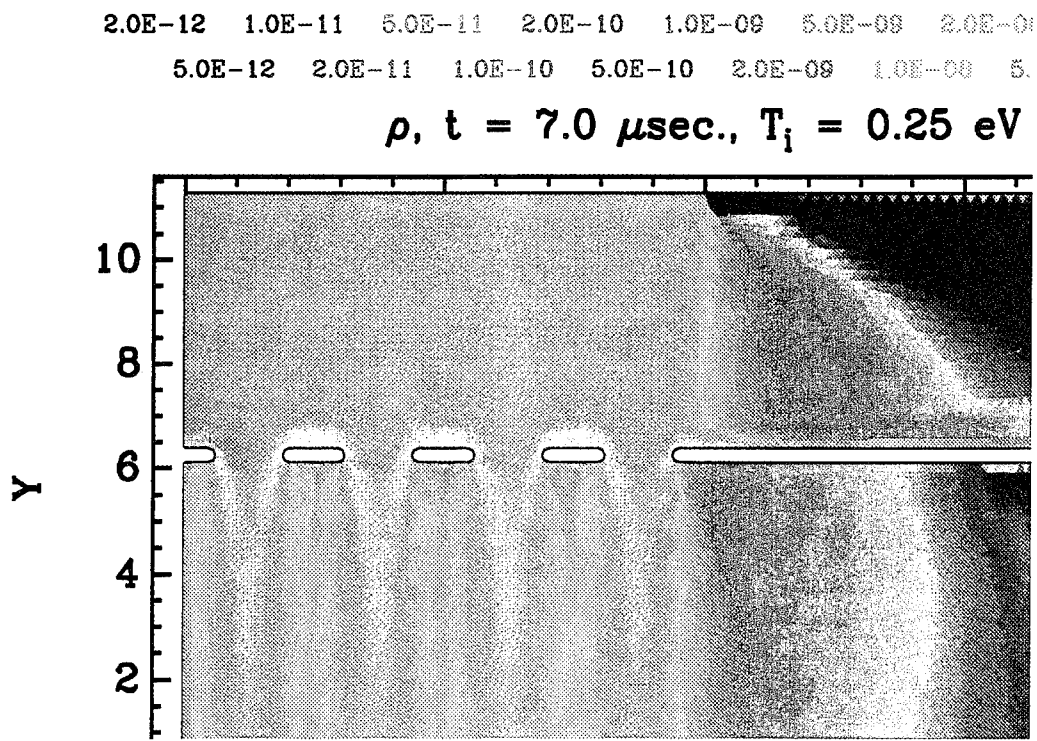
Figure 2-4. Injected plasma density with T_i = 0.25 eV.

Figure 2-4 shows a calculation in which the injected plasma was taken to have an internal energy/unit mass of 6×10^{10} ergs/gm, which would correspond to a temperature of 0.25 eV if we assumed that the plasma consisted of singly-ionized carbon, or 0.5 eV if we assumed neutral carbon. At this energy, the plasma basically just streamed through the mesh gaps,

without significantly diffusing to fill in the "shadowed" regions. There was little diffusion downstream of the switch region, as well. In contrast, when an injection energy of 1.2×10^{12} ergs/gm was used (corresponding to 5 eV for singly-ionized carbon), the simulation yielded the results in Figure 2-5.
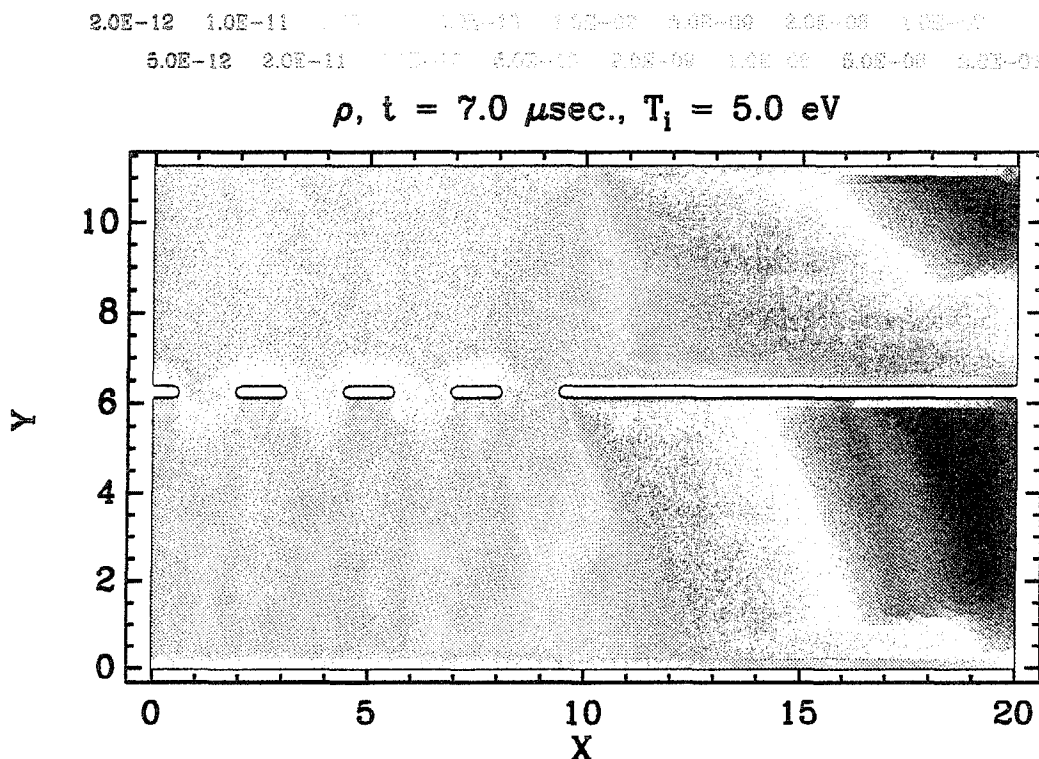
Figure 2-5. Injected plasma density with $T_i = 5.0$ eV.

Here, the plasma diffused to fill the anode-cathode region much more uniformly, and there was some downstream diffusion as well.

To distinguish adequately between these two cases would require further measurements. As it happens, ACE 4 has recently been converted from a double-disk to a coaxial POS configuration which means that those measurements are not yet available. Accordingly, we are proceeding to model the coaxial POS using the same code, in hopes of being able to get the necessary data. Work on this simulation is currently underway.

SECTION 3

A PLASMA OPENING SWITCH MODEL WITH LAUNCHED ELECTRONS AND MAGNETICALLY ENHANCED ION EROSION

3.1   INTRODUCTION.

The physical mechanism underlying the operation of long conduction time (~1 µs) plasma opening switches have been the object of intensive research over the last decade (Cooperstein, Ottinger, 1987). Although the physics of conduction in the POS is not completely understood, recent experiments point to the importance of Hall fields as well as ordinary magnetohydrodynamic (MHD) forces (resulting in a snowplow of the plasma) in the low voltage, conduction phase of the switch. As a result of theories elaborated by Fruchtman (1991), and by Kingsep, *et al*, (1990) the role of Hall fields in low density plasmas has been clarified and the physics of conduction set on firmer ground, for conduction times ranging from about 100 µs to more than 1 µs.

The physical mechanisms that operate during current switchout to produce voltage in the switch remain less well understood, certainly quantitatively, than those that control conduction. Notwithstanding this, it is likely that plasma erosion, MHD forces, or both are involved in the opening process.

Commisso, *et al*., have described the POS in terms of switch limited operation and load limited operation (Commisso, *et al*., 1992). An open circuited load is an example of the former case, and the circuit I-V characteristic is that of the switch. Waisman, *et al*., (1990) have suggested that even for finite (but not too small) load impedance and for a switch characteristic corresponding to magnetically insulated electron flow, the circuit characteristic remains that of the switch, independent of the load. This property for magnetically insulated flow will be clarified in Sections 3-3 through 3-5, and in Appendix A.

That the circuit properties are determined completely by the switch for sufficiently high load impedance carries with it the implication that for discharge of an inductively stored energy into a parallel switch-load combination in which the load impedance begins at a finite value, the time evolution of switch voltage remains independent of the load for some time. This notion to which the model set forth in this paper conforms is confirmed by PIC calculations for electron flow in a narrow gap opening into a vacuum feed terminated by a resistive load.

Here the model for opening is based on the formation by erosion of a low density sheath in the plasma across which the sheath voltage appears. The theory is completed by invoking a balance of particle and electromagnetic momentum flows in the sheath, together with a generalization Creedon's theory of magnetically insulated (Brillouin) electron flows (Creedon, 1977), which includes the effects of ion space charge. The model reproduces some, but not all, significant features of load and switch limited regimes observed in the HAWK accelerator (Weber, *et al*., 1991, 1992).

3.2 THE OPENING GAP: EFFECTS OF IONS.

The physics of the opening phase of the switch is believed to involve the formation of a sheath, or gap of size D(t) which varies with time, across which the flow of electrons is inhibited by the magnetic field. The location of the sheath is not known with certainty; it may separate the cathode or anode from the bulk plasma, or it may be in the interior of the plasma separating regions of different densities. For simplicity, we shall refer to this gap on the anode-cathode (A-K) gap, wherever it is located. Figure 3-1 illustrates the basic elements of the model and helps to establish notation.
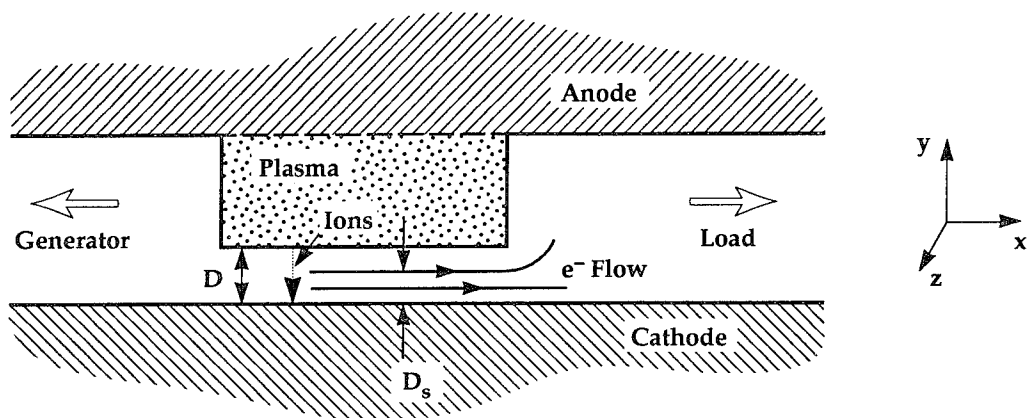
Figure 3-1. The Opening Model. The opening model for the switch is a one-dimensional model, assuming Brillouin electron flow parallel to the cathode and space charge limited ion flow from plasma to cathode. The gap D forms through ion erosion of the switch plasma. The height of the sheath above the cathode is D_s.

The determination of gap voltage and its rate of development require models for D and its rate of growth. According to the erosion model (Commisso, *et al.*, 1992) the gap growth rate is related to the ion current density j_i in the switch by

$$\dot{D} = \frac{j_i}{en_i Z} - V_T \qquad (3.1)$$

where n_i (V_T) is the plasma ion number density (velocity) at the time and location of opening and Z is the mean ion charge in units of e, the magnitude of the electronic charge. The ion current density j_i can be related to the voltage and the magnetic fields at the boundary surfaces of the gap. Their relation follows from conservation of total momentum, electromagnetic plus particle, in the gap. Briefly we use

$$\frac{\partial B}{\partial y} = +\frac{4\pi nev_x}{c} \qquad (3.2)$$

$$E = -\frac{v_x B}{c} \qquad (3.3)$$

$$\frac{\partial E}{\partial y} = +4\pi ne(NZ - n) \qquad (3.4)$$

where $B = -B_z$ is the magnitude of the magnetic field, $E < 0$ is the electric field component in the y direction, N and n the ion and electron densities, respectively. The electron velocity $v_x > 0$ in Equation (3.3) is the E x B drift speed corresponding to Brillouin flow. Substituting Equation (3.3) into Equation (3.2) and using Equation (3.4) to eliminate the electron density, yields

$$\frac{1}{2}\frac{\partial}{\partial y}\left(B^2 - E_y^2\right) = -4\pi NeZE_y \ . \qquad (3.5)$$

Since we assume that ion transit times across the A-K gap are much shorter than ion cyclotron times, magnetic effects on ion motion are negligible and, the density of ions of mass M in the gap is given by

$$NeZ = \frac{j_i}{\left[\dfrac{2eZ}{M}/(\varphi_0 - \varphi)\right]^{1/2}} = -2^{1/2}j_i\frac{\partial}{\partial\varphi}\left(\frac{\varphi_0 - \varphi}{eZ/M}\right)^{1/2} \qquad (3.6)$$

where $\varphi = \varphi(y)$ is the electric potential at the distance d above the cathode. Here we have assumed that ions start from rest at the effective anode where the electric potential is φ_0 relative to the cathode's zero potential. Since

$$E = -\frac{\partial\varphi}{\partial y} \qquad (3.7)$$

Equation (3.5) has the first integral

$$\frac{B^2 - E^2}{8\pi} + j_i\left(\frac{2M}{eZ}\right)^{1/2}(\varphi_0 - \varphi)^{1/2} = C_1$$

$$= \frac{B_c^2}{8\pi} + \left(\frac{2M}{eZ}\right)^{1/2}j_i(\varphi_0)^{1/2} \qquad (3.8)$$

where we determine the integration constant C_1 by requiring that the electric field vanish at the cathode where $B = B_c$. Between the electron sheath and the anode, the magnetic field is constant in y, and momentum conservation gives

$$-\frac{E^2}{8\pi} + j_i \left(\frac{2M}{eZ}\right)^{1/2} (\varphi_0 - \varphi)^{1/2} = 0 \tag{3.9}$$

for space charge limited emission of ions from the anode. Integration of Equation (3.9) gives the Child Langmuir law for ion current in the gap between the anode and the top of the electron sheath at $y = D_s$.

$$j_i = \frac{2}{9\pi} \left(\frac{eZ}{2M}\right)^{1/2} \frac{(\varphi_0 - \varphi_s)^{3/2}}{(D - D_s)^2} . \tag{3.10}$$

Since B at the top of the sheath is the anode magnetic field, it also follows from Equations (3.8), (3.9) and (3.10) that

$$C_1 = B_a^2 / 8\pi \tag{3.11}$$

$$j_i = \frac{B_a^2 - B_c^2}{8\pi} \left(\frac{eZ}{2\varphi_0 M}\right)^{1/2} . \tag{3.12}$$

The solution to Equation (3.8) is reduced to a quadrature if we assume, following other authors, (Creedon, 1977) (Ron, *et al.*, 1973) not only Brillouin flow but energy conservation as well so that all electrons, having started at the cathode, have zero energy

$$\gamma = 1 + \frac{e\varphi}{mc^2} . \tag{3.13}$$

Since

$$\gamma^2 \frac{v^2}{c^2} = \gamma^2 - 1 \tag{3.14}$$

$$B^2 = \frac{\gamma^2 E^2}{\gamma^2 - 1}; \tag{3.15}$$

and Equation (3.8) becomes

$$\frac{E^2}{\gamma^2 - 1} = B_a^2 - 8\pi j_i \left(\frac{2M}{eZ}(\varphi_0 - \varphi)\right)^{1/2} \tag{3.16}$$

$$= B_a^2 - \frac{8\pi j_i}{eZ} \left[2MmZc^2(\gamma_0 - \gamma)\right]^{1/2} . \tag{3.17}$$

Using Equation (3.12) to eliminate j_i we find

$$\frac{eB_c y}{mc^2} = \int_1^\gamma \frac{d\gamma}{\left(\gamma^2 - 1\right)^{1/2}} \left[1 + \frac{B_a^2 - B_c^2}{B_c^2}\left(1 - \left(\frac{\gamma_0 - \gamma}{\gamma_0 - 1}\right)^{1/2}\right)\right]^{-1/2} . \tag{3.18}$$

Evaluating Equation (3.17) at the sheath boundary and combining it with the magnetic field form of the ion current density Equation (3.12), and using Equation (3.15) to eliminate E, yields

$$B_a^2 \left[1 - \gamma_s^2 + \gamma_s^2 \left(\frac{\gamma_0 - \gamma_s}{\gamma_0 - 1}\right)^{1/2}\right] = \gamma_s^2 B_c^2 \left[\frac{\gamma_0 - \gamma_s}{\gamma_0 - 1}\right]^{1/2} . \tag{3.19}$$

The terms in square brackets account for the effects of ion space charge; in the absence of ions, we would obtain Creedon results $B_a = \gamma_s B_c$.

Using Equations (3.10) and (3.19), to eliminate B_c and j_i, Equation (3.12) leads to the additional useful relation

$$\frac{eB_a D}{mc^2} = \frac{eB_a D_s}{mc^2} + \frac{4}{3}\frac{\gamma_s(\gamma_0 - \gamma_s)}{\left(\gamma_s^2 - 1\right)^{1/2}} . \tag{3.20}$$

Finally, using Equation (3.19) to eliminate B_c from Equation (3.18), Equation (3.20) becomes

$$\frac{eB_a D}{mc^2} = \int_1^{\gamma_s} \frac{d\gamma}{\left(\gamma^2 - 1\right)^{1/2}} \left[1 - \left(1 - \frac{1}{\gamma_s^2}\right)\left(\frac{\gamma_0 - \gamma}{\gamma_0 - \gamma_s}\right)^{1/2}\right]^{-1/2} + \frac{4}{3}\gamma_s \frac{\gamma_0 - \gamma_s}{\left(\gamma_s^2 - 1\right)^{1/2}} . \tag{3.21}$$

The results, Equations (3.19) and (3.21) should be compared with the corresponding results obtained by Creedon (1977) for the case without ions.

3.3   COMPARISON WITH ION FREE CASE.

For the geometry of Figure 3-1, Creedon (1977) derived the following relation between gap voltage V, sheath voltage V_m and anode current for Brillouin flow of electrons in the gap D,

$$\frac{eB_a D}{mc^2} = \gamma_s \left[\ell n\left[\gamma_s + \left(\gamma_s^2 - 1\right)^{1/2}\right] + \frac{\gamma_0 - \gamma_s}{\left(\gamma_s^2 - 1\right)^{1/2}}\right] . \tag{3.22}$$

The cathode boundary current I_c at the cathode for these solutions is given by

$$I_c = \frac{I}{\gamma_s} \tag{3.23}$$

a result which holds for the flow patterns other than Brillouin flow.

The value of γ_s does not follow a priori from Creedon's analysis, nor is it readily accessible by experiment. Wang and DiCapua (1980) have proposed that γ_s follows from a minimum total energy principle, electromagnetic energy plus electron kinetic energy, and have examined the consequences of this principle for one-dimensional (1D) systems.

One consequence of their analysis is that over a wide range of voltages there is little quantitative difference between the value of γ_s determined from the minimum energy principle and the value determined by requiring that the current be a minimum with respect to γ_s:

$$\frac{\partial I}{\partial \gamma_s} = 0 \;. \tag{3.24}$$

Moreover, in magnetically insulated transmission line experiments Mendel, *et al*, (1983) observed that current and voltage closely followed the minimum current requirement over a substantial portion of the voltage pulse. Creedon reports a similar behavior in his analysis of magnetically insulated transmission lines.

The minimum current condition, Equation (3.24) yields the following relation between the diode and sheath values of γ_0

$$\gamma_0 = \gamma_m + \left(\gamma_m^2 - 1\right)^{3/2} \ell n\left[\gamma_m + \left(\gamma_m^2 - 1\right)^{1/2}\right] \tag{3.25}$$

where γ_m is the value of γ_s at the current minimum. Together with Equation (3.22), this result constitutes a unique diode current-voltage (I-V) characteristic. In the following we will apply Creedon's I-V characteristic to the opening phase of the plasma opening switch.

Figure 3-2 compares the quantity eB_aD/mc^2 with and without ions as a function of γ_s for a fixed anode voltage corresponding to $\gamma_0 = 4.25$. In general, the differences between the two curves are substantial, although in the neighborhood of the minimum, both of which occur near $\gamma_s = 1.5$, the two quantities differ by only 30-40%. For the case with ions, the range of γ_s is limited to $\gamma_s \cong 2.5$, whereas for the case without ions, γ_s extends to the maximum allowed value, $\gamma_{smax} = \gamma_0$, corresponding to a fully saturated gap. In the case with ions saturation is impossible, since the condition of zero electric field at the anode surface is incompatible with $\bar{E} \times \bar{B}$ drifting electrons having kinetic energy equal to the anode voltage. This is a consequence of the requirement of energy conservation and that all electrons are created at the cathode.
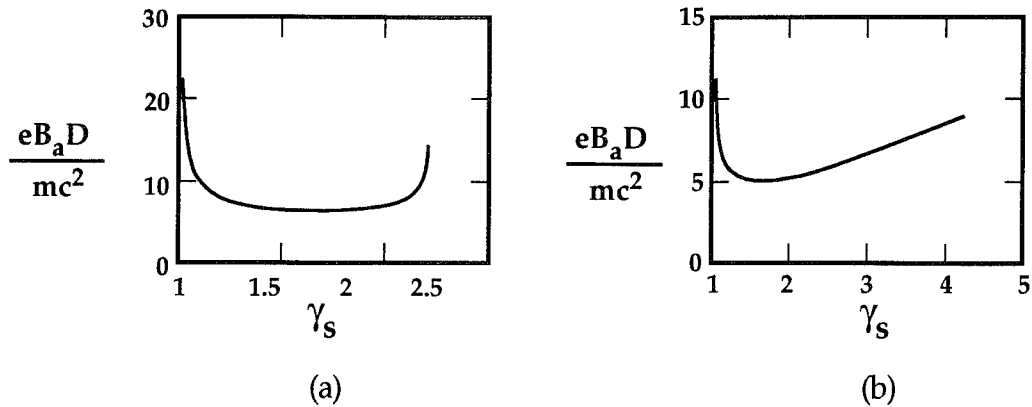
Figure 3-2. Comparison of eB_aD/mc^2 as a function of sheath potential (a) with ions (b) without ions for $\gamma_0 = 4.25$. At current minimum, the ion effect can amount to several tens of percent. (Note difference in scales.)

The limitation on sheath potential follows directly from Equation (3.21) and the requirement that the quantity in the square bracket within the integral sign be positive. For a given γ_s and γ_0, this quantity is least positive for $\gamma = 1$. The requirement of positivity over the entire range of integration is therefore that

$$1 > \left(1 - \frac{1}{\gamma_s^2}\right)\left(\frac{\gamma_0 - 1}{\gamma_0 - \gamma_s}\right)^{1/2} \tag{3.26}$$

or

$$\gamma_0 > \frac{\gamma_s^5 - (\gamma_s^2 - 1)^2}{2\gamma_s^2 - 1}. \tag{3.27}$$

When the equality applies, the integrand has a non-integrable singularity of order $(\gamma-1)^{-1}$ at $\gamma=1$, and by Equation (3.19) the cathode magnetic field B_c vanishes.

As with other one-dimensional theories of Brillouin flow of electrons in a gap, the value of γ_s is open. If γ_s were known, as a function of γ_0 for example, then the anode current, which is proportional to B_a, would be determined as a function of gap size D and voltage. Unless otherwise stated, we shall assume in the following that the appropriate value of γ_s is that corresponding to the current minimum.

It is of interest to consider the implications of the previous analysis to the rate of erosion of a magnetized cold plasma near a cathode surface. A flux of ions into the cathode from a cold plasma at a potential above the cathode potential must result from erosion of the plasma. In these circumstances, ignoring the effect of finite ion transmit times, the erosion rate is given by

$$nD = j_i / eZ \qquad (3.28)$$

where n is the density of the eroding plasma.

If we ignore the ion space charge effect, we can use Equation (3.12) to estimate $\dot{D}/D$. In the limit of small voltages $\gamma_0-1 \ll 1$ and with $\gamma_s \approx \gamma_0$, as evaluated from Equation (3.25), Equations (3.12) and (3.22) give

$$\frac{1}{\tau} = \frac{\dot{D}}{D} = \frac{1}{2} \frac{\omega_c^2}{\omega_p^2} \omega_c \left(\frac{m}{MZ} \right)^{1/2} \qquad (3.29)$$

where

$$\omega_c = eB_a/mc \qquad (3.30)$$

$$\omega_p = (4\pi ne^2/m)^{1/2}. \qquad (3.31)$$

For $B_a = 3 \times 10^4$ gauss and a plasma of singly charged carbon ions with a density of $2 \times 10^{14}/cm^3$,

$$\tau \cong 1.3 \cdot 10^{-9} \sec.$$

We show in the next section that the exponential growth of the gap lasts but a short time before non-linear effects come into play. (In Section 3.4, we use the relatively simple Creedon formulas to describe the switch). The effect of ions on the growth rate of small gaps is difficult to determine because of the non-analytic character of Equation (3.21) in the vicinity of $\gamma = 1$.

3.4 ANALYSIS OF A SIMPLE CIRCUIT.

We now consider the behavior of a circuit containing a hypothetical switch element with a current voltage relationship characterized by Equations (3.22) and (3.25). We suppose that the switch element is part of the circuit represented in Figure 3-3. At t = 0, we impose the initial condition that the switch carries the entire current I_0 in the inductor, while the current I_L in the load vanishes. For t > 0, current is switching into the load.
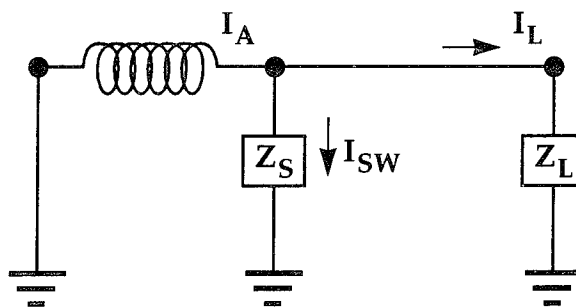
Figure 3-3. Circuit model with switch element characterized by
Equations 3.22 and 3.25.

We assume that until the load current is large enough to equal the cathode current required for magnetically insulated flow, the switch operates at the current minimum, and that otherwise the value of γ_s is determined by the load current. Specifically

$$\gamma_s = \min\left(\gamma_m, I_A/I_L\right). \tag{3.32}$$

We shall refer to switch or load limited phases, respectively, according as γ_s is given by γ_m or I_A/I_L. In the initial phase of opening (ignoring a brief Child-Langmuir bipolar erosion phase), while $I_L \ll I_A$, the circuit is switch limited.

The equations of the circuit are

$$L\frac{dI}{dt} = -V_0(\gamma - 1) = -I_L Z_L(t)$$

$$n\dot{D} = \frac{B_A^2}{8\pi}\frac{\left(\gamma_s^2 - 1\right)}{\gamma_s^2}\frac{1}{\left[2MmZc^2(\gamma - 1)\right]^{1/2}} - nV_T$$

together with Equations (3.22) and (3.25). The most general form of load that we consider here consists of a fixed load inductance L_L and a specified dynamic resistance $R(t)$.

The following figure show current and voltage waveforms, the gap D and the erosion velocity as functions of time for simulations of a HAWK (Commisso, *et al.*, 1992) experiment. The voltage is independent of the load for

$$\gamma_m \frac{I_L}{I} < 1 \quad \left(\text{Figure } 3-4g\right).$$

The assumed circuit and switch plasma parameters are:

$$
\begin{aligned}
L_0 &= 675\,\text{nh} \\
L_{\text{load}} &= 30\,\text{nh} \\
a\ (\text{cathode radius}) &= 5\,\text{cm} \\
D_0\ (\text{initial gap}) &= 0.01\,\text{cm} \\
V_T\ (\text{plasma thermal speed}) &= 3 \times 10^6\,\text{cm/sec} \\
n &= 2 \times 10^{14}\,\text{cm}^{-3}.
\end{aligned}
$$
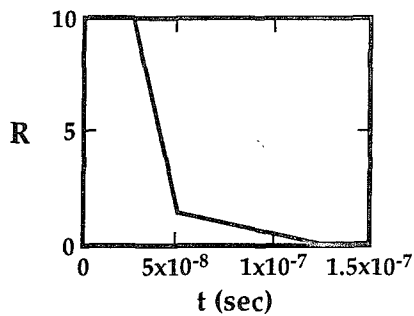
a. Assumed Load Impedance (ohms)
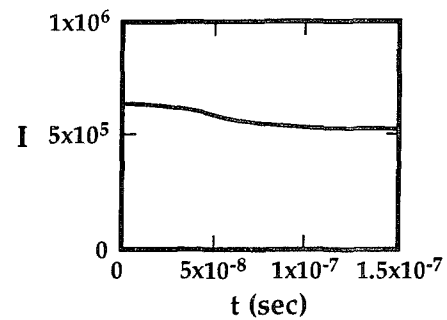
b. Generator Current (amps)
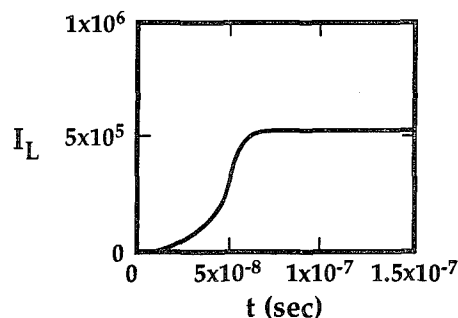
c. Load Current (amps)
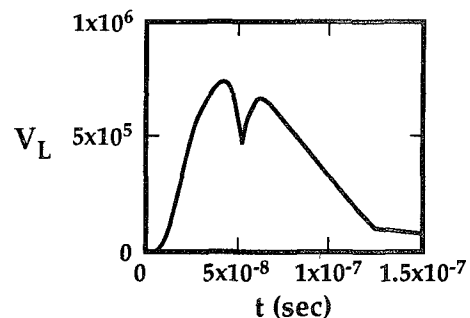
d. Load Voltage (Volts)
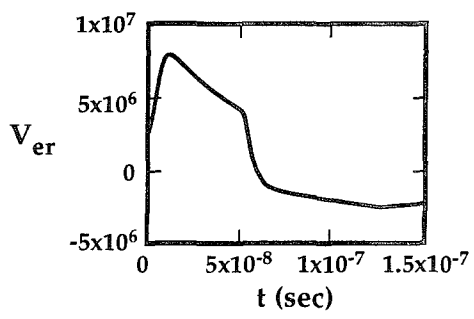
e. Erosion Velocity (cm/sec)
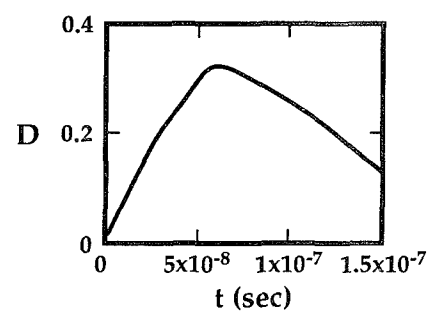
f. Gap (cm)
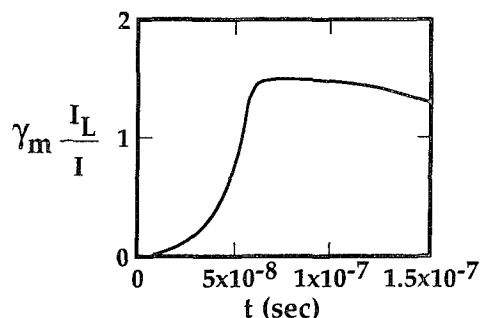
g. Switch Limited Parameter
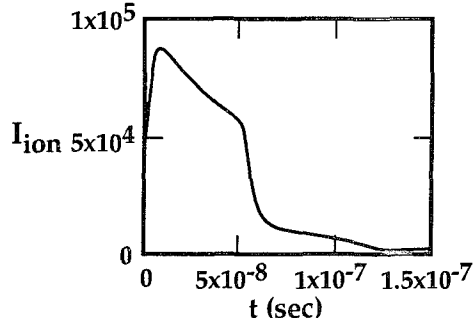
h. Ion Current (amps)

Figure 3-4. Model results for assumed load impedance R(t).

The model presented here compares favorably with the current and voltage wave forms given by Weber, *et al*, using a reasonable value of the plasma density. There are however, a number of parameters in the model, the values of which are uncertain at the onset of the opening phase of the switch. These parameters include the switch density n and switch length l at the onset of opening, neither of which can be inferred with certainty from measurements made prior to or even during the conduction phase. The results are relatively insensitive to V_T for V_T ranging up to a few times 10^6 cm/sec, and to D_0, for D_0 less than a few tenths of a millimeter. Observe also that the ion current, Figure 3-4 h, is ≤ 20 percent of the generator current; this justifies a posteriori its neglect in the circuit equations. A major uncertainty is in the load impedance; the rapidly varying impedance of brems and PFD loads certainly have a considerable influence on measured current and voltage waveforms. Although with a reasonable choice of parameters, we can calculate current and voltage waveforms which agree with experiment, this cannot be considered a validation of the model.

3.5   COMPARISON WITH PIC CALCULATIONS.

Calculations were performed with the FRED particle-in-cell code to evaluate the accuracy of the analytic treatment of the electrons in the switch gap, to test the assumption that for small load currents the switch voltage is load independent, and to determine the fate of the electrons as they drift out of the gap. The geometry used for the calculations is shown in Figure 3-5.
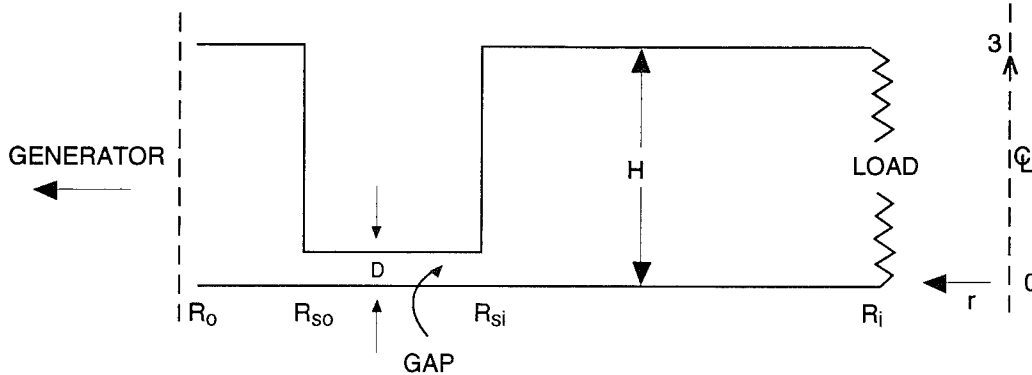
Figure 3-5. Geometry for PIC calculations.

The axisymmetric geometry corresponds to the top one-half of ACE-4, (Thompson, *et al.*, 1994) the bottom half given by reflection of the figure in the plane z = 0. Relevant dimensions are H = 5 cm, R_i = 20 cm, R_0 = 50 cm, R_{si} = 40 cm and R_{s0} = 45 cm. The switch gap D is fixed at 0.4 cm. The tangential electric field vanishes in all boundaries except at r = R_i and r = R_0. The entire cathode surface is capable of space charge limited emission of electrons. Ions are not included in the calculations.

At the input boundary at R = R_0, the current increases on a linear ramp for 5 ns at which time it becomes constant at 4.3 MA. The load is a fixed resistor extending from cathode to anode, and for the calculations that follow is given values of 15.3 Ω, 1 Ω, 1/3 Ω and zero ohms, the first corresponding closely to open circuit conditions, the latter to more nearly matched load

conditions and to an inductively short-circuited load, respectively. The inductance of the system between R_o and R_i is about 8 nH, giving L/R times (in vacuum) ranging from about 0.5 ns at 15.3 Ω to about 25 ns at R = 1/3 Ω. We attempt to run the calculations until the system reaches a steady, or quasi-steady state corresponding to the asymptotic input current of 4.3 MA.

Figure 3-6 shows the voltage waveforms at various radial positions for the three values of resistance. In the 15.3 Ω and 1 Ω cases corresponding to switch limited operation the voltage achieves a steady value, apart from small oscillations, consistent with a switch impedance of about 1/3 Ω. In both cases the characteristic time to achieve "steady state" voltage after allowing for the current rise time of 5 ns is consistent with the L/R time.

Run 5: 15.3 Ohm Load, 0.4 cm Gap   Run 10: 1 Ohm Load, 0.4 cm Gap   Run 8: 1/3 Ohm Load, 0.4 cm Gap
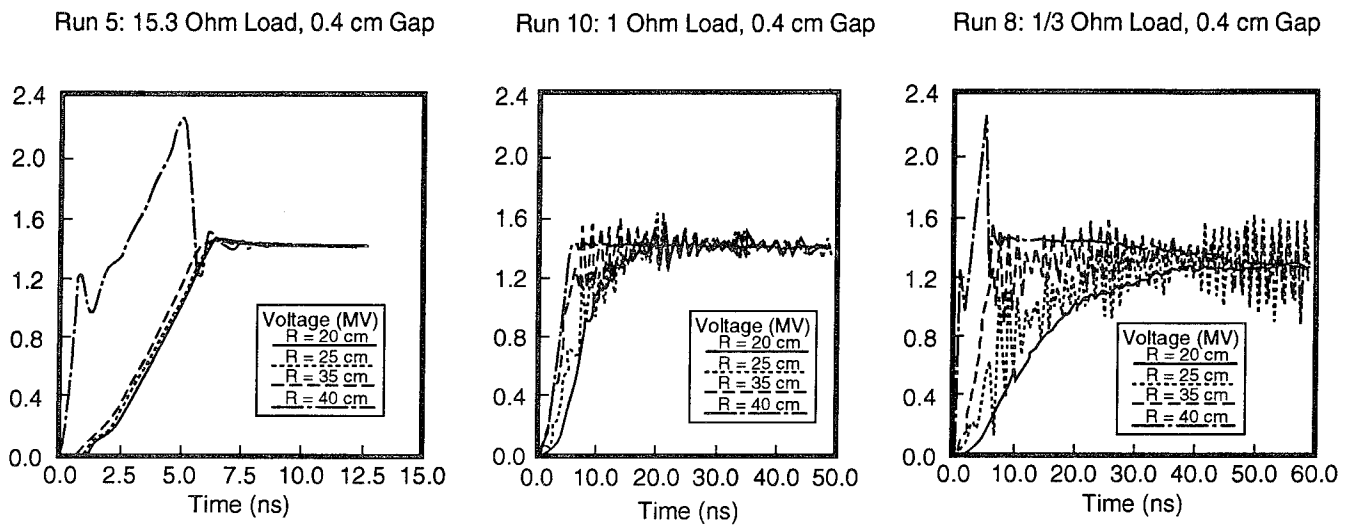
Figure 3-6. Voltage histories at various points in the diode for three values of load resistance.
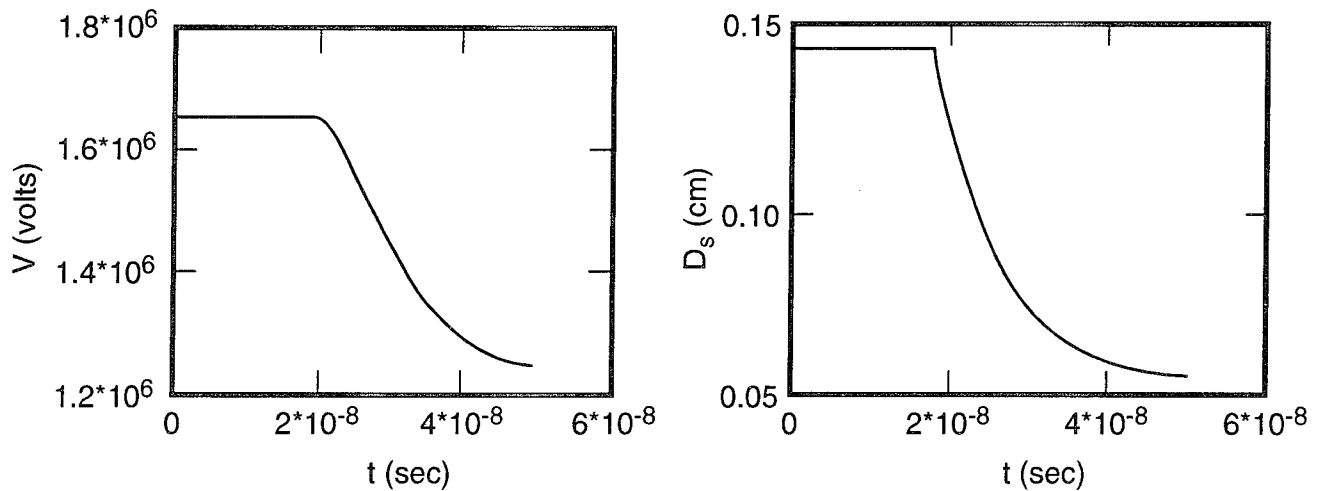
Figure 3-7. Shows voltage and sheath size of a 1/3 Ω load.

The value of switch voltage, 1.4-1.5 MV, and impedance, 1/3 Ω, determined from the PIC results compare favorably with the results calculated from the model, Figure 3-7 which gives V = 1.65 MV, Z = 0.38 Ω and a sheath height D_s = 0.145 cm. The sheath height inferred from the PIC generated results shown in Figures 3-8 and 3-9 is $D_s \cong 0.2$ cm.

Figure 3-9 also shows the ratio $rob2 = \omega_p^2 / \gamma \omega_c^2$ where

$$\omega_p^2 = 4\pi n e^2 / m_0$$

$$\omega_c^2 = \left(\frac{eB}{m_0 c} \right)$$

where m_0 is the rest mass of the electron. According to the theory we should find

$$rob2 = 1 .$$

The corresponding PIC values fluctuate, ranging from about 0.5 to 1.3 over most of the gap.
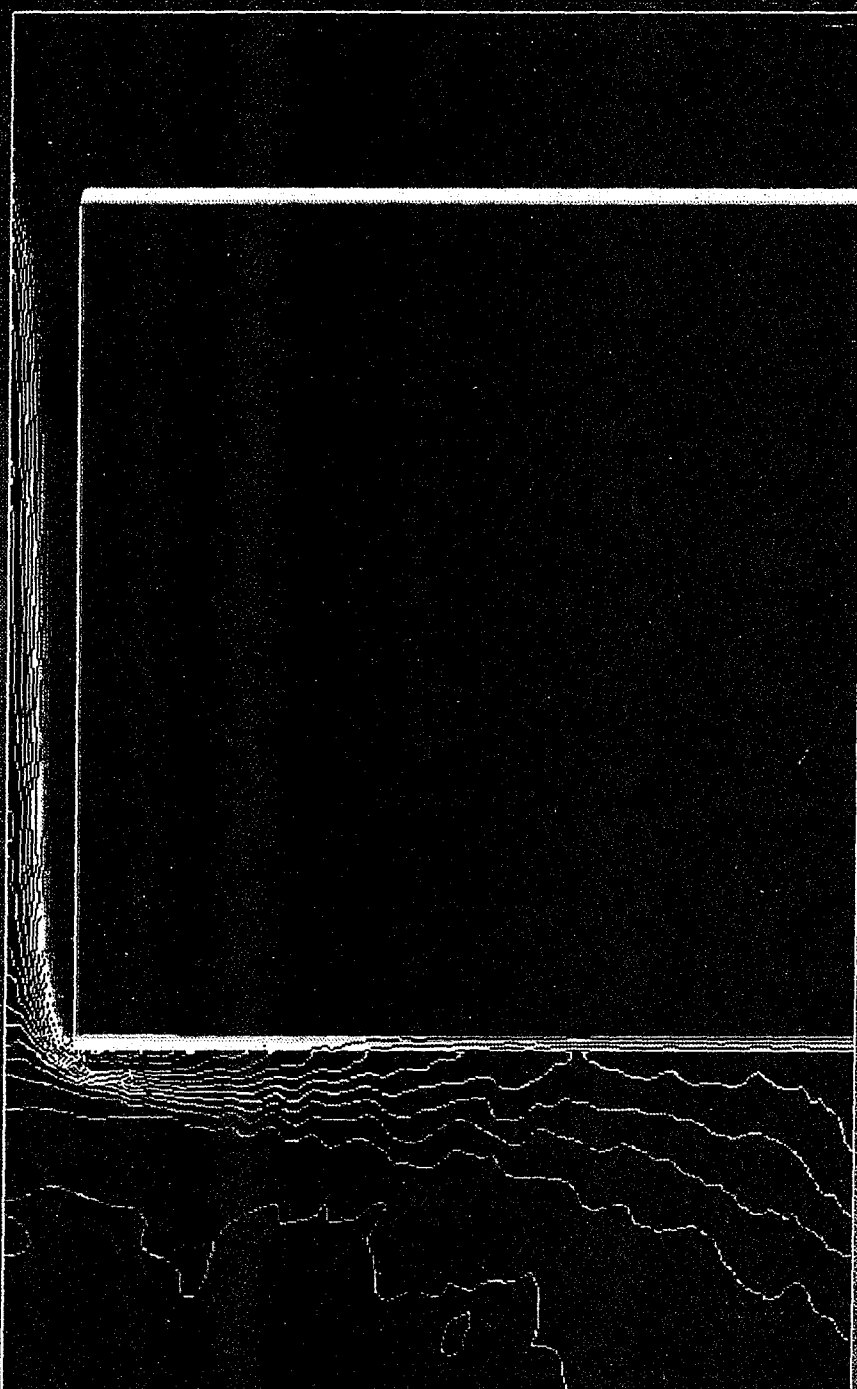
Figure 3-8. Sheath height inferred from PIC generated results.
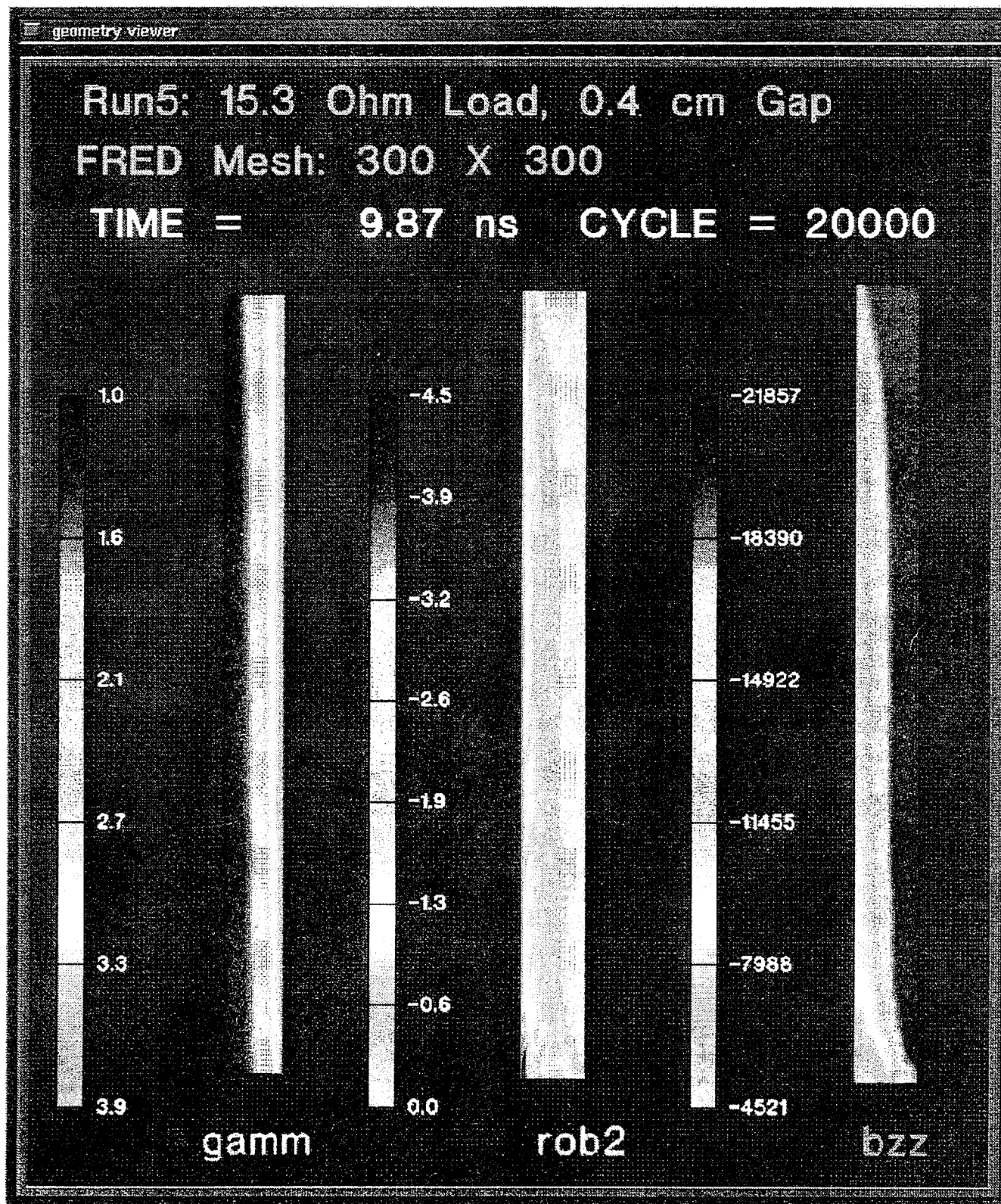
Figure 3-9. Sheath height inferred from PIC dgenerated results.

The corresponding results for the case of a 1 Ω load are shown in Figures 3-10 and 3-11. These results, and their comparison with analytic results, are similar to the case of the 15.3 Ω load. The analytic results are precisely the same as for the 15.3 Ω case, based on the criterion of Equation (3.25) whereby the value of γ_s still is that corresponding to minimum current.

The largest perceptible differences between the 15.3 Ω and 1Ω cases occur in the feed on the load side of the 0.4 cm gap. Figure 3-10 shows the relevant results for Y (gamm), the axial component of electric field (exx) and the magnetic field (bzz). The salient features are the development of a potential minimum, the reversal of electric field at the cathode (exx > 0), the apparent tendency toward formation of a diamagnetic current loop shielding the interior of the region from the magnetic field of the surface currents, and the closure of current paths at the cathode surface just on the upstream (generator) side of the load. This closure evidently corresponds to the return of launched electrons to the load. Similar results are reported by Swanekamp, *et al*, 1994.

The patterns observed for the case of a 1 Ω load are even more pronounced for the 1/3 Ω load, Figure 3-12, a case which illustrates a departure from the apparent switch limited behavior for 15.3 Ω and 1 Ω loads. The potential hill and the diamagnetic current loop appear more fully developed for this case. Perhaps the most noticeable difference from the 1 Ω case is the substantial decrease in height of the electron sheath in the 0.4 cm gap, Figure 3-13. In this case, the load current is about 1.2 MV/(1/3 Ω) = 3.6 MA. According to Equation (3.38), we should be in the load limited regime with a sheath $Y_s \approx 4.3/3.6 \approx 1.2$ and a sheath height $D_s \cong .06$ cm. The sheath height from the PIC calculation appears to be about .08 - 0.10 cm. In both cases, the change in sheath height from the 1 Ω case is substantial, although the analytic value of D_s remains noticeably smaller than that estimated from the PIC calculations.

The results of the calculations for an inductive short circuit load (Figures 3-14 and 3-15) provide the most striking example of dynamic switch limited operation. As with a resistive termination, a voltage plateau of 1.4 MV develops in the interval between about 7 ns and 20 ns, followed by a voltage collapse ending in a steady oscillation of voltage about a small value. The occurrence of this transition at about 20 ns is analogous to the one observed in the 1/3 Ω case at about 35 ns, but which is absent during the computational time interval of the 15.3 Ω and 1 Ω cases.

The oscillations appearing in Figure 3-14 are probably not associated with the electron cloud that persists in the vacuum feed. We have observed the same ~ 10 ns period in simulations of the system shown in Figure 3-5 where electron emission was suppressed. The corresponding current for the vacuum case oscillated between zero and about 8 MA with a mean of 4 MA. They are evidently related to light transit time effects and to the pulse distortion occurring in cylindrical systems. To verify this conclusion, the calculations were repeated with the D=0.4 cm gap removed, having a radial feed with a constant height of 5 cm. This system, when driven by a step function current (rising to 4.3 MA in 0.5 ns), rang with a principal period of about 4 one-way transit times, as expected on the basis of elementary considerations. Thus, although trapped electrons may effect the amplitude of the ringing, they appear not to be its source.
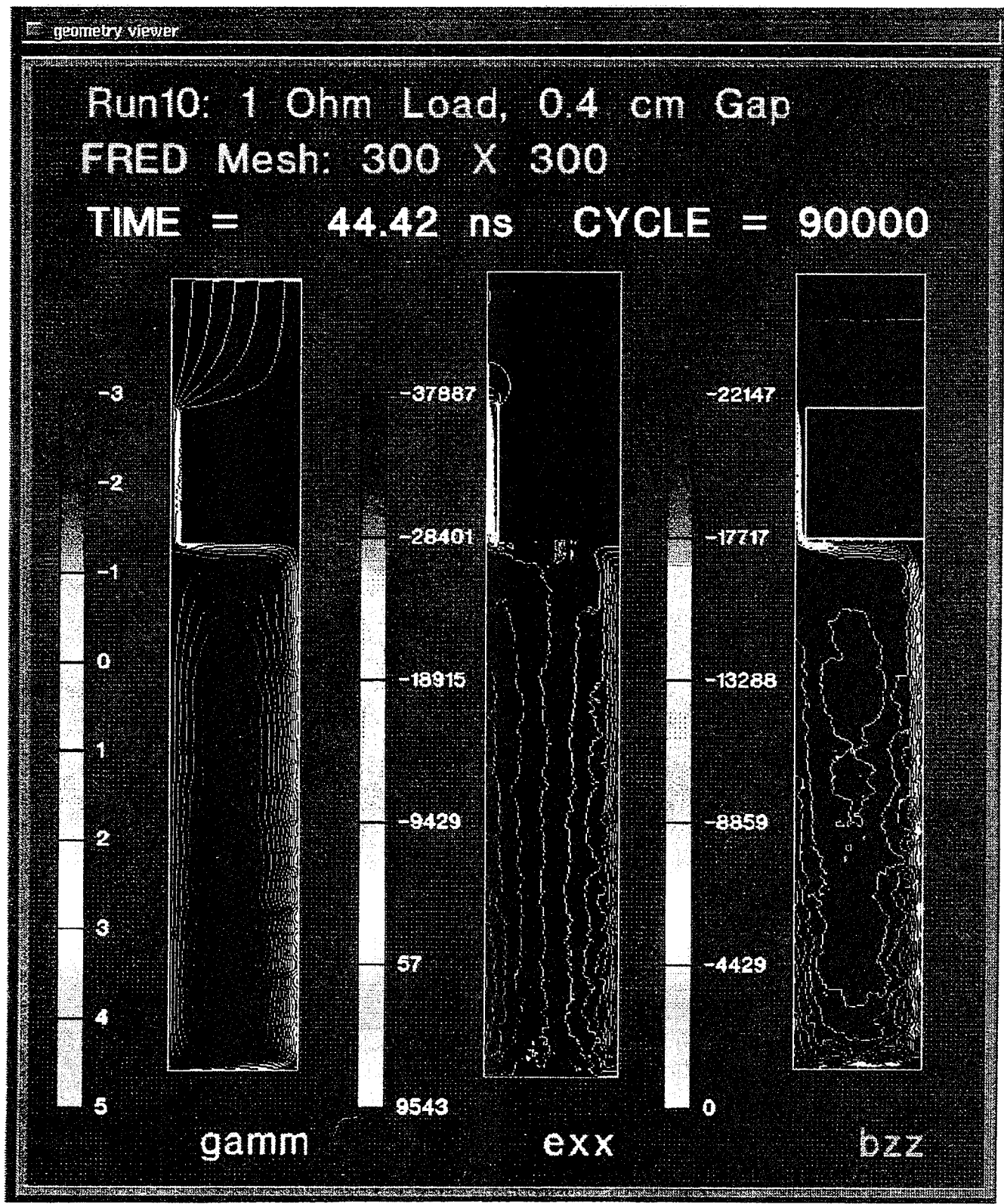
Figure 3-10. Corresponding results for the case of a 1Ω load.
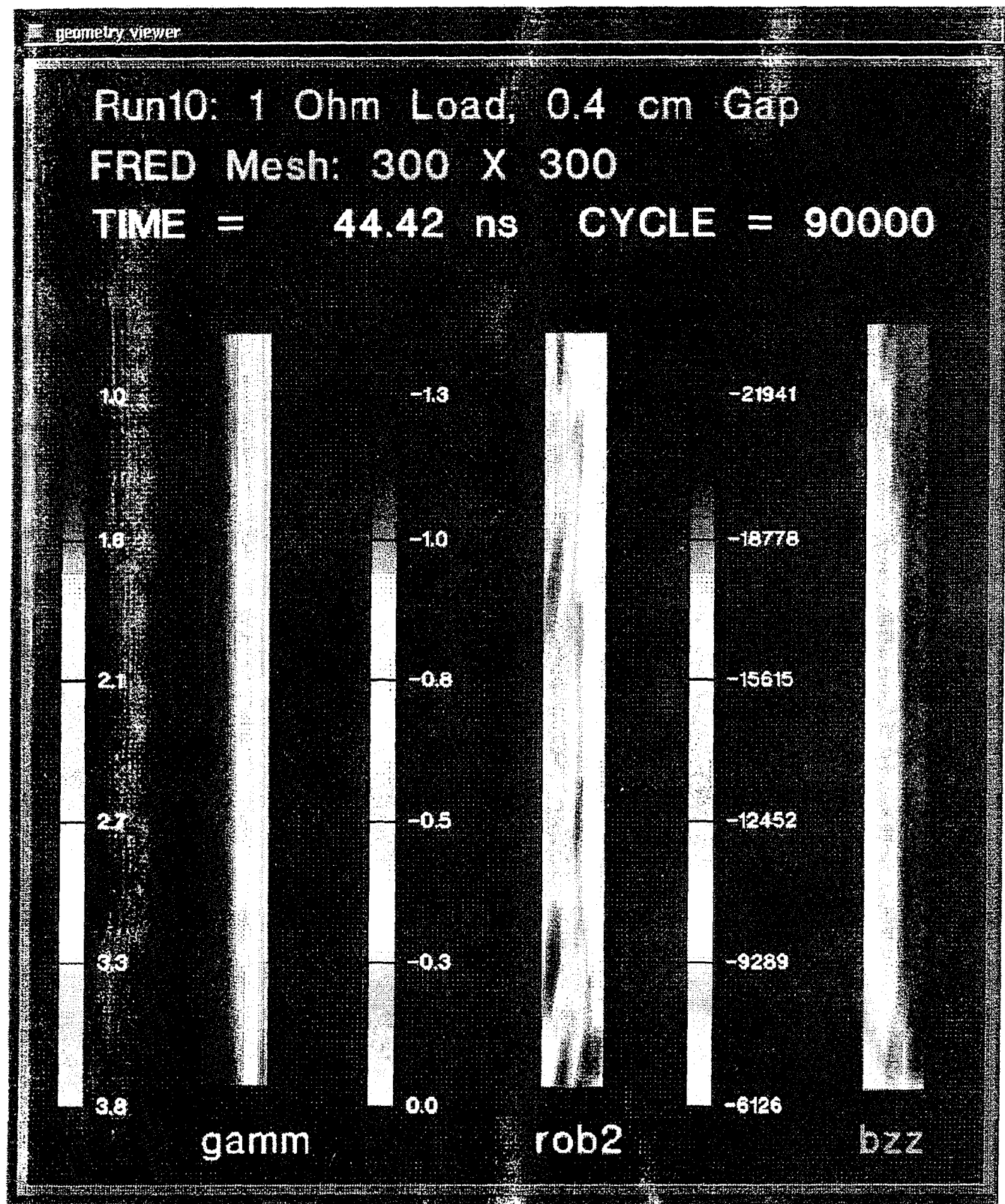
Figure 3-11. Corresponding results for the case of a 1 Ω load.
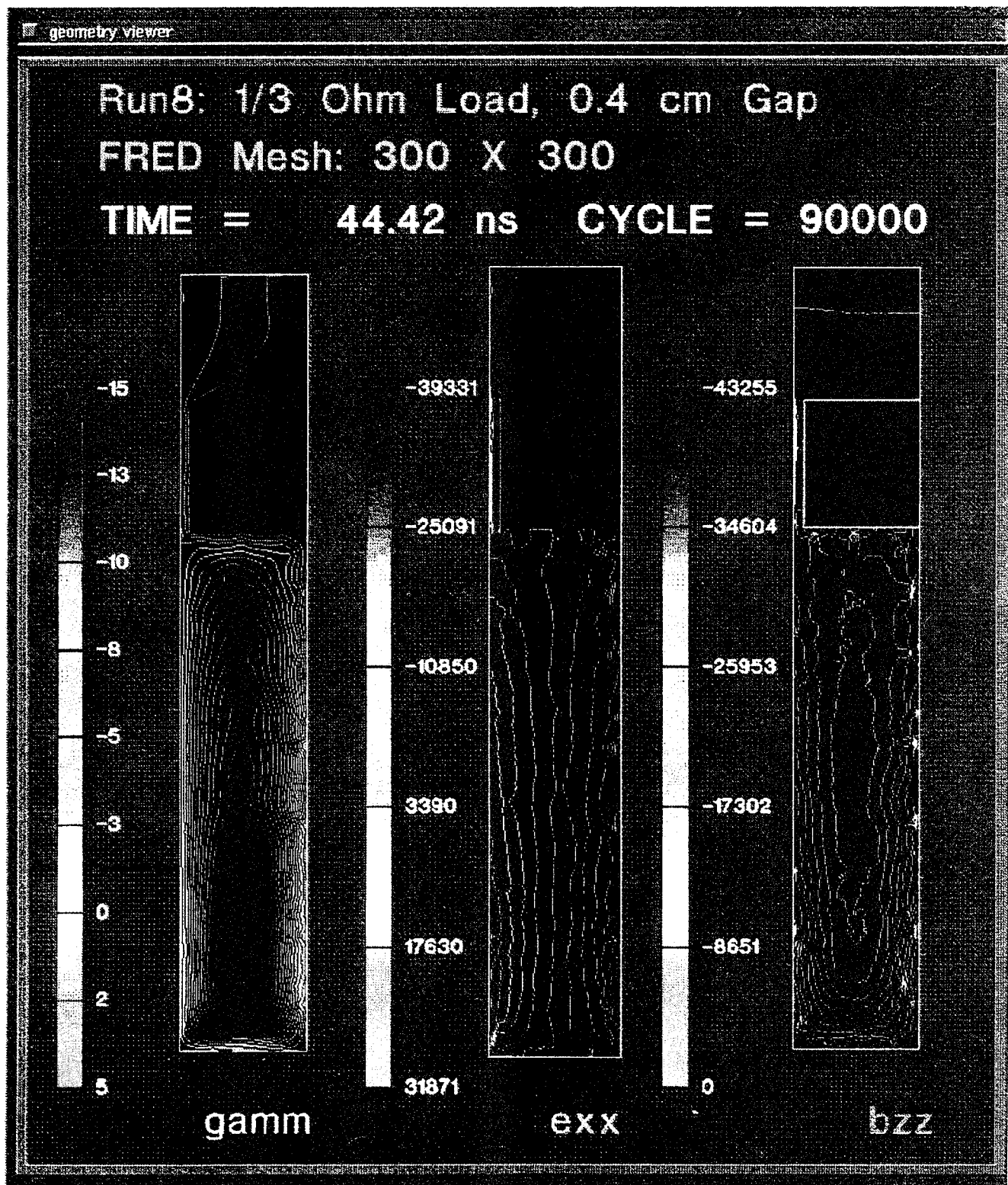
Figure 3-12. Illustration of a departure from the apparent switch limited behavior for 15.3 Ω and 1 Ω loads.
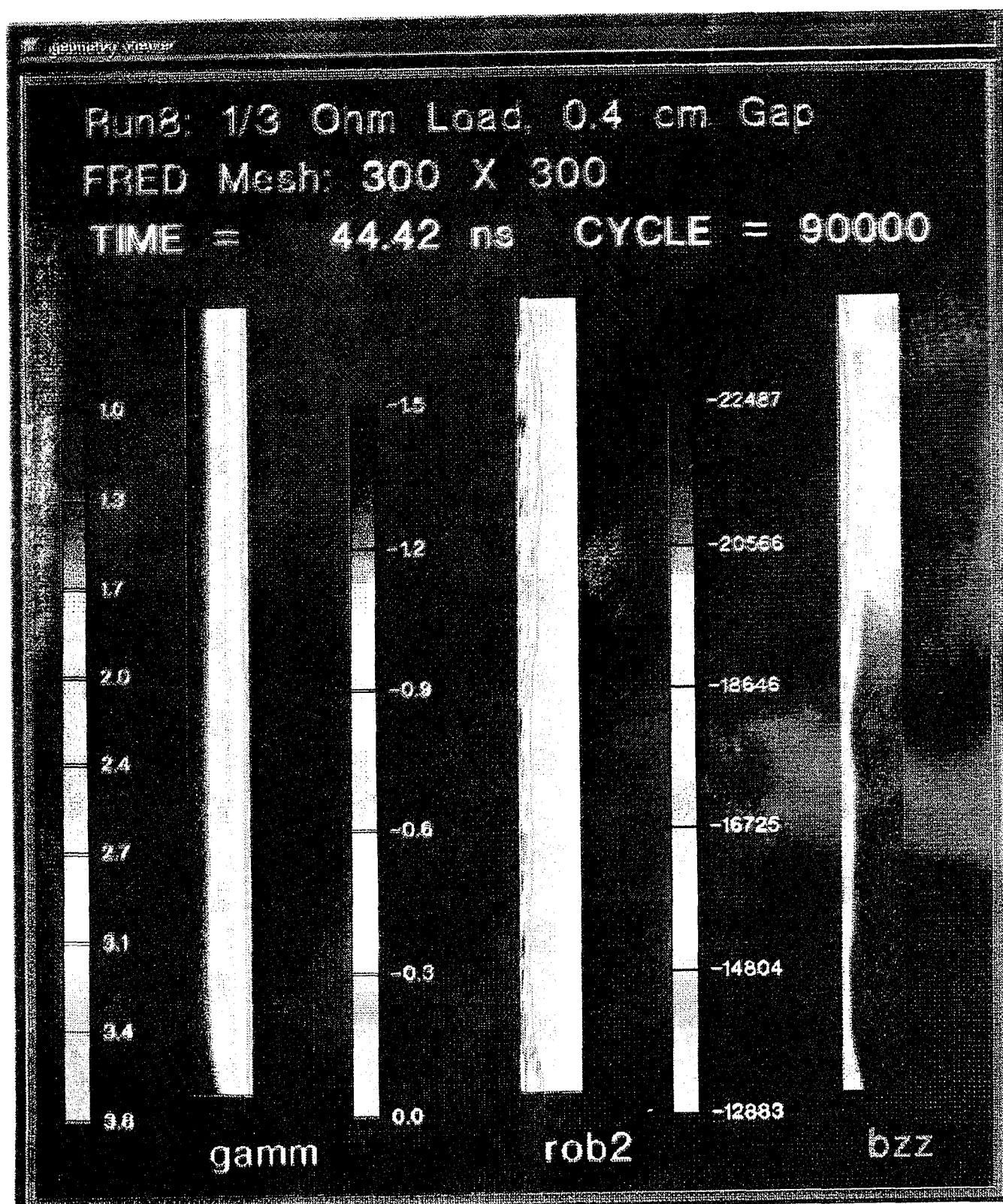
Figure 3-13. Substantial decrease in height of the electron sheath in the 0.4 cm gap from the 1 Ω case.

FRED 2-D PIC SIMULATION OF ACE 4
RADIAL GEOMETRY SWITCH DESIGN
SHORTED LOAD, 0.4 cm GAP
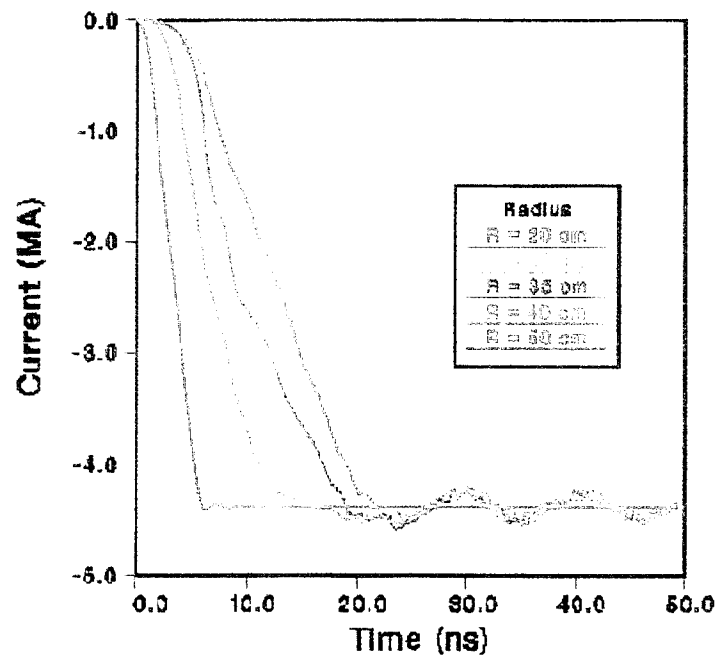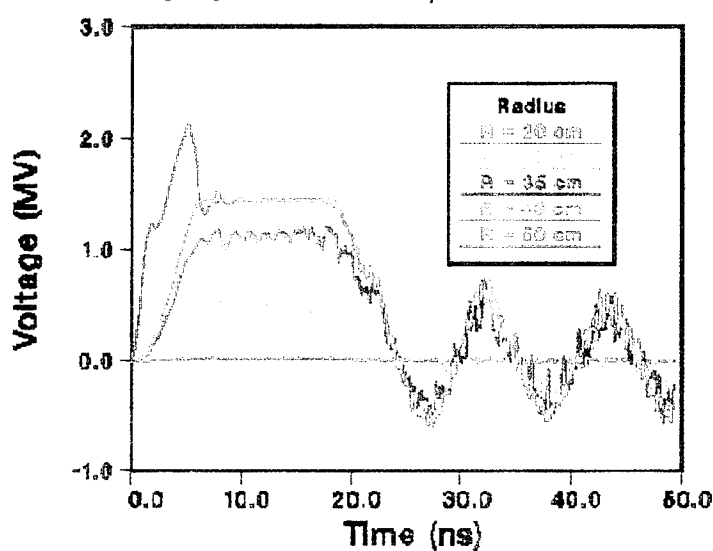
Figure 3-14. Results for the calculations for an inductive short circuit load.
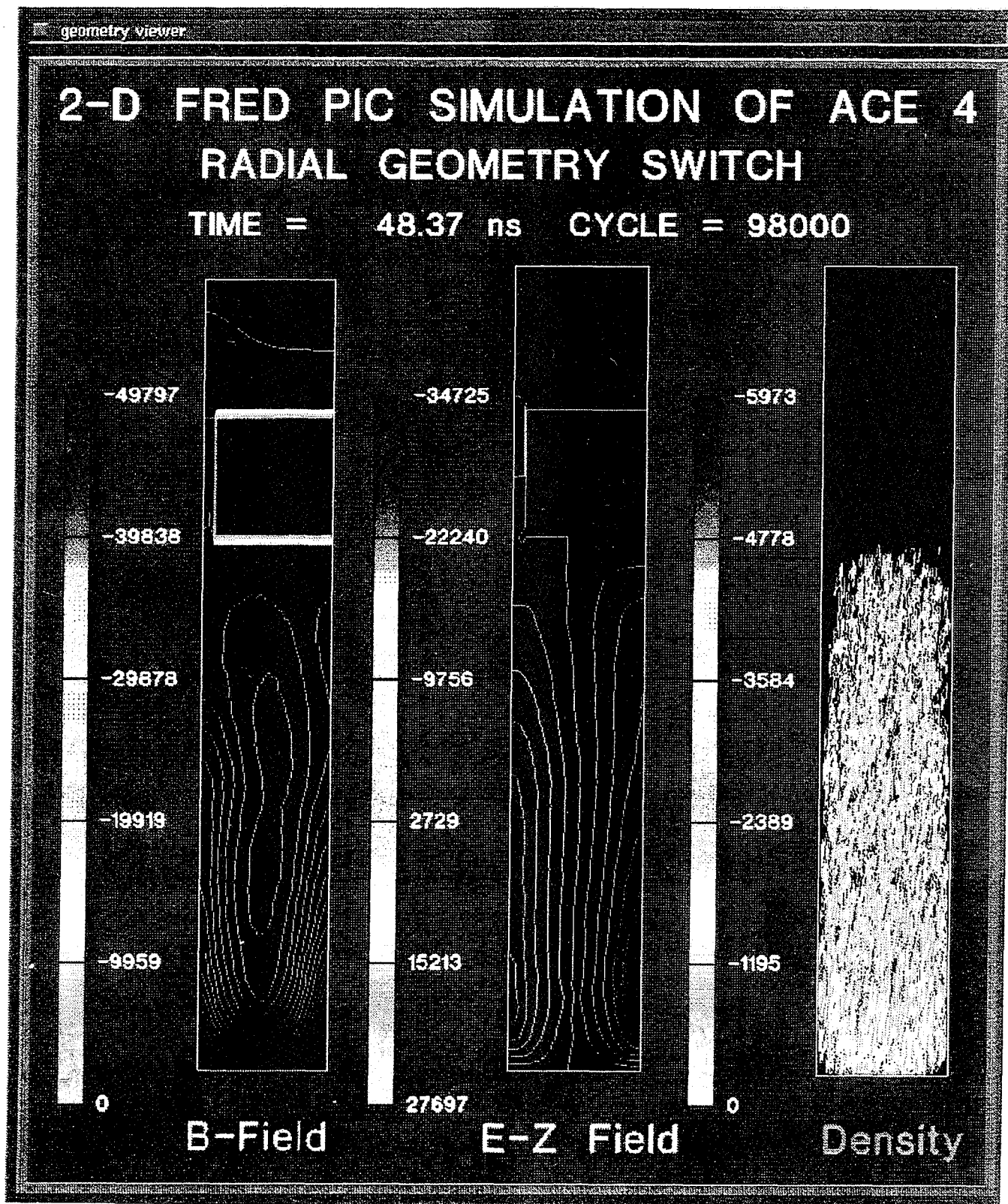
Figure 3-15. Results for the calculations for an inductive short circuit load.

SECTION 4

CODE UPGRADES

We have made a number of significant upgrades to three of our codes, S3Snow, S3Circuit and S3Mesh, used for analysis of ACE-4, HAWK and other machines. The upgrades are as follows:

1. The S3Snow and S3Circuit codes have been supplied with a nonlinear least-squares curve-fitting package to allow the analysis of any curve that can be plotted. Currently, fits can be made to linear, quadratic, cubic, exponential, gaussian, and damped sinusoidal curves. An example of the use of this package is to fit the current derivative measured in an ACE-4 calibration shot. By fitting the measured curve to a damped sinusoid, it is then easy to determine the total series inductance and resistance, assuming the capacitance of the Marx banks is known.

2. We have added some new parameters to S3Snow to allow the study of the chordal line-integrated density measurements taken at ACE-4 and HAWK. The parameters specify the spread upstream and downstream during the conduction phase, and allow a good fit to be made to the snowplow trajectory.

3. A snapshot capability has been added to S3Snow, giving a rough picture of the snowplow plasma distribution as it approaches the line of sight of a chordal line-integral. We compute an estimate of the chordal line-integral due to the flashboard plasma without pulsed power, and subtract this from the measured chordal line-integral with pulsed power. The remainder is interpreted as the line-integral of the snowplow front alone. This line-integral is corrected for the time dependence of the mass within the snowplow front. We then use the computed position of the snowplow as a function of time to transform the time-sampled signal to a spatial snapshot of the snowplow front. We have made an attempt to sharpen the snapshot using deconvolution techniques. So far, the results have been unsatisfactory.

4. We have added rectangular geometry to the list of geometries supported by S3Snow. The reason for this upgrade is to allow us to study data taken in the rectangular switches being studied at NRL and at HY-Tech Research Corporation.

5. We have upgraded S3Snow so that it can simulate the POS conduction phase for arbitrary boundary configurations. Previously, the code assumed that the switch was contained between two parallel electrodes. With the new upgrade, the electrodes can be specified as an arbitrarily long sequence of connected straight line segments. Termination of the run takes place when the snowplow front intersects some user-specified terminus curve. Plasma density is defined on a triangular mesh that covers the switch region. Examples of the problems that can be studied with this new version of the code include:

a) The ACE-4 coaxial POS, including the high-inductance region downstream of the switch,

b) The ACE-4 tandem puff coaxial fast-pinch device,

c) The HAWK machine with conical cathode,

d) The DECADE switch with stepped anode,

e) Switches like those used by the Russians, with bends in the powerflow region downstream of the switch.

6. The triangular mesh generator S3Mesh was ported to the SGI Indigo workstation. S3Mesh was originally written on a Stellar GS1000workstation. The Stellar is now getting old, and it seemed best to get the code running on the most commonly used platform here at S-Cubed. We use S3Mesh constantly to create triangular meshes for 2D fluid calculations using our in-house code DELTA.

7. As the number of POS geometry options in S3Snow has multiplied over the last few years, it has become clear that the best way to handle the vast array of possible configurations is to use the techniques of object-oriented programming. We have begun work on an object-oriented data-import module written in C++, to allow us to import arbitrarily many experimental data curves and manipulate them easily. Currently, the module handles only one-dimensional functions. Our plan is to extend this to functions on two and three dimensions. Data can be specified in a large number of different formats in 2D, and one of the most interesting of these is an unstructured triangular mesh of the type generated by S3Mesh.

SECTION 5

POWER FLOW EXPERIMENTS

5.1 RADIAL GEOMETRY PLASMA OPENING SWITCH POWER FLOW EXPERIMENTS.

5.1.1 Background.

ACE-4 shown in Figure 5-1, is a 4 MJ compact pulsed power generator based on inductive energy storage technology utilizing Plasma Opening Switches (POS) for power conditioning. The prime power consists of 24 sub-Marxes, organized in four oil tanks. The sub-Marxes each drive multiple parallel plate transmission lines to a load coupler, at which the power flow is split, feeding two parallel oil-vacuum interfaces. Each oil-vacuum interface drives power to one of two back-to-back large area POS. Figure 5-2 shows the ACE-4 geometry with each POS driving separate short circuit loads. In this configuration, ACE-4 is capable of delivering up to 5 MA in 1.6 μs to each of the two radial POS.
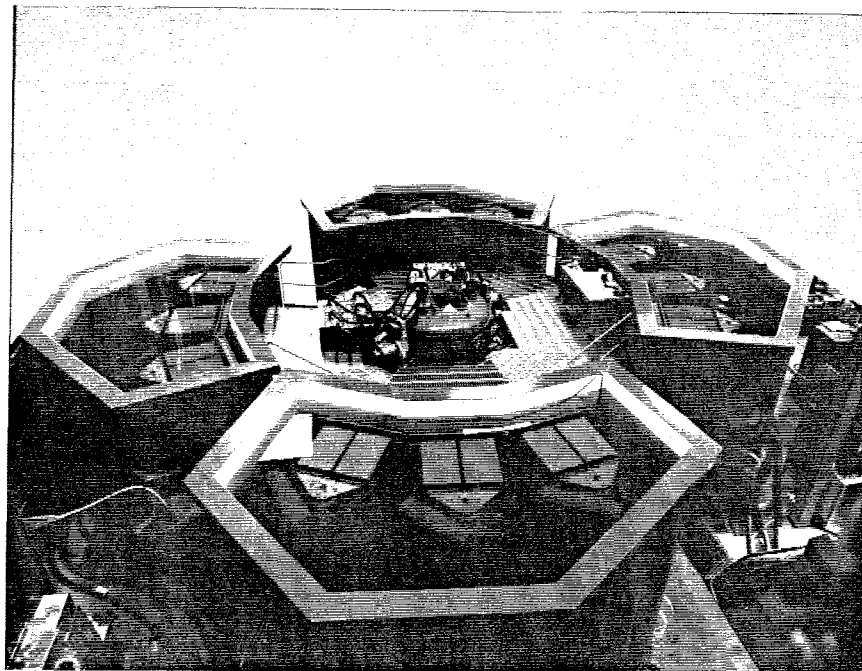
Figure 5-1. ACE-4.
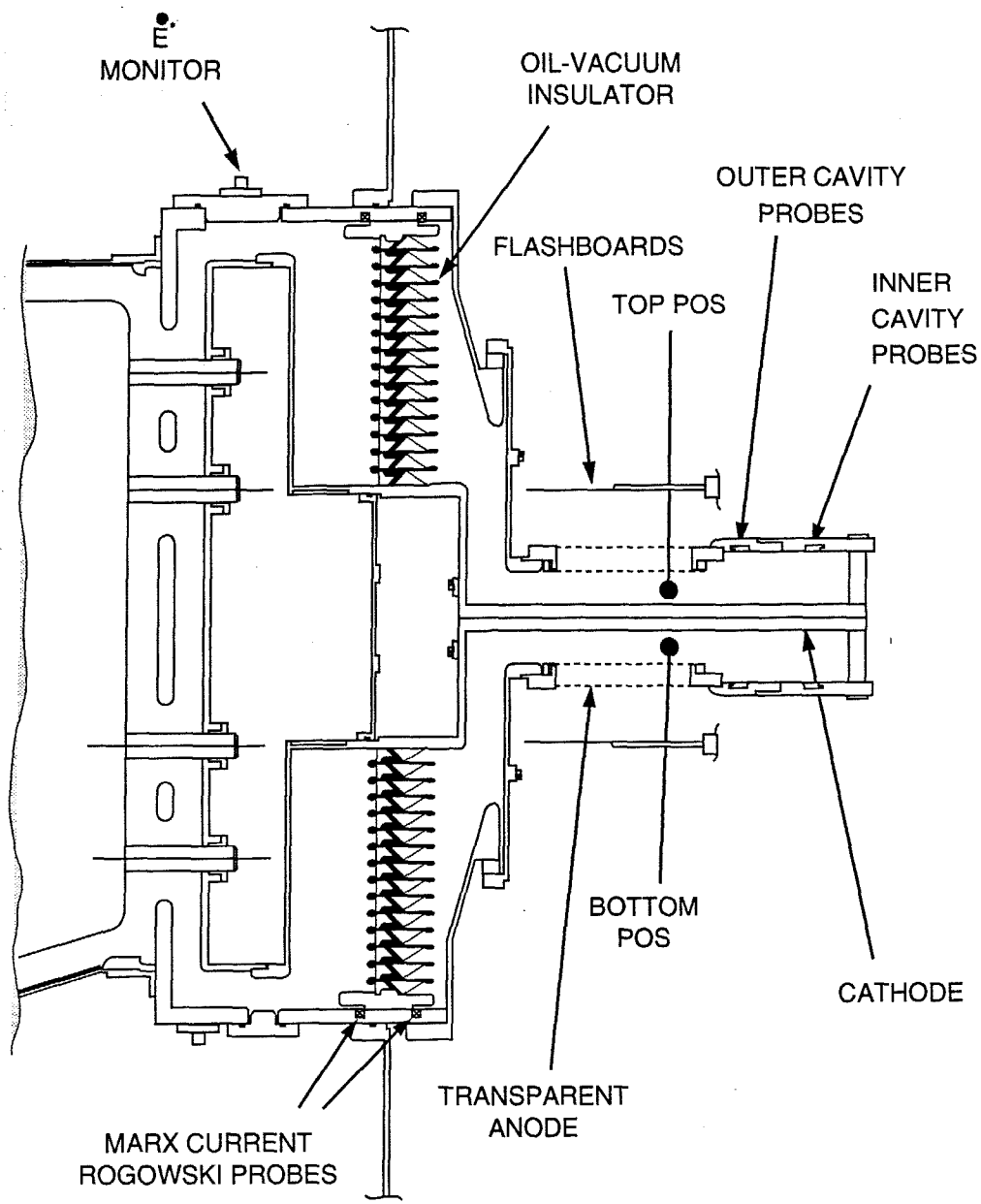
Figure 5-2. ACE-4 radial POS driving a short circuit load.

The previous ACE-4 optimization efforts focused primarily on optimization of the ACE-4 radial POS. The program used a POS design methodology based on theoretical and experimental work originated by S-Cubed and the Naval Research Laboratory (Ingermanson, et al., 1993) (Hinshelwood, et al., 1992). The optimization and design approach assumed the physics of high plasma density POS operation during the conduction phase is dominated by hydrodynamic effects. This view explains how a long conduction time, high density POS can open rapidly. Rapid opening requires that low plasma densities be present at the time of opening. If the initial plasma density distribution has the right mass density profile across the

gap, the current front develops a bow which pushes much of the plasma off to the sides, thinning the plasma in the region where a gap can be opened. An example of this process is shown in Figure 5-3, which gives the results of a simple two-dimensional snowplow calculation for the slow plasma flashboard source tested on ACE-4. Here the 16 cm radial switch length, defined by the anode opening, is used to convert measured line density to electron density. In the case of the radial ACE-4 geometry, where there is no magnetic field gradient across the gap, a minimum in the initial intergap density profile is required, as shown in Figure 5-3(a). Because of the intergap density minimum, the current front develops a bow, as shown in Figure 5-3(b). Figure 5-3(c) shows the thinning effect in terms of the modeled integrated line density along the direction of power flow; the average ionization state is taken to be one. According to the model, the integrated line density is reduced by an order of magnitude by the time the current front reaches the end of the POS. The actual density at the point of opening is a function of the physical length (thickness) of the plasma front. This length has not been determined by either our simple snowplow models or our experimental measurements on ACE-4.

An important part of the optimization program was the development of a plasma source consistent with the above POS design criteria (Thompson, 1993). A significant portion of the work involved the design of a new, slow plasma flashboard source which would be reliable, reproducible, capable of generating a minimum in the initial intergap density profile, and able to supply a sufficient plasma density to conduct the required $I_c^*T_c$ product. Pulsed power testing demonstrated reliability, reproducibility, and sufficient plasma densities to conduct for times in excess of 1 μs, but displayed poor or non-existent opening, as shown for the top POS in Figure 5-4. In this case opening was not as good as predicted. The reason may be related to switch plasma motion past the end of the POS injection region. A significant time delay was observed between the outer current monitors just downstream of the POS injection region and the inner current monitors located farthest downstream indicating that current continued to be carried by the plasma past the end of the POS injection region. Also, the current monitors farthest downstream did not show current transfer consistent with the calculated POS voltage, which was inductively corrected from E-dot voltage monitors in the oil. The calculated relative inductance downstream of the E-dot monitor as a function of time is overlaid in Figure 5-4. During most of the conduction phase the inductance changes by approximately 6 nH, a value consistent with the POS region vacuum inductance. At the time the outer cavity probes begin to come up, the inductance begins to increase more rapidly, and then plateaus shortly after the farthest downstream current monitor indicates current. The observed 10 nH change corresponds to about 90 percent of the vacuum inductance downstream of the POS. This suggests that some portion of the POS plasma carrying the current across the anode-cathode gap was pushed beyond the end of the physical POS to the short 25 cm downstream. The observed POS voltage can be completely accounted for by plasma motion (IdL/dt) downstream of the physical POS.

LEGEND
- N at T = 1.000E-07
- N at T = 2.500E-07
- N at T = 4.000E-07
- N at T = 5.500E-07
- N at T = 7.000E-07
- N at T = 8.500E-07
- N at T = 1.000E-06
- N at T = 1.150E-06
- N at T = 1.255E-06
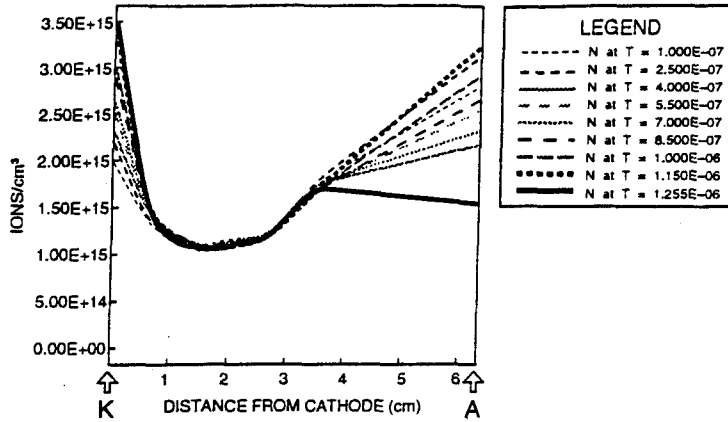
(a) Flashboard density profiles.

LEGEND
- T = 2.500E-07
- T = 4.000E-07
- T = 5.500E-07
- T = 7.000E-07
- T = 8.500E-07
- T = 1.000E-06
- T = 1.150E-06
- T = 1.255E-06

"OPENS" 1.4 cm FROM CATHODE
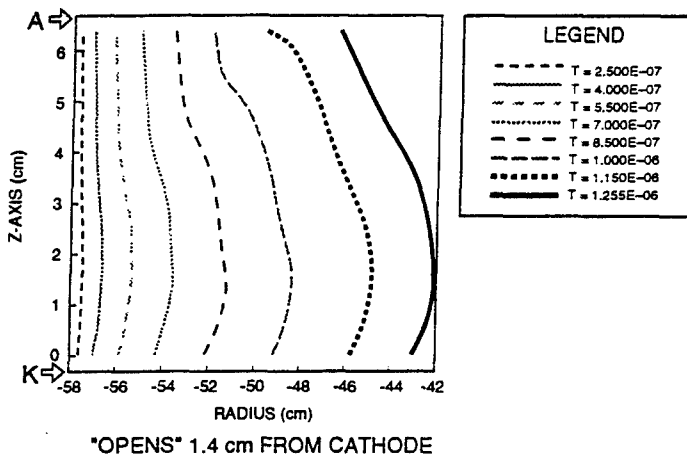
(b) Snowplow fronts. Model indicates maximum thinning 1.4 cm from cathode.

All Computed Line Integrals

- Z = 0.200 cm
- Z = 0.400 cm
- Z = 0.600 cm
- Z = 0.800 cm
- Z = 1.00 cm
- Z = 1.20 cm
- Z = 1.40 cm
- Z = 1.60 cm
- Z = 1.80 cm
- Z = 2.00 cm
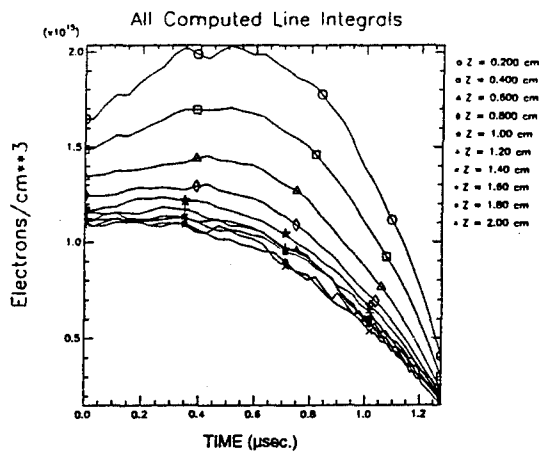
(c). Radial density line integrals. Model indicates a minimum line integral density of $\int n_e dl = 2.5 \times 10^{15} \, cm^{-2}$.

Figure 5-3. Application of snowplow model to ACE-4 Shot 821. In (b) and (c), origin of time corresponds to the instant that current begins to flow in the switch. (a) Shows the variation of plasma density over the conduction time interval in the absence of pulsed power.
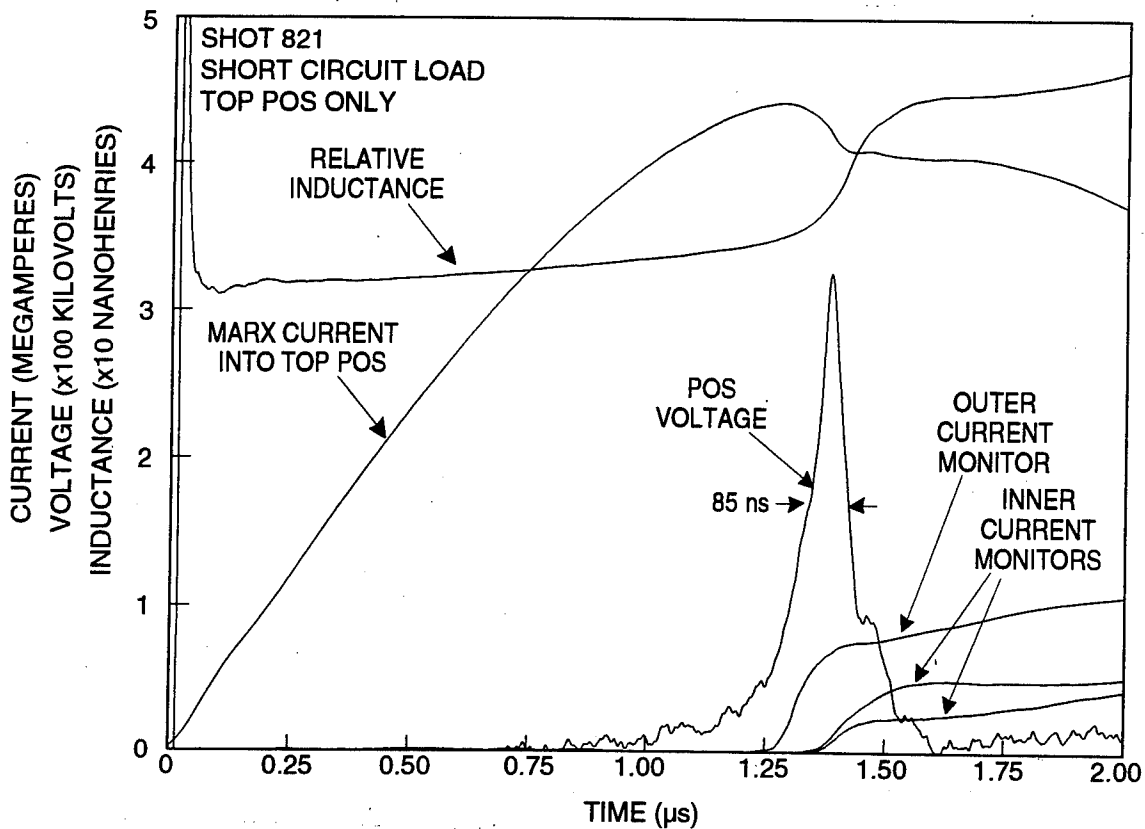
Figure 5-4. ACE-4 POS performance with optimized switch plasma distribution.

Modeling of this shot showed that the integrated electron line density at the time the current channel reached the end of the POS was 1.5×10^{15} electrons/cm^{-2} (Figure 5-5). The predicted rate of thinning at the end of the conduction time in ACE-4 is about an order of magnitude less than seen in HAWK. It should be noted that the modeling of HAWK data, though it qualitatively predicts the observed integrated electron line density during most of the conduction phase, does not agree well with the final observed thinning rate. This may be related to the assumption that HAWK opens at the physical end of the POS, not further downstream where the A-K gap opens up.

During the course of testing, the slow plasma flashboards suffered damage to the exposed inner conductors, which extended across the face of the flashboard. The damage, which occurred only on the cable side facing the POS, appeared as crazing caused by either ultraviolet light or high energy electrons. This observed degradation of the exposed cables demonstrated that the slow flashboard configuration was not practical to maintain, and resulted in the abandonment of the source configuration before density measurements were made in this configuration with pulsed power. This failure occurred late enough in the testing that the results described above were not affected by the rapid failure onset leading to abandonment of the slow plasma flashboard configuration.

5-5
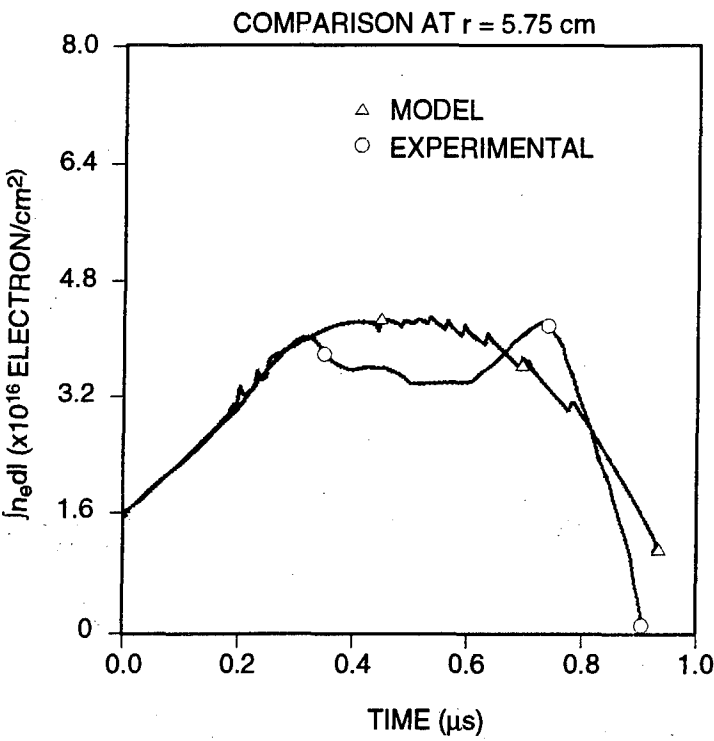
Figure 5-5. Comparison of snowplow predictions and measurements in HAWK of density line-integrals. Observed time to opening is 0.93 µs.

To permit the comparison of POS modeling with experiment in the radial ACE-4 geometry, the flashboards were reconfigured with the current returns (the cable inner conductors) located behind the flashboard. This change effectively converted the slow plasma flashboards, which have a free space $v_{plasma} \sim 5$ cm/µs, to fast plasma flashboards, with $v_{plasma} \sim 15$-20 cm/µs. The resultant POS intergap density profiles with the fast plasma source did not have the well defined intergap density minimum located away from the anode and cathode as required by the above design methodology, but did allow the snowplow model to be benchmarked in the radial geometry.

5.1.2 Experimental Radial Pos Results.

Table 5-1 summaries a series of ACE-4 shots taken in May of 1994. The primary objective of the series was to obtain POS interferometric data with and without pulsed power. Good switch performance was neither expected nor observed.

The data were limited to radial integrated electron line density measurements as shown in Figure 5-6, as time did not allow for chordal measurements. As this was the first series for interferometry with pulsed power on ACE-4, most of the experiment was devoted to making the interferometry diagnostics work. Initial data-taking required breaking vacuum for each shot to replace mirrors and resulted in a shot rate of only one to two shots per day. Improvements utilizing windows and baffles allowed multiple shots to be taken, increasing the shot rate to four per day. The radial geometry POS configuration for this series had a 12 cm injection length with a 5 cm anode - cathode (A-K) gap. A 50 percent transparent screen was

Table 5-1. ACE-4 radial switch interferometric diagnostic shot series.

| Shot Type	Shot Number	Shot Date	Marx Charge (kV)	Flashboard Charge (kV)	Top Flashboard Delay (ms)	Bottom Flashboard Delay (ms)	Comments
Calibration	876	05-17-94	480	30			Current probe timing and calibration checkout
Calibration	877	05-17-94	480	30			Marx prefire
POS	878	05-17-94	480	30	4.0	4.0	
Calibration	879	05-23-94	480	30			Current probe timing and calibration checkout
POS	880	05-24-94	480	30	4.0	4.0	
POS	881	05-24-94	480	30	4.0	4.0	
POS	882	05-24-94	480	30	4.0	4.0	
POS	883	05-25-94	480	30	4.5	4.5	
POS	884	05-25-94	480	30	4.5	4.5	
POS	885	05-25-94	480	30	4.5	4.5	
POS	886	05-26-94	480	30	4.0	4.0	
POS	887	05-26-94	480	30	3.75	3.75	
POS	888	05-27-94	480	30	4.5	4.5	
POS	889	05-27-94	480	30	4.0	4.0	
POS	890	05-27-94	480	30	3.0	3.0	
POS	891	05-27-94	480	30	3.0	3.0	Marx prefire
POS	892	05-31-94	480	30	4.5	4.5	
POS	893	05-31-94	480	30	3.0	3.0	Marx prefire
Calibration	894	05-31-94	480	30			Current probe timing and calibration checkout
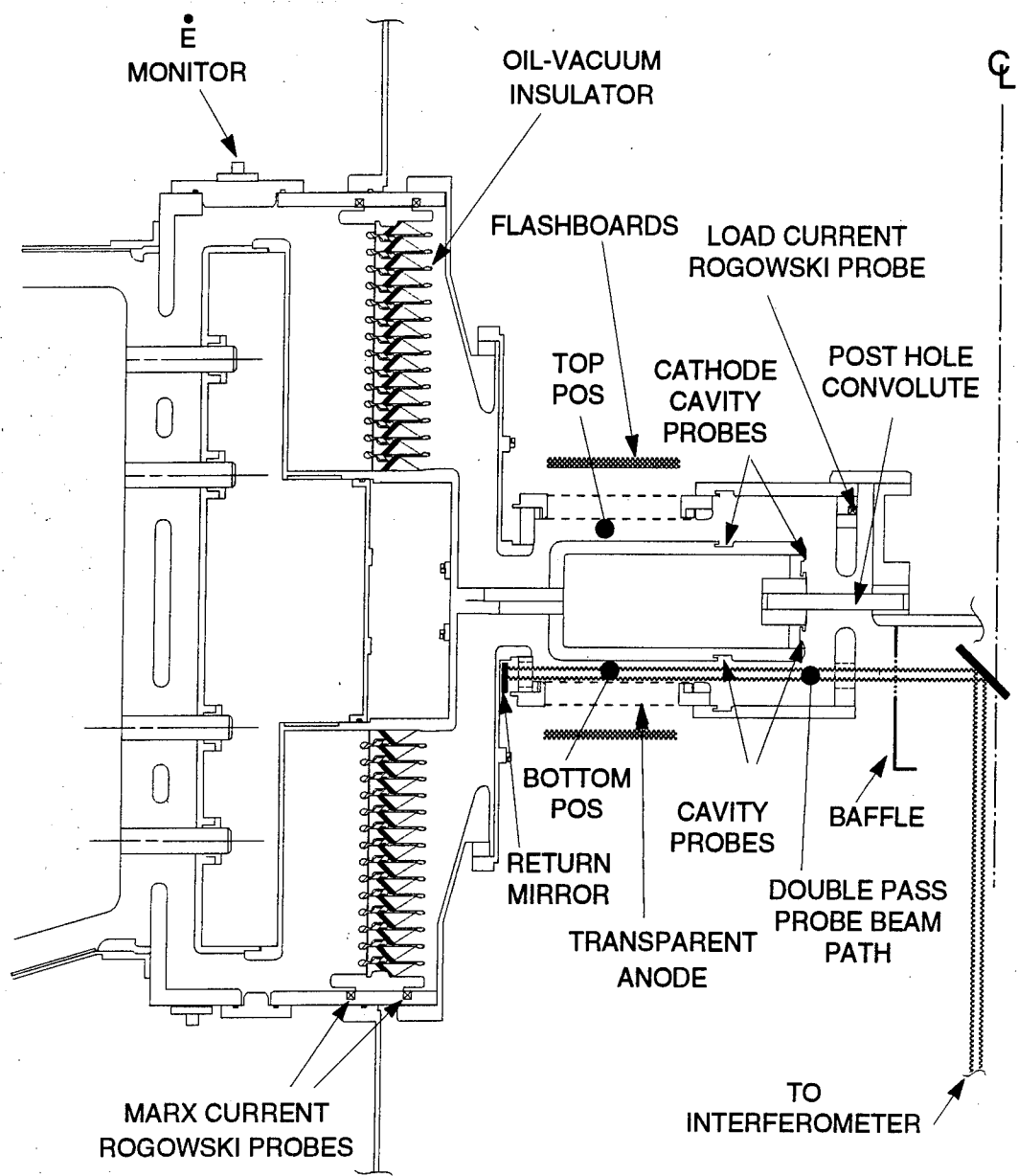
Figure 5-6. ACE-4 convoluted short circuit load configuration with interferometry.

used for the anode structure. Typical Marx operation was at 480 kV with flashboard-to-Marx delay ranging from 3.0 to 4.5 μs for the series. The flashboards were operated at -30 kV in a low current, 8 kA/gap-chain configuration.

Interferometric measurements of electron density were made using a 35 mW HeNe laser in the configuration shown in Figure 5-6. Interferometric measurements were made only of the bottom POS. The HeNe output was split into two beams using an acousto-optic Bragg cell resulting in a 40 MHz shifted reference beam and an unmodulated probe beam. Cylindrical lenses were used to configure both the probe and reference beams as ribbons beams. After passing the probe beam through the POS plasma the reference and probe ribbon beams were recombined and softly focused by another cylindrical lens, on a linear fiber optic array. The individual fibers delivered the light to eight or nine photo-detectors, allowing simultaneous measurements of the line integrated electron density, $\int n_e dl$, evolution at different points across the A-K gap. Here n_e is the electron density, in electrons/cm^3. The photodetector-amplifier output was hardware filtered with both a high and low pass filter and then digitized at a rate of 2 ns/sample. Observed changes in the base 40 MHz beat frequency corresponded to changes in $\int n_e dl$ along the line of sight. Knowing an average ionization state and an effective plasma path length allows the ion density or mass density to be calculated. It should be noted that the hardware filters used introduced a frequency dependent phase change which introduced a systematic error in $\int n_e dl$ when the density was rapidly changing in time. As such it was not a cumulative error, being affected only by frequency dependence, not phase difference of the probe relative to the reference beam. For the data discussed here, this error was relatively small and had little effect on the conclusions drawn. For density thinning rates an order of magnitude larger than observed to date this error could significantly affect the calculated dn_e/dt trajectory, but would not affect the data during periods in which the density is nominally constant, or slowly changing.

Figure 5-7 gives the typical POS intergap density profile for the fast plasma flashboard source. The interferometry channel position relative to the cathode is given in the table in Figure 5-7. The channels show a density increase from the anode towards the cathode, the direction of plasma flow. A feature typically seen but not understood is that the channel nearest the cathode rises significantly later than its neighboring channels. This is associated with how close the probe is to the cathode. Realignment of the interferometry, by moving the inner most channel further away from the cathode, eliminates this signature. This effect may be associated with neutralization of ions rebounding from the cathode and their interaction with the incoming ions, which changes the local average ionization state. Since the phase shift produced by neutrals is opposite to that produced by electrons, the input to the model underestimates the electron densities near the cathode. Note that the design of the slow plasma flashboard source attempted to generate the intergap density minimum away from both the anode and cathode because of concerns with boundary conditions.
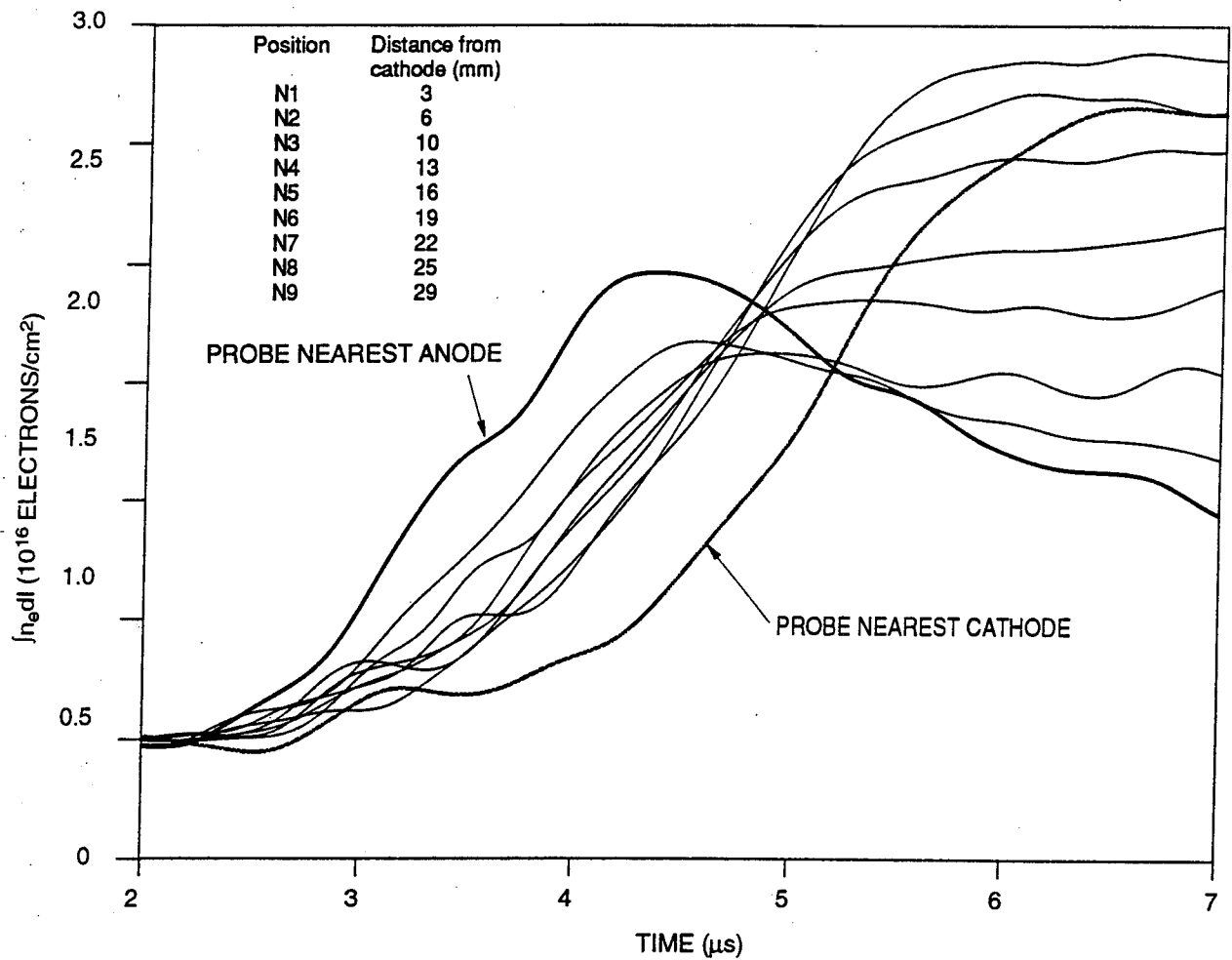
Figure 5-7. Typical POS intergap density profile for fast plasma flashboard source.

Two issues with the interpretation of the interferometry with pulsed power became apparent during the series. It was observed that at the end of the conduction phase the 40 MHz beat signal magnitude varied significantly and was typically lost for extended times. Figure 5-8 shows the beat signal magnitude for two channels on shot 885. The cause of this loss of signal is almost certainly due to additional background light generated by the POS at opening time, which causes saturation of the amplifiers used with the photodetectors. This is discussed further in Section 5-2, Coaxial Geometry Plasma Opening Switch Power Flow Experiments.

The second issue is related to unphysical, negative densities at the time of opening. A similar effect on HAWK was caused by high energy electron bombardment of a downstream window. Their simple solution of placing bending magnets between the POS and the downstream optics, could not be implemented in the compact ACE-4 geometry. This effect means that the magnitudes of the observed densities at the time of opening are not reliable, but that the channel-to-channel relative magnitude relation is likely valid. This is because the downstream mirror distance from the POS was much greater than the interferometry channel separation so
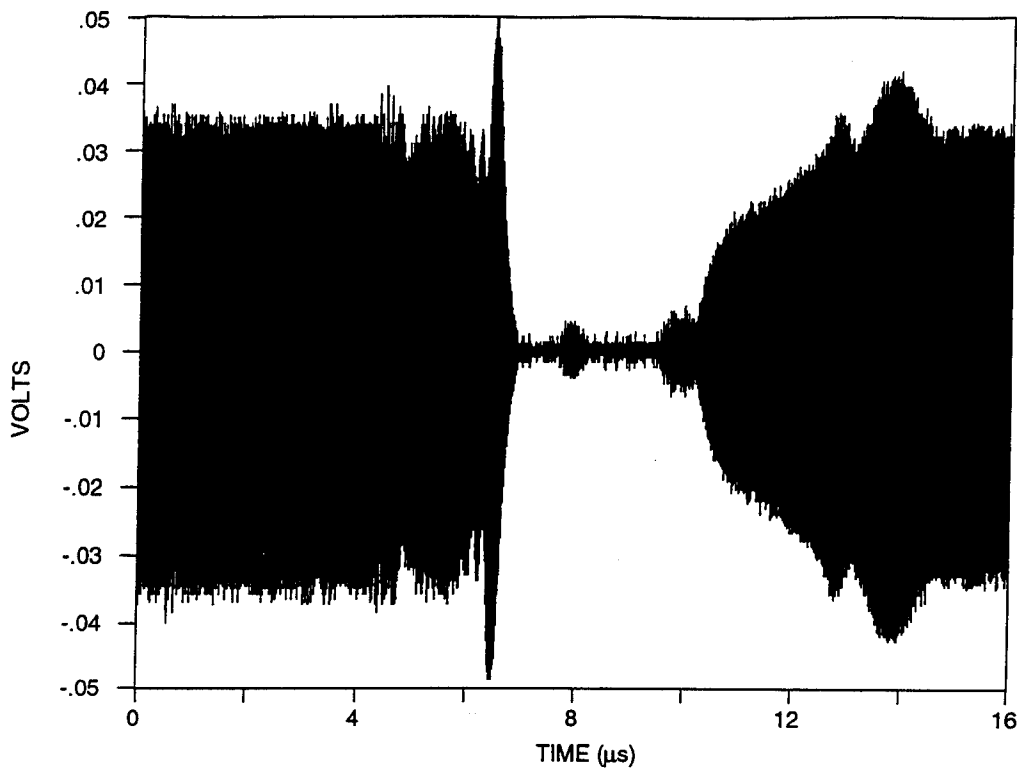
(a) Channel 4, 40 MHz envelope for Shot 885.
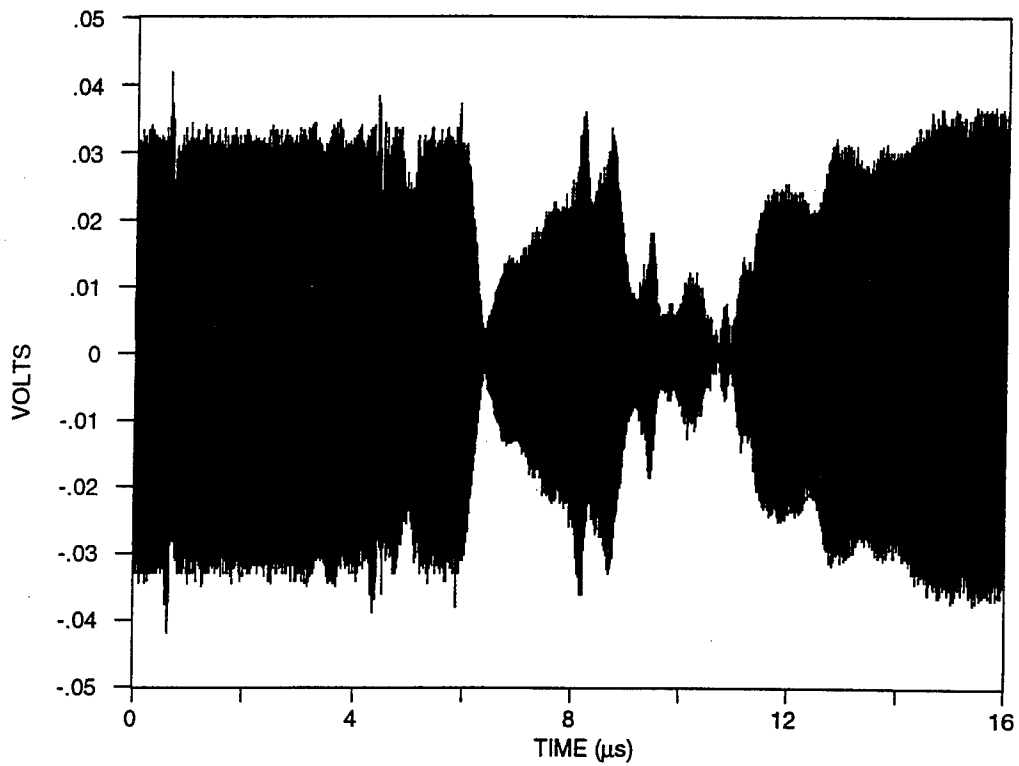
(b) Channel 9, 40 MHz envelope for Shot 885.

Figure 5-8. Examples of amplitude variations of interferometry signals with pulse power. The disappearance of the beat signal close to opening time is caused by additional background light saturating the detectors.

that to first order the mirror should be affected uniformly over the region of the probe beam. In all figures the integrated electron line densities are terminated when the interferometric beat signal becomes small.

Figure 5-9 shows the level of reproducibility for four POS shots with the same initial conditions for two channel positions. Reproducibility at early times is related to the flashboard source reproducibility. A full summary for shot 885 of the raw beat and processed integrated electron line density data for all channels can be found in Appendix B. Figure 5-10 gives the relative timing between the integrated electron line density channels and the electrical waveforms for the bottom POS. The unphysical, negative going densities appear about the time current begins to rise in the downstream current monitors. Figure 5-11(a) shows the observed density time histories for the nine intergap probe positions denoted in the figure. The spatial ordering of the channel magnitudes suggests that opening begins near or inboard of channel three. In the case of channels one and two the beat frequency tracking is too erratic to follow the density up to the time of opening. This could be caused by refraction due to density gradients near the cathode early in the conduction phase.

5.1.3 Model Comparison With Experimental Results In The Radial Configuration.

Figure 5-11(b) gives the calculated time evolution of $\int n_e dl$ with pulsed power using an initial condition density profile taken from a non-pulsed power, flashboards only interferometry shot. As can be seen by comparing Figure 5-11(a) and 5-11(b), the calculated electron line densities are less peaked in time than are the experimentally observed ones. This disagreement is believed to be a result of ionization produced during the power pulse. The ionization process is not taken into account in the present snowplow code, but will be incorporated in the future.
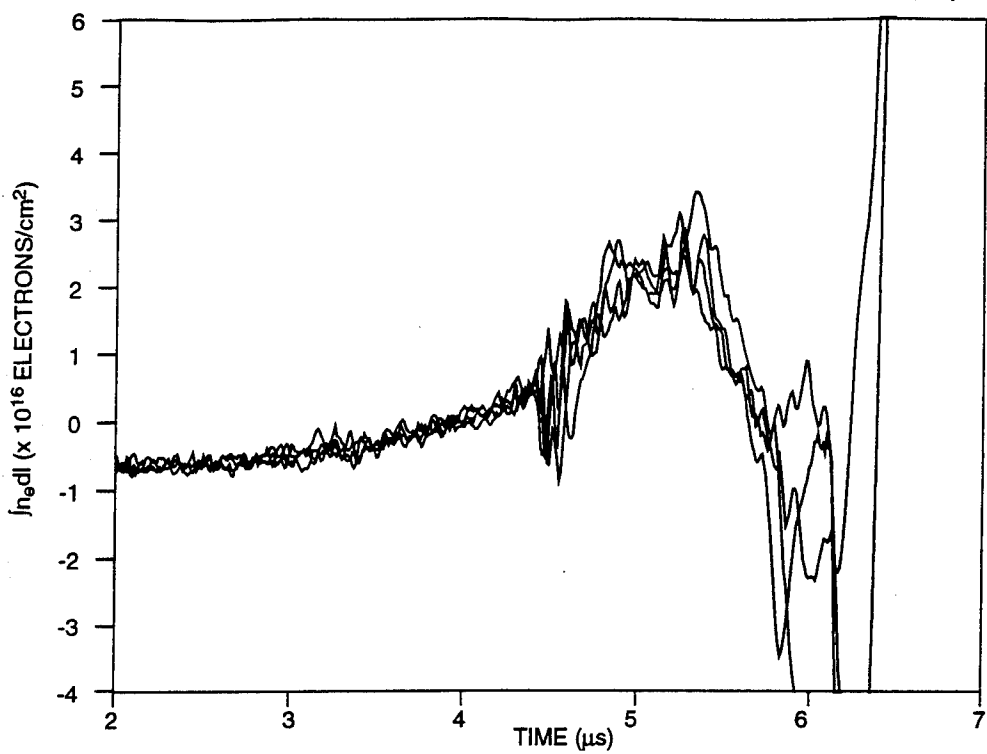
(a) Integrated line densities, 13 mm from cathode.
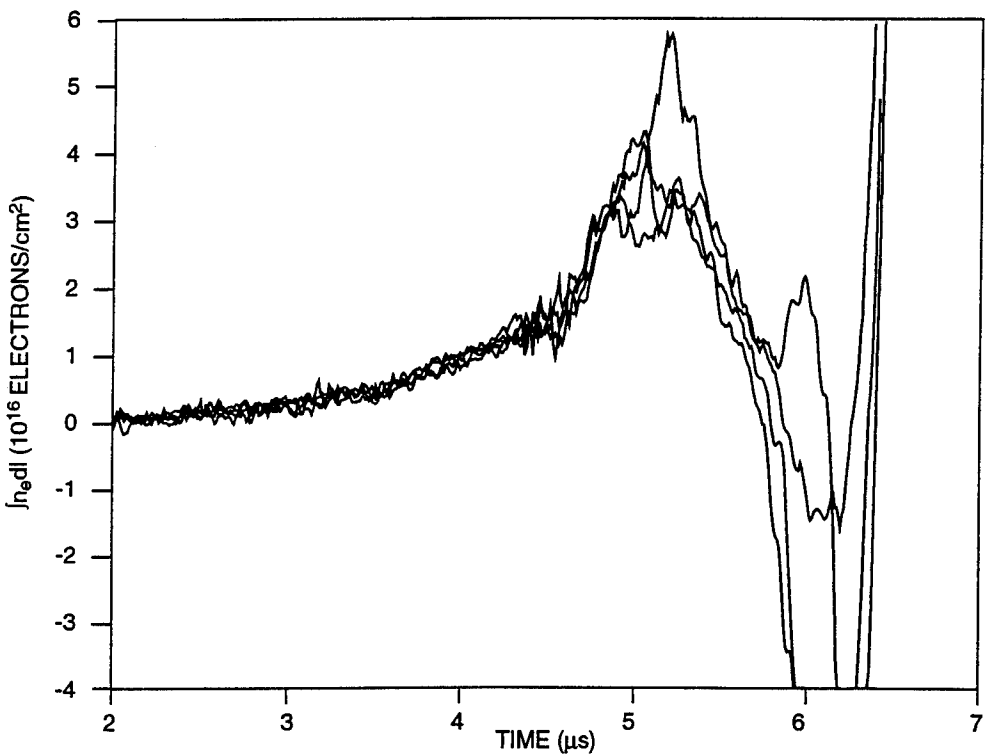
(b) Integrated line densities, 16 mm from cathode.

Figure 5-9. Reproducibility of integrated electron line densities for Shots 883, 884, 885, and 888.
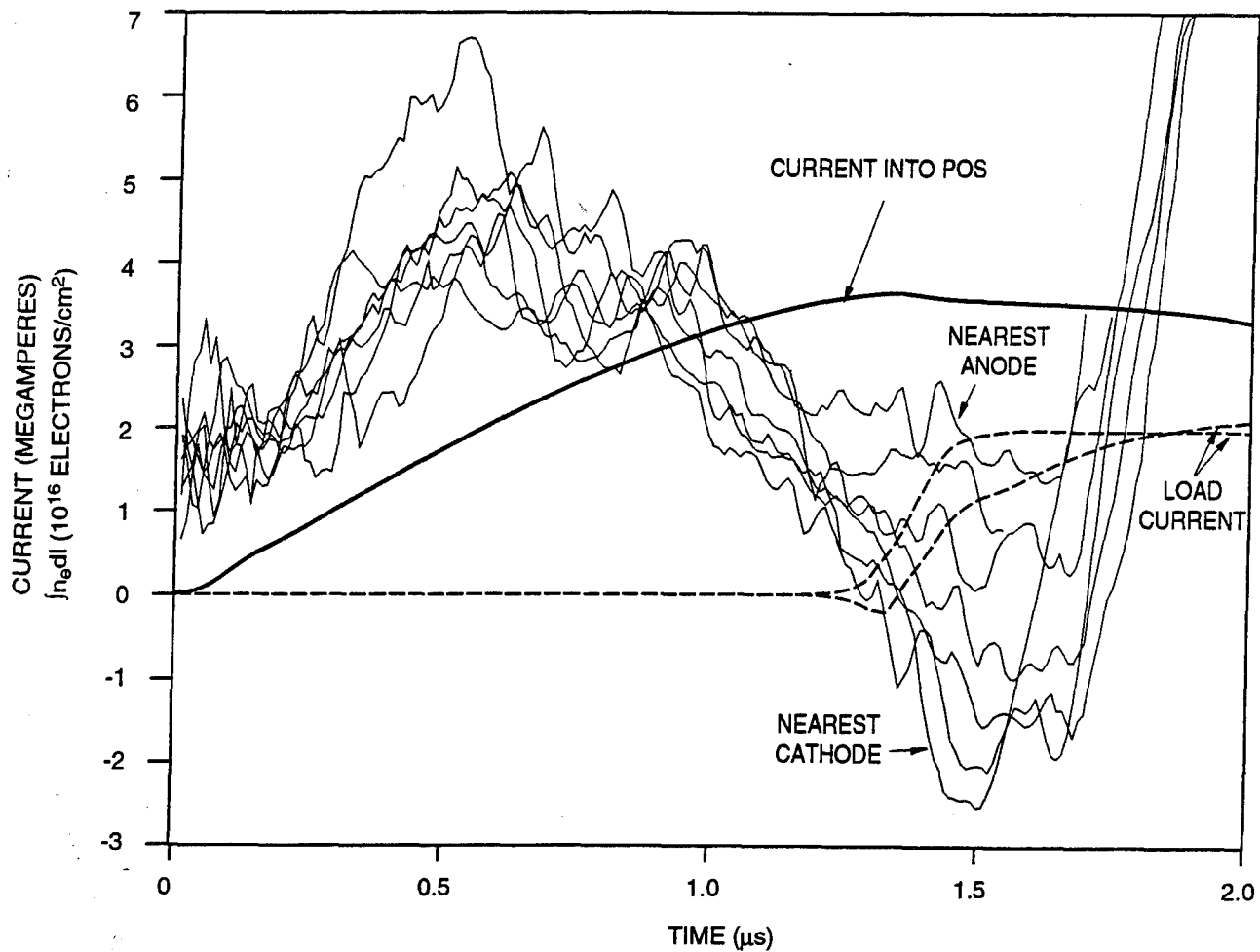
Figure 5-10. Relative timing of line integrated electron densities and current waveforms. Magnitude of dip near 1.56 μs varies systematically from cathode to anode. Unphysical negative densities may be related to neutrals formed by electron bombardment of the on axis turning mirror.

5.1.4 Radial Pos Result Summary.

Interferometry was performed with pulsed power for the first time on the ACE-4. Characterization of the time evolution of the measured integrated electron line densities was made both with and without pulsed power. The measurements were made using a fast plasma flashboard source in the radial POS geometry. Interferometric measurements were made in the radial line of sight, along the direction of power flow. A comparison with predicted snow-plow model time evolution of $\int n_e dl$ showed significant disagreement, even considering the magnitude of uncertainty of the measurement near the time of switch opening. This is not understood at this time but may be related to snowplow model boundary conditions, or temporal or spatial dependence of the average ionization states used to infer the mass distribution from the measured integrated electron line densities.

5-14
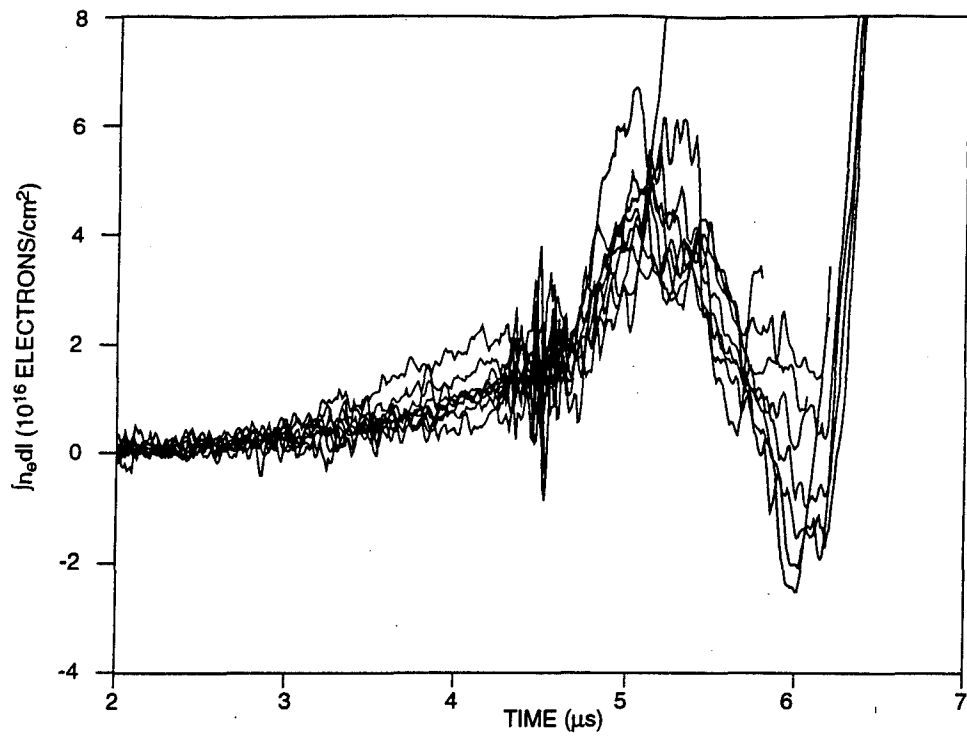
(a) Time evolution of $\int n_e dl$ measured with pulse power (Shot 885).
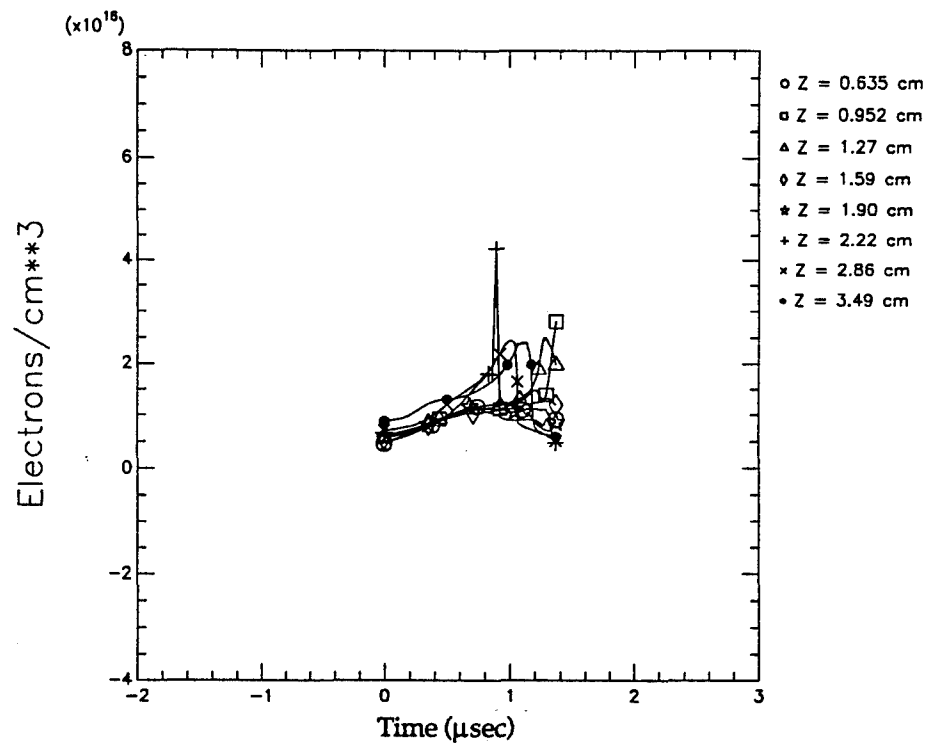
(b) All computed line integrals (Shot 885).

Figure 5-11. A comparison of calculated and measured line integrated electron densities. Agreement is poor.

5.2   COAXIAL GEOMETRY PLASMA OPENING SWITCH POWER FLOW EXPERIMENTS.

5.2.1   Background.

Coaxial geometry based Plasma Opening Switches (POS) were investigated for the first time on ACE-4 this year. The three primary geometry variations of the coaxial POS evaluated were the standard coaxial, plasma anode, and conical geometries. Flashboard or cable gun sources were used to provide the POS plasma, depending on the configuration.

The design of the standard coaxial POS, shown in Figure 5-12, was chosen with the goal of demonstrating a modular, high voltage opening switch in the 1 μs conduction time regime. The primary design criteria for the switch and load geometry were based on two observations from coaxial POS experiments performed on other pulsed power drivers. The first observation, based on the model of magnetic insulation, was that a gap formed in the POS at the time of opening. The maximum effective gap inferred from any previous experiments was three to four millimeters. Taking this maximum effective gap as a design point, the maximum POS opening voltage expected would then only depend on the local magnetic field or current density. The cathode diameter was then selected based on the desired opening switch voltage and the expected switch current at the time of opening. This resulted in the selection of a six cm cathode radius based on a peak switch current of 4 MA and a desired opening voltage of 5 MV. The second observation was that the maximum inferred switch gap observed experimentally was independent of load impedance when the load impedance was greater than the POS impedance (Commisso, *et al.*, 1992). This regime is referred to as "switch limited". To allow a high shot rate and ease of diagnosis an inductive short circuit load was selected. To assure switch limited operation, a 200 nH, large volume, inductive load was located immediately downstream of the POS. The physical length of the POS was set by plasma source requirements based on the hydrodynamic snowplow model of conduction time, and the physical length of the 20 cm flashboard. A two cm POS A-K gap was selected for low inductance and similarity to physical gap dimensions in other POS that have demonstrated the three to four millimeters effective opening gap. Both flashboards and cable gun sources were tested with this configuration. Figure 5-13 shows one of the cable gun source implementations.

The design of a plasma anode POS configuration, shown in Figure 5-14, was based on a variation of the standard coaxial POS as suggested by experiments performed at Physics International (Goyer, 1994). In this configuration the anode structure is mechanically disconnected in the plasma injection region of the POS. Cable guns were used to provide a local plasma injected through the disconnected region, and in this region the plasma anode electrically connects the separated metallic anodes. In experiments at Physics International they found improved switch performance compared to their standard coaxial configuration for conduction times greater than 250-300 ns. For shorter conduction times the performance of the two configurations was similar.
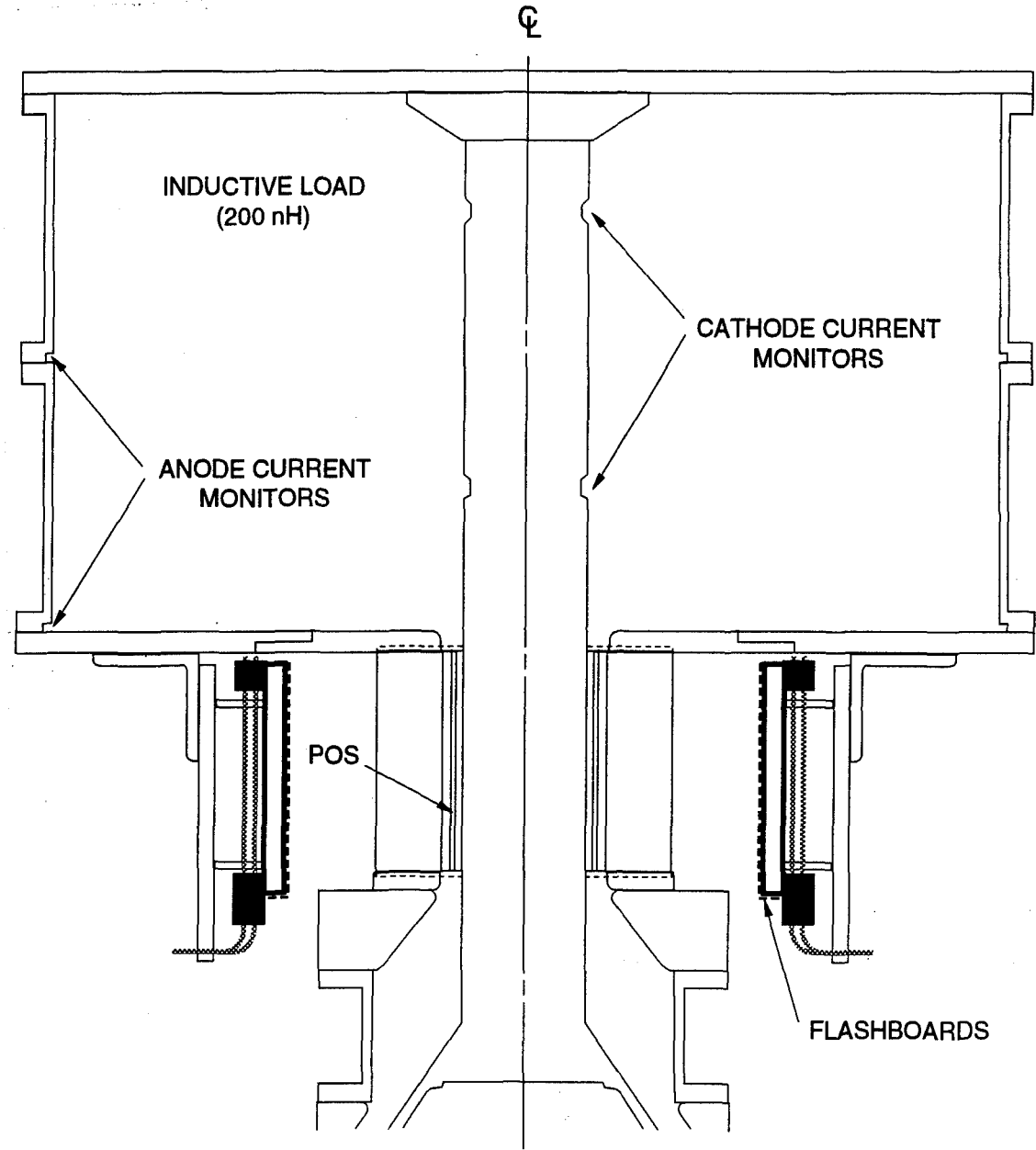
Figure 5-12. ACE-4 standard coaxial POS configuration with high inductance short circuit load.
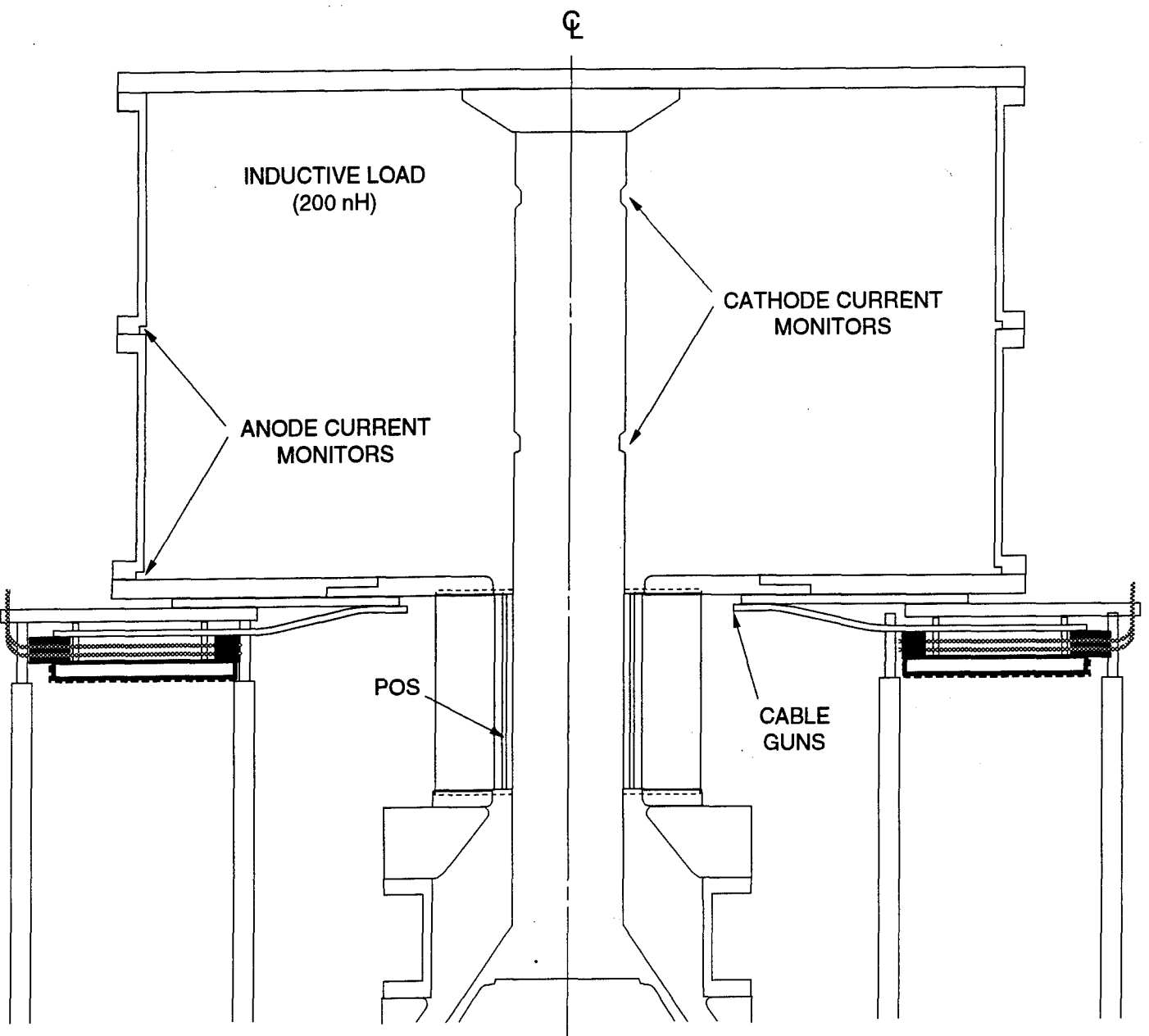
Figure 5-13. Cable gun plasma source used in standard coaxial POS configuration.
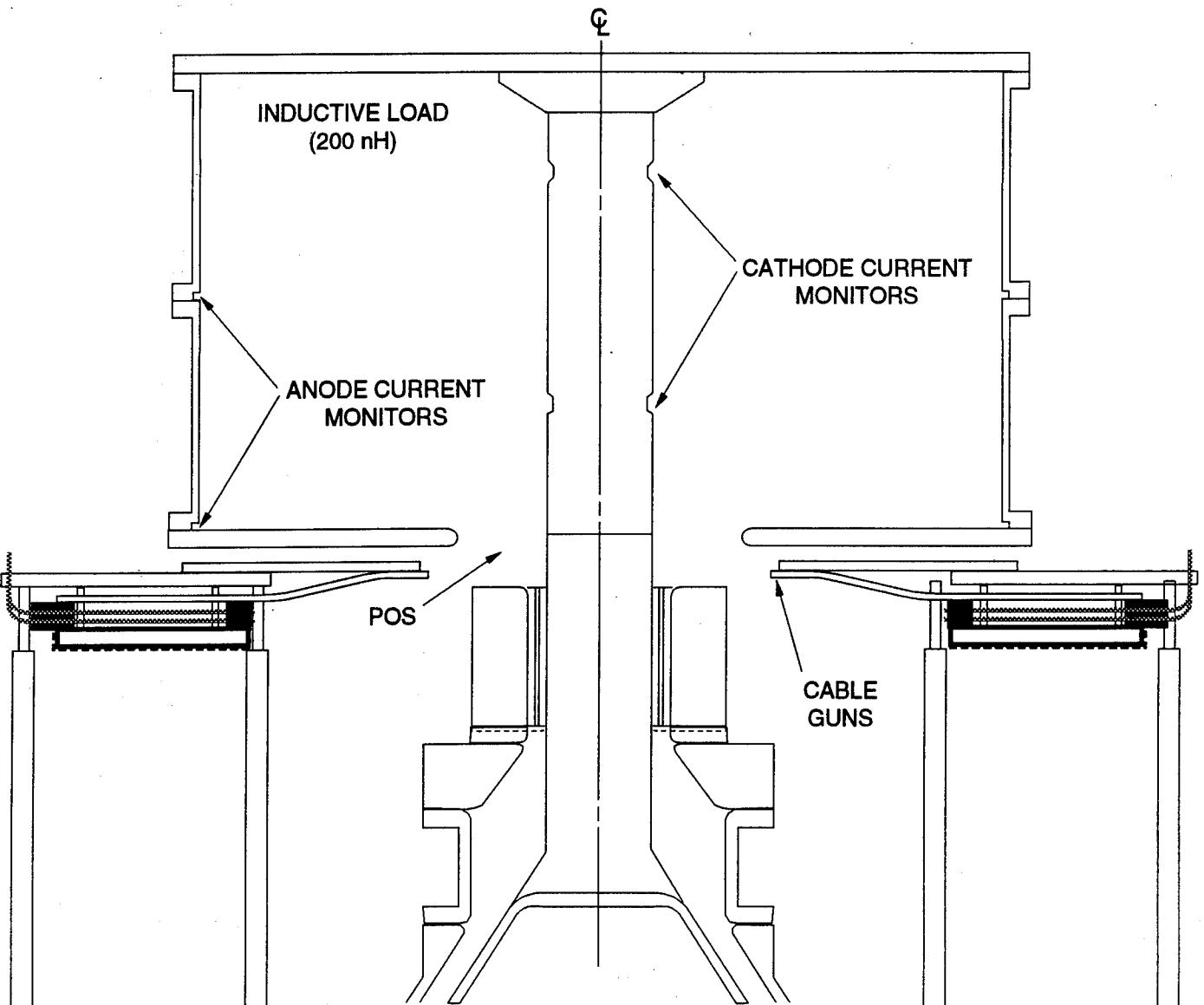
Figure 5-14. Plasma anode POS. Note that the anode has a physical gap at the end of the POS region.

The design of the conical POS configuration, shown in Figure 5-15, was based on a conical POS configuration tested by the Naval Research Laboratory (Goodrich, 1993). This consisted of a converging conical cathode in the region of the POS, and used flashboards as the plasma source in the converging region. In experiments at the Naval Research Laboratory they found they could increase the POS conduction time while maintaining the switch opening performance of a standard coaxial configuration with the same final small cathode diameter.

A comparison between the different coaxial POS configurations tested on ACE-4 showed that the standard coaxial POS geometry using a flashboard plasma source performed best in both conduction time-current product and opening switch voltage. Figure 5-16(a) through Figure 5-16(c) show current and POS voltage waveforms for shots at three different Marx charges.

The observed conduction time-current product scaled in accordance with the simple $T_c I_c \propto \sqrt{n}$ snowplow scaling, where T_c is the conduction time, I_c is the peak conduction current, and n is the electron density. The observed switch voltages were consistent with a fixed POS gap, independent of Marx charge. The calculated effective gap based on magnetic insulation and opening at the cathode resulted in an effective gap of only 1.0-1.5 mm, short of the four millimeters design point. The power flow research for the balance of year was performed using this standard coaxial switch geometry with the flashboard plasma source.

5.3 DOWNSTREAM GEOMETRY EFFECTS ON POS PERFORMANCE.

An experiment was designed to study load coupling issues downstream of the POS. With the intent of coupling the POS to a PRS load, the primary issues were minimization of the inductance coupling the switch to the load, keeping switch plasma out of the load, and maintaining the original opening switch performance. The opening switch configuration chosen for this set of experiments was the standard coaxial POS described above. Figure 5-17(a) is a photograph looking down at the inside of the 200 nH inductor with its end plate removed. Figure 5-17(b) is a photograph of the transparent anode in the POS region with the bottom of the 200 nH inductive load located at the top of the picture. The cathode stalk had been removed in the photograph as were the 15 flashboards normally arrayed about the anode.

While operating with the standard coaxial configuration we observed that the anode and cathode surfaces were ablated not only in the POS region, but also for some distance downstream of the POS. We interpret this ablation as showing where the current attached to the electrodes up to the time of switch opening. This interpretation implies that the current channel propagated some distance beyond the physical POS injection region before opening. Figures 5-18(a) and 5-18(b) show the ablation pattern on the anode and cathode stalk. The ruler marks are in inches. The ablation pattern on the anode extends about four to five cm radially beyond the A-K gap. The ablation pattern on the cathode extended seven to eight cm beyond the end of the POS anode structure. The location of the suggested current channel at the time of switch opening is shown in Figure 5-19. Gap formation was assumed to occur near the cathode.
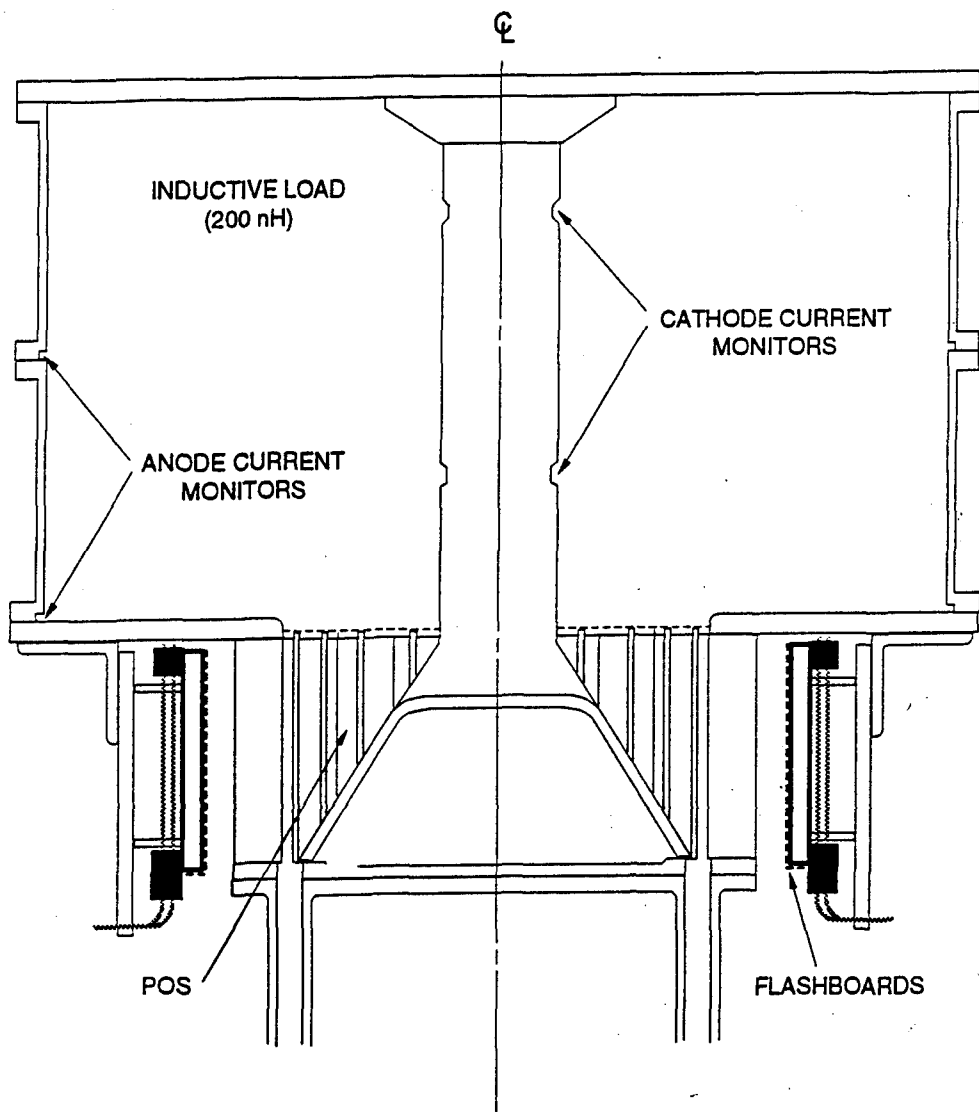
Figure 5-15. Conical POS configuration.
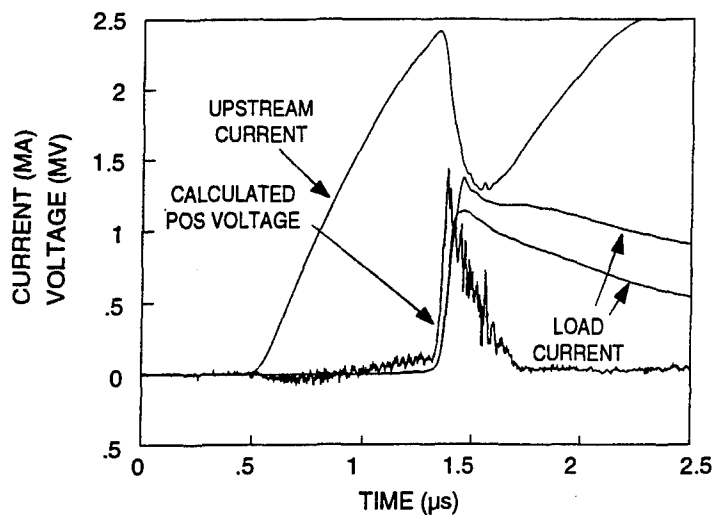
(a) Current and voltage waveforms at 480 kV Marx charge. (Shot 925)
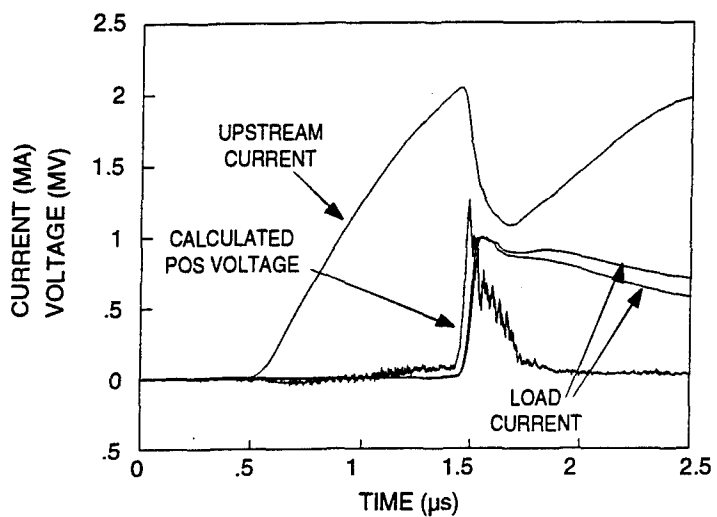
(b) Current and voltage waveforms at 360 kV Marx charge. (Shot 924)
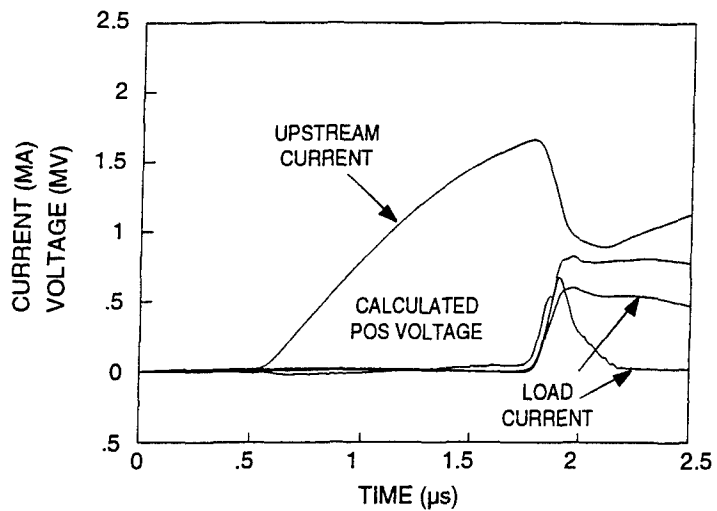
(c) Current and voltage waveforms at 240 kV Marx charge. (Shot 919)

Figure 5-16.   Current and voltage waveforms at various Marx charge voltages.

(5a) The interior of the 200 nH inductive load
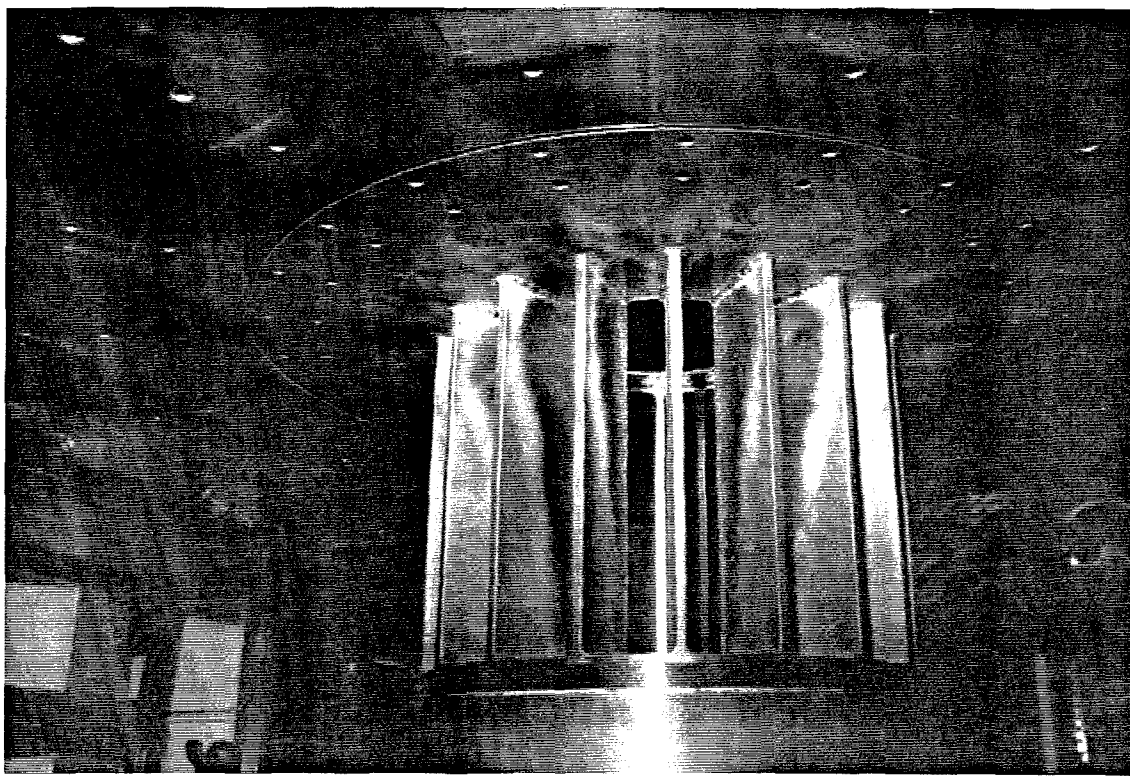
(5b) The rib sturcture of the transparent anode.

Figure 5-17. Photographs of the inductive load and the transparent anode structure used in coaxial POS experiments.
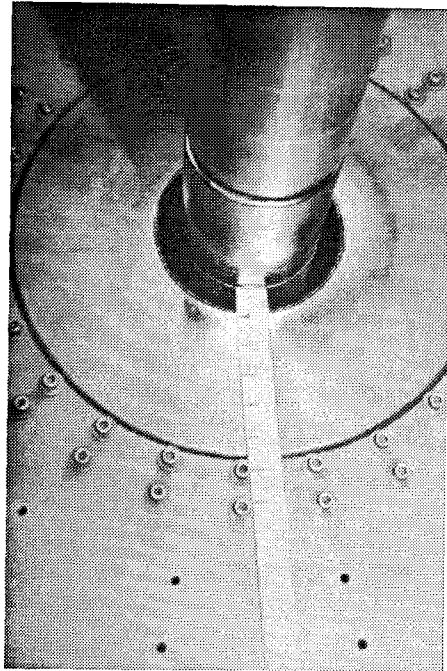
(6a) Ablation pattern on anode. Marks are inches.
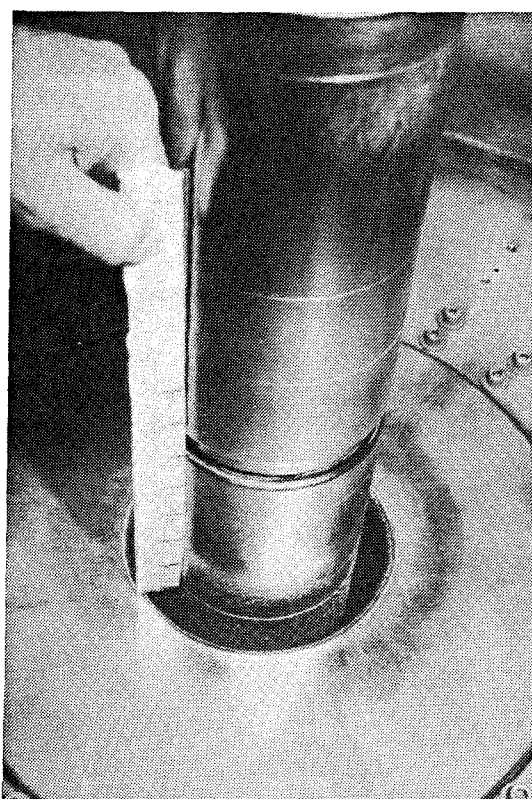
(6b) Ablation pattern on cathode stalk. Marks are inches.

Figure 5-18. Anode and cathode surfaces show ablation downstream of the POS, suggesting that opening occurs well beyond the end of the POS injection region.

30 cm DIA.
25 cm DIA.
20 cm DIA.

PRESUMED
CURRENT CHANNEL AT
TIME OF OPENING

ABLATION

POS

FLASHBOARDS
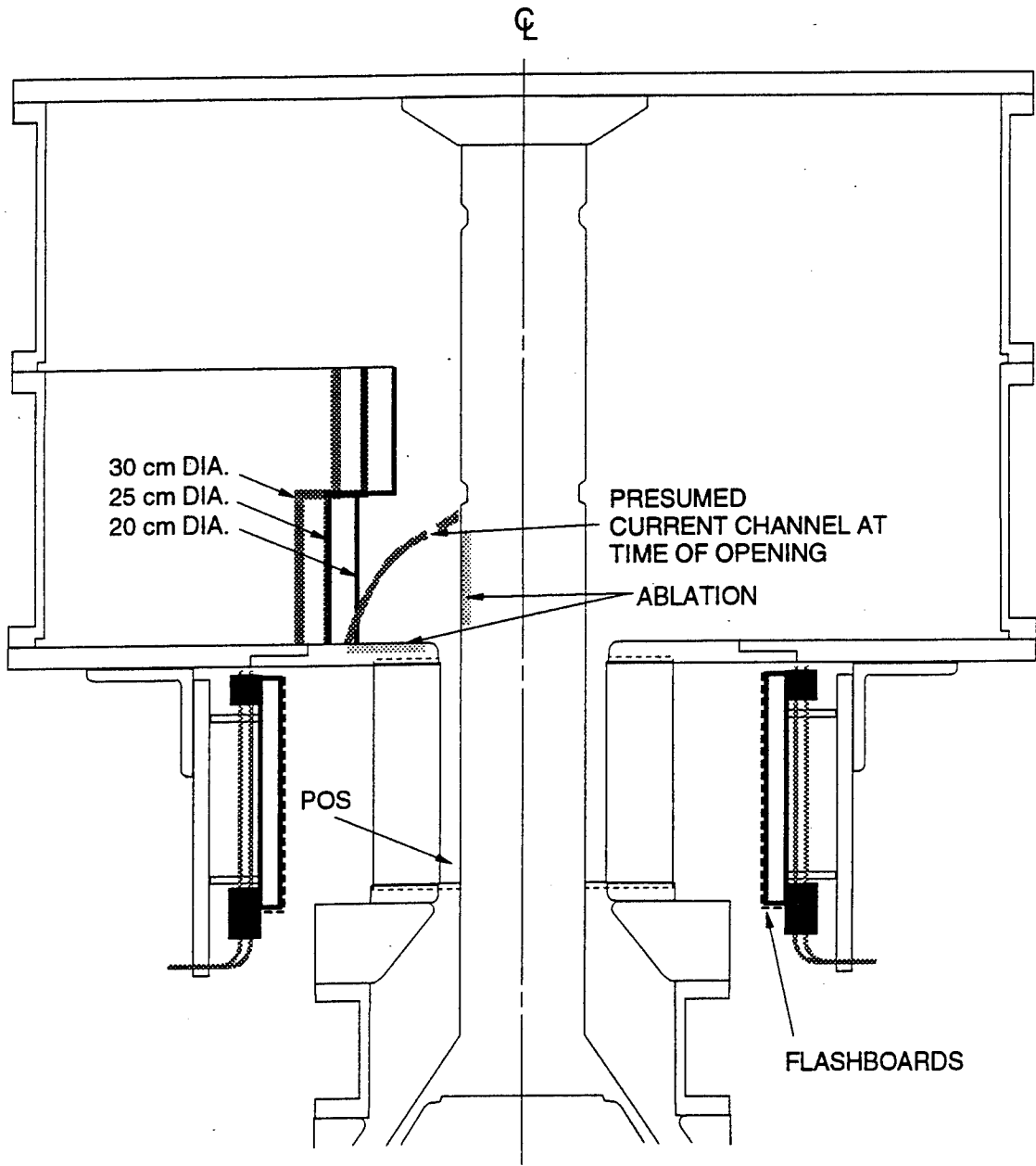
Figure 5-19. Three downstream geometry configurations. The extent of anode and cathode ablation in the downstream region is shown. The gap formed at the time of opening was thought to be near the cathode.

Based on this picture of opening the downstream geometry was modified allowing the options indicated by the cross hatched lines in Figure 5-19. Downstream of the POS an initial expansion region is followed by a reduced inductance coaxial section. To determine the effect of the downstream geometry change on the POS performance in terms of voltage, or equivalently gap formation, the load was once again a large inductor, putting the experiment in the switch limited regime. Three sets of hardware changing the initial radial expansion volume were constructed with diameters of 20, 25, and 30 cm. The largest placed the anode wall just outside of the anode ablation pattern. The two smaller were in the region of ablation, but were expected not to interfere with opening if the actual gap formation was near the cathode. Figure 5-20 shows the intermediate, 25 cm diameter, radial expansion hardware and the location of six Rogowski current monitors distributed along the length of the transition region between the POS and the 100 nH inductive load. The inductance of the transition region is 40 nH.

Table 5-2 gives a summary of the shots taken in the experimental series. Only the 25 cm and 30 cm diameter expansion configurations were tested; the variables for each configuration were the Marx charge and the flashboard-to-Marx delay. The typical flashboard density distribution in the POS injection region is shown in Figure 5-21, the signals rising sequentially as the interferometer positions move from near the cathode (N1) toward the anode. The intergap plasma density is a few times $10^{15}/cm^3$ mid-gap and relatively flat over four to eight μs. The relative flatness in time of the density distribution across most of the A-K gap accounts for the relatively small variations in conduction time over the large range of the flashboard-to-Marx delay times. The results for both expansion diameters tested indicate that the POS opening performance was significantly reduced. An extension of the model of plasma motion to downstream of the POS explains the observed data, and will be developed as the data is discussed.

5.3.1   Electrical Diagnostics And Interpretation.

Results with the intermediate, 25 cm expansion configuration pictured in Figure 5-20 are typified by shot 991. Operating parameters for this shot were a Marx charge of 360 kV and a flashboard-to-Marx delay of 5 μs. Figure 5-22 shows the upstream and downstream current waveforms, the voltage at the end of the POS plasma injection region, and the calculated inductance downstream of the voltage monitors located near the oil-vacuum interface. The voltage is inductively corrected from the upstream voltage monitors using a simple $L\frac{dI}{dt}$ term where L is the inductance to the end of the POS injection region. The time of POS opening is taken to be when the near simultaneous rise of current occurs in the physically separated anode and cathode current monitors in the 100 nH load region. The sequential appearance of current at the anode monitors in the transition region, beginning about 100 ns prior to seeing load current, suggests that plasma motion carries the current channel through the entire transition region. Ablation, suggesting current connection through a plasma channel, was also observed throughout the transition region, though it extended only about one to two cm into the 100 nH inductive load region. Generally, current probes in a plasma serve as an upper limit to the time of current appearance at the probe location; the observed current magnitude is typically reduced because of shorting of the probes by the plasma. In this case, as higher currents appeared downstream of the transition region, it is clear that the probes were shorted.
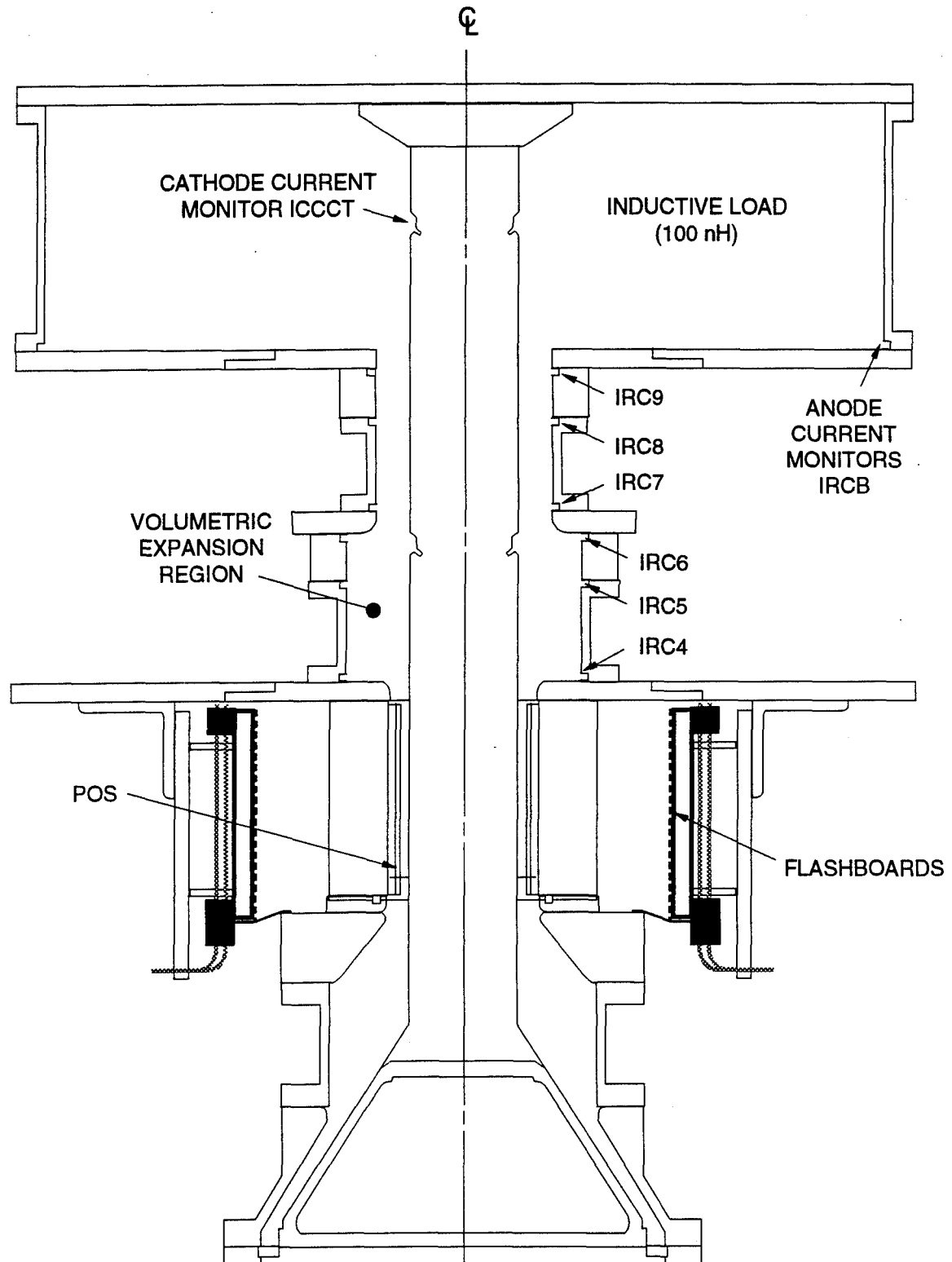
Figure 5-20. Intermediate, 25 cm diameter expansion volume configuration. Note anode probe locations along downstream transition region.

Table 5-2a. ACE 4 coaxial switch downstream power flow diagnostic shot series, 25 cm diameter configuration.

Shot Type	Shot Number	Shot Date	Marx Charge (kV)	Flashboard Charge (kV)	Coaxial Flashboard Delay (ms)	Comments
Calibration	983	08-02-94	240	30		Current probe timing and calibration checkout
Calibration	984	08-02-94	240	30		Current probe timing and calibration checkout
Calibration	985	08-02-94	240	30		Current probe timing and calibration checkout
POS	986	08-03-94	240	30	6.0	
POS	987	08-03-94	240	30	6.0	
POS	988	08-03-94	360	30	6.0	
POS	989	08-03-94	360	30	6.0	
POS	990	08-03-94	360	30	6.0	
POS	991	08-03-94	360	30	5.0	
POS	992	08-04-94	360	30	4.0	
POS	993	08-04-94	360	30	7.0	
POS	994	08-04-94	360	30	5.0	Marx prefire
POS	995	08-04-94	360	30	5.0	
POS	996	08-04-94	360	30	5.0	
POS	997	08-04-94	360	30	6.0	
POS	998	08-04-94	360	30	6.0	
POS	999	08-04-94	360	30	7.0	
POS	1000	08-04-94	360	30	3.5	
Calibration	1001	08-04-94	240	30		Current probe timing and calibration checkout
Calibration	1002	08-04-94	240	30		Current probe timing and calibration checkout

Table 5-2b.   ACE 4 coaxial switch downstream power flow diagnostic shot series, 30 cm diameter configuration.

| Shot Type	Shot Number	Shot Date	Marx Charge (kV)	Flashboard Charge (kV)	Coaxial Flashboard Delay (ms)	Comments
Calibra-tion	1003	08-08-94	240	30		Current probe timing and calibration checkout
Calibra-tion	1004	08-08-94	240	30		Current probe timing and calibration checkout
Calibra-tion	1005	08-08-94	240	30		Current probe timing and calibration checkout
POS	1006	08-08-94	360	30	7.0	
POS	1007	08-08-94	360	30	7.0	
POS	1008	08-09-94	360	30	6.0	Marx prefire
POS	1009	08-09-94	360	30	6.0	
POS	1010	08-09-94	360	30	6.0	
POS	1011	08-09-94	360	30	5.0	
POS	1012	08-09-94	360	30	5.0	
POS	1013	08-09-94	360	30	8.0	
POS	1014	08-10-94	360	30	4.0	
POS	1015	08-10-94	360	30	3.0	
POS	1016	08-10-94	360	30	10.0	
POS	1017	08-10-94	360	30	12.0	
POS	1018	08-10-94	360	20	6.0	
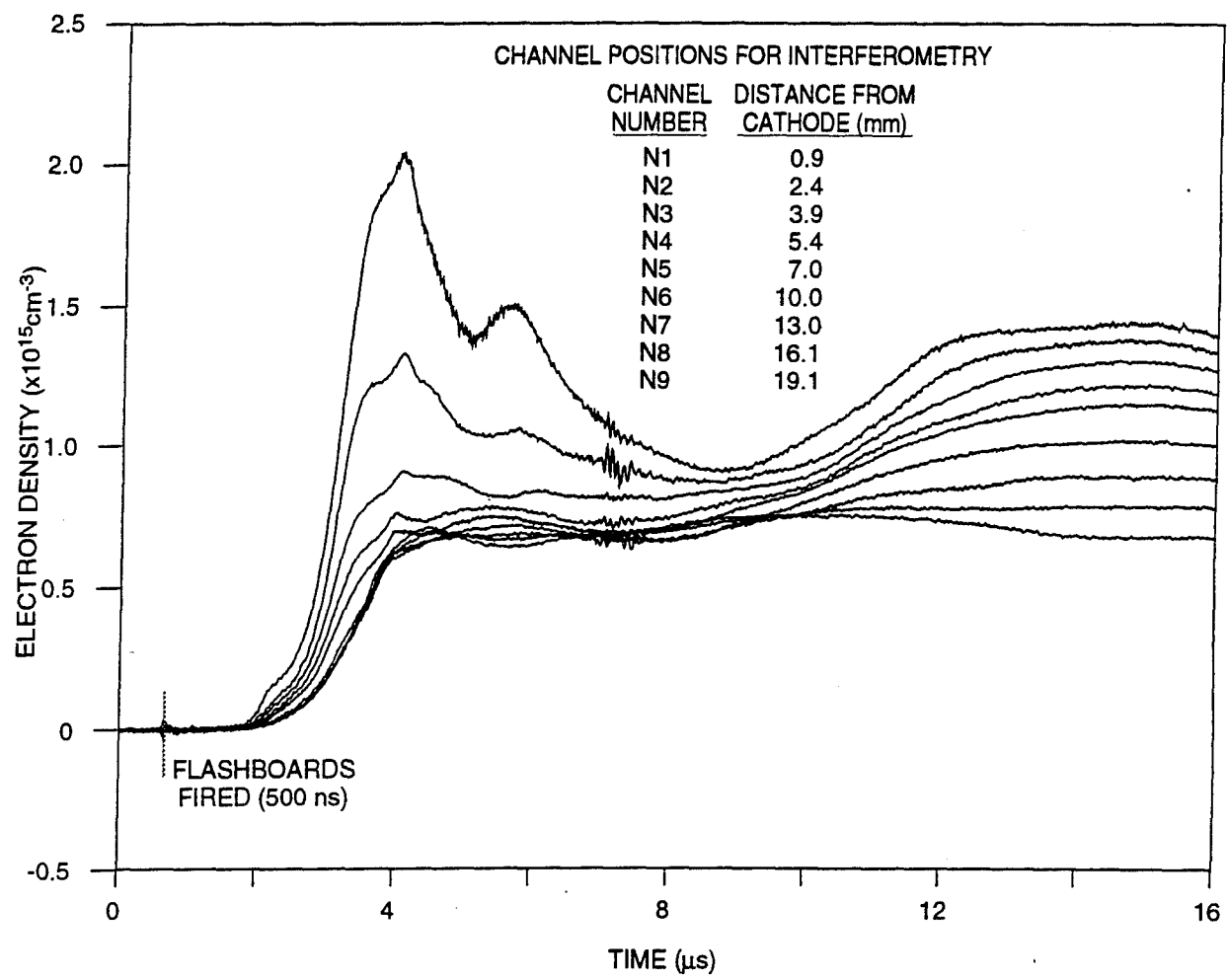
Figure 5-21. Typical density distribution in the POS. The signals come up sequentially as the interferometer positions move from near the cathode toward the anode.

The picture of the current channel being carried by plasma from the end of the POS to the load inductor is also supported by the observed change in inductance. During the time prior to the first anode probe registering current in the transition region, the inductance change is consistent with the nominal vacuum inductance of the POS. During the time between this first appearance of current downstream of the POS and the appearance of current in the load the observed change in inductance is about 85 percent of the vacuum inductance of the transition region. The observed voltage prior to the appearance of load current is then consistent with a changing inductance due to plasma motion, and the actual POS opening voltage is the lower voltage seen during the time of load current rise. Figure 5-23 compares the inductively corrected upstream voltage using the inductance to the end of transition region and the voltages calculated from $L\dfrac{dI}{dt}$ using the two downstream probes, assuming the full 100 nH load inductance. The match between upstream and downstream estimates of the voltage at the end of the transition region supports our interpretation of a current channel moving through the transition region between the POS injection region and the 100 nH inductor. Opening occurs near the transition into the 100 nH inductor.

The time between when the current reached the end of the POS injection region, and when the switch opened ranged from 100 to 125 ns, with no clear dependence on the plasma injection time. This was true over a range of delays corresponding to application of pulsed power from 1.5 to 5.0 µs after plasma reached the POS cathode. This suggested that the current channel motion downstream of the physical POS is not dominated by plasma leakage from the POS prior to application of pulsed power.

Results with the large, 30 cm diameter expansion configuration were typified by shot 1014. Operating parameters for this shot were a Marx charge of 360 kV and a flashboard-to-Marx delay of four µs. Figure 5-24(a) shows the upstream and downstream current waveforms. The time of POS opening is identified with the near simultaneous rise of current at the physically separated anode and cathode current monitors in the load region. The appearance of current at the anode monitors in the transition region is again somewhat sequential. There is, however, a significant difference in the initial time history for the anode probes in the transition region. As shown in Figure 5-24(b) all the anode probes begin to come up at nearly the same time, but current increase hesitates in the three current monitors furthest downstream , then display a sequentially delayed current increase. The relative timing of the final increase of the furthest downstream transition region monitor and the load currents with respect to the first anode monitor downstream of the POS are the same as seen in the medium, 25 cm expansion configuration.
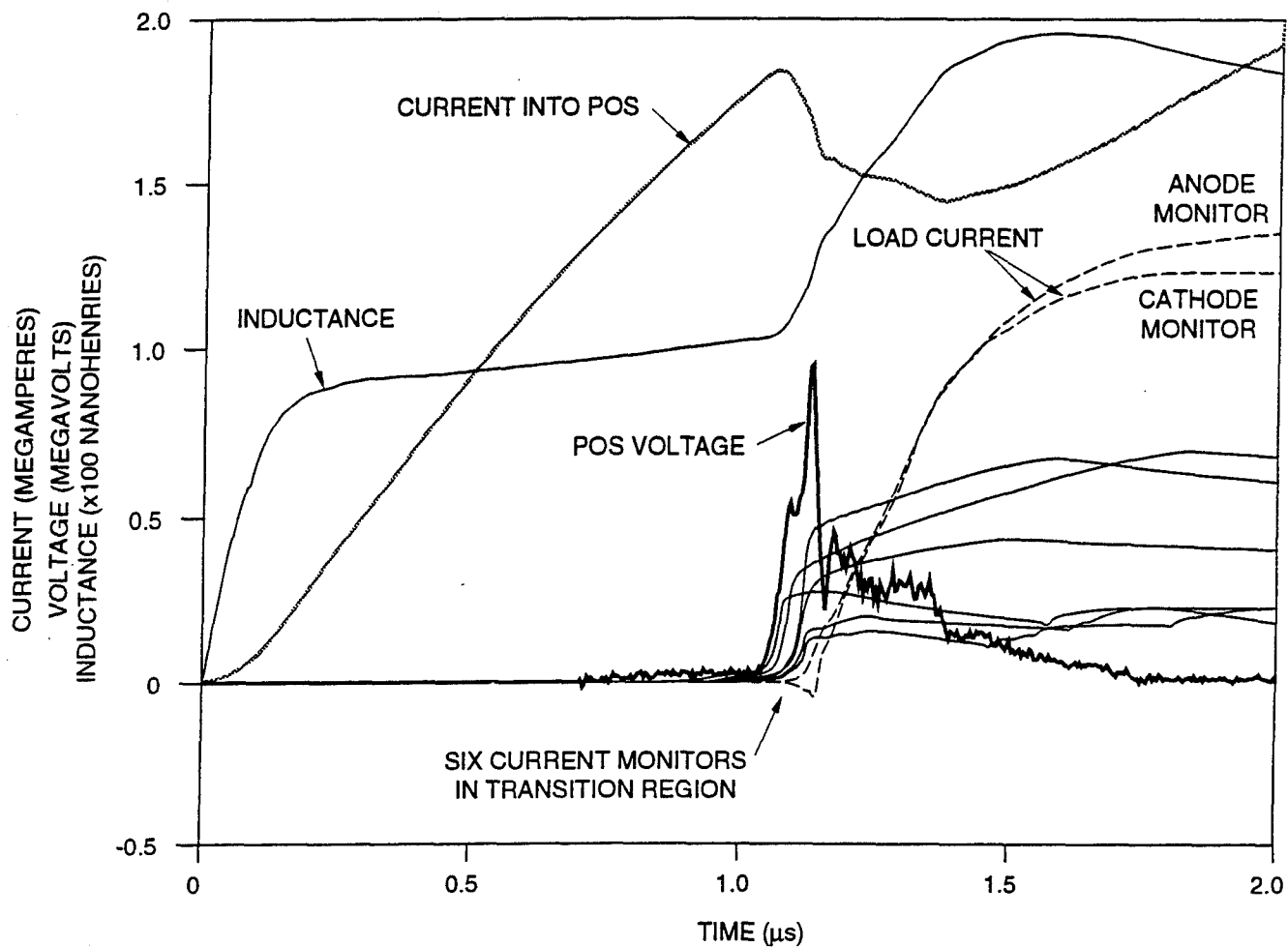
Figure 5-22. Current, voltage and inductance waveforms from the intermediate, 25 cm expansion configuration (Shot 991). The inductance is calculated as [∫Vdt]/I, where V is the voltage measured near the oil-vacuum interface, and I is the current into the POS. The sequential appearance of current at the six anode monitors suggests that plasma motion carries the current channel through the entire transition region.
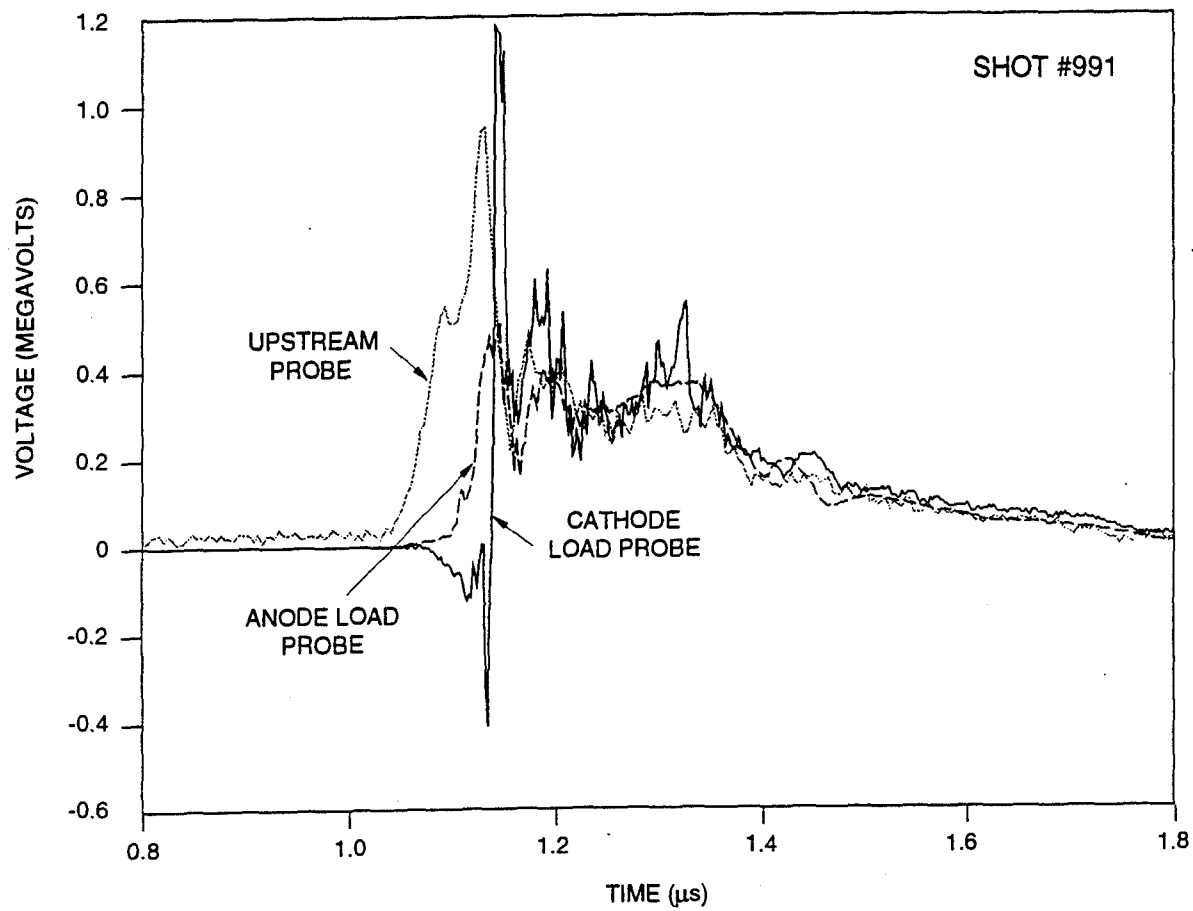
Figure 5-23. Comparison of inductively corrected voltages using upstream and downstream current probes. The voltage calculated using the upstream probe uses the geometrical inductance up to the end of the transition region. The voltages calculated using the downstream load probes use the full 100 nH inductance.

5.3.2 Revised Picture Of The Ace-4 Standard Coaxial Pos Opening.

Two questions arise. Why does the downstream transition region affect opening, and why do the current histories for the two different diameter downstream expansion transition regions differ significantly? A relatively simple explanation consistent with the data follows. The concept shown in Figure 5-19 showing the location of plasma channel carrying the current when its switch opening begins is nominally correct, but the opening is located near the anode, as shown in Figure 5-25, not near the cathode. Under this interpretation the switch would not open near the POS injection region in the 25 cm diameter transition case, but could begin to open there in the 30 cm case. The reclosure of the POS could be caused by the motion of the plasma channel into the anode structure, possibly as pictured in Figure 5-25. The plasma motion near the cathode would be little affected by the change in the outer diameters, resulting in similar transit times for the overall current from the physical POS to the end of the transition region as seen in the experiments for both diameters tested.

This interpretation of the location of the POS gap increases the previous estimate of the effective gap produced in the case of the 200 nH experiment by about two because of the lower magnetic field at the larger radius. This interpretation also suggests that thinning due to expansion, and inertial effects that limit the amount of plasma that can go around a corner can dominate opening behavior over snowplow thinning, where front curvature due to B^2/n variation along the front dominates. Here B and n are the local magnetic field and density in the plasma channel front.

5.4 INTERFEROMETRIC DIAGNOSTIC INTERPRETATION.

Interferometric measurements of electron density were made using a 35 mW HeNe laser in the configuration shown in Figure 5-26. The HeNe output was split into two beams using a acousto-optic Bragg cell resulting in a 40 MHz shifted reference beam and a probe beam. Using a combination of cylindrical lenses both the reference and probe beams were configured out as one-dimensional ribbon beams. After passing the probe beam through the plasma the reference and probe ribbon beams were recombined and softly focused, using another cylindrical lens on a linear fiber optic array. The individual fibers delivered the light to eight or nine photodetectors, allowing simultaneous measurements of the line integrated electron density time evolution at different points across the A-K gap. The photodetector-amplifier output was hardware filtered with both a high and low pass filter and then digitized at a rate of two ns per sample. Observed changes in the base 40 MHz frequency then corresponded to changes in $\int n_e dl$ of the plasma. If we know the average ionization state and an effective plasma path length, the ion density or mass density can be calculated.
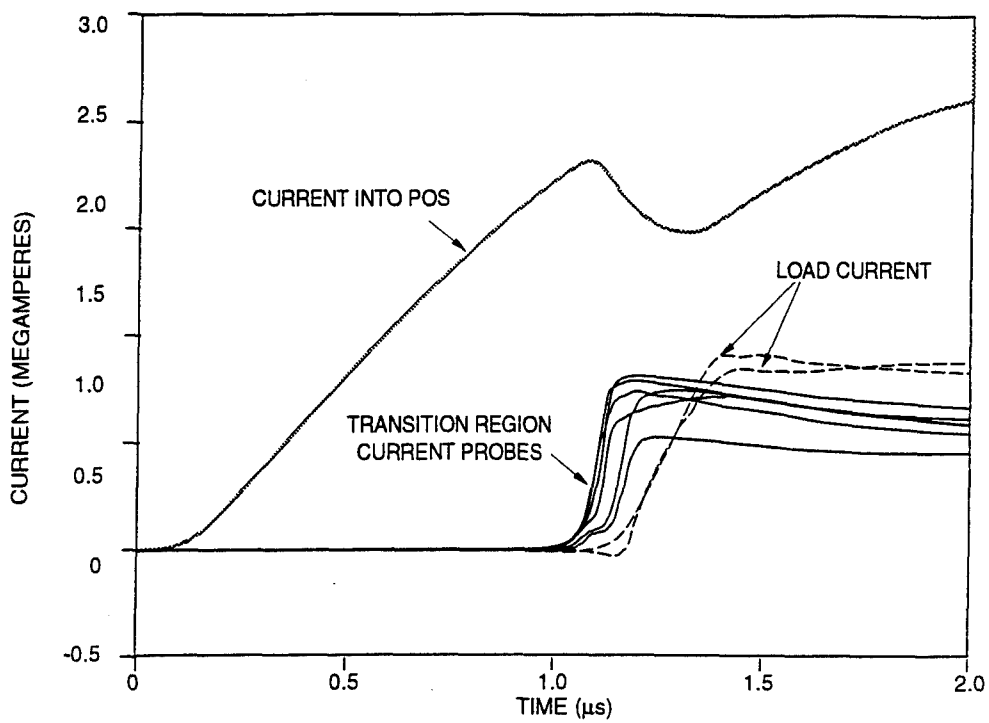
(a) Current waveforms from a typical shot in the 30 cm diameter expansion configuration (Shot 1014).
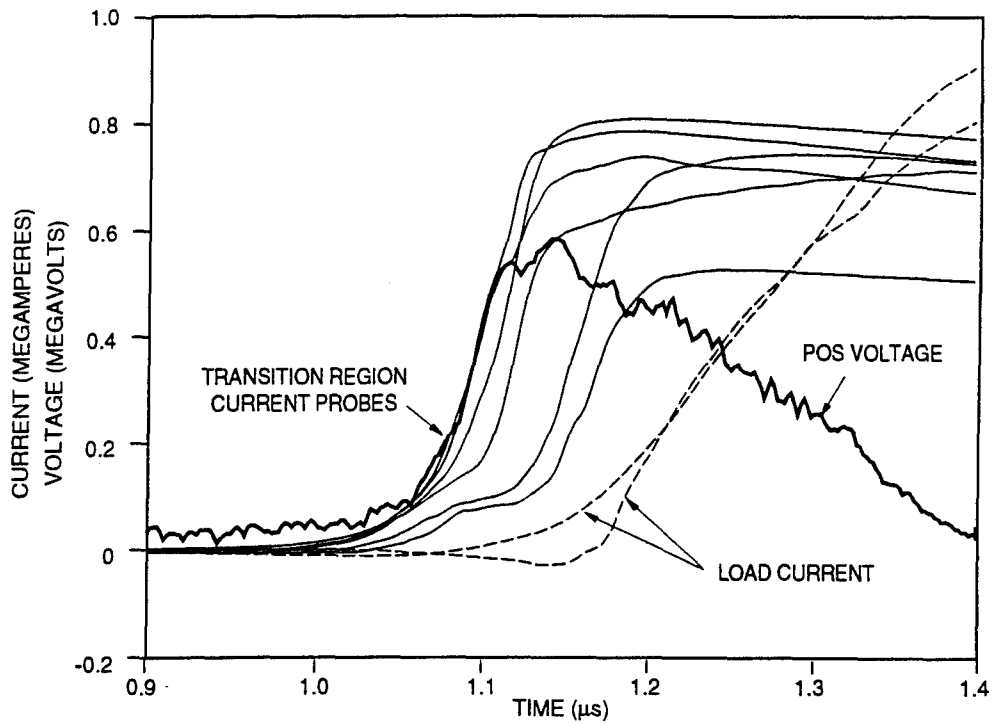
(b) Expanded view of transition region probes and the POS voltage for Shot 1014.

Figure 5-24. Electrical waveforms of the large, 30 cm diameter expansion configuration.
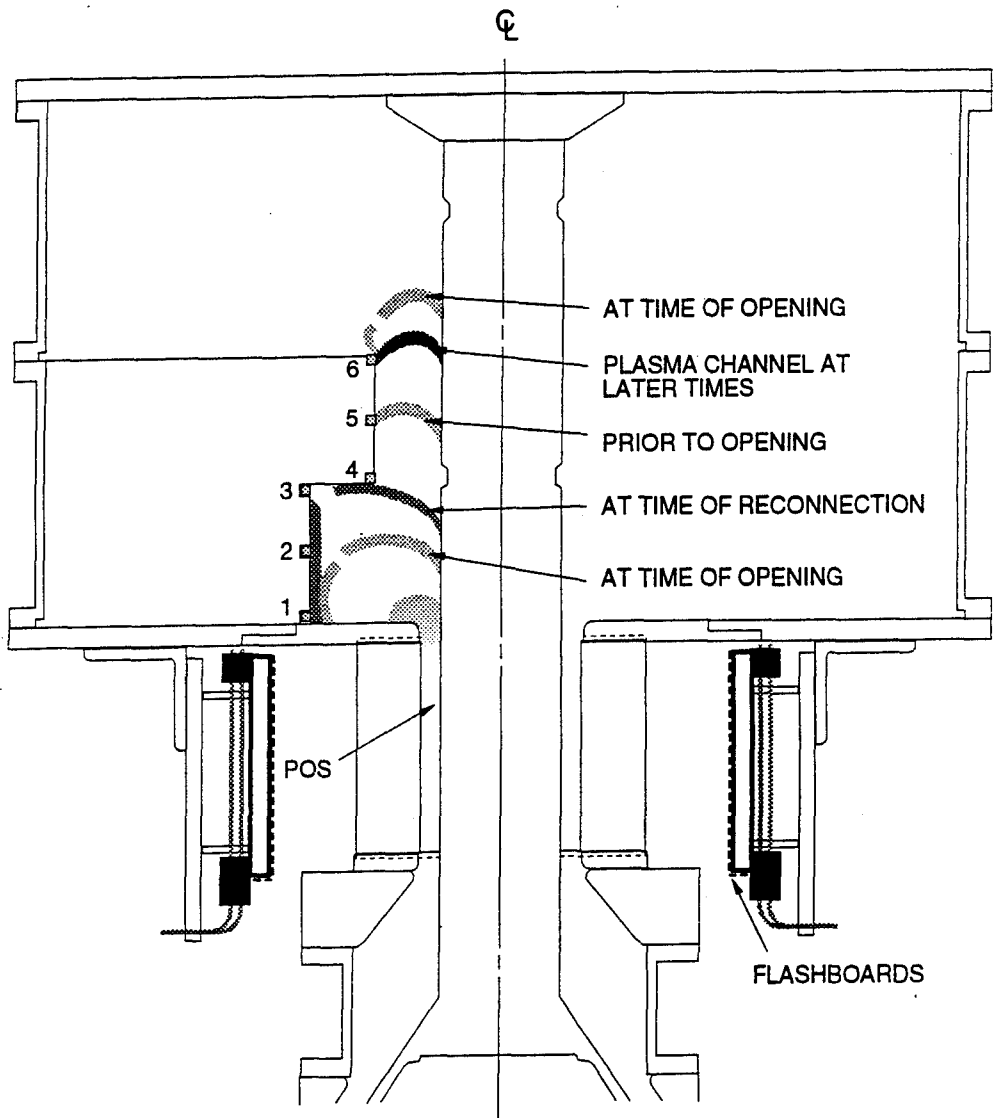
Figure 5-25. Interpretation of opening behavior for the 30 cm diameter expansion configuration. Note that the experiment indicates that the gap at opening occurs near the anode, not near the cathode.
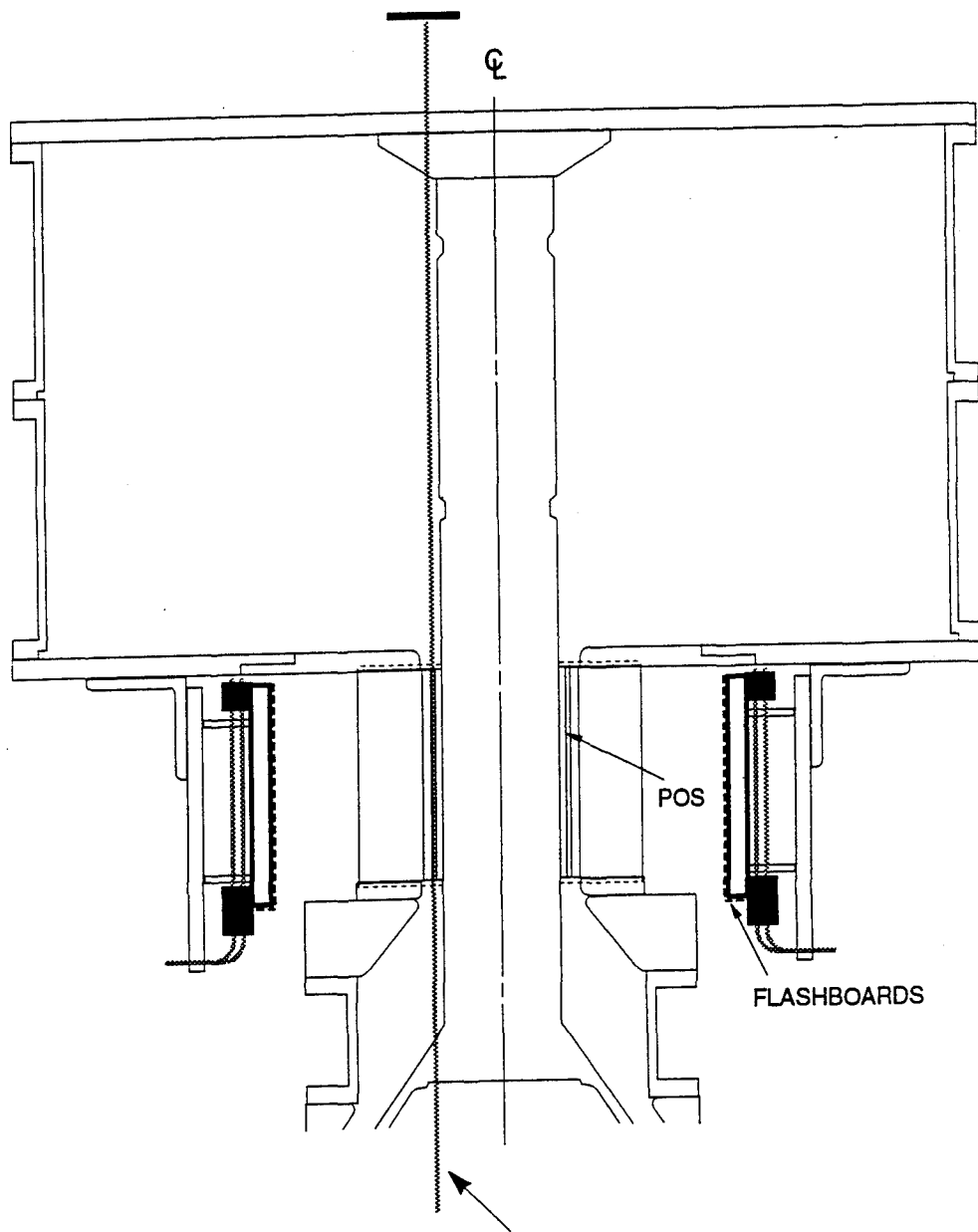
Figure 5-26. The arrow indicates the probe path through the plasma opening switch.

Figures 5-27(a) and 5-27(b) give an example of a typical measurement along one axial line through the POS region near the cathode with pulsed power. The actual conversion of the nominally 40 MHz beat data to line integrated electron density involves comparing the observed zero crossing times relative to what is expected for a pure 40 MHz beat frequency. The deviation between zero crossings times correspond to a change in the $\int n_e dl$ along the probe path. This example shows a number of issues involved in the interpretation of the calculated line integrated electron density.

The hardware filters used introduced a frequency dependent phase change, which introduced a systematic error in $\int n_e dl$ while the density was changing. As such it is not a cumulative error, being affected only by frequency dependence, not phase difference of the probe relative to the reference beam. For the data to be discussed this error was relatively small and had little affect on the conclusions drawn. For large density thinning rates this could affect the calculated dn/dt trajectory, but would have no affect during the periods in which the density is changing slowly.

Electrical noise pick up can reduce the measurement resolution during the time of the noise, but unless the noise is large enough to cause a zero crossing to be missed or added, it does not affect later time $\int n_e dl$ measurements. In this example the noise pickup at the time the Marx is fired only affects the measurements during the noise interval, as no zero crossings are added or missed.

Refraction of the probe beam caused by density gradients perpendicular to the line of sight can cause systematic errors in the effective path length. These show up generally as changes in the beat magnitude during the conduction phase as shown in Figure 5-27. Depending on the initial colinearity of the probe and the reference beam, the beat signal, may get larger or smaller because of this effect. Again, if zero-crossings are not missed the effect on the measurement is only local in time to the occurrence of the gradient.

An optical background can cause saturation of the photodetectors. A large, broadband background light emission has been seen associated with switch opening in time resolved photomultiplier spectroscopic measurements looking between spectral lines. In the Tandem Puff radiation source configuration amplifier saturation and loss of the 40 MHz beat has been also been explicitly observed. Saturation of the detectors due to a broadband background light emission from the plasma is consistent with the observed disappearance of the beat signal for microseconds near the time of switch opening. Extending the interferometry measurement through the time of switch opening is a diagnostic issue that will need to be further addressed.
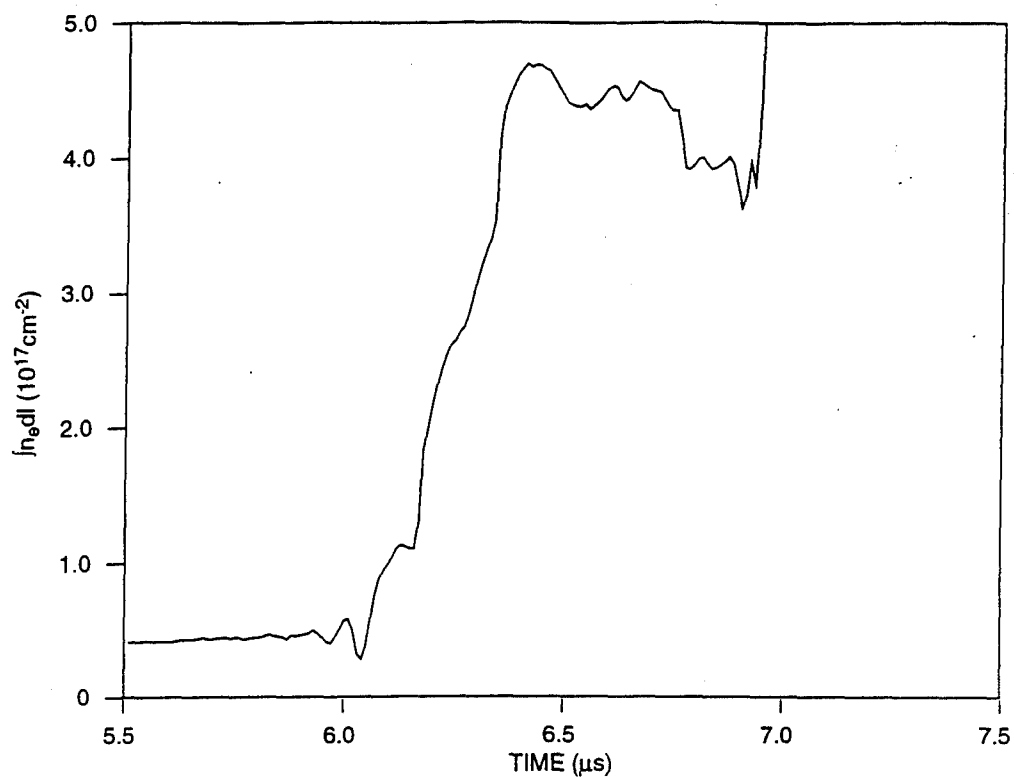
(a) Line integrated electron density near cathode with pulsed power (Shot 925, Channel 1)
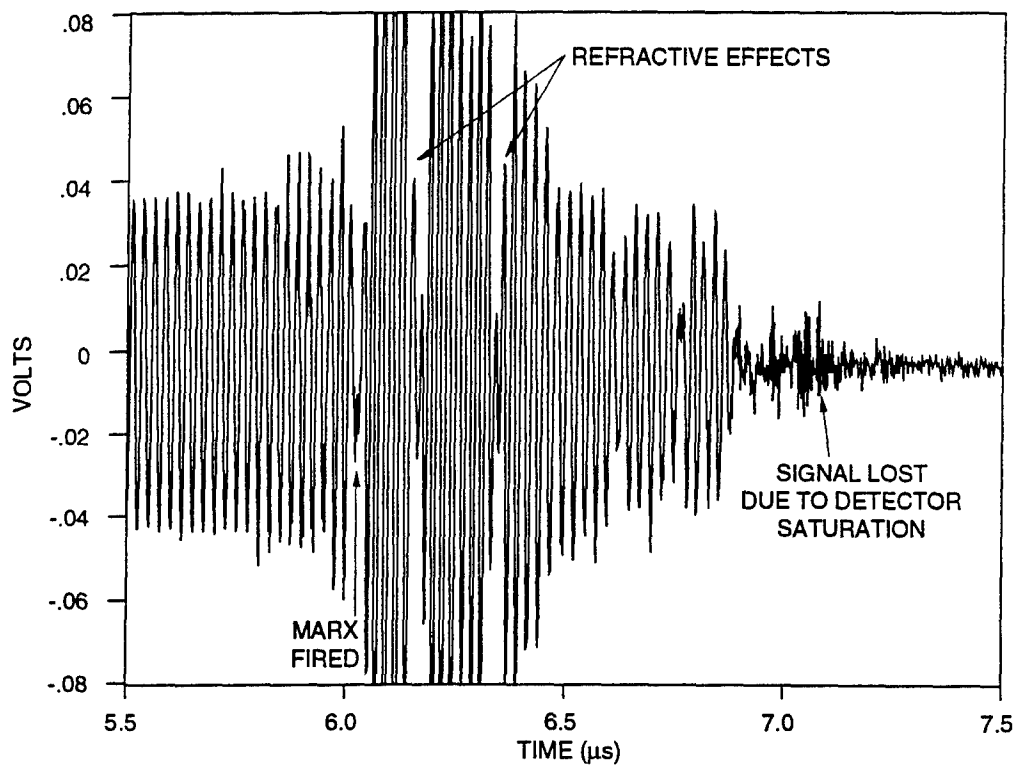
(b) Raw data for density calculation (Shot 925, Channel 1)

Figure 5-27. Typical measurement of one interferometric axial channel with pulse power.
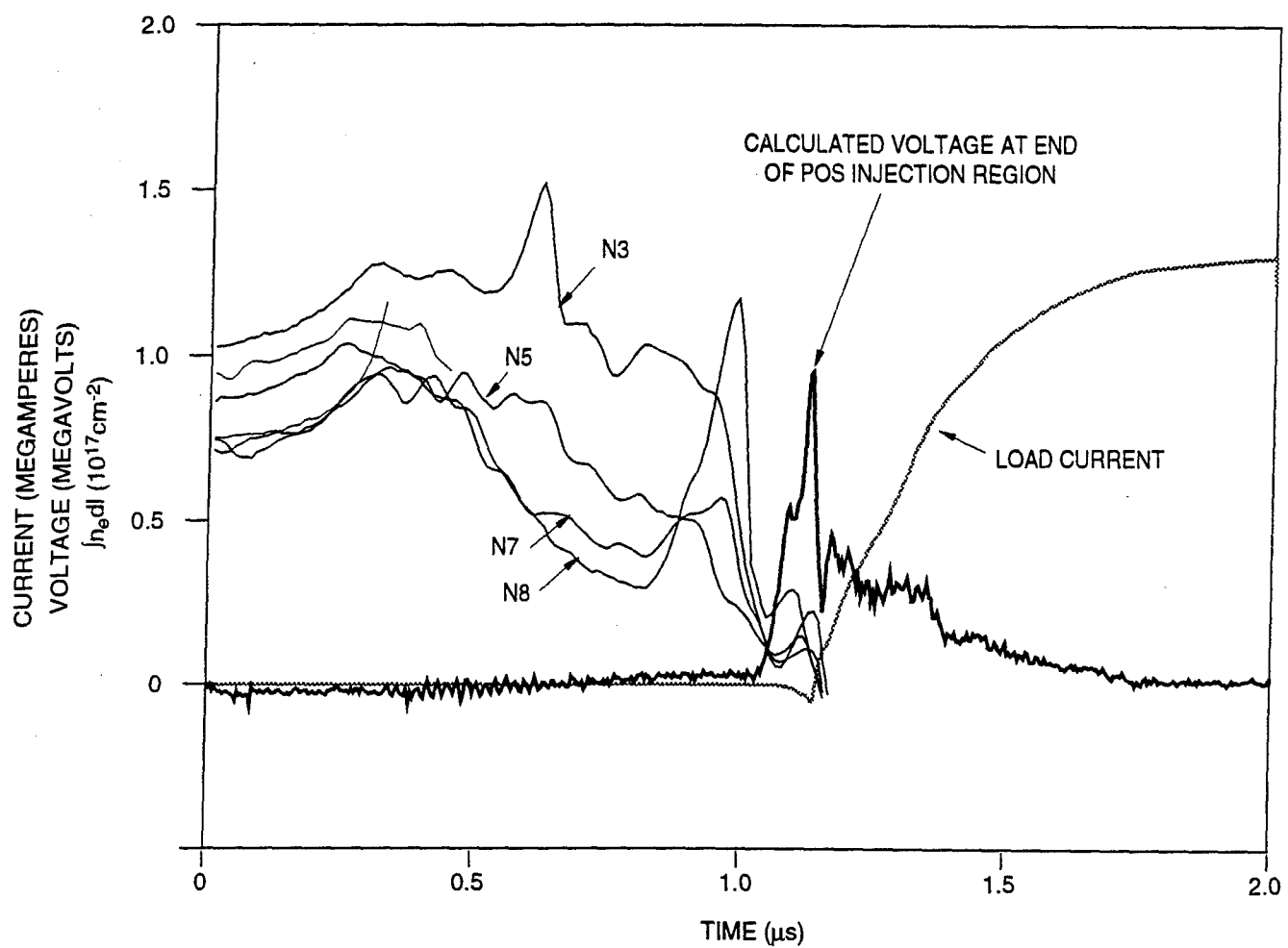
Figure 5-28. Line integrated electron densities (N3, N5, N7, N8), with POS voltage and load current for Shot 991. Positions of interferometric channels are listed in Figure 5-21.
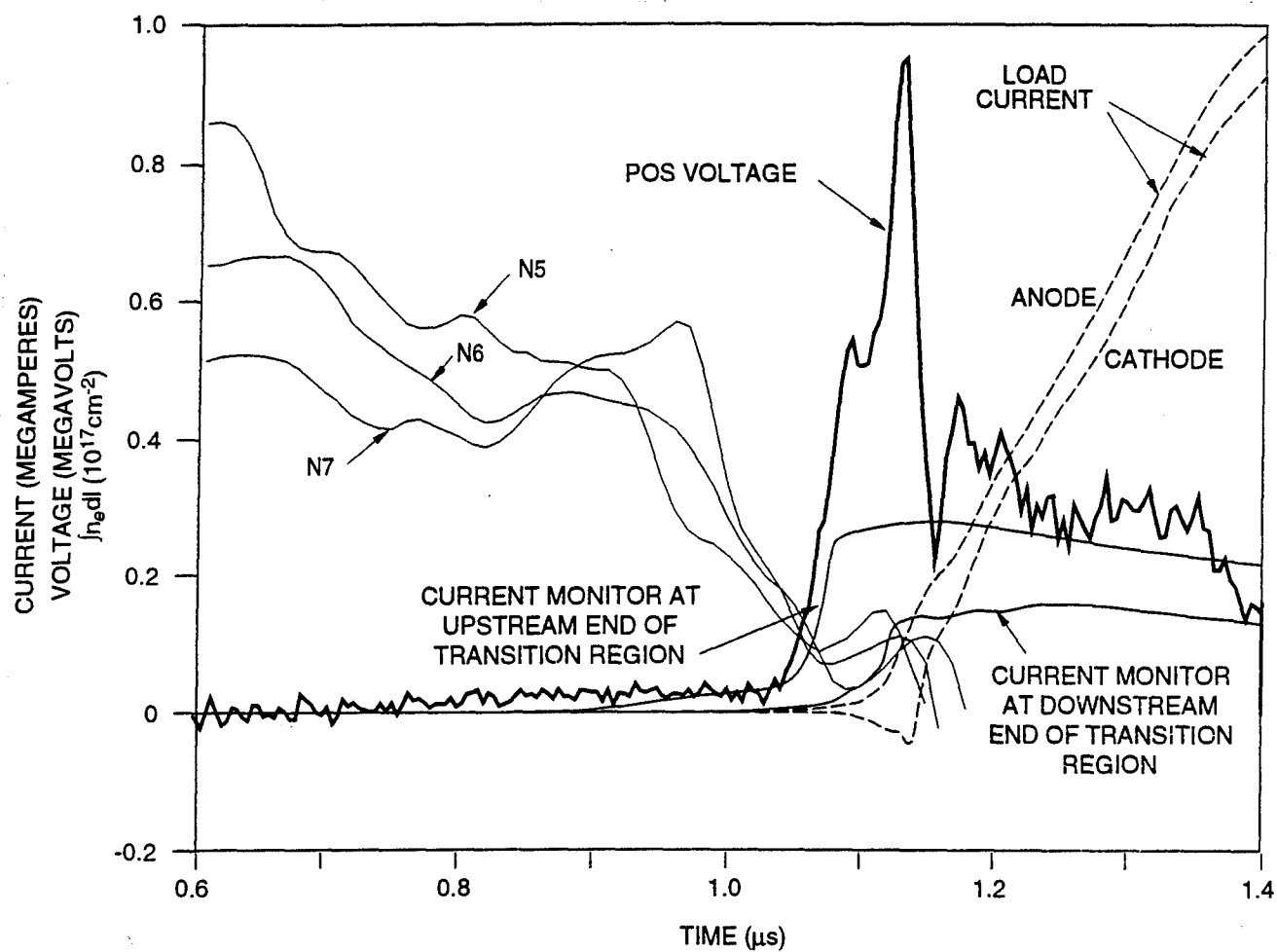
Figure 5-29. Expanded view of waveforms from Shot 991.

5.5 AXIAL INTERFEROMETRIC RESULTS.

Results of a typical axial $\int n_e dl$ measurement with pulsed power are shown in Figure 5-28. In this shot nine axial measurements at different radial positions within the POS A-K gap were made. The radial distance from the cathode for each axial measurement is indicated in the table in Figure 5-21 with N1 nearest the cathode and N9 nearest the anode. Truncation in time of individual probe measurements is based on the observation of zero crossing errors in the raw data due to noise, refraction, or loss of beat signal. Axial measurement channels not shown were lost when the Marx was fired or early on during the conduction time. Unphysical negative integrated line densities typically occur when the beat signal goes away at the time of switch opening. For shot 991 only axial measurement channels N3, N5, N7, and N8 are valid to the time of opening. Appendix C gives the raw data vs. processed data for all the axial positions.

Upon application of pulsed power the integrated line electron densities initially increase beyond those without pulsed power across the entire A-K gap, a likely signature of further ionization of either the bulk gap plasma, or of the plasma swept up in the snowplow front. About one-quarter of the way through the conduction phase, $\int n_e dl$ begins to decrease across the center portion of the gap and later in time begins to increase nearer to the cathode and anode. Figure 5-29 shows an enlarged overlay of the electrical and $\int n_e dl$ measurements. The observed decrease or thinning of plasma near the end of the conduction phase stalls and decreases again at about the time of opening. The late time momentary increase of the integrated electron line density is consistent with the current channel being located in the reduced coax section just before the large inductive volume downstream, with final thinning beginning when the last anode probe begins to show current. This observation of plasma along the axial line of sight during this period of time fits in with the picture that a plasma channel carries the current from the physical POS to the end of the transition region.

5.6 SNOWPLOW MODELING.

Modeling of the time evolution of the integrated electron line densities was performed using the S-Cubed snowplow model. The model input were the integrated line density measurements made without pulsed power. An effective Z_{avg} to atomic mass ratio was chosen to match the conduction time to the end of the physical POS. Figure 5-30(a) compares the model predicted time evolution of $\int n_e dl$ to the experimental data. The model does not show the initial increase seen in the data, but does show a small increase about half way through the conduction phase on some channels. The late time behavior of the model agrees well with the data in the relative magnitude and thinning rate. A disagreement is suggested, however, by the inner most calculated positions, which show $\int n_e dl$ very close to zero near the cathode at the end of the physical POS. This implies that switch opening occurs at the end of the POS injection region. Computationally the propagation of the current front along the cathode to the end of the large inductor occurs in significantly less time than the experimentally observed 100-125 ns. A possible explanation could be that mass from the electrodes modifies the snowplow front near the cathode, and prevents model predicted thinning near the cathode, or that mass swept into the cathode by the snowplow modifies the snowplow front near the
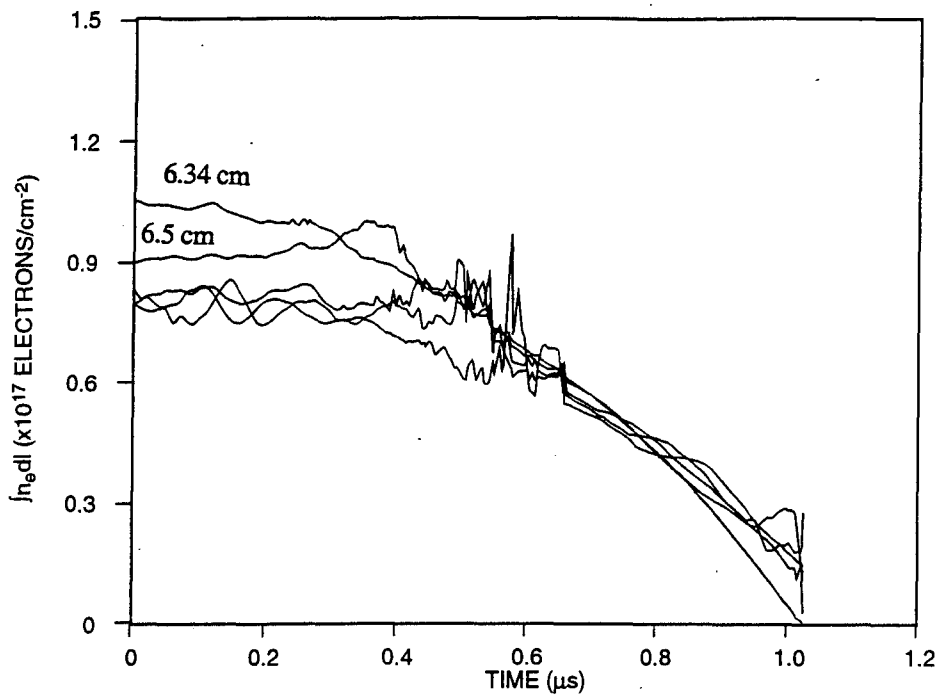
(a) Model. The top most trace and next topmost trace at t=0 are calculated at distances of 3.4 mm and 5.0 mm from the cathode, respectively.
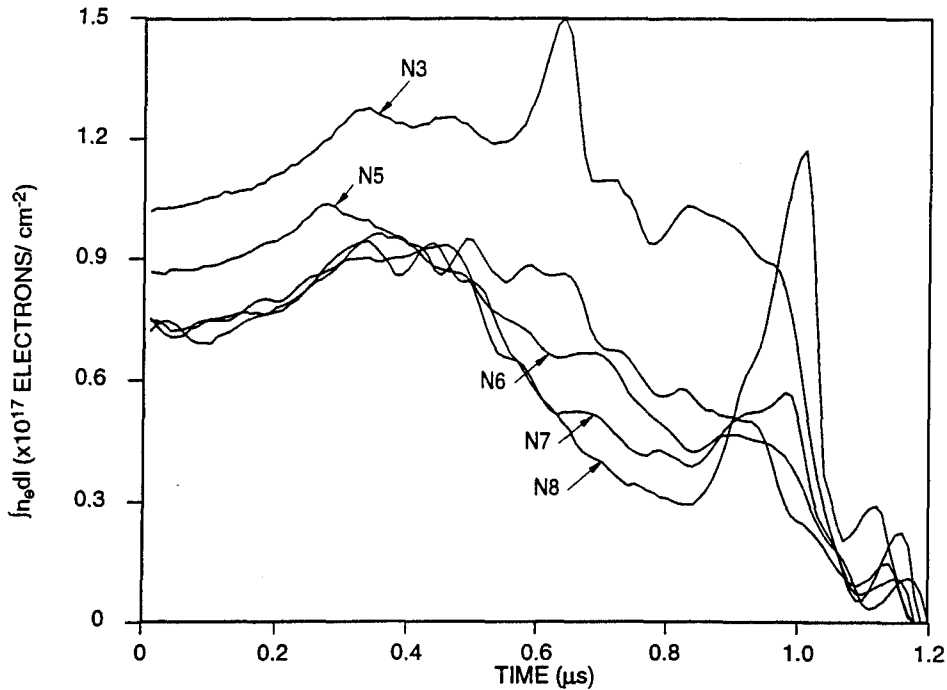
(b) Experimental data. N_3 and N_5 are at 3.9 mm and 7 mm from the cathode, respectively.

Figure 5-30. Comparison of model to experimental data. The model used measure initial line integrals of electron densities.

electrode. One can compare the mass required to account for the inferred transition region propagation time of ~100 ns due to JXB forces with the experimentally observed $\int n_e dl$ at the time the current channel is at the end of the physical POS. For shot 991 using an average ionization state of 1.5, the 35 cm long transition region, and a 1.6 MA mean current during the 100 ns period requires an $\int n_e dl$ of about 5×10^{16} cm^{-2}, assuming no thinning during this phase. This level can be compared with the observed $\int n_e dl$ range of $5-10 \times 10^{16}$ cm^{-2}.

An issue not yet addressed by the modeling is the three dimensional nature of the actual transparent anode structure. The cross-section of the anode structure is seen in Figure 5-31, which shows the density distribution at one time during a computer simulation of plasma inflow from the flashboards. Figure 5-31 shows that there is an azimuthal variation of density in the gap due to both shadowing and convergence effects of the anode structure. This variation is also dependent on the radial distance from the cathode. Modeling to consider the effects of this azimuthal variation has not yet been performed. All axial interferometric measurements to date have been made on a radial diameter oriented between two anode ribs.
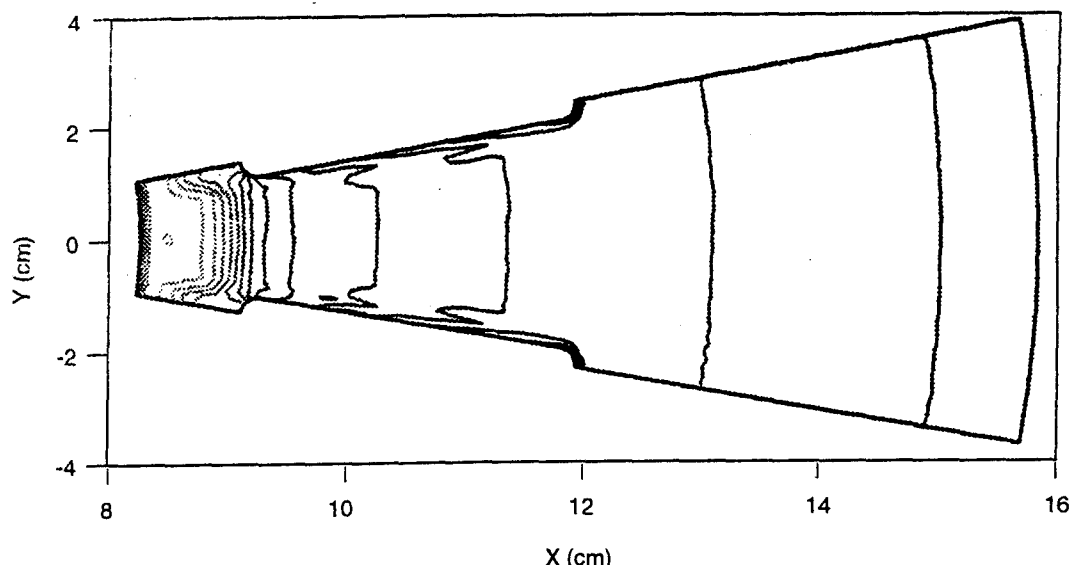

Figure 5-31.   Azimuthal density variations in the anode-cathode gap arise from shadowing due to the anode ribs, and from convergence effects. The initial injection density time distribution was arbitrary. 5.6.1 Chordal Interferometric Measurements Downstream Of The Standard POS.

5.6.1   Chordal Interferometric Measurements Downstream of the Standard POS.

In view of the above observations an experiment allowing interferometric measurements of plasma downstream of the injection region POS was performed. The original standard coaxial switch geometry with the 200 nH load inductor immediately downstream of the POS was chosen for reasons of demonstrated POS performance and diagnostic ease. Interferometry was reconfigured to look across a chordal view in the 200 nH inductor as shown in Figure 5-32,

PROBE DISTANCE
FROM ANODE PLATE

1 - 4.61 cm
2 - 4.00 cm
3 - 3.39 cm
4 - 2.78 cm
5 - 2.17 cm
6 - 1.56 cm
7 - 1.10 cm
8 - 0.95 cm
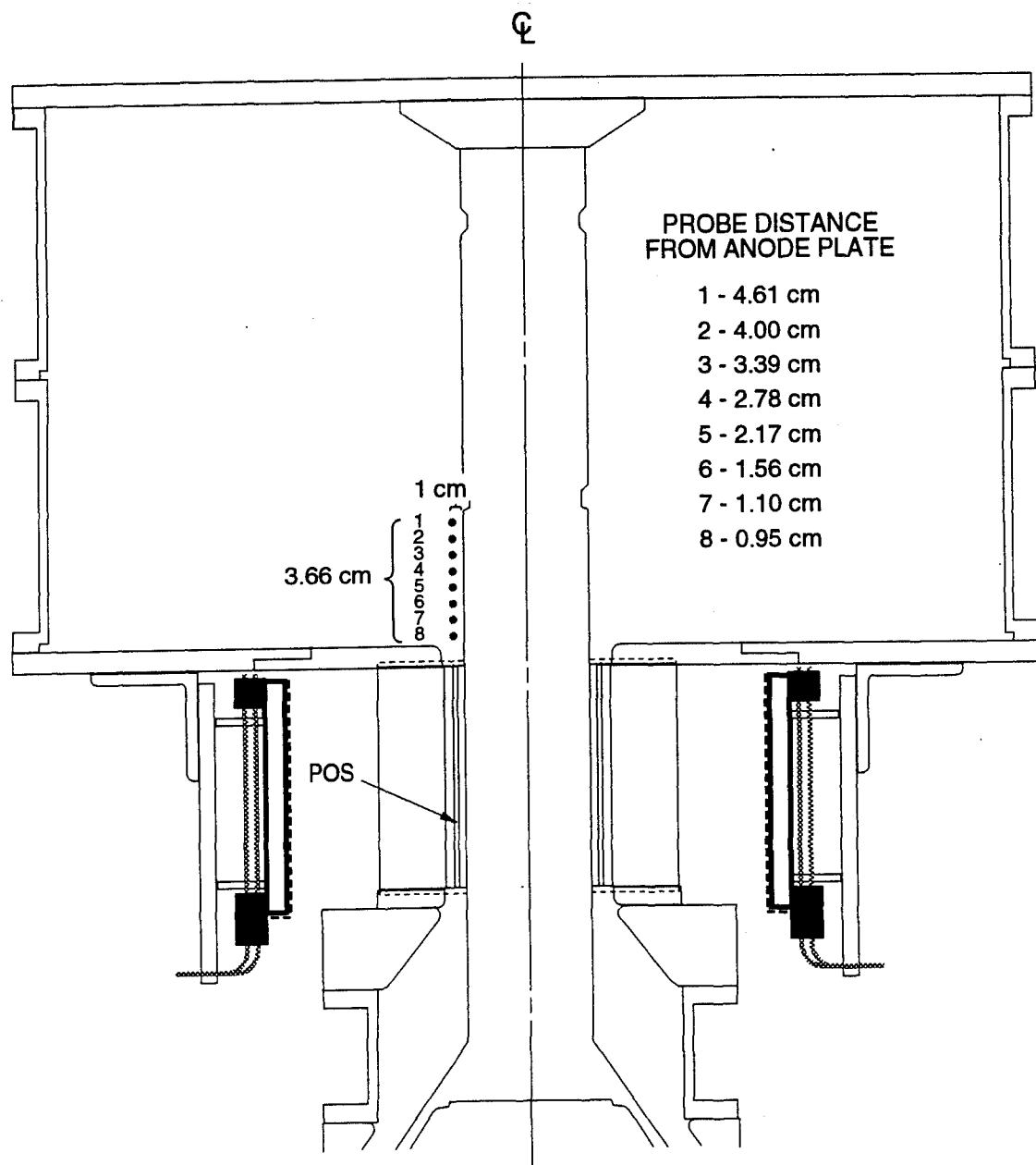
Figure 5-32. Chordal interferometry measurements "downstream" of POS.

with the ribbon probe beam oriented parallel to the cathode. The inner most approach of the chord was located one cm from the cathode. Integrated line electron density measurements were made at eight positions near the end of the POS injection region in the large inductor.

Figure 5-33 shows the observed $\int n_e dl$ for a non-pulsed power, flashboards only pre-shot. The position of the individual chordal interferometric channels were shown in Figure 5-32. The flashboards were fired at a relative time of 500 ns. Based on the axial interferometry, the first plasma from the flashboards reaches the cathode at about 2 µs, corresponding to an injected plasma velocity of 10-15 cm/µs. Figure 5-33 shows that within the $\int n_e dl$ resolution of about 1×10^{15} electrons/cm^2, plasma begins to appear at about five µs at the first interferometric chordal position downstream of the POS. The peak $\int n_e dl$ of 6×10^{15} electrons/cm^2 drops by a factor of two over a distance of 3.66 cm and, based on the evolution of peak locations, appears to be spreading downstream at about 3-4 cm/µs. This is a few times larger than the speed (~1/cm/µs) estimated from time of first arrival at a given location. The chordal measurement allows a reasonable measurement of the timing and velocity of the plasma leaking downstream from the POS region, but estimating the actual density requires modeling to unfold the effective path length. This modeling has not been performed.

Figure 5-34 shows the observed $\int n_e dl$ for pulsed power shot 1030 overlaid by the observed electrical waveforms. The operating parameters for this shot were a Marx charge of 360 kV and a flashboard-to-Marx delay of 6 µs. Within the resolution of a few times 10^{15} cm^{-2} there appears to be no plasma downstream of the POS until just before the load current monitors indicate switch opening. At that time the integrated electron line density rises to a little over 1×10^{17} cm^{-2} and then begins to drop, at which time the 40 MHz beat signal was lost. To estimate the actual density observed modeling is required, but in line with the model of a plasma channel swept through this region, a rough estimate of the width of the channel is (40 cm/µs)(100 ns) = 4 cm, where 40 cm/µs is the velocity of the current channel at the end of the POS injection region and 100 ns is a rough FWHM estimate of the density timing profiles. This channel width is consistent with the estimates obtained by S-Cubed modeling of HAWK chordal measurements in the POS region.

5.6.2   Ace-4 Versus Hawk Coaxial POS.

The observed integrated electron line densities at the time the snowplow reaches the end of the plasma injection region differ significantly between HAWK and the ACE-4 standard coaxial POS experiment. The minimum observed $\int n_e dl$ in the gap falls to about 10^{15}/cm^2 in HAWK, but only to 10^{16}/cm^2 in ACE-4. The snowplow modeled $\int n_e dl$, while qualitatively following the HAWK experimental data, does not agree with the magnitude at the gap position located at r = 5.75 cm where the fastest thinning rate occurs. A possible explanation is that the actual opening was downstream of the POS injection region and that the thinning rate increased beyond the POS due to expansion in to the larger A-K gap downstream. The data suggest an increase in the thinning rate about 30 ns prior to opening.
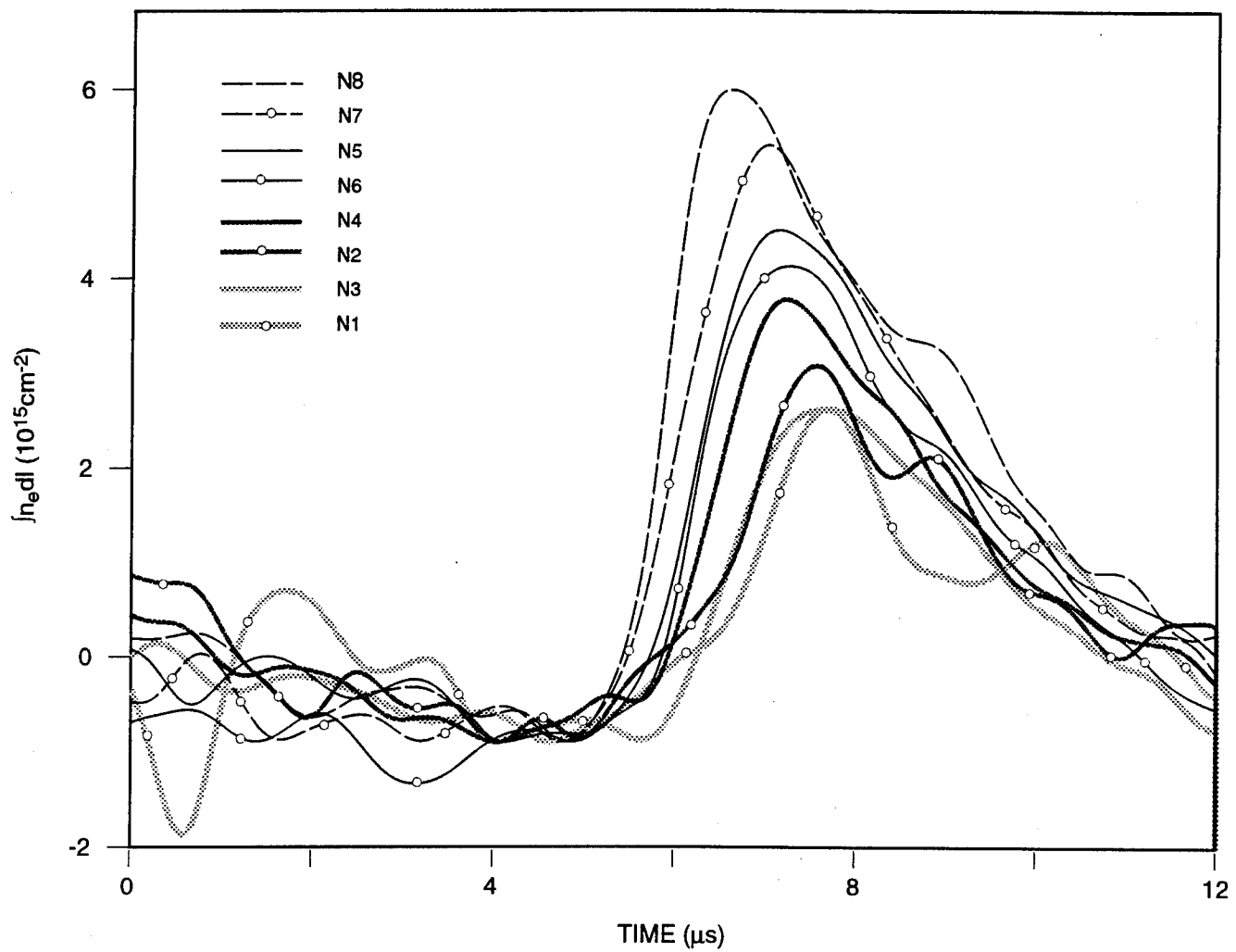
Figure 5-33. Chordal interferometry with no pulsed power (Preshot 1030).
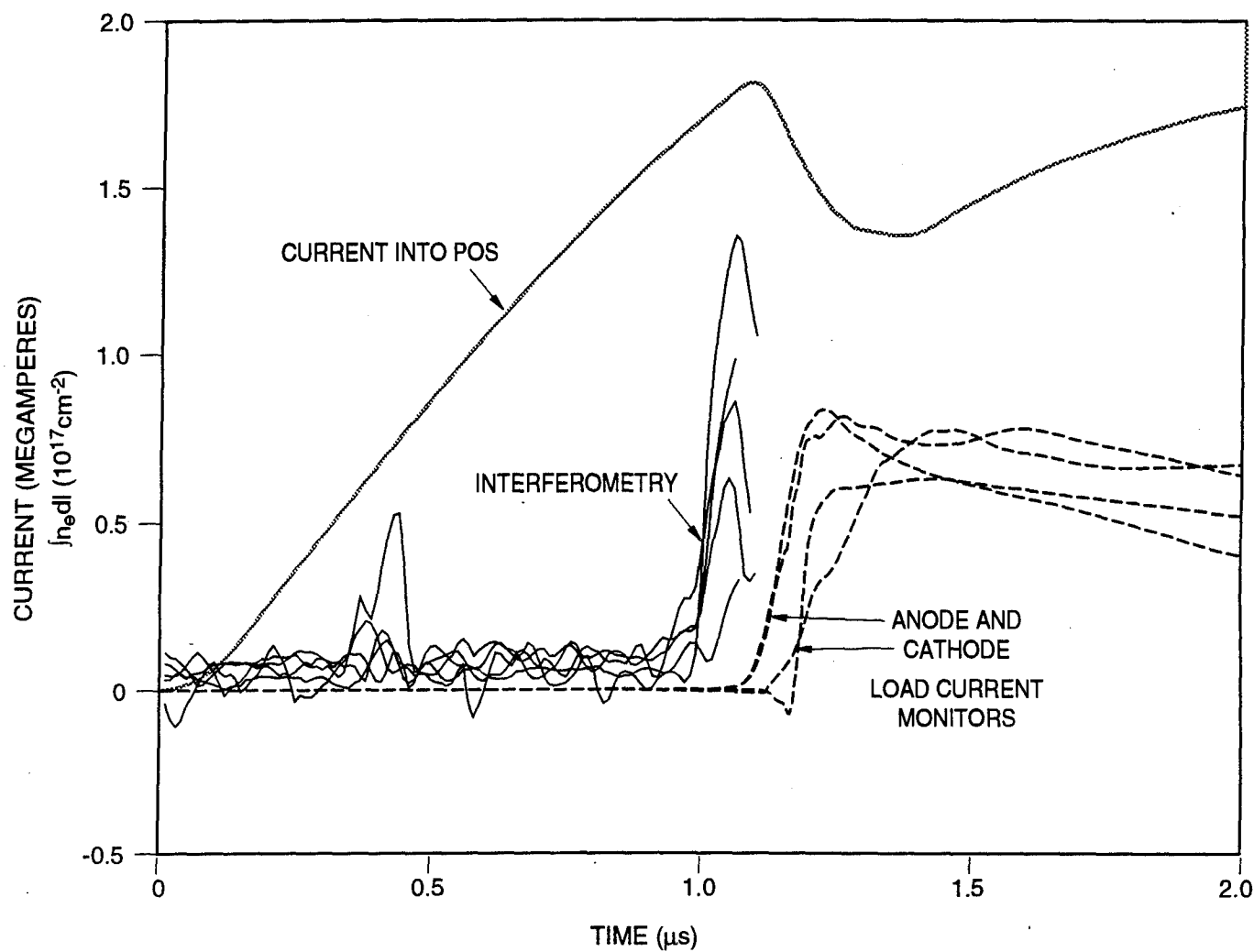
Figure 5-34. Current and chordal interferometry measurements.

For both ACE-4 and HAWK cases the model uses a mass density determined from flashboard-only line integrated electron densities, takes the nominal POS injection length as the plasma length, and determines the average ionization state using the observed conduction time and assuming opening at the end of the POS injection region. The calculated integrated electron line densities mid-gap at the time the snowplow reaches the end of the POS differ between ACE-4 and HAWK, with the final density in HAWK being significantly lower. Thus opening in HAWK may be closer to the end of the physical POS injection region than in ACE 4, where the corresponding ion density could be as high as several times 10^{15} cm^{-2}.

5.6.3 Summary And Discussion.

Coaxial POS experiments on ACE-4 have been performed which provide new insight into understanding how plasma thinning and downstream geometry may affect long conduction time opening switches. A phenomenological model to explain the observed POS operation with and without a transition region downstream of the POS has been proposed that is consistent with the observed plasma and electrical measurements. The model assumes that current is carried downstream of the POS injection region by the plasma channel, which exists at the end of the snowplow process in the POS injection region. Although some plasma leakage downstream without pulsed power is observed it appears not to dominate the downstream current propagation process. Interferometry suggests that in the case of the standard ACE-4 coaxial POS, thinning near the end of the POS injection region is insufficient to allow opening there. This model does not specifically address the opening process that occurs when the plasma channel finally thins sufficiently for the POS to open. The existing snowplow model underestimates the integrated electron density near the cathode. This may be due to densities near the cathode that are higher than measured because of the neutralization effect discussed earlier, or because of a modification to the snowplow front due to mass introduction from the cathode. This mass could be associated with actual cathode material or stagnation of snowplowed POS plasma at the cathode surface.

A series of experiments both in the test stand and in ACE-4 are planned to address the measurement and modeling questions raised in this report.

5.7 SPECTROSCOPIC DIAGNOSIS OF ACE-4 PLASMA OPENING SWITCH.

5.7.1 Background.

We are developing of spectroscopic diagnostic tools for the plasma opening switch. The purpose of this effort is to obtain detailed, time resolved information about the switch plasma parameters that can be used in the modeling of the POS.

In the case of snowplow modeling, for example, the initial intergap density profile is based on interferometric measurements which measure integrated electron line densities. To determine the mass density distribution an average ionization state and mass must be assumed. Several effects can cause time and spatial dependencies of these average plasma parameters. Injected plasma contact with the POS anode and cathode structure may change the degree of ionization from that of the free space flashboard plasma. The average ionization state may also change

with the application of pulsed power affecting the interpretation of interferometry with pulsed power. In the case of cable gun sources data at NRL on HAWK the data suggest exactly that. Spectroscopic measurements coupled to modeling allow an independent measure of the electron density and provide an estimate of the average ionization state.

5.7.2   Survey Of Visible Spectral Lines In The Flashboard Plasma.

In order to identify the spectral lines that can be used for time resolved measurements and to obtain an assessment of the composition of the flashboard plasma, we have obtained a survey of visible spectral lines. The spectra were obtained with the McPhearson 209, a 1.33 meter spectrometer equipped with a linear array detector (Princeton Applied Research, OMA 1205). The measurements were time integrated over the entire pulse length of the flashboard. The spectral range covered by the survey was restricted by the OMA detector sensitivity to the range from 390 nm to 700 nm. A 300 lines/mm grating was used, giving the spectral resolution of about 0.062 nm per pixel, more than the expected line width of about 0.03 nm. With 500 pixels, the OMA detector provided simultaneous spectral coverage over 31 nm. The wavelength calibration of the spectrometer was performed using a mercury spectral wavelength standard.

The survey was conducted in a test stand, using a geometry resembling that of the radial switch. As shown in Figure 5-35, a lens was used to image the flashboard plasma onto the entrance slit of the spectrometer and the observation was in the direction parallel to the flashboard surface, along its long side. Fast plasma flashboards with v_{plasma}~15-20 cm/μs constructed with a Teflon substrate were used in this characterization. Data was obtained for the following three configurations:

- Flashboard only,
- Flashboard with screen in front
  (screen was used to simulate the radial POS transparent anode)
- Flashboard and simulated anode-cathode structure.

The spectra obtained for these three configurations are qualitatively consistent and are dominated by carbon and fluorine (the components of Teflon) and hydrogen. The lines of singly and doubly charged carbon, singly charged fluorine and (neutral) hydrogen were observed. Some of the lines were tentatively attributed to copper and several lines were not positively identified.

In general, the same spectral lines were observed in all the configurations. Although the intensities of lines depended on the presence of material obstacles in front of the plasma source and/or on the distance from the source, the relative intensities of the most prominent lines do not appear to be vary significantly. This is illustrated in Figure 5-36 which shows the spectra obtained for the configuration with anode screen in front of the flashboard. The spectra were obtained for three different sightlines: 1.5 cm upstream from the screen (i.e., between flashboard and the screen) top trace, and 1 cm and 2 cm downstream from the screen in the middle and lower traces, respectively. Note that the intensity of carbon lines decreases rapidly in the direction downstream from the flashboards (there may be an error in the determination

5-50
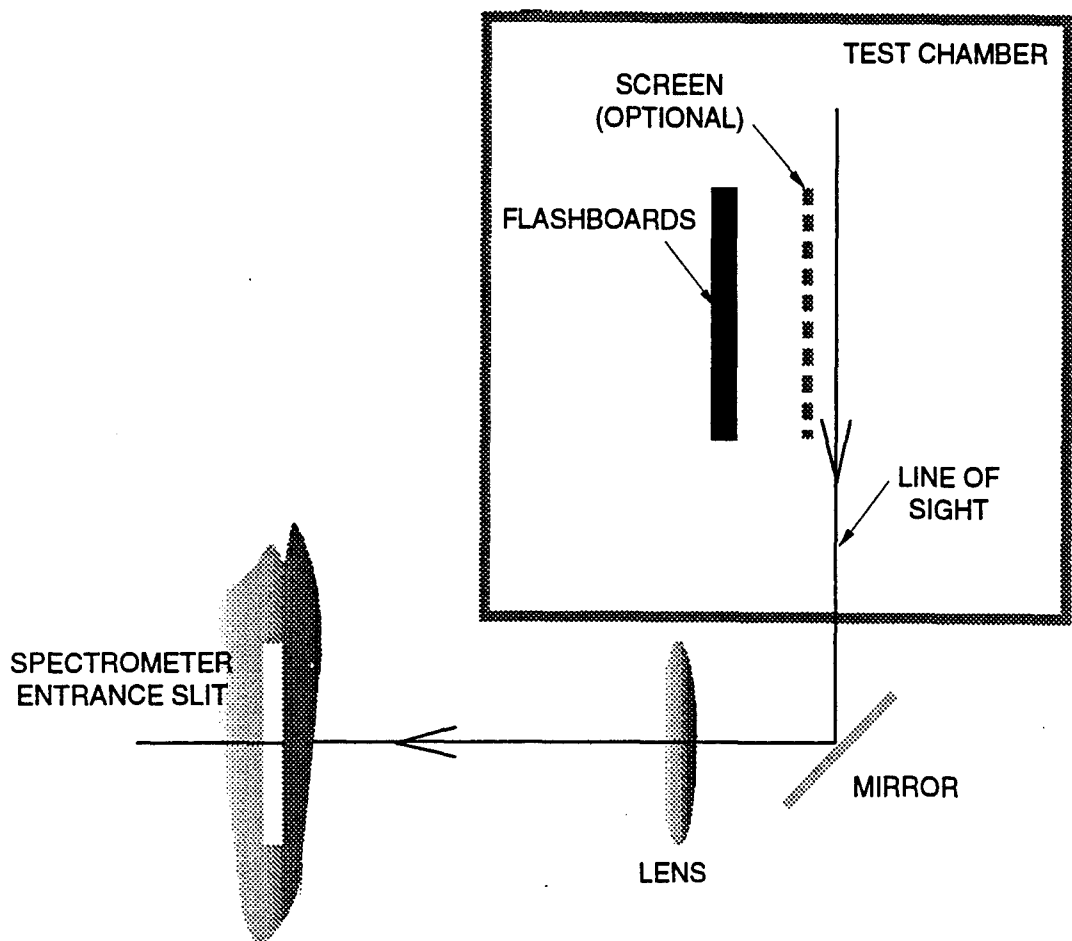
Figure 5-35. Diagram of the experimental set up for the test stand spectral survey of the flashboard generated plasma.

of relative intensities due to the irreproducibility of the flashboard discharges). The line intensity ratios obtained in the configuration without the screen are similar to those obtained for the downstream sightlines with the screen. The constant line intensity ratios are consistent with estimates of the recombination time for the carbon plasma with temperature of several eV and density of the order of 10^{13} cm^{-3}, as these conditions imply decay times of the order of 10 100 μs. Thus, the intensity decay may be attributed to the plasma expansion as it moves away from the source and to the attenuation of the particle flux by the screen. Figure 5-37 shows interferometry taken in a ribbon across the region of the screen. The top set of channels in Figure 5-37 are between the flashboard and the screen, while the bottom set of channels are downstream of the screen as shown in Figure 5-35. A reduction in magnitude and a time delay of the integrated electron line densities downstream of the screen is observed.
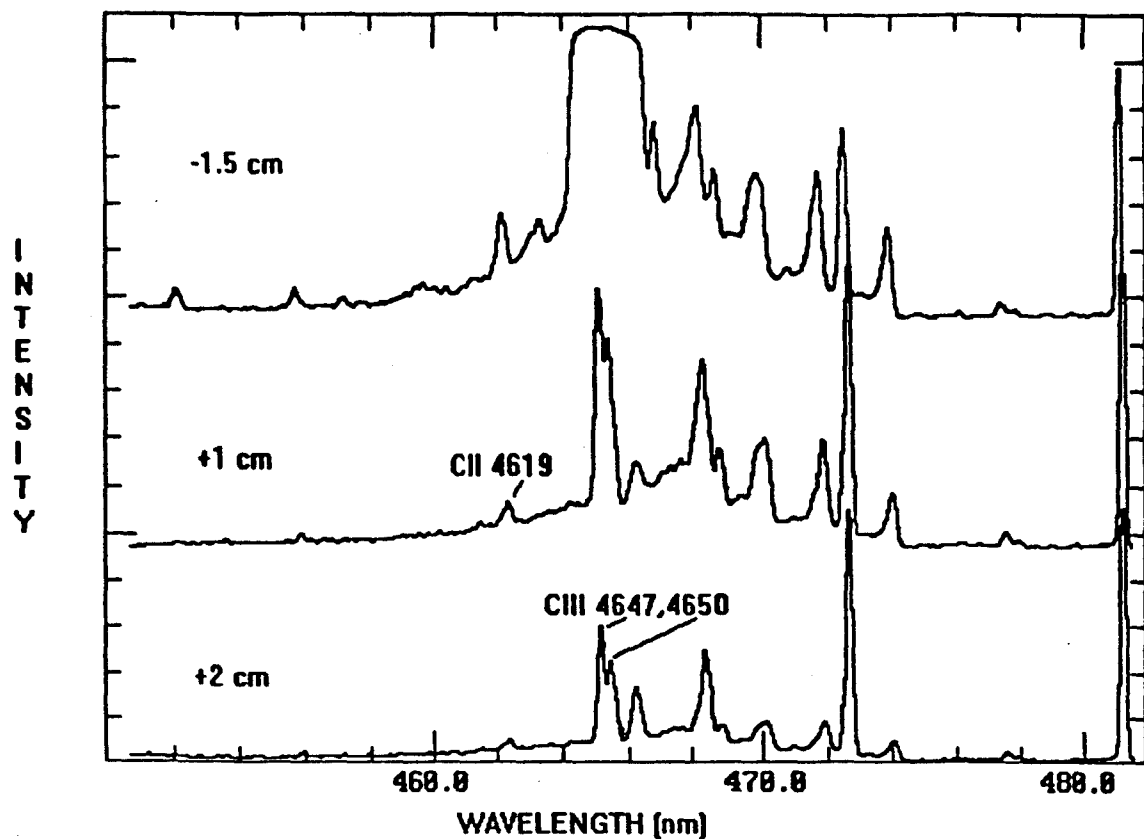
Figure 5-36. Relative time integrated spectral intensity as a function of distance from the flashboard (with screen).

5.7.3 Radial Plasma Opening Switch Observations.

The experimental set-up for study of the radial geometry POS is shown in Figure 5-38. The switch plasma was observed through an opening in a center of one of the flashboards. A 5 cm, f=50 cm lens was used to collimate the plasma light, and a 7.5 cm, f=50 cm lens was used to focus (image) the light on the slit of the spectrometer. In this arrangement, the f-number of the collecting optics was somewhat smaller than the f-number of the spectrometer (f/11.6), assuring full utilization of the spectrometer throughput. The spectrometer and detector were as described above.

The spectra were recorded without pulsed power (flashboards only) and with pulsed power. Only time integrated data could be obtained with the available OMA detector. As the signals obtained with pulsed power were much stronger than those obtained with the flashboards only, the sensitivity of the spectrometer was reduced for the pulsed power shots by a factor of about 3, by decreasing the width of the input slit.
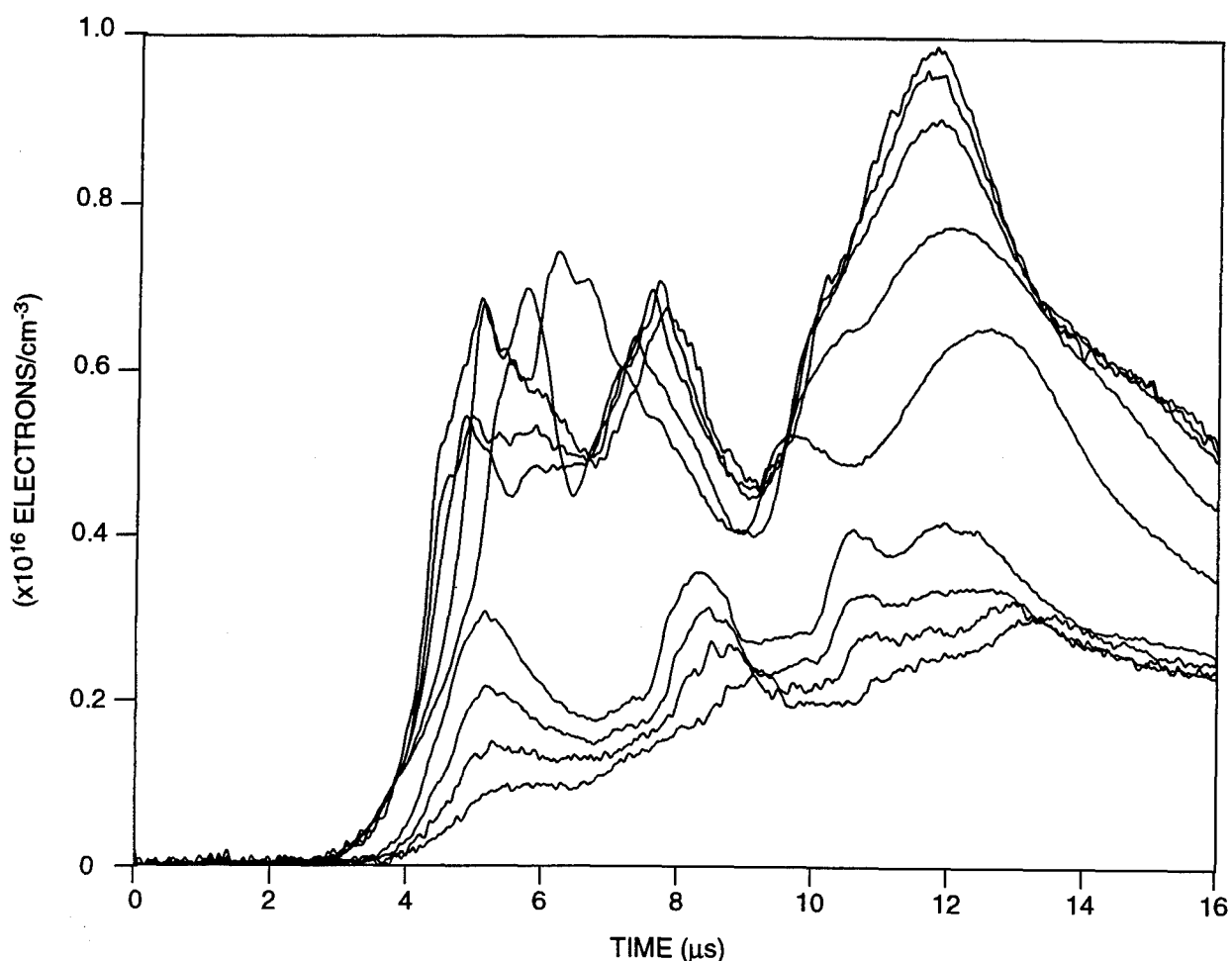
Figure 5-37. Interferometry taken upstream and downstream of screen shown in Figure 5-35.

A detailed survey of the spectral lines was obtained in the range from 380 to 680 nm. The spectra obtained without pulsed power were very similar to those obtained in the test stand on the downstream side of the anode screen. With the application of pulsed power, an overall increase of the time-integrated line intensities was observed. This increase was larger for the shots with larger delay time between the flashboard pulse and the application of pulse power. Also, a number of new lines appeared in the spectrum. Most of the prominent lines of neutral iron were identified in the spectra obtained with pulse power, indicating that the electrode material is ablated and excited when the conduction current flows through the switch. The influx of iron is illustrated in Figure 5-39, which shows the spectra in the vicinity of the strong CII 4267 A line (saturated signal) obtained for flashboards only, and with pulsed power applied 3.0 μs and 3.5 μs after the start of flashboard pulse, respectively. The measured intensities
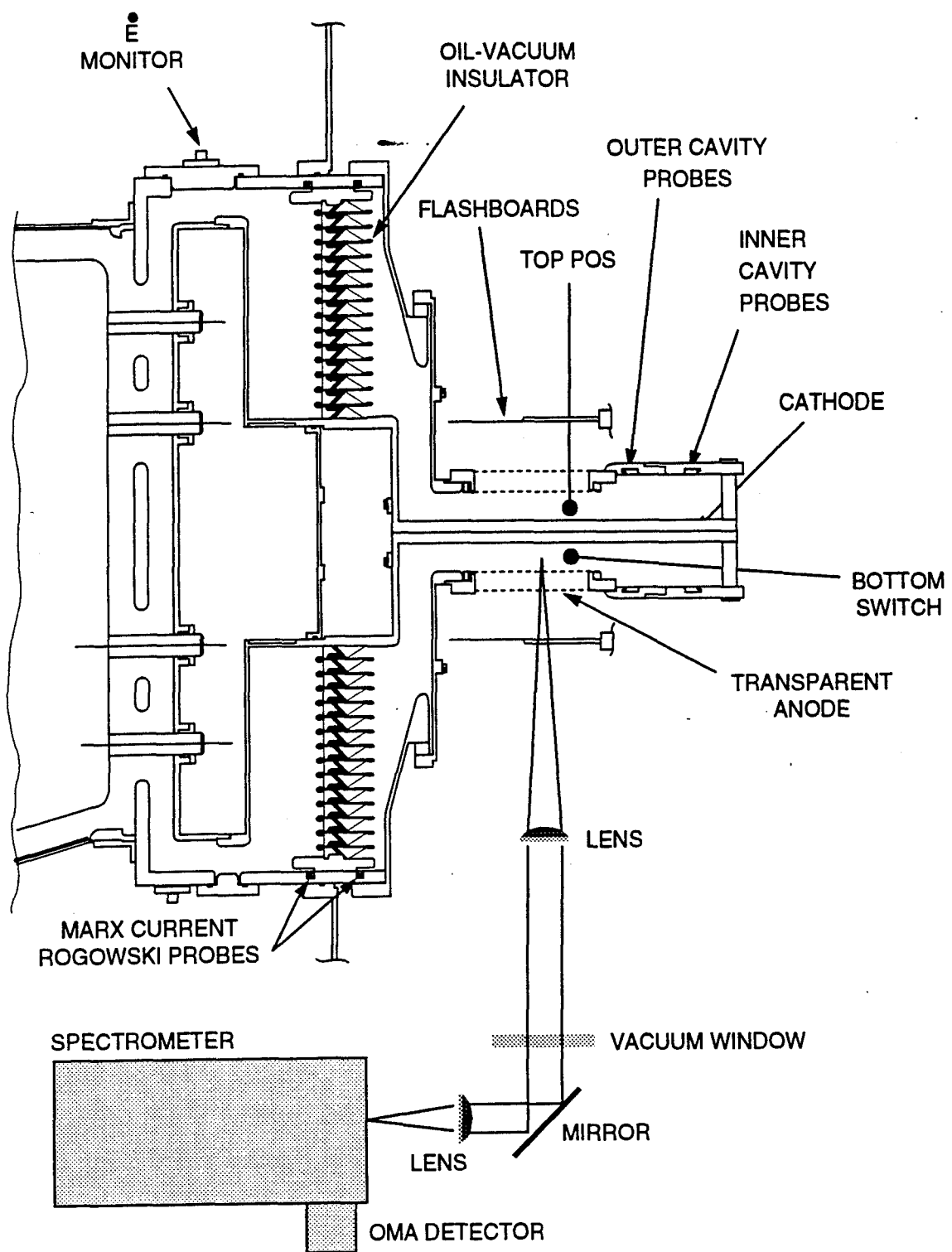
Figure 5-38. Experimental set up for spectroscopic study of the radial geometry POS.

were corrected for the difference in the spectrometer entrance slit width. Most of the lines appearing with the application of pulse power are (tentatively) identified as lines of neutral iron. Note that the intensity of the lines increases with the delay time consistent, for the presented case, with somewhat larger conduction current flowing through the switch and longer conduction time, i.e., with more energy delivered to the switch plasma.

5.7.4   Coaxial Plasma Opening Switch Observations.

For the coaxial POS configuration, a fiber optic bundle was employed to transmit the light from the switch to the spectrometer. The bundle consists of ninety 50 μm core fused silica fibers. On the spectrometer end the fibers are arranged in a row that matches five millimeters high and 50 μm wide slit, and on the POS viewing end the bundle is circular. We used the fiber both without any additional optics, resulting in a rather large field of view, and with a fused silica collimating lens, f=2.5 cm and a 1 cm diameter, to reduce the diameter of the observed volume to about 1.5 cm. The switch plasma was observed both in radial direction, with the fiber placed slightly behind the flashboard surface between flashboards, and in the axial direction, with the fiber placed on the top of the load looking down at the POS A-K gap. Both flashboards and cable guns were used as the plasma source. The following observations were made:

- Without pulsed power the time integrated spectra obtained for flashboard and cable guns were nearly identical, indicating very similar composition and temperature of the plasma. As the only difference, several CuII lines were identified in the spectrum of cable gun plasma.

- No major differences were observed in the spectra obtained for the radial and axial views. This comparison was made for the data obtained using a higher resolution grating, 1200 line/mm instead of 300 line/mm, with a correspondingly smaller simultaneous spectral coverage.

- In most of the cases, the application of the pulsed power results in a significant increase in the level of light. Very often the OMA detector was saturated even when the width of the input slit was significantly reduced. This high intensity light appears to be broadband, without any discernible line structure.

- The time integrated intensity of the light burst associated with the application of pulsed power seems to be correlated with the switch performance, the light intensity increasing with the POS opening voltage.
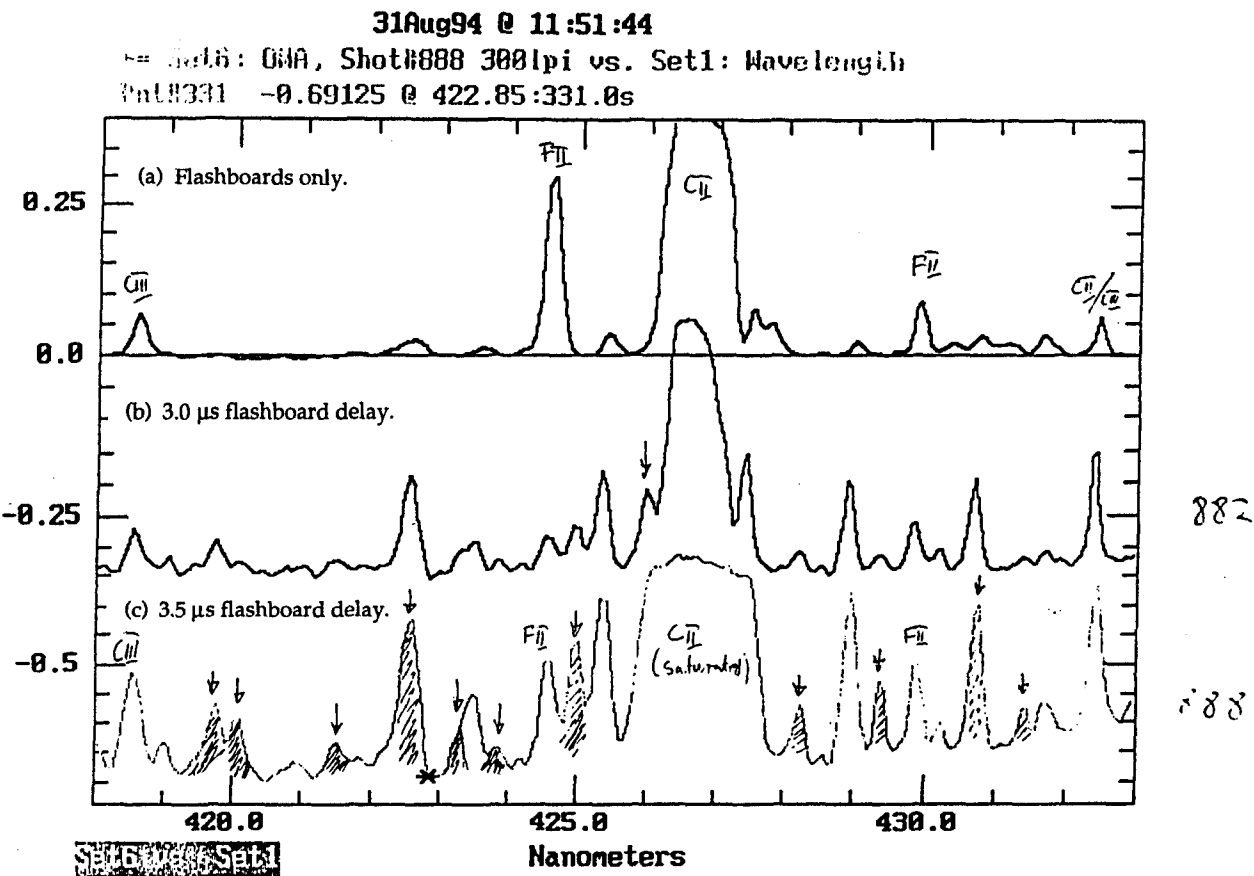
Figure 5-39. Time integrated axial view spectroscopic measurements in coaxial switch geometry.

5.7.5 Time Resolved Measurements Of Line Intensities.

Preliminary measurements of time resolved line intensities in the coaxial POS were made. The light in the POS region was collected axially by the fiber optic bundle, using the lens collimator described above, coupled to the spectrometer entrance slit. The high resolution (1200 line/mm) grating was used giving about a 0.03 nm bandpass with a 50 μm effective slit width, comparable to the expected line width. A second identical bundle was coupled to the exit slit and connected to a 600 μm diameter single fused silica fiber that carried the light to a photomultiplier tube. The photomultiplier tube and a fast signal amplifier were placed in the screen room to minimize the noise interference. The time resolved data were obtained both without-pulsed power and with pulsed power.

Figure 5-40 shows the data obtained for the flashboard plasma only, without pulse power. The time dependent intensities of CIII 4647 Å and CII 4267 Å lines, smoothed by averaging over 400 ns, are displayed. Also shown in Figure 5-40 is the time history obtained at 4262 Å showing the negligible level of background or continuum radiation. The onset of the line radiation is well correlated with the onset of electron density, as measured by the axially looking interferometer. We have also observed that the time interval between the flashboard pulse and the light onset is proportional to the distance from the flashboard to the A-K gap. The data shown in Figure 5-40 suggest that the ionization stage of the flashboard plasma in the switch region decays rapidly. The plasma seems to arrive doubly ionized, but after only about 2-3 µs the radiation of the singly ionized ions becomes dominant. This may indicate a fast decay of the plasma temperature.
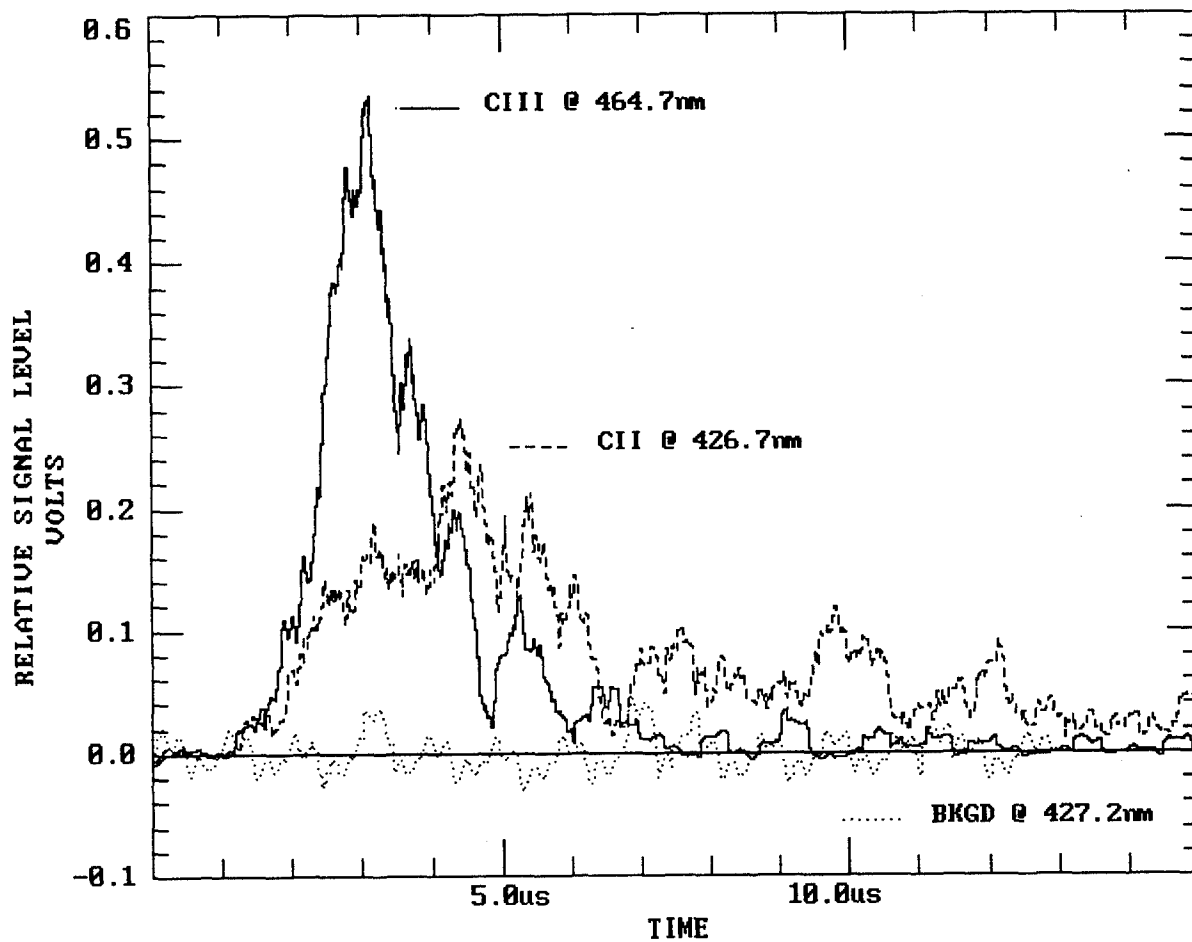
Figure 5-40. Time resolved line intensity measurements in coaxial switch geometry.

As mentioned above, high intensity, broadband light is detected when the pulsed power is applied. Preliminary time-resolved measurements indicate that onset of this light coincides with the opening of the switch, and that the pulse duration is of the order of 2 μs. This is consistent with the observation of low level of continuum radiation for the shots with poor switch opening. The intensity of the light emitted after the switch opens is about two orders of magnitude larger than the emission during the conduction phase. We did not collect enough time resolved data to be able to confirm that the intensity of the radiation burst is correlated with the quality of switch opening.

5.8 Summary.

The survey of spectral lines indicates that the flashboards produced plasma containing singly and doubly ionized carbon and fluorine. Roughing pump oil is thought to be the main source of hydrogen. The intensity of hydrogen lines varied considerably between the different series of measurements and may be correlated with the quality of vacuum or how recent the vacuum chamber was pumped down after opening. Most measurements were made for the flashboard plasma but the data obtained for the cable guns indicate that the plasmas were of similar composition.

The ionization state or effective charge of the plasma (Z_{avg}) is one of the parameters that may be readily incorporated into the models of the conduction phase. Presently this parameter is deduced from the measured electron density and conduction time using the snowplow model. Measurement of Z_{avg} would allow us to validate the snowplow model by comparing the measured and predicted conduction times. Z_{avg} may be deduced from the time resolved measurement of line intensity ratios.

An initial estimate of the Z_{avg} of the flashboard plasma from the time integrated measurements of line intensities has been made. The time dependent calculations of level populations in singly and doubly ionized carbon were provided by Y. Maron. In his model the evolution of level populations was calculated assuming constant electron temperature and density (10^{15} cm^{-3}), and an initial condition of all ions in the ground level of the singly charged carbon. A semi-equilibrium is approached after 1 μs of evolution. The line intensity ratios calculated in the model for different electron temperatures are compared with the measured, time-integrated intensity ratios. The measured ratios did not take into account the dependence of the detector sensitivity on the wavelength and irreproducibility of flashboard discharges. Thus, they may be accurate to within a factor of two. The ratios of CII 4267 A, CII 3920 A, and CIII 4647 A lines were considered. According to the model, the intensity ratio of CII lines is rather insensitive to the assumed electron temperature in the range from 2-10 eV, as may be expected from the fact that the upper levels for these two transitions are close to each other, but the ratios of CII to CIII intensities are very sensitive to the electron temperature. This is shown in Figure 5-41. Table 3 gives the calculated intensity ratios as a function of electron temperature based on Figure 5-41 and the measured intensity ratios.

Table 5-3. Line intensity ratios.

Electron Temperature (eV)	CII 3920 /CII 4267	CII 3920 / CIII 4647	CII 4267 /CIII 4647
3	0.021	7.3	350
5	0.015	0.15	9.5
10	0.015	0.00055	0.038
Measured	0.21	0.56	3.4

We first note that the calculated ratio of CII(3920)/CII(4267) is about one order of magnitude smaller than the measured ratio. This may indicate that the present model is not fully adequate or be an effect of the time integrated spectral measurement. We are working on resolving this question with use of a time gated spectrometer in the future. For example, we will consider the importance of the initial condition on the result of the calculation, as according to our preliminary time resolved data, the flashboard plasma starts in a higher ionization stage than assumed in the model.

The electron temperature may be estimated from the measured intensity ratios of CII to CIII lines. Due to the inconsistency with the model of the CII relative intensities, the electron temperature of about 4 eV is estimated from the ratio CII 3920 to CIII 4647 lines, and of about 7 eV from the ratio of CII 4267 to CIII 4647 lines. This is equivalent in our model to a time-averaged Z_{avg} in the range 1.1-1.7.

The preliminary time resolved data indicate that the flashboard plasma consists mainly of higher ionization stages at the beginning of the discharge and thus, the initial condition used in the model, that of ground state, singly ionized ion is not adequate to describe the observed evolution of the line intensities. It is not clear at this point how this disagreement will influence the conclusions based on time integrated measurements.

The application of pulse power considerably alters the radiated spectrum. In the case of the radial POS, we were able to detect an influx of neutral iron, presumably ablated from the electrode surface. For the coaxial POS, the time integrated measurements were often overwhelmed by a high intensity burst of continuum light which, based on our preliminary time-resolved measurements, seems to be associated with the opening process. This is consistent with the observation the coaxial POS configurations tested generally opened to much higher voltages than those observed in the radial POS configuration. As the intensity of this light seems to increase with the voltage developed by the switch, one may speculate that high energy particles produced during the opening ablate the electrode surface material in the form of macro-particles, as no line spectrum is observed that could be attributed to atomic particles. Consistent with poor or no-opening in the radial POS, the continuum light was not observed in this configuration. It is interesting to note that the high intensity continuum light was also seen with radial observation in the center of the coaxial switch, indicating that it is produced in the whole switch volume and not only in the region where the switch opens.

As the continuum light appears after the switch opening, this phenomenon may not influence the switch performance. On the other hand, the influx of cold particles during the conduction phase, as observed in the radial switch and most probably occurring also in the coaxial switch, may have an effect on the opening process. Both of these phenomena should be further studied and eventually included in the POS modeling.

SECTION 6

REFERENCES

Commisso, R.J., P.J. Goodrich, J.M. Grossman, D.D. Hinshelwood, P.F. Ottinger, and B.V. Weber, "Characterization of a Microsecond-Conduction-Time Plasma Opening Switch," *Phys. Fluids* B4 (71), p. 2368, 1992.

Cooperstein, G and P.F. Ottinger, "Guest Editorial: Fast Opening Vacuum Switches for High-Power Inductive Energy Storage," IEEE Transactions on Plasma Science, Vol. P5-15, 6, p. 629, 1987.

Creedon, J.M., "Magnetic Cutoff in High Current Diodes," *J. Appl. Phys.* 48 (3), p. 1070, 1977.

Fruchtman, A. "Penetration and Expulsion of Magnetic Fields in Plasmas Due to Hall Field," *Phys. Fluids B*. # (8) 1908, 1991.

Goodrich, P.J., D.D. Hinshelwood, R.J. Commisso, J.M. Grossmann, J.C. Kellogg and B.V. Weber, "High Power Opening Switch Operations on HAWK", Proceedings of the 9th IEEE International Pulsed Power Conference, Albuquerque, NM, p. 510, 1993.

Goyer, J.R. *et al.*, "Improved Performance of a Plasma Opening Switch Using a Novel Anode Configuration," IEEE Transactions on Plasma Science, Vol. 22, No. 3, pp. 242-245, June 1994.

Hinshelwood, D.D., *et al.*, "Density Measurements of Microsecond-Conduction Time POS," Beams 92 paper, PI-35.

Ingermanson, R., *et al.*, "Effects of Space-Time Density Variations on Microsecond Plasma Opening Switches," Proceedings of the 9th IEEE International Pulsed Power Conference, Albuquerque, NM, p. 799, 1993.

Kingsep, A.S., K.V. Chukbar, and V.V. Yan'kov, in Reviews of Plasma Physics ed. B. Kadomtsev, vol. 16, p. 243, Consultant Bureau, New York, 1990.

Mendel, C.W., Jr., D.B. Seidel and S.E. Rosenthal, "A Simple Theory of Magnetic Insulation from Basic Physical Considerations," Laser and Particle Beams, 1 (3), p. 311, 1983.

Swanekamp S., J. Grossman, P. Ottinger, R. Commisso and J. Goyer, "Power Flow Between a Plasma-Opening Switch and a Load Separated by a High-Inductance Magnetically Insulated Transmissions Line," *J. Appl. Phys.* 76 (5) 2648, Sept. 1994.

Swanekamp S., J. Grossman, R. Commisso, P. Goodrich, P. Ottinger and B. Weber, "Simulations of Vacuum Electron Flow in Inductive-Energy-Store Pulsed Power Systems," Proceedings of the 10th International Conference on High Power Particle Beams, pg. 303, San Diego, CA, June 20-24, 1994.

Thompson, J., *et al.*., "Flashboard Plasma Source Characterization for Microsecond Plasma Opening Switches," Proceedings of the 9th IEEE International Pulsed Power Conference, Albuquerque, NM, p. 524, 1993.

Thompson, J., *et al.*., "ACE-4 Microsecond Plasma Opening Switch and Plasma Filled Diode Load Characterization," Proceedings of the 9th IEEE International Pulsed Power Conference, Albuquerque, NM, p. 119, 1993.

Thompson, J., P. Coleman, C. Gilbert, D. Husovsky, A.R. Miller, J. Rauch, W. Rix, K. Robertson and E. Waisman, Proceedings of the 10th International Conference on High Power Particle Beams, San Diego, CA, June 20-24, 1994.

Ron, A., A.A. Mondelli, and N. Rostoker, IEEE Transactions on Plasma Science, Vol. P5-1, p. 85, 1973.

Waisman, E., *et al.*., Above Ground Test (AGT) Evaluation Support Program, S-Cubed Quarterly Report, SSS-DPR-90-11948, Nov. 1990.

Wang, M.Y., M.S. DiCapua, "Operating Point of Long Magnetically Insulated Vacuum Transmission Lines," *J. Appl. Phys.* $\underline{51}$ (11), p. 5610, 1980.

Weber, B.V., R.J. Commisso, P.J. Goodrich, J.M. Grossman, D.D. Hinshelwood, J.C. Kellogg and P.F. Ottinger, "Investigation of Plasma Opening Switch Conduction and Opening Mechanisms," IEEE Transactions on Plasma Science, Vol. P5-19, p. 757, 1991.

Weber, B.V., J.R. Boller, R.J. Commisso, P.J. Goodrich, J.M. Grossman, D.D. Hinshelwood, J.C. Kellogg, P.F. Ottinger and G. Cooperstein, "Microsecond-Conduction-Time POS Experiments," 9th International Conference on High-Power Particle Beams, Vol. 1, p. 375, Washington, D.C., May 25-29, 1992.

APPENDIX A

CIRCUIT CHARACTERIZATION OF MAGNETICALLY INSULATED ELECTRON FLOW

from the BEAMS Proceedings, San Diego, CA June 1994

CIRCUIT CHARACTERIZATION OF MAGNETICALLY INSULATED ELECTRON FLOW

Donald E. Parks, Paul Steen
S-Cubed, Division of Maxwell Laboratories, Inc.
3398 Carmel Moutain Road
San Diego, CA 92121-1095

Abstract

We consider a switch characteristic corresponding to magnetically insulated electron flow in a gap between an effective cathode and anode. The current voltage relationship in a circuit containing parallel switch and load elements remains that of the switch independent of the load for load impedance which is not too small. This concept to which the analytic model investigated in this paper conforms is confirmed by two-dimensional PIC calculations for electron flow in a magnetically insulted gap leading into a vacuum feed terminated by a resistive load.

1. Introduction

The physical mechanisms underlying the operation of long conduction time (~1 µs) plasma opening switches have been the object of intensive research over the last decade. Although the physics of conduction in the POS is not completely understood, recent experiments point to the importance of Hall fields as well as ordinary magnetohydrodynamic (MHD) forces (resulting in a snowplow of the plasma) in the low voltage, conduction phase of the switch. The physical mechanisms that operate during current switchout to produce voltage in the switch remain less well understood, certainly quantitatively, than those that control conduction. Notwithstanding this, it is likely that plasma erosion, MHD forces, or both are involved in the opening process.

Commisso et al, have described the POS in terms of switch limited operation and load limited operation. [1] An open circuited load is an example of the former case, and the circuit I-V characteristic is that of the switch. Waisman [2] has suggested that even for finite (but not too small) load impedance and for a switch characteristic corresponding to magnetically insulated electron flow, the circuit characteristic remains that of the switch, independent of the load. This property for magnetically insulated flow will be clarified below. That the circuit properties are determined completely by the switch for sufficiently high load impedance carries with it the implication that for discharge of an inductively stored energy into a parallel switch-load combination in which the load impedance begins at a finite value, the time evolution of switch voltage remains independent of the load for some time. This notion to which the model set forth in this paper conforms is confirmed by PIC calculations for electron flow in a narrow gap opening into a vacuum feed terminated by a resistive load.

2. The Opening Gap

The physics of the opening phase of the switch is believed to involve the formation of a sheath, or gap of size D(t) which varies with time, across which the flow of electrons is inhibited by the magnetic field. Figure 1 illustrates the basic elements of the model and helps to establish notation.
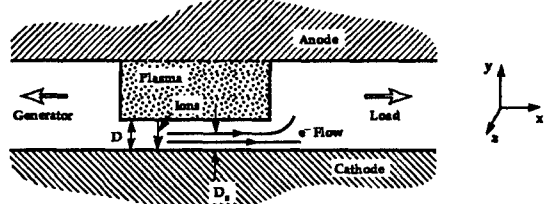
Figure 1. The Opening Model. The opening model for the switch is a one-dimensional model, assuming Brillouin electron flow parallel to the cathode and space charge limited ion flow from plasma to chathode. The gap D forms through ion erosion of the switch plasma. The height of the sheath above the cathode is D_S.

For the geometry of Figure 1, Creedon [3] derived the following relation between gap voltage V, sheath voltage V_s and anode magnetic field for Brillouin flow of electrons in the gap D,

$$\frac{eB_a D}{mc^2} = \gamma_s \left[\ell n \left[\gamma_s + \left(\gamma_s^2 - 1 \right)^{1/2} \right] + \frac{\gamma_0 - \gamma_s}{\left(\gamma_s^2 - 1 \right)^{1/2}} \right] (1)$$

where $\gamma = 1 + eV/mc^2$.

The cathode boundary field B_c for these solutions is given by $B_c = B_a/\gamma_s$, a result which holds for the flow patterns other than Brillouin flow. The value of γ_s does not follow a priori from Creedon's analysis. Wang and DiCapua [4] have proposed that γ_s follows from a minimum total energy principle, electromagnetic energy plus electron kinetic energy, and have examined the consequences of this principle for one-dimensional systems. One consequence of their analysis is that over a wide range of voltages there is little quantitative difference between the value of γ_s determined from the minimum energy principle and the value determined by requiring that the current be a minimum with respect to γ_s.

The minimum current condition yields the following relation between the diode and sheath values of γ_0

$$\gamma_0 = \gamma_m + \left(\gamma_m^2 - 1 \right)^{3/2} \ell n \left[\gamma_m + \left(\gamma_m^2 - 1 \right)^{1/2} \right] \quad (2)$$

where γ_m is the value of γ_s at the current minimum. Together with eq. (1), this result constitutes a unique diode current-voltage (I-V) characteristic. In the following, we will apply Creedon's I-V characteristic to the opening phase of the plasma opening switch.

3. Analysis of a Simple Circuit

We now consider the behavior of a circuit containing a hypothetical switch element with a current voltage relationship characterized by equations (1) and (2). We suppose that the switch element is part of the circuit represented in Figure 2 and is driven by a constant current generator. At t = 0, we impose

the initial condition that the switch carries the entire current I_0, while the current I_L in the load vanishes. For t > 0, current is switching into the load.
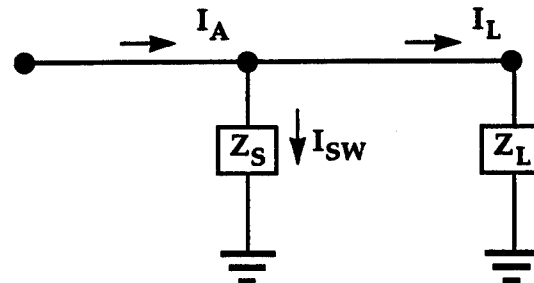
Figure 2. Circuit model with switch element charcterized by eqs. 1 and 2.

We assume that until the load current is large enough to equal the cathode current required for magnetically insulated flow, the switch operates at the current minimum, and that otherwise the value of γ_s is determined by the load current. Specifically

$$\gamma_s = \min \left(\gamma_m, I_A/I_L \right). \quad (3)$$

We shall refer to switch or load limited phases, respectively, according as γ_s is given by γ_m or I_A/I_L. In the initial phase of opening (ignoring a brief Child-Langmuir bipolar erosion phase), while $I_L \ll I_A$, the circuit is switch limited.

4. Comparison with PIC Calculations

Calculations were performed with the FRED particle-in-cell code to evaluate the accuracy of the analytic treatment of the electrons in the switch gap, to test the assumption that for small load currents the switch voltage is load independent, and to determine the fate of the electrons as they drift out of the gap. The geometry used for the calculations is shown in Figure 3.
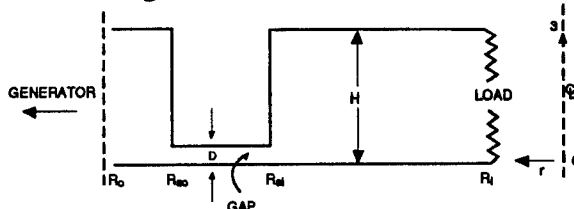
Figure 3. Geometry for PIC calculations.

The axisymmetric geometry corresponds to the top one-half of ACE-4,[5] the bottom half given by reflection of the figure in the plane z = 0. Relevant dimensions are H = 5 cm, R_i = 20 cm, R_0 = 50 cm, R_{si} = 40 cm and R_{s0} = 45 cm. The switch gap D is fixed at 0.4 cm. The tangential electric field vanishes in all boundaries except at r = R_i and r = R_0. The entire cathode surface is capable of space charge limited emission of electrons.

At the input boundary at R = R_0, the current increases on a linear ramp for 5 ns at which time it becomes constant at 4.3 MA. The load is a fixed resistor extending from cathode to anode, and for the calculations that follow is given values of 15.3 Ω, 1 Ω, 1/3 Ω and zero ohms, the first corresponding closely to open circuit conditions, the latter to more nearly matched load conditions and to an inductively short-circuited load, respectively. The inductance of the system between R_0 and R_i is about 8 nH, giving L/R times (in vacuum) ranging from about 0.5 ns at 15.3 Ω to about 25 ns at R = 1/3 Ω. We attempt to run the calculations until the system reaches a steady, or quasi-steady state corresponding to the asymptotic input current of 4.3 MA.

Figure 4 shows the voltage waveforms at various radial positions for the three values of resistance. In the 15.3 Ω and 1 Ω cases corresponding to switch limited operation the voltage achieves a steady value, apart from small oscillations consistent with a switch impedance of about 1/3 Ω. In both cases the characteristic time to achieve "steady state" voltage after allowing for the current rise time of 5 ns is consistent with the L/R time.

Run 10: 1 Ohm Load, 0.4 cm Gap
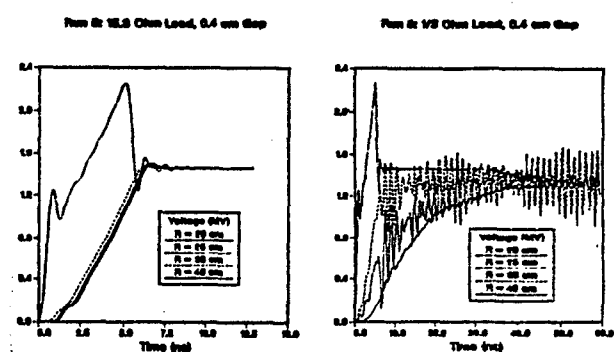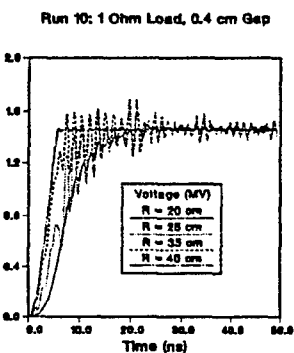
Figure 4. Voltage histories at various points in the diode for three values of load resistance.

The value of switch voltage, 1.4-1.5 MV, and impedance, 1/3 Ω, determined from the PIC results compare favorably with the results calculated from the model, Figure 5.
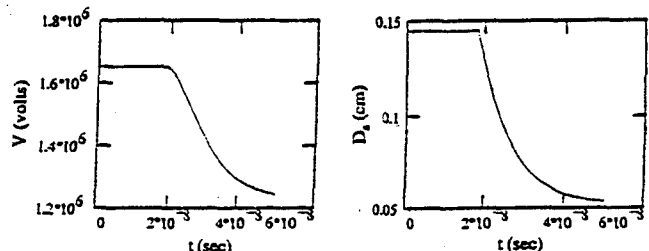
Figure 5. Gap voltage and sheath height for R_L =1/3 Ω.

The corresponding analytic result for the case of a 1 Ω and 15.3 Ω loads are precisely the same, namely, V = 1.66 MV, for t < 50 ns, based on the criterion of eq. (3) whereby the value of γ_s still is that corresponding to minimum current.

The largest perceptible differences between the 15.3 Ω and 1 Ω cases occur in the feed on the load side of the 0.4 cm gap. The salient features are the development of a potential minimum, the electron repelling electric field at the cathode, the apparent tendency toward formation of a diamagnetic current loop shielding the interior of the region from the magnetic field of the surface currents, and the closure of current paths at the cathode surface just on the upstream (generator) side of the load.[6] This closure evidently corresponds to the return of

launched electrons to the load. Similar results are reported by Grossman and Swankamp. [7]

The patterns observed for the case of a 1 Ω load are even more pronounced for the 1/3 Ω load, a case which illustrates a departure at t ≈ 20 ns from the apparent switch limited behavior for 15.3 Ω and 1 Ω loads. The potential hill and the diamagnetic current loop appear more fully developed for this case. [6]

The results of the calculations for an inductive short circuit load, Figures 6 and 7, provide the most striking example of dynamic switch limited operation. As with a resistive termination, a voltage plateau of 1.4 MV develops in the interval between about 7 ns and 20 ns, followed by a voltage collapse ending in a steady oscillation of voltage about a small value. The occurrence of this transition at about 20 ns is analogous to the one observed in the 1/3 Ω case at about 35 ns, but which is absent during the computational time interval of the 15.3 Ω and 1 Ω cases.

Figure 7. Voltage and load current for short circuit (RL=0.01Ω).

REFERENCES
1. Commisso, R.J., P.J. Goodrich, J.M. Grossman, D.D. Hinshelwood, P.F. Ottinger, and B.V. Weber, "Character-ization of a Microsecond-Conduction-Time Plasma Opening Switch," *Phys. Fluids* B4 (71), p. 2368, 1992.
2. Waisman, E., et al., Above Ground Test (AGT) Evaluation Support Program, S-Cubed Quarterly Report, SSS-DPR-90-11948, Nov. 1990.
3. Creedon, J.M., "Magnetic Cutoff in High Current Diodes," *J. Appl. Phys.* 48 (3), p. 1070, 1977.
4. Wang, M.Y., M.S. DiCapua, "Operating Point of Long Magnetically Insulated Vacuum Transmission Lines," *J. Appl. Phys.* 51 (11), p. 5610, 1980.
5. Thompson, J., P. Coleman, C. Gilbert, D. Husovsky, A.R. Miller, J. Rauch, W. Rix, K. Robertson and E. Waisman, Proceedings of the 10th International Conference on High Power Particle Beams, San Diego, CA, June 20-24, 1994.
6. Parks, D. P. Steen, R. Ingermanson, and E. Waisman, "A Plasma Opening Switch Model with Launched Electrons and Magnetically Enhanced Ion Erosion," S-Cubed Topical Report, SSS-DTR-94-14769, September 1994.
7. Grossman, J. and S. Swanekamp, BEAMS proceedings, San Diego, CA, June 1994.

Figure 6. FRED 2-D PIC simulation of ACE-4 radial geometry swtich design.

APPENDIX B

RAW DATA AND LINE INTEGRALS OF ELECTRON DENSITY
RADIAL GEOMETRY SWITCH
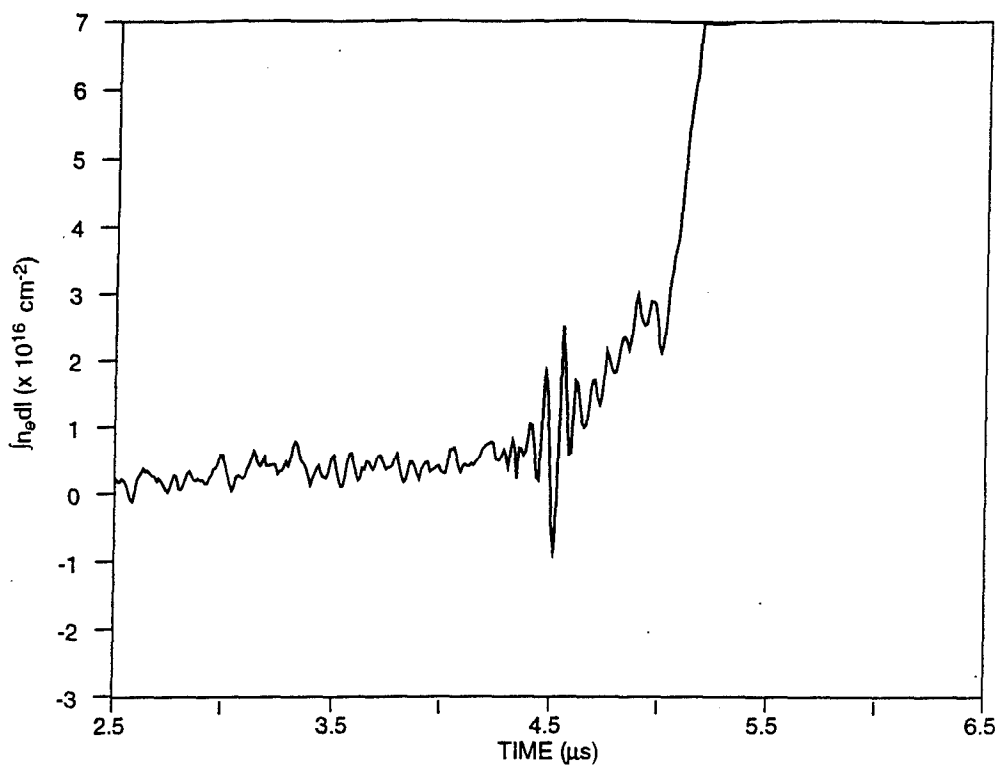
(a) Line integral of electron density, Channel 1, Shot 885
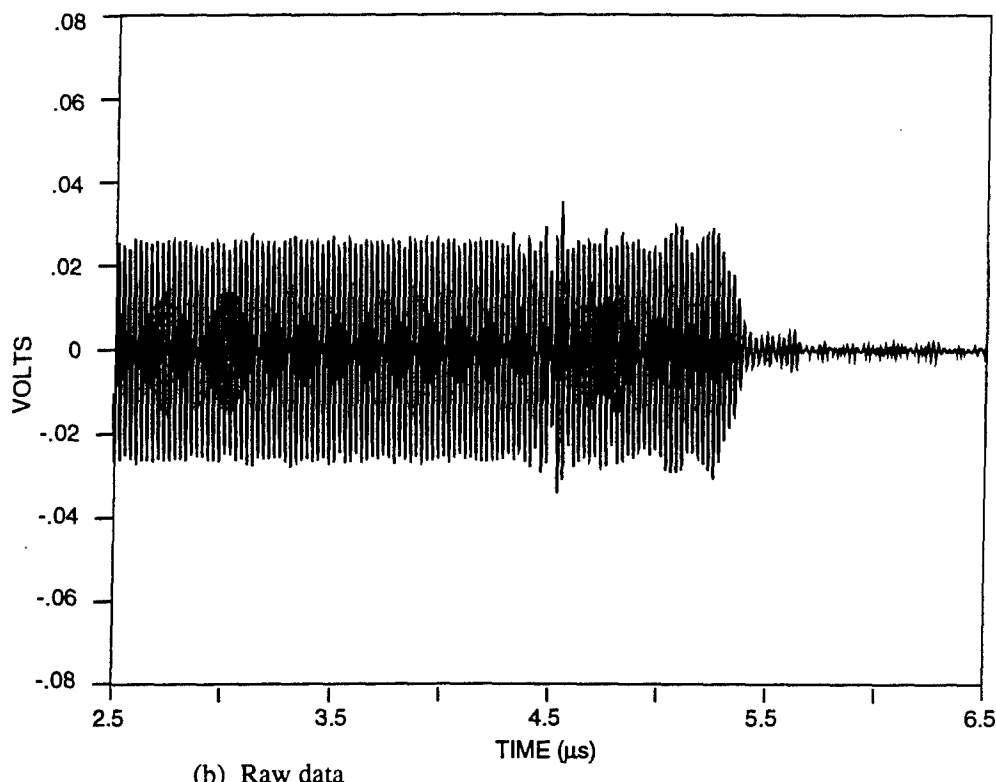
(b) Raw data

Figure B-1. Channel 1.
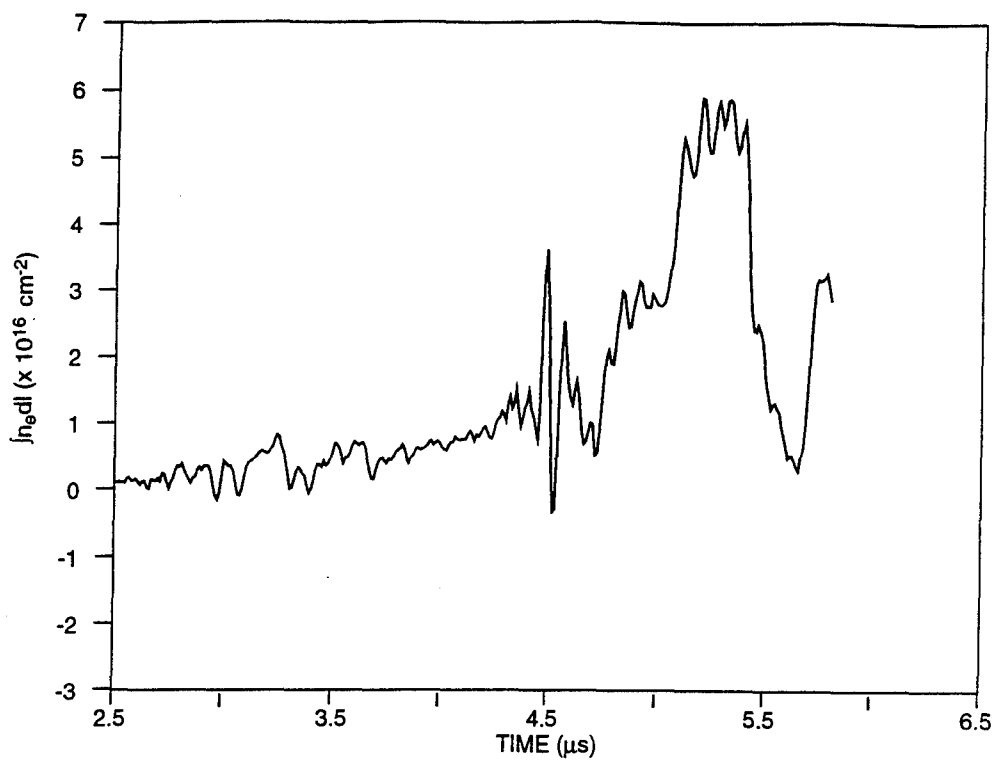
(a) Line integral of electron density, Channel 2, Shot 885
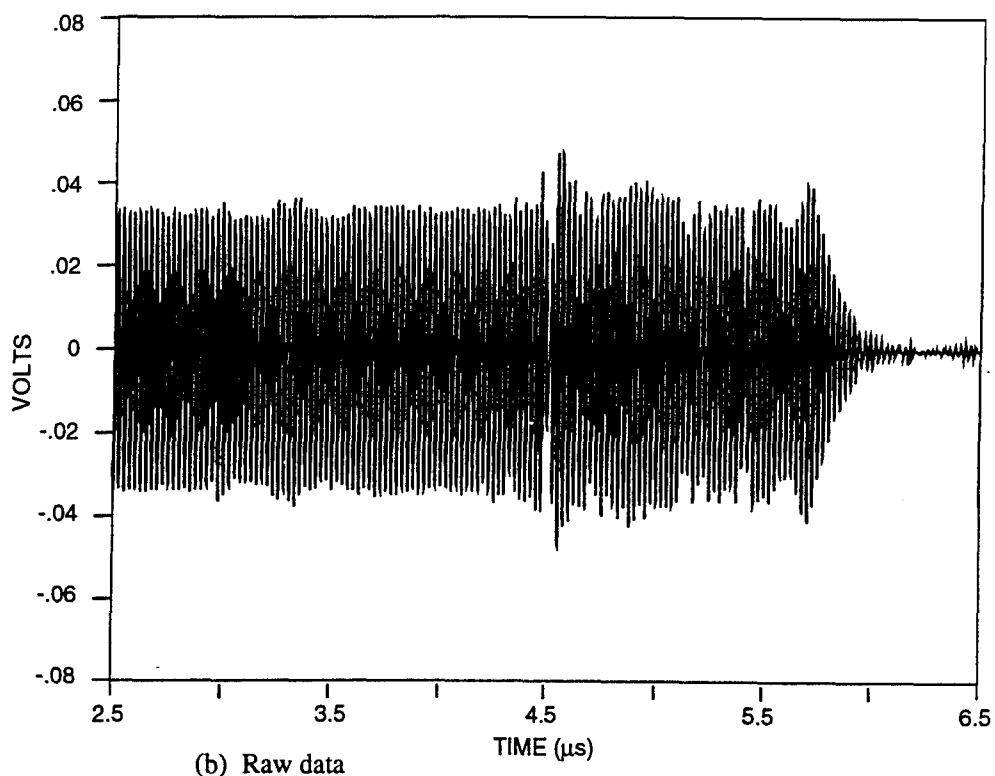
(b) Raw data

Figure B-2. Channel 2.
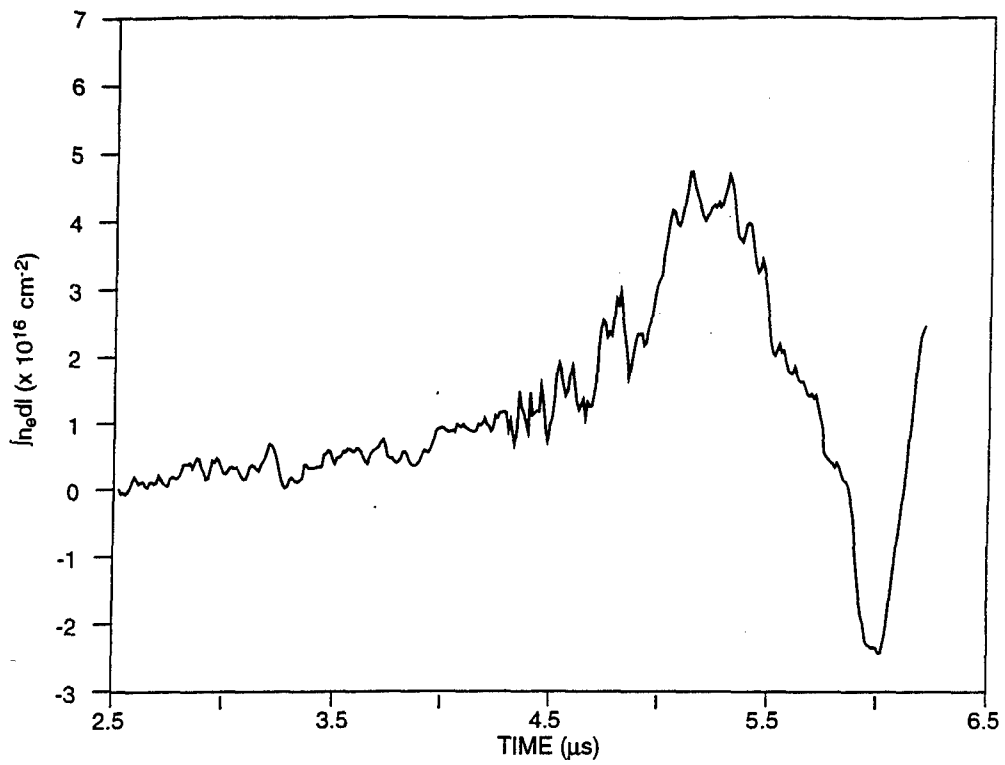
(a) Line integral of electron density, Channel 3, Shot 885
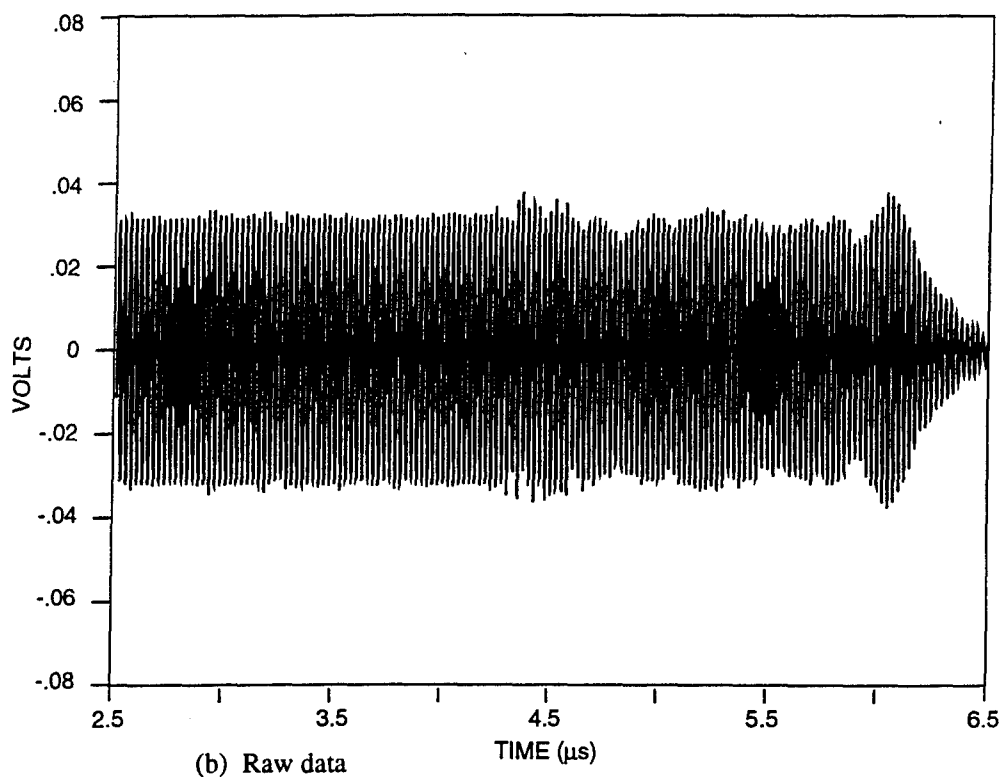
(b) Raw data

Figure B-3. Channel 3.

B-4
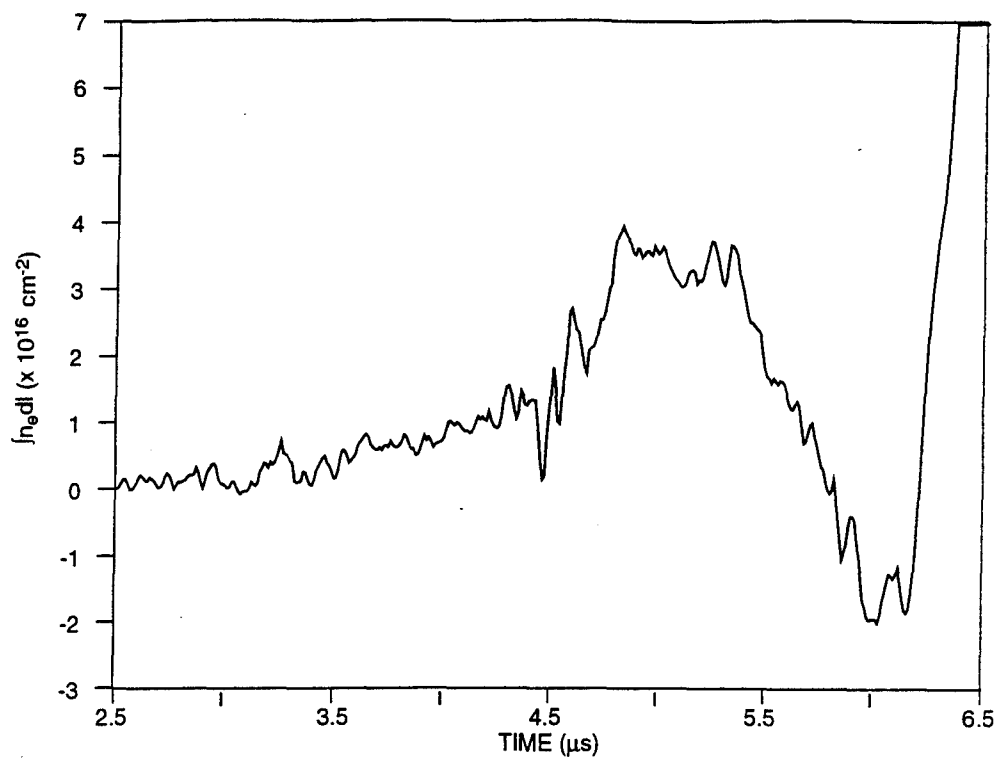
(a) Line integral of electron density, Channel 4, Shot 885
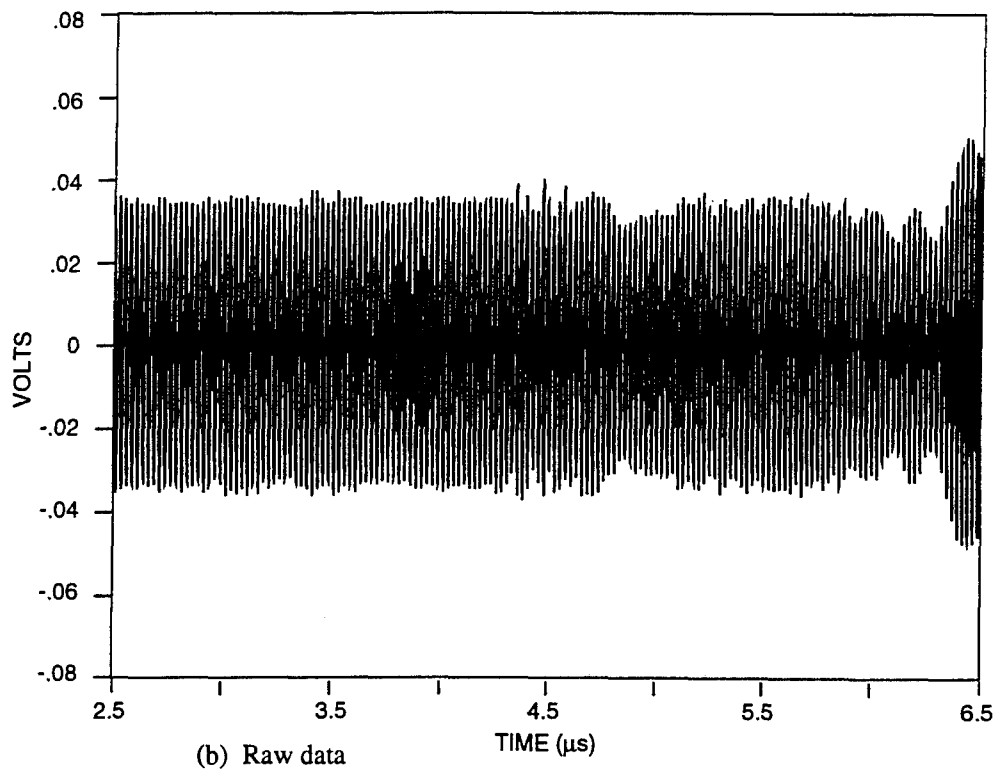
(b) Raw data

Figure B-4. Channel 4.
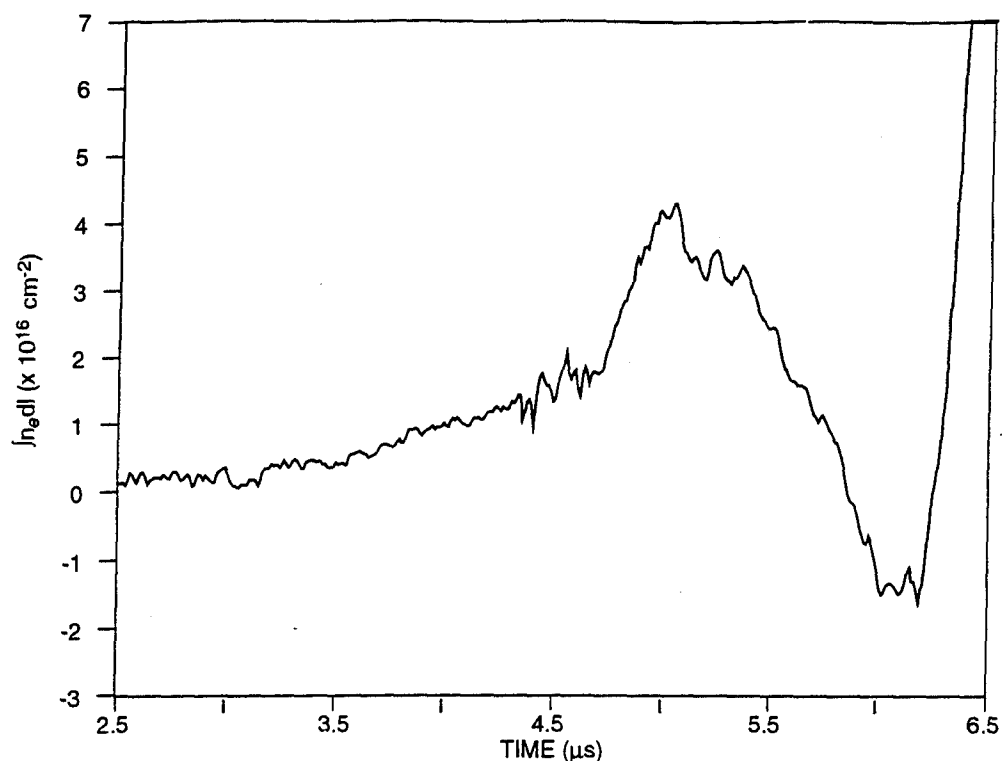
(a) Line integral of electron density, Channel 5, Shot 885
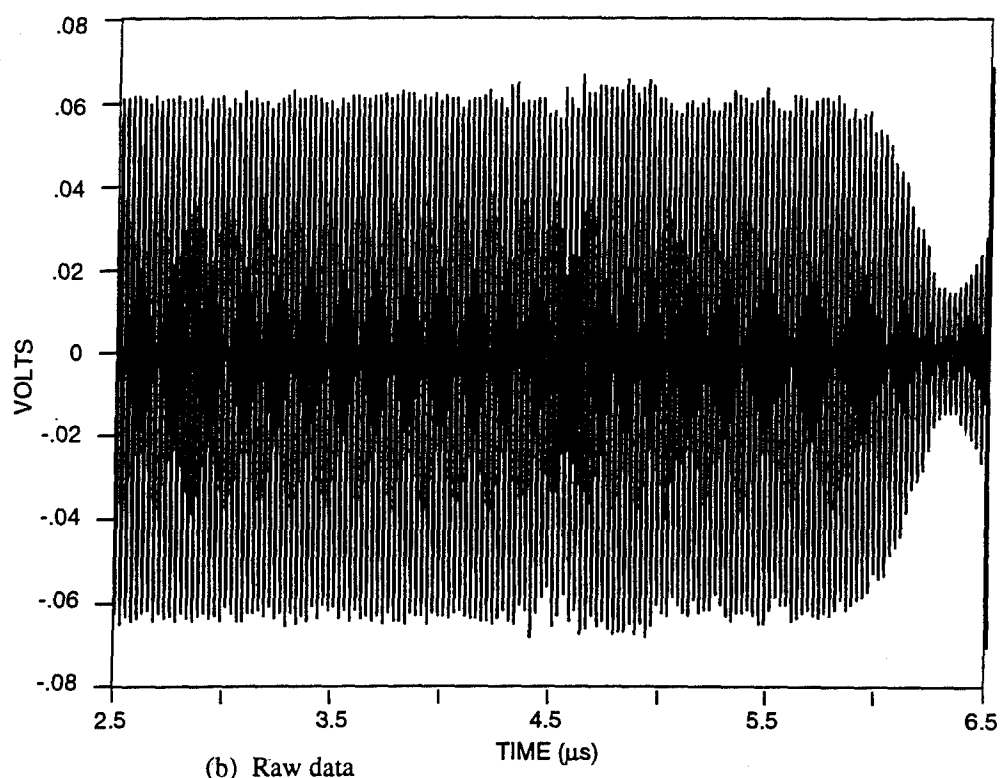
(b) Raw data

Figure B-5. Channel 5.
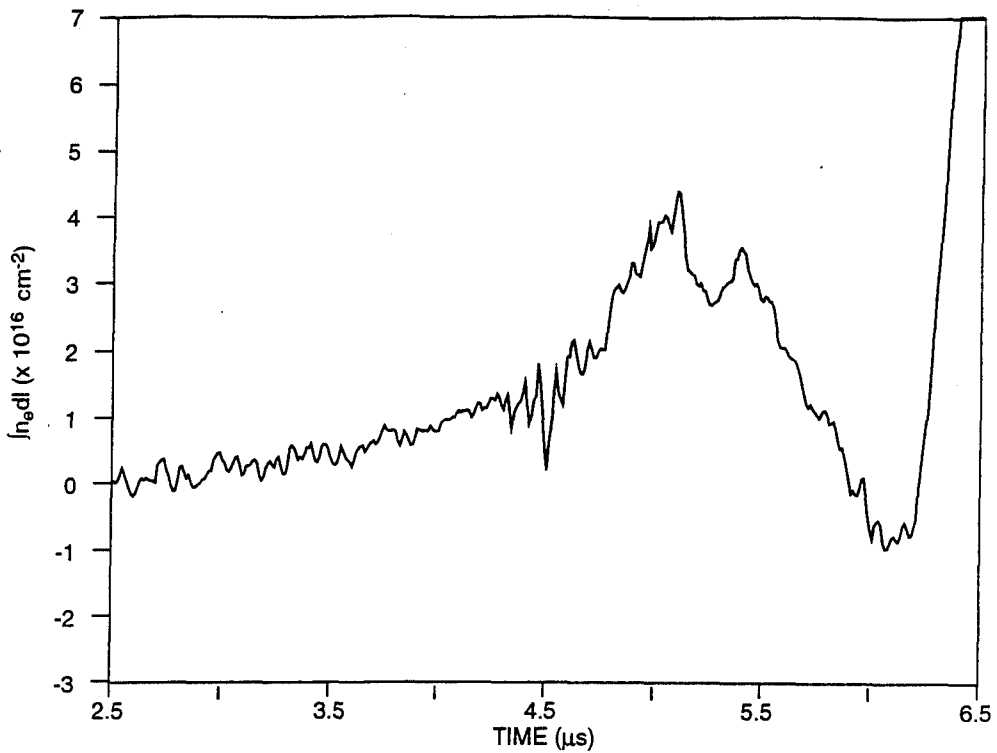
(a) Line integral of electron density, Channel 6, Shot 885
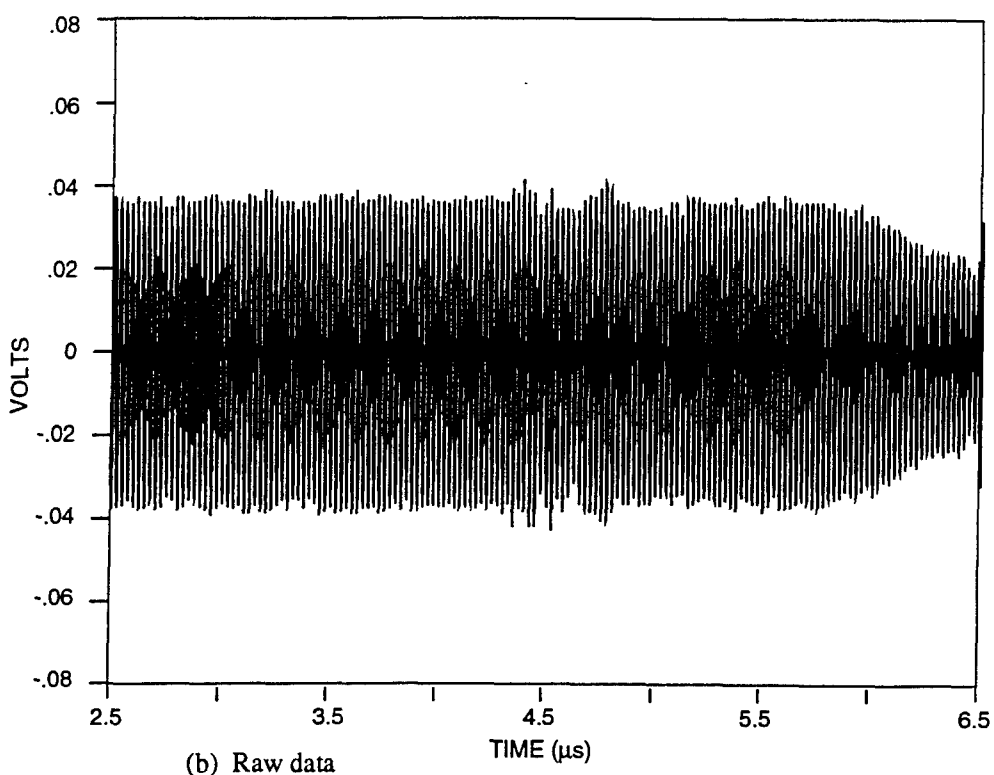
(b) Raw data

Figure B-6. Channel 6.
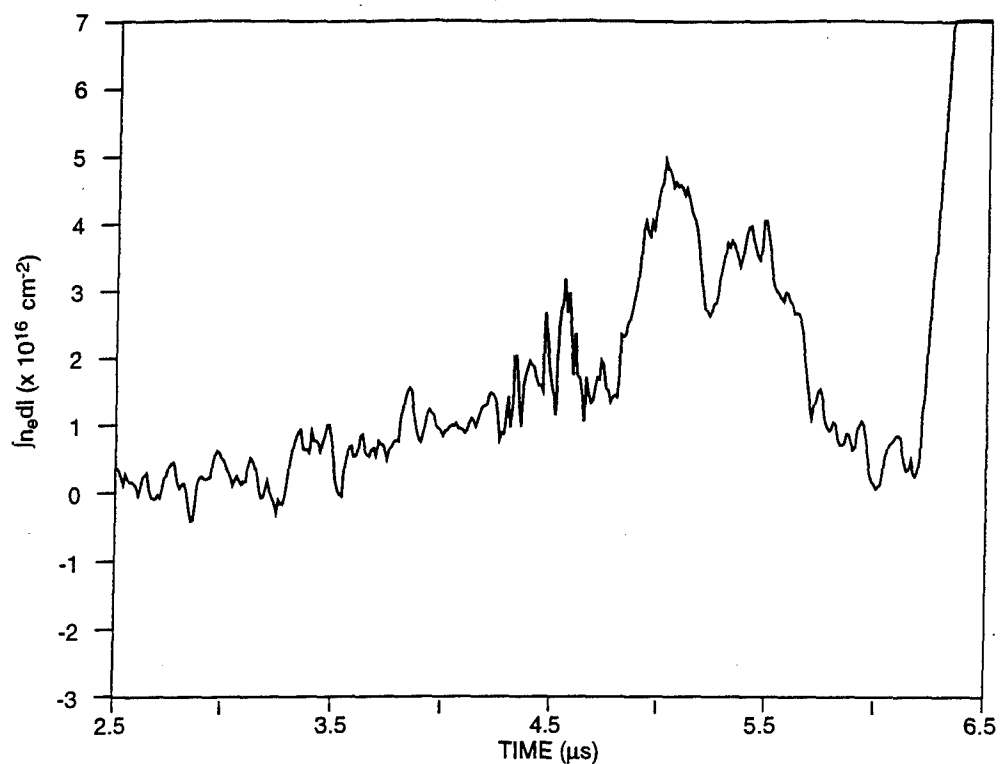
(a) Line integral of electron density, Channel 7, Shot 885
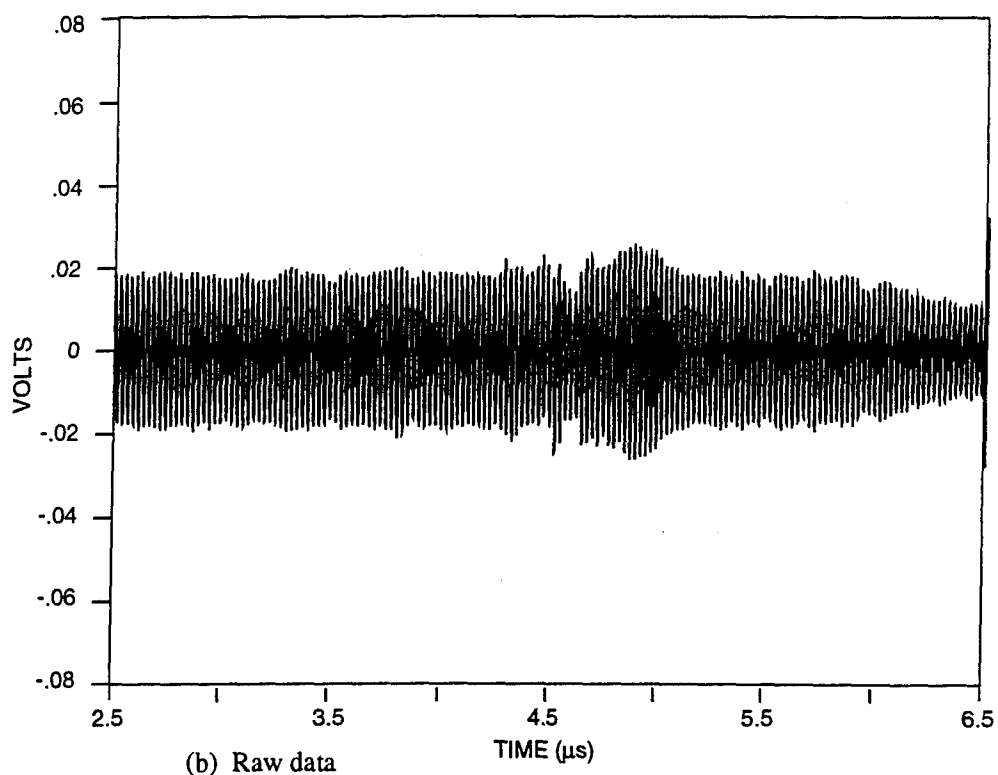
(b) Raw data

Figure B-7. Channel 7.
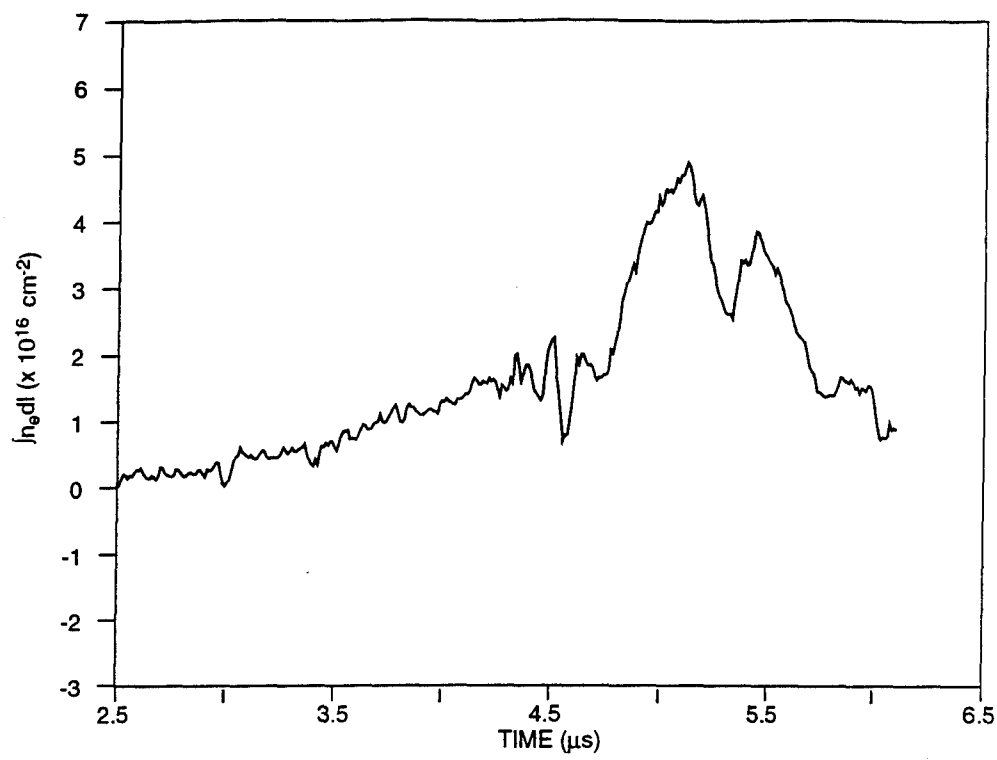
(a) Line integral of electron density, Channel 8, Shot 885
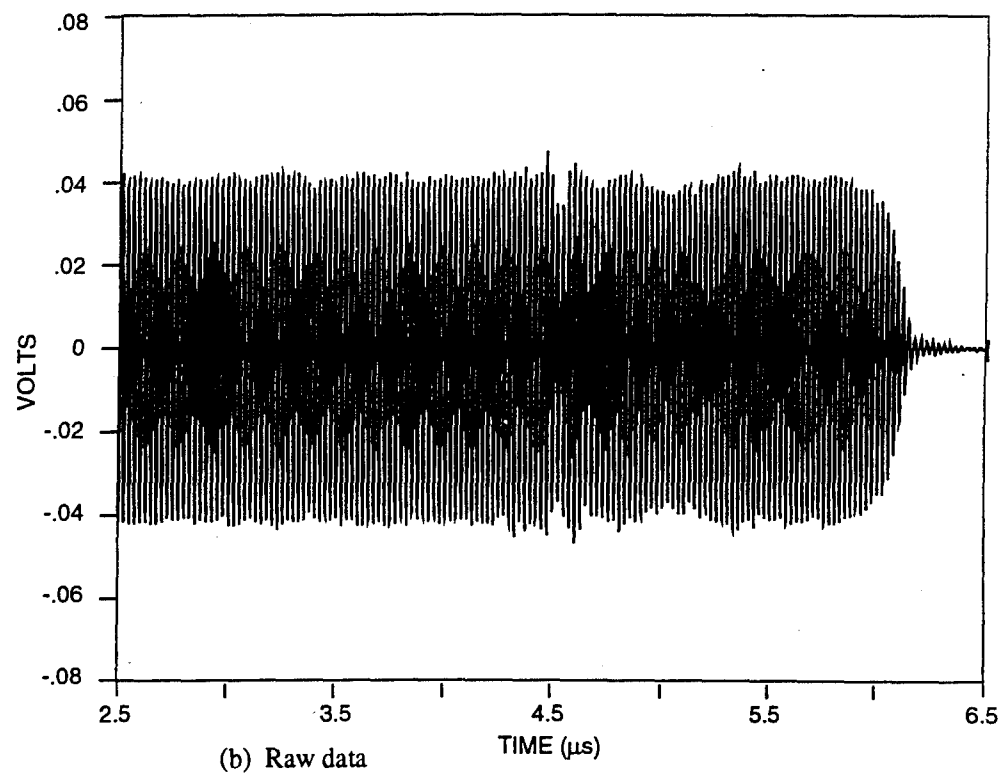
(b) Raw data

Figure B-8. Channel 8.
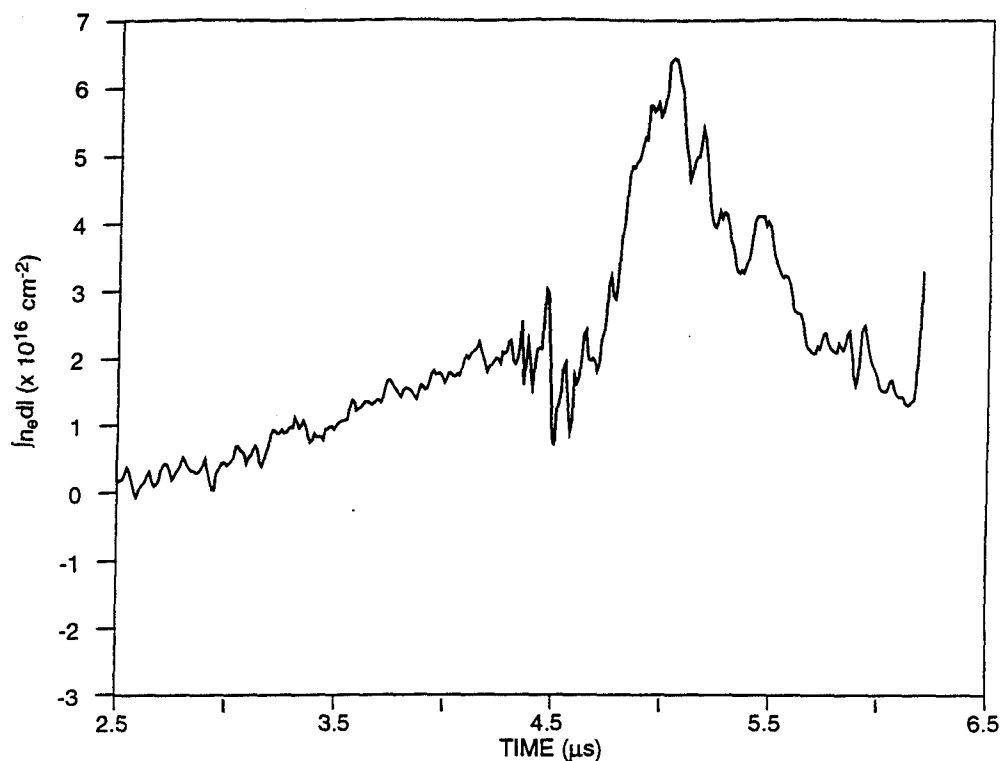
(a) Line integral of electron density, Channel 9, Shot 885
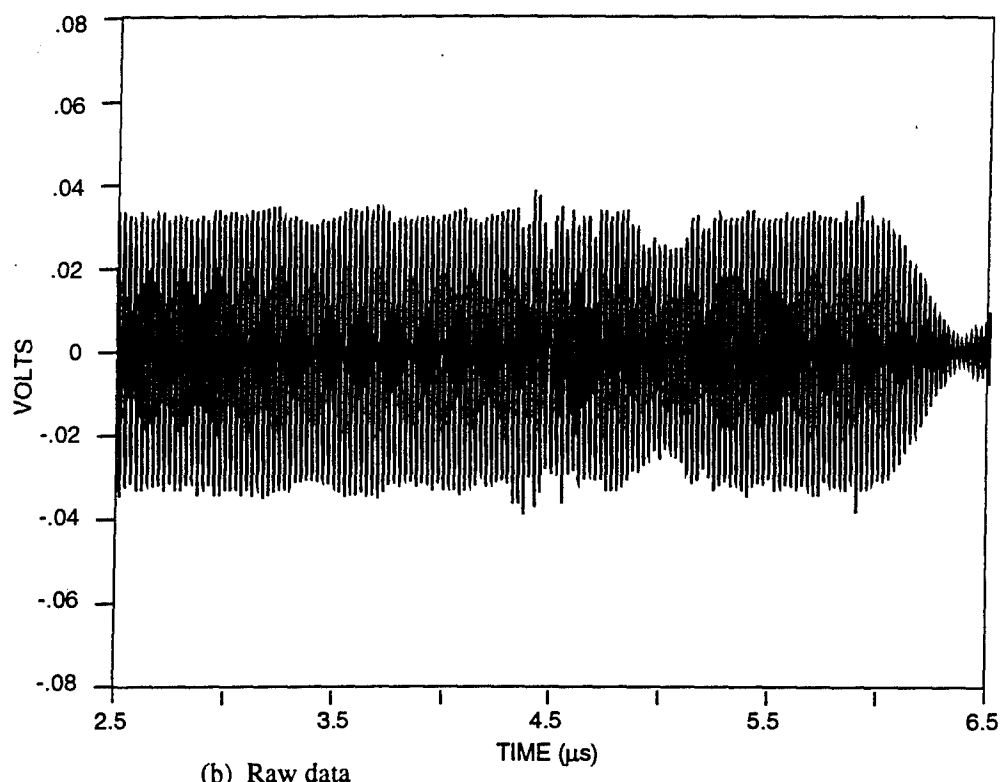
(b) Raw data

Figure B-9. Channel 9.

APPENDIX C

## RAW DATA AND LINE INTEGRALS OF ELECTRON DENSITY
COAXIAL SWITCH
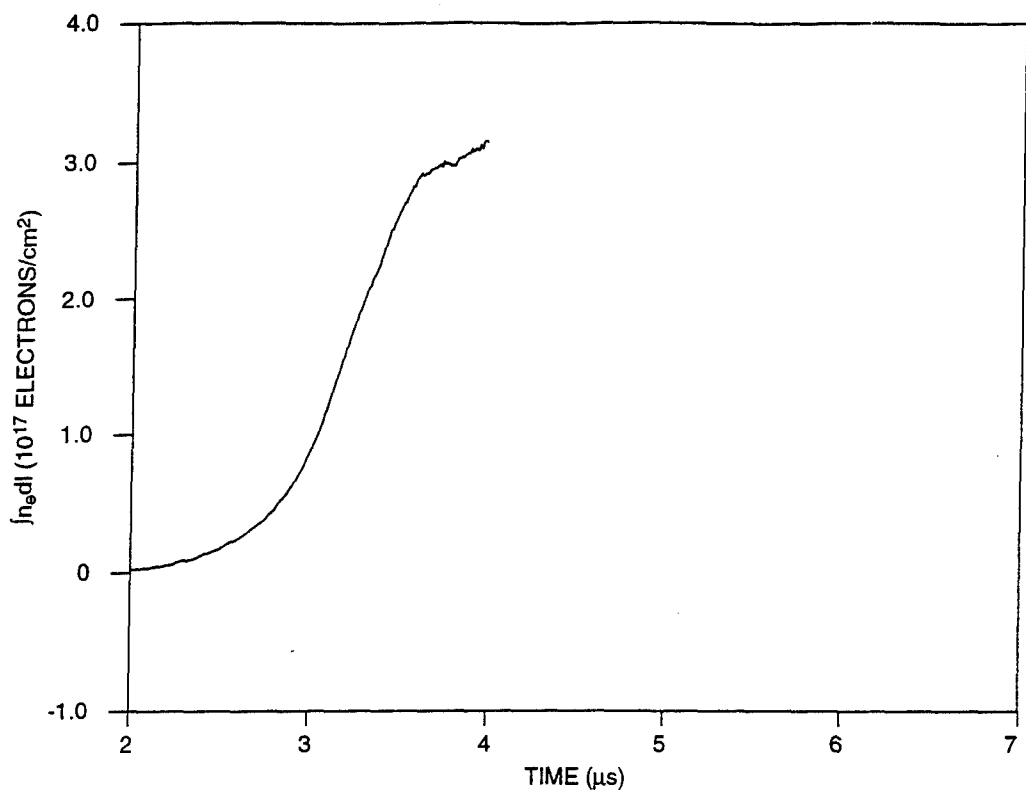
(a) Line integral of electron density, Channel #1, Shot 991
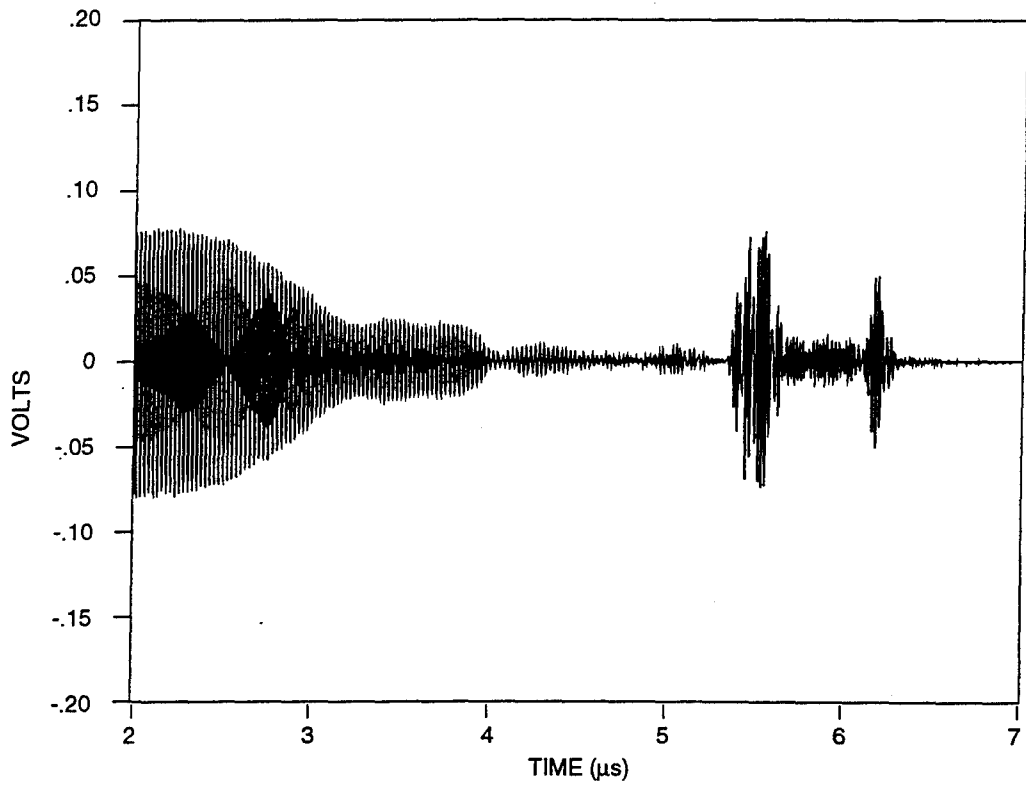
(b) Raw data from which electron densities are calculated, Channel #1, Shot 991.

Figure C-1. Channel 1.

C-2
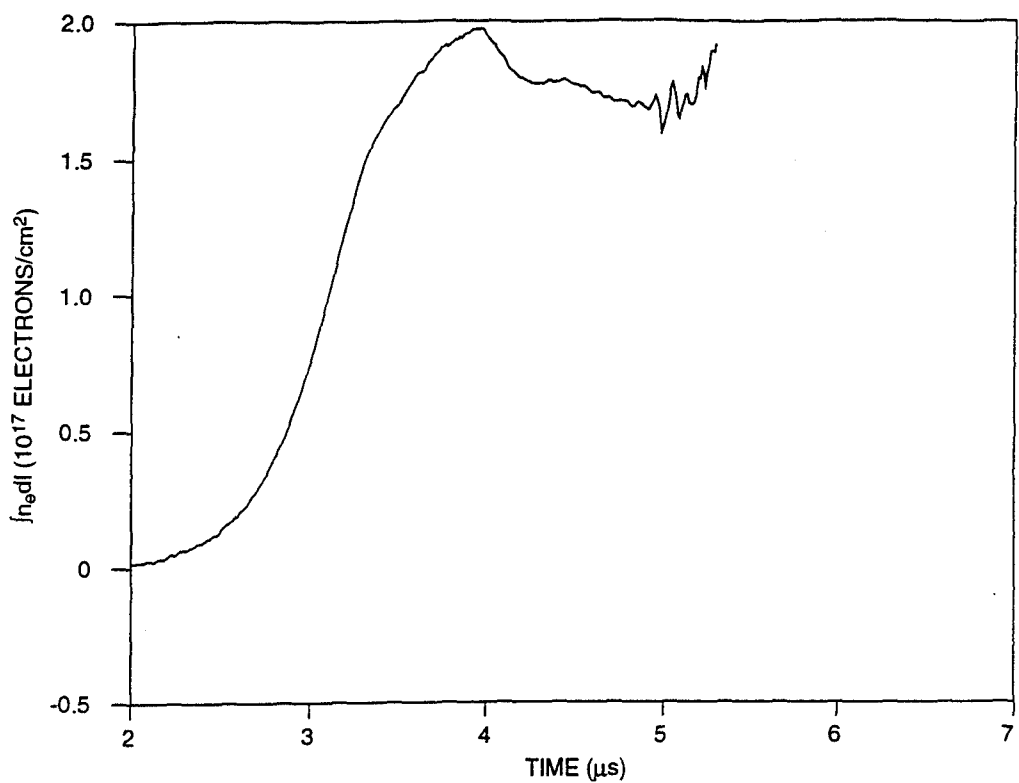
(a) Line integral of electron density, Channel #2, Shot 991
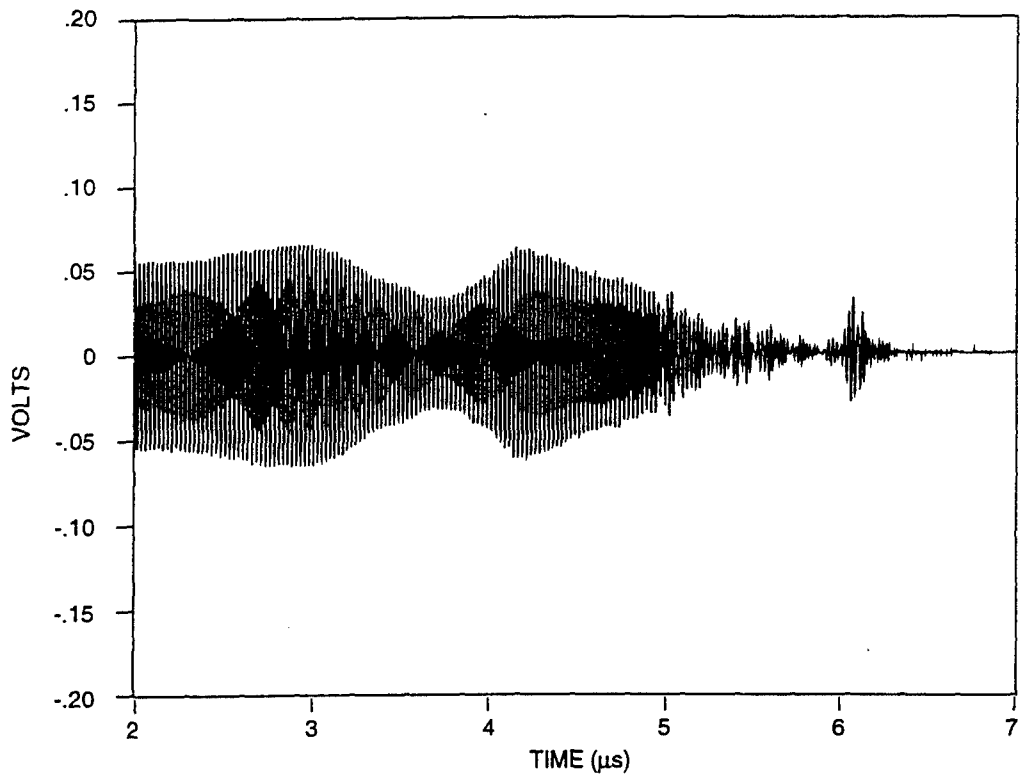
(b) Raw data from which electron densities are calculated, Channel #2, Shot 991.

Figure C-2. Channel 2.
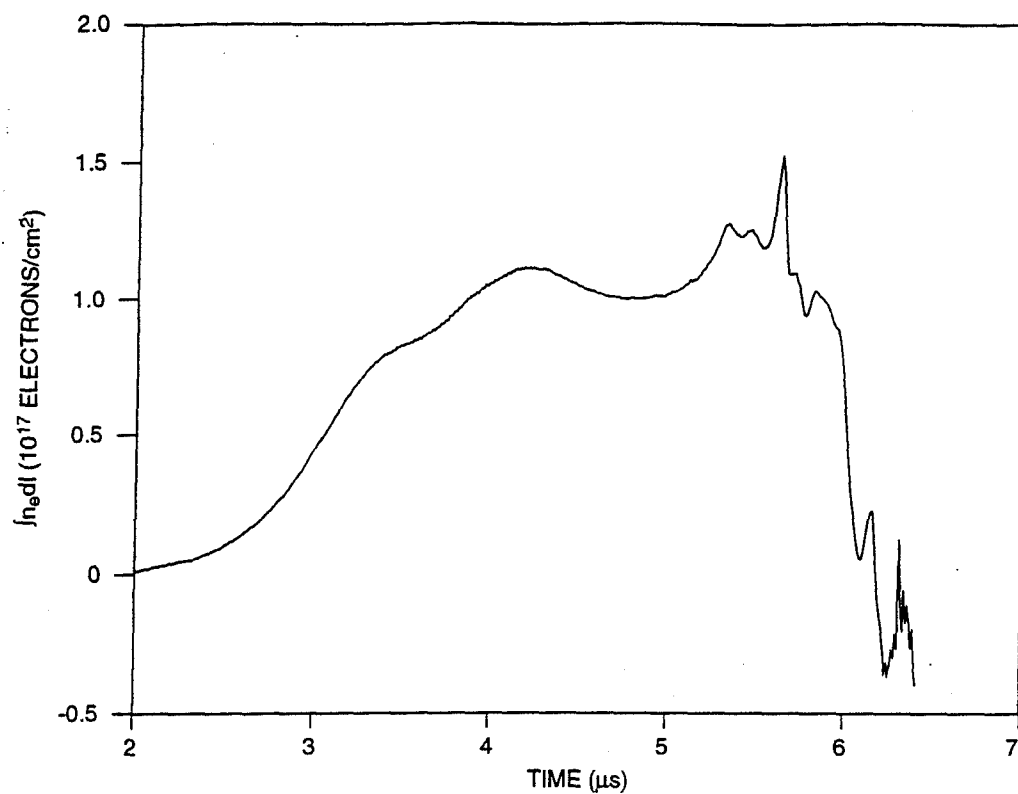
(a) Line integral of electron density, Channel #3, Shot 991
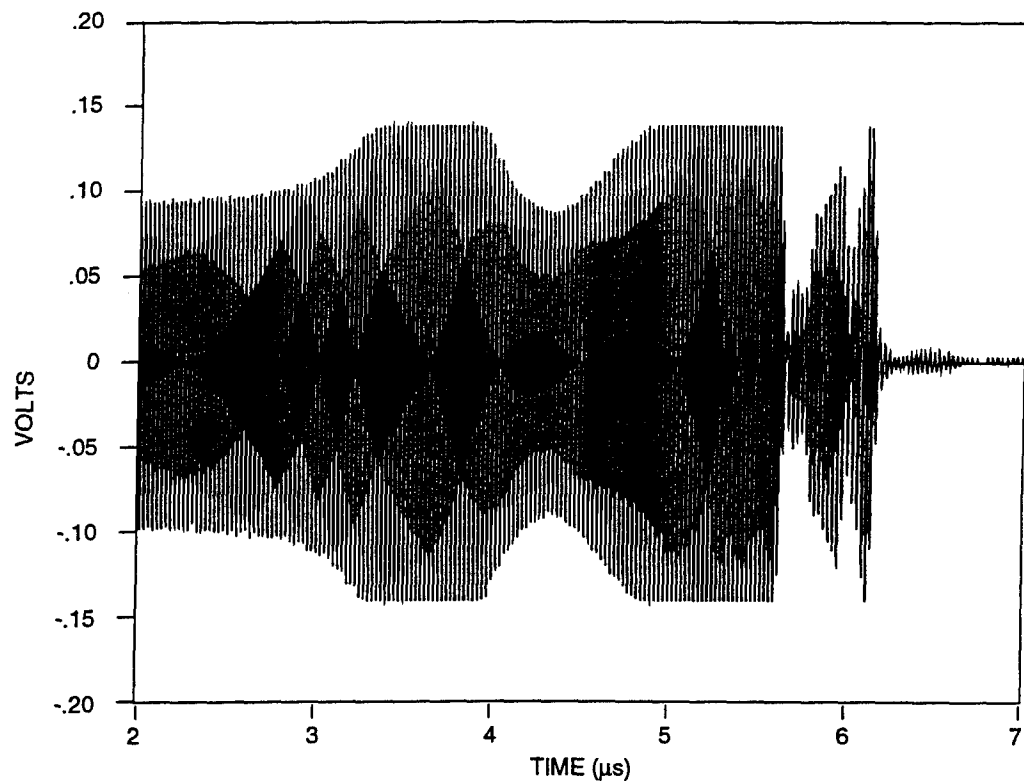
(b) Raw data from which electron densities are calculated, Channel #3, Shot 991.

Figure C-3. Channel 3.

C-4
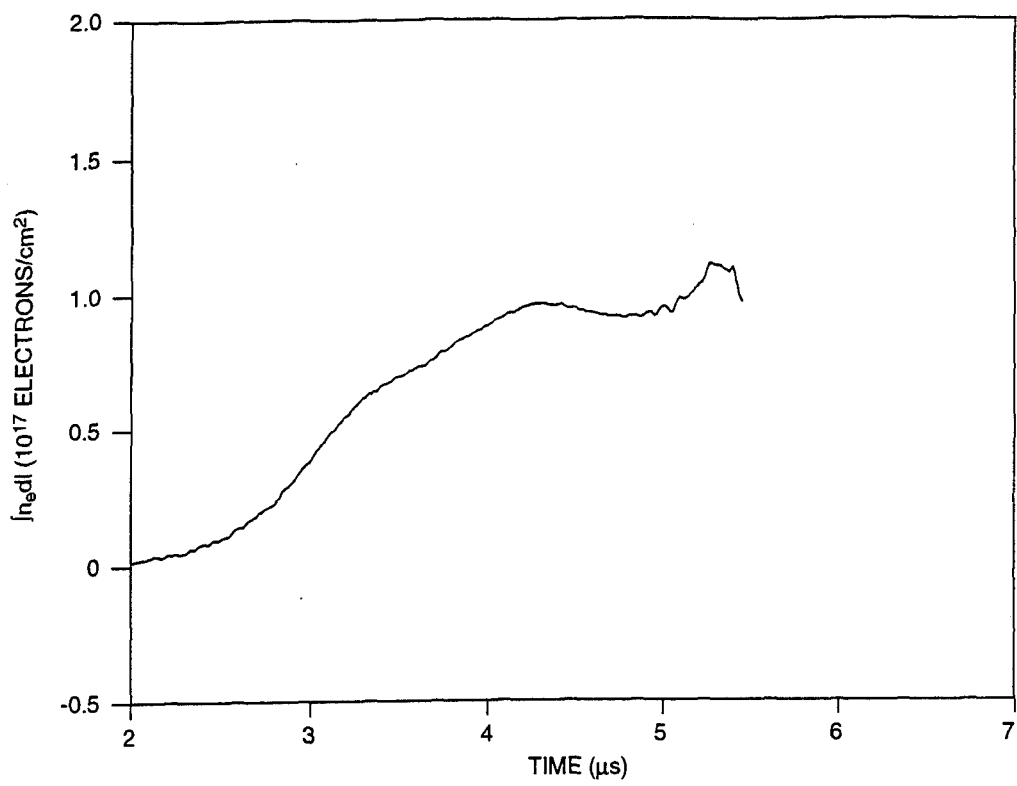
(a) Line integral of electron density, Channel #4, Shot 991
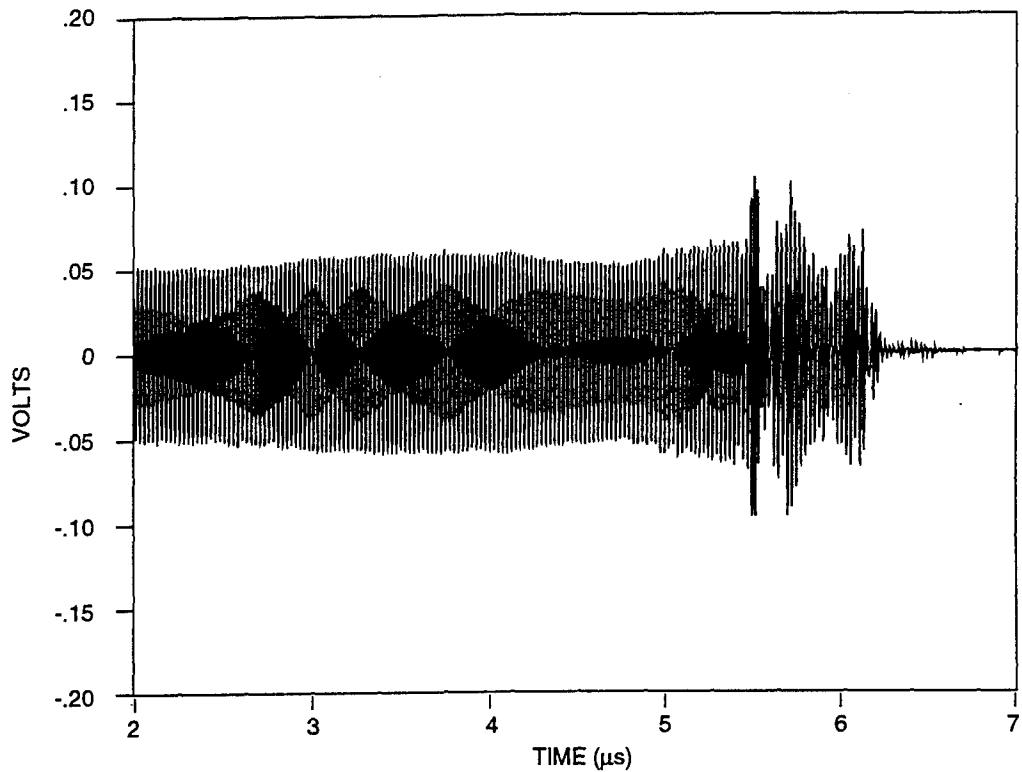
(b) Raw data from which electron densities are calculated, Channel #4, Shot 991

Figure C-4.   Channel 4.

C-5
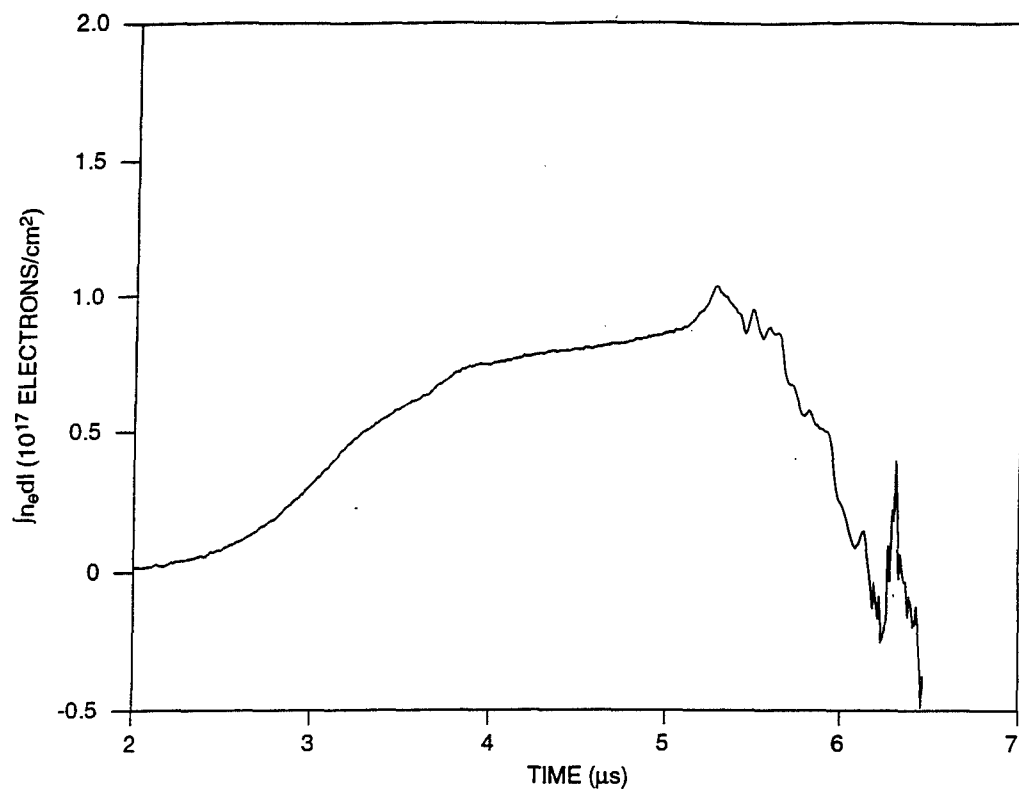
(a) Line integral of electron density, Channel #5, Shot 991
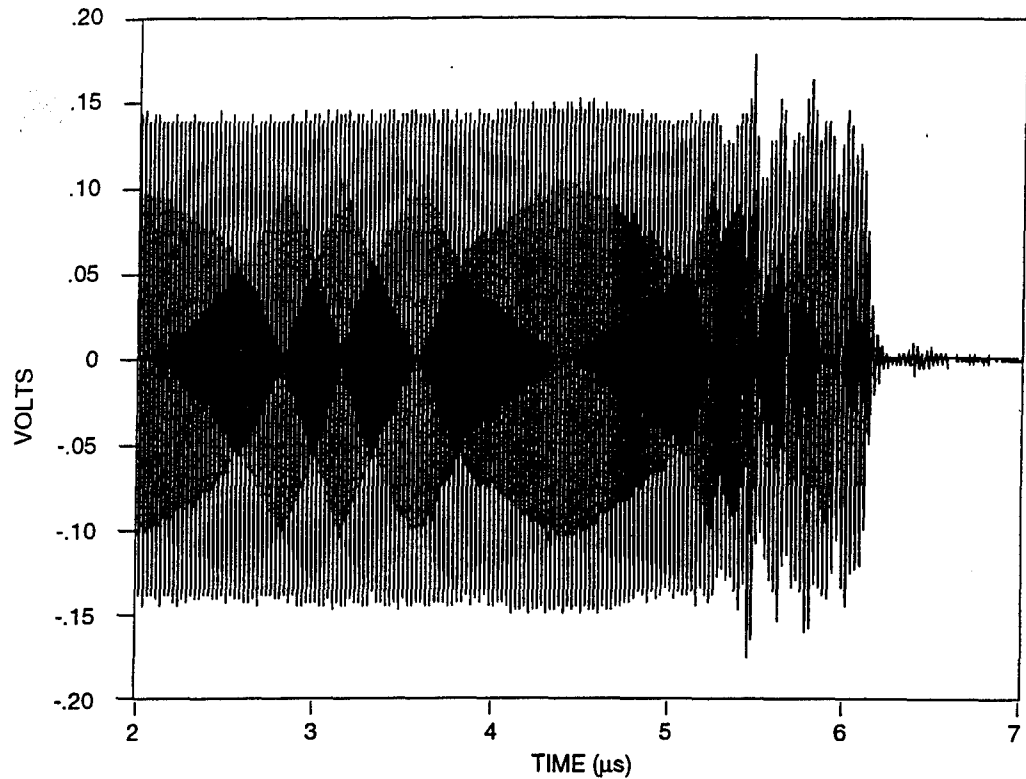
(b) Raw data from which electron densities are calculated, Channel #5, Shot 991

Figure C-5. Channel 5.
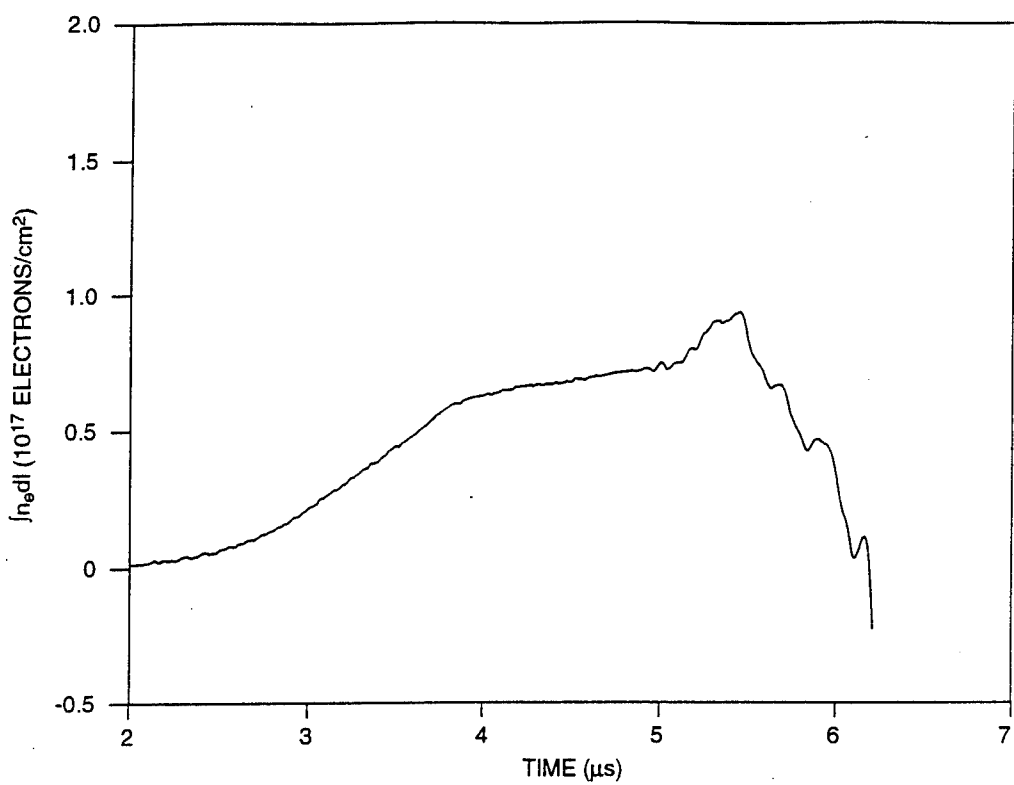
(a) Line integral of electron density, Channel #6, Shot 991
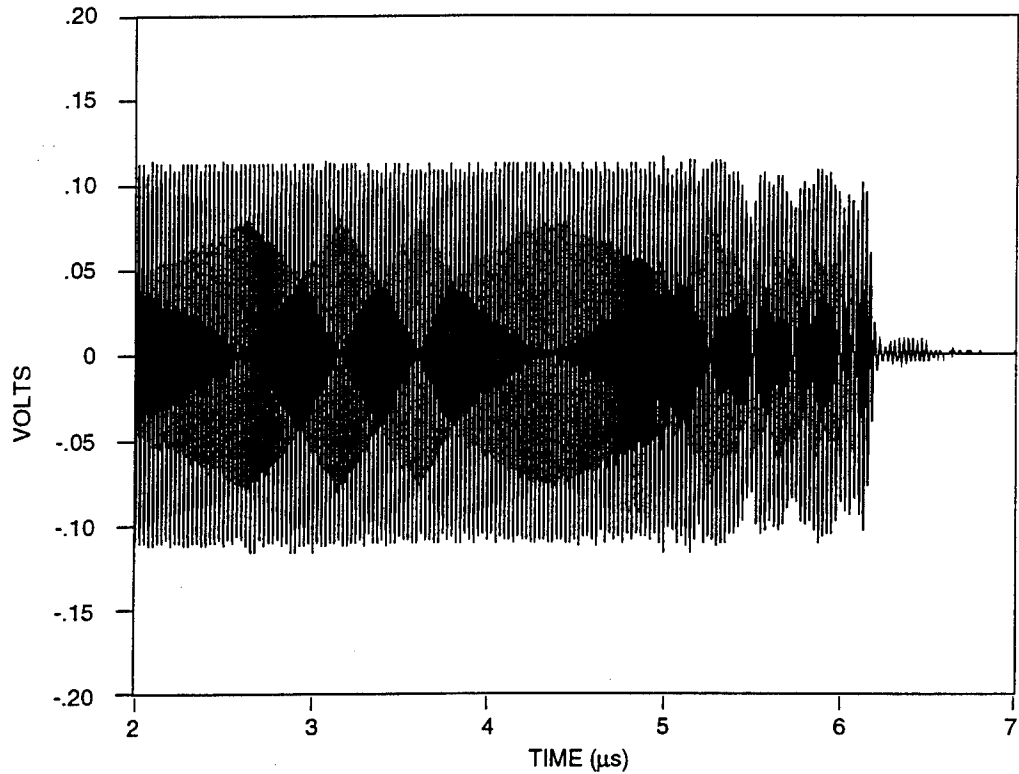

(b) Raw data from which electron densities are calculated, Channel #6, Shot 991

Figure C-6. Channel 6.
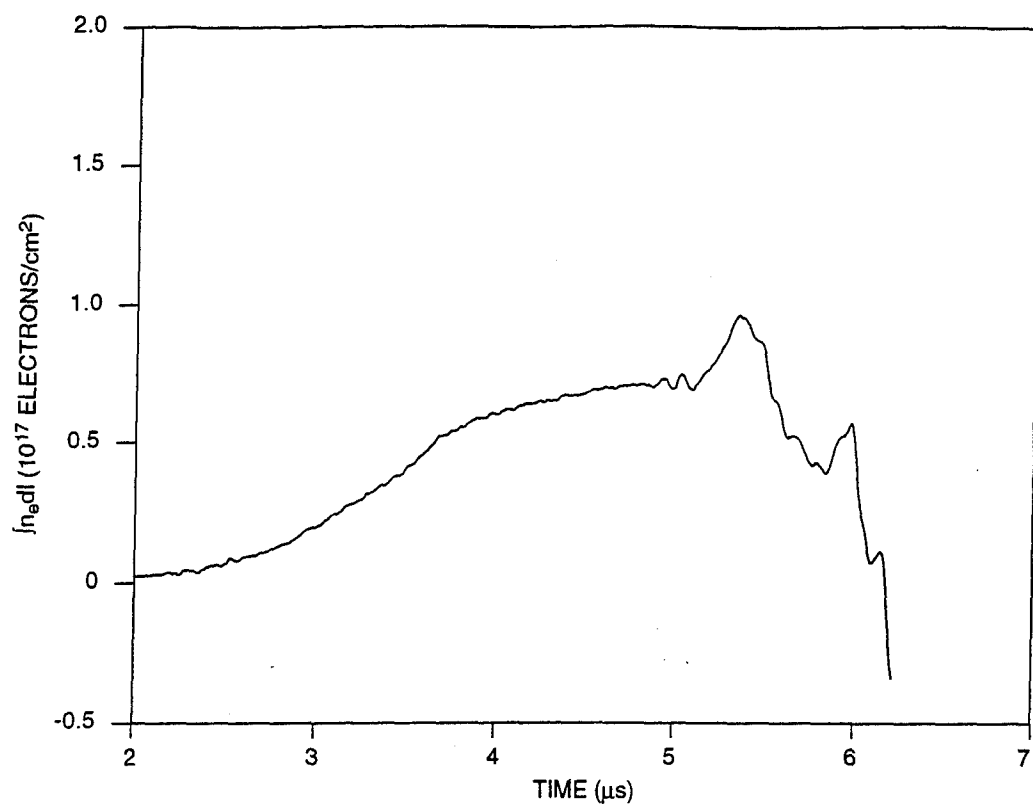
(a) Line integral of electron density, Channel #7, Shot 991
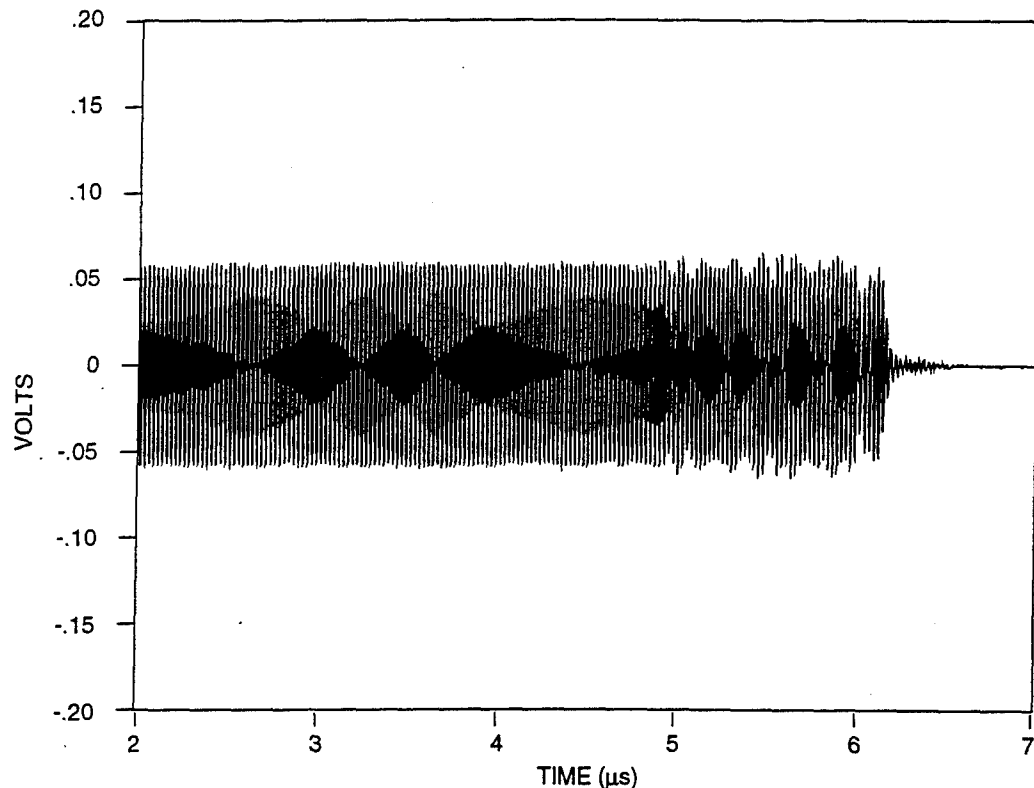
(b) Raw data from which electron densities are calculated, Channel #7, Shot 991

Figure C-7. Channel 7.

C-8
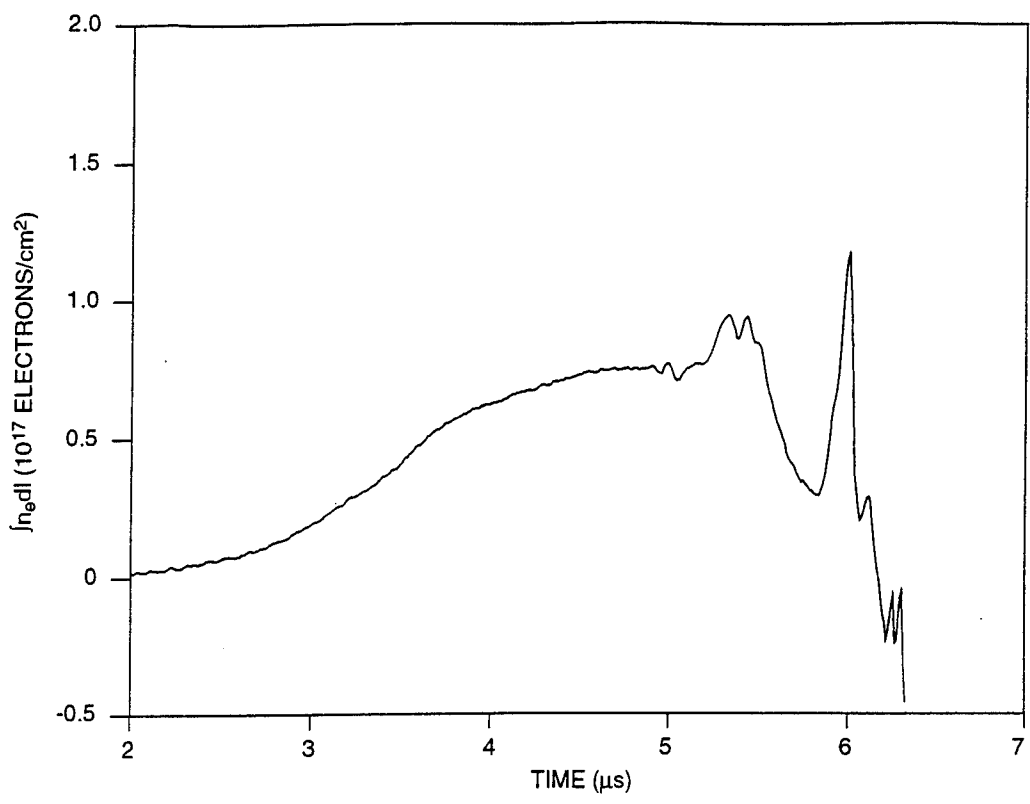
(a) Line integral of electron density, Channel #8, Shot 991
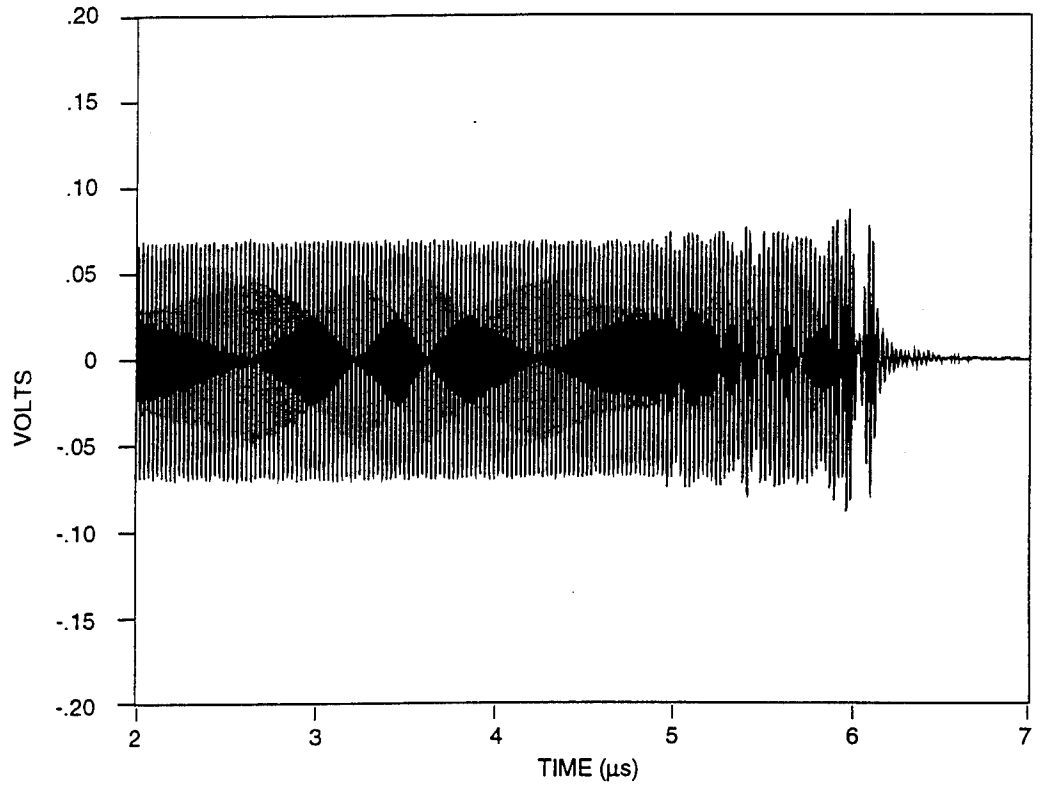
(b) Raw data from which electron densities are calculated, Channel #8, Shot 991

Figure C-8. Channel 8.
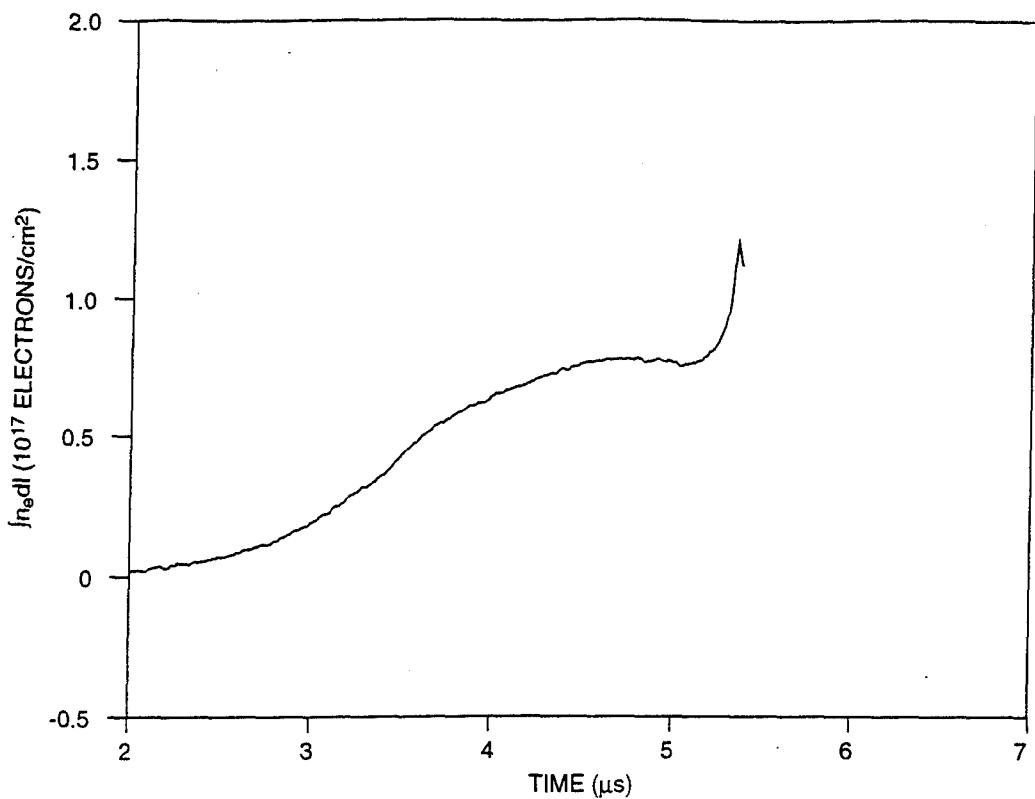
(a) Line integral of electron density, Channel #9, Shot 991
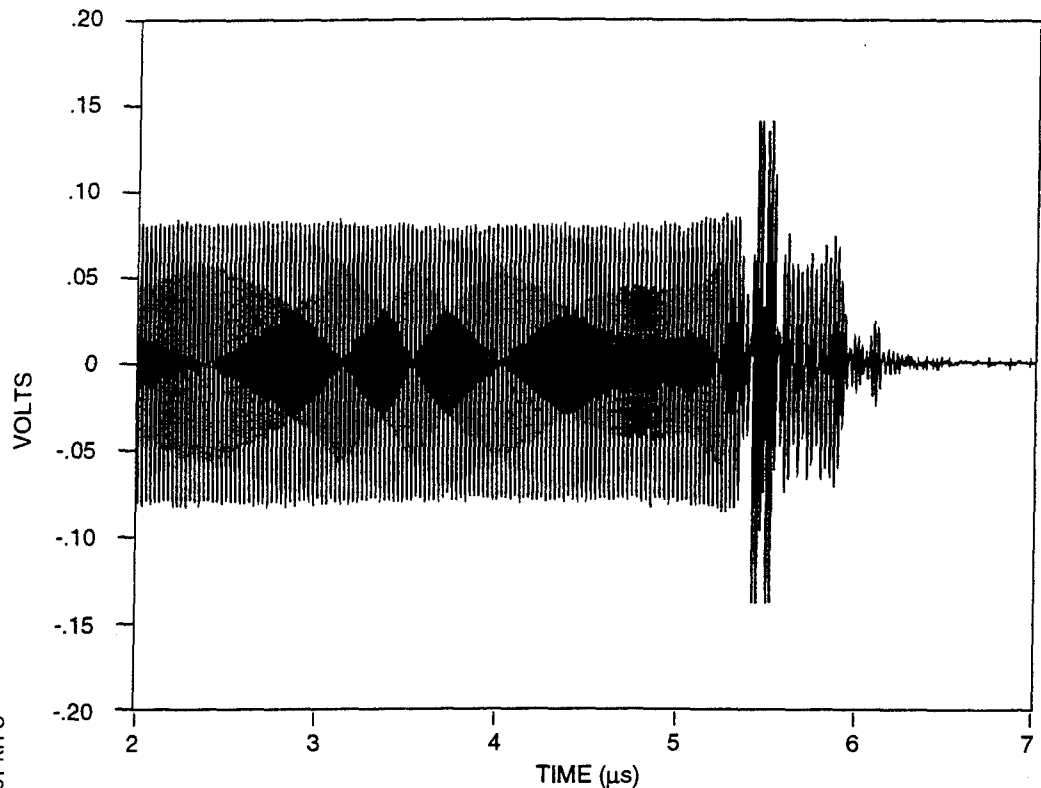
(b) Raw data from which electron densities are calculated, Channel #9, Shot 991

604-38091-KR-C

Figure C-9. Channel 9.

C-10

DISTRIBUTION LIST

DNA-TR-95-59

DEPARTMENT OF DEFENSE

DEFENSE NUCLEAR AGENCY
    ATTN: ESA W SUMMA
    ATTN: EST K WARE
2 CY ATTN: ISST

DEFENSE TECHNICAL INFORMATION CENTER
2 CY ATTN: DTIC/OCP

FIELD COMMAND DEFENSE NUCLEAR AGENCY
    ATTN: FCTT DR BALADI

DEPARTMENT OF THE ARMY

ELECTRONICS TECH & DEVICES LAB
    ATTN: PULSE POWER CTR
    ATTN: SLCET-D C THORNTON

DEPARTMENT OF THE NAVY

DEPARTMENT OF THE NAVY
    ATTN: CODE H23 V KENYON

NAVAL POSTGRADUATE SCHOOL
    ATTN: CODE 61SW F SCHWIRZKE

NAVAL RESEARCH LABORATORY
    ATTN: CODE 4770 R COMMISSO
    ATTN: CODE 6700 S OSSAKOW
    ATTN: CODE 6750 R MEGER
    ATTN: CODE 6770 G COOPERSTEIN

NAVAL SURFACE WARFARE CENTER
    ATTN: CODE B-20

DEPARTMENT OF THE AIR FORCE

AIR FORCE OFFICE OF SCIENTIFIC RSCH
    ATTN: DR R BARKER

AIR WEATHER SERVICE, MAC
    ATTN: AWS TECH LIBRARY

DEPARTMENT OF ENERGY

LOS ALAMOS NATIONAL LABORATORY
    ATTN: R REINOVSKY
    ATTN: J BROWNELL

SANDIA NATIONAL LABORATORIES
    ATTN: DIV 9341 J LEE
    ATTN: J MARTIN
    ATTN: M BUTTRAM
    ATTN: ORG 2251 J HARRIS
    ATTN: ORG 9300 RICH WESTFALL
    ATTN: ORG 9303 W BEEZHOLD
    ATTN: P ROGERS

OTHER GOVERNMENT

CENTRAL INTELLIGENCE AGENCY
    ATTN: OSWR J PINA

NASA
    ATTN: J LEE

NATIONAL INSTITUTE OF STANDARDS & TECHNOLOGY
    ATTN: R HEBNER

DEPARTMENT OF DEFENSE CONTRACTORS

APPLIED PHYSICAL ELECTRONICS RESEARCH CENTER
    ATTN: DR W NUNNALLY

BERKELEY RSCH ASSOCIATES, INC
    ATTN: R KARES
    ATTN: S BRECHT

ENERGY COMPRESSION RESEARCH CORP
    ATTN: D S WEIN

FORD MOTOR COMPANY CORPORATION
    ATTN: M MOSBROOKER

FORD MOTOR COMPANY CORPORATION
    ATTN: C NAKAYAMA

GA TECHNOLOGIES, INC
    ATTN: DOCUMENT CONTROL

JAYCOR
    ATTN: CYRUS P KNOWLES

KAMAN SCIENCES CORP
    ATTN: D MOFFETT

KAMAN SCIENCES CORPORATION
    ATTN: DASIAC

LORAL VOUTHG SYSTEMS CORP
    ATTN: LIBRARY

MAXWELL LABS, INC
2 CY ATTN: D PARKS
2 CY ATTN: E SALBERTA
2 CY ATTN: J THOMPSON
2 CY ATTN: P STEEN
2 CY ATTN: R INGERMANSON

MINNESOTA MINING &
    ATTN: D REDMOND
    ATTN: E HAMPL

MISSION RESEARCH CORP
    ATTN: B GOPLEN

PHYSICS INTERNATIONAL CO
    ATTN: C STALLINGS
    ATTN: P SINCERNY

PULSE SCIENCES, INC
    ATTN: P W SPENCE

TETRA CORP
    ATTN: W MOENY

TEXAS TECH UNIVERSITY
    ATTN: DR M KRISTIANSEN

UNIVERSAL VOLTRONICS CORP
    ATTN: W CREWSON

W J SCHAFER ASSOCIATES, INC
    ATTN: E ALCARAZ

WESTINGHOUSE STC
    ATTN: DR A H COOKSON

DIRECTORY OF OTHER

AUBURN UNIVERSITY
    ATTN: M ROSE

UNIVERSITY OF NEW YORK-BUFFALO
    ATTN: R DOLLINGER

UNIVERSITY OF CALIFORNIA-DAVIS
    ATTN: J S DEGROOT